UNIVERSITÀ DEGLI STUDI DI PADOVA

UNIVERSITY OF PADUA

CENTER OF STUDIES AND ACTIVITIES FOR SPACE - CISAS "G. COLOMBO"

Ph.D School in Sciences Technologies and Measures for Space - STMS

Astronautics and Satellite Sciences

XXVI Cycle

GEOLOGICAL CHARACTERISATION and SURFACE SPECTROSCOPY of MARS DRAINAGE NETWORKS

Ph.D School Director: Ch.mo Prof. Giampiero Naletto
Supervisor: Ch.mo Prof. Cesare Barbieri
Co-supervisor: Prof. Marcello Coradini

Ph.D Student: MAURIZIO PAJOLA

UNIVERSITÀ
DEGLI STUDI
DI PADOVA

UNIVERSITA' DEGLI STUDI DI PADOVA

CENTRO INTERDIPARTIMENTALE di STUDI ed ATTIVITA' SPAZIALI - CISAS "G. COLOMBO"

Scuola di Dottorato in Scienze Tecnologie e Misure Spaziali - STMS

Tesi di Dottorato in Astronautica e Scienze da Satellite

Ciclo XXVI

CARATTERIZZAZIONE GEOLOGICA e SPETTROFOTOMETRIA SUPERFICIALE di BACINI di DRENAGGIO MARZIANI

Direttore Scuola di Dottorato: Ch.mo Prof. Giampiero Naletto
Relatore: Ch.mo Prof. Cesare Barbieri
Correlatore: Prof. Marcello Coradini

Dottorando: MAURIZIO PAJOLA

PERASPERA AD SIDERA

to my Perseverance

FRANGAR NON FLECTAR

Sommario

Uno dei principali campi di ricerca riguardanti Marte è lo studio degli antichi processi idrologici avvenuti sulla sua superficie: se in passato vi sono state condizioni atmosferiche che hanno permesso all'acqua di essere allo stato liquido sulla superficie, si ritiene che queste possano aver favorito una chimica prebiotica Marziana, se non addirittura aver permesso la vita stessa (Ori et al., 2000). Oggigiorno, a seguito di fenomeni di metamorfismo, subduzione, vulcanismo ed erosione, la maggior parte dei fenomeni geologici avvenuti sulla crosta Terrestre nei primi miliardi di anni dalla formazione del pianeta risultano per lo più nascosti o cancellati. Nell'emisfero meridionale Marziano, al contrario, si sono preservate prove evidenti dei processi geologici attivi nel primo miliardo di anni (Milton, 1973; Schultz et al., 1973; Pieri, 1976, 1980; Carr et al., 1981). In queste zone è infatti possibile identificare antiche tracce di laghi, alvei fluviali, ed estuari.

L'aspetto più controverso che riguarda gli antichi alvei fluviali Marziani è l'origine dell'acqua che li alimentava. Nelle prime pubblicazioni scientifiche a riguardo, le frequenti morfologie a teatro dalle quali questi corsi d'acqua sembrano originarsi vengono comparate ai fenomeni erosivi simili formatisi a seguito di risorgive nel sud-ovest degli Stati Uniti e nelle Hawaii. Nei lavori di Pieri (1980) e di Pieri (1981), la caratteristica morfologica più evidente delle valli è la presenza di pareti ripide e scoscese situate alle sorgenti dei più piccoli alvei fluviali. In questi primi lavori, non fu osservata alcuna evidenza morfologica che suggerisse un'origine pluviale per queste antiche reti fluviali. Le caratteristiche topologiche di queste reti di drenaggio indicavano raffioramenti superficiali d'acqua infiltrata nel sottosuolo e la successiva formazione di un corso d'acqua. Sulla base di questi primi studi, risultò che le reti dendritiche di origine pluviale, prevalenti sulla Terra, fossero del tutto assenti su Marte. Sebbene tale conclusione rimanesse comunque incerta a causa della scarsa risoluzione delle immagini ottenute dalle sonde spaziali Mariner 9 e Viking (pari a 100-200 m), l'ipotesi che le acquee sotterranee potessero essere la causa della formazione del reticolo fluviale su Marte ottenne ampio consenso da parte della comunità scientifica internazionale (Carr, 1995).

D'altro canto, per poter incidere un alveo fluviale tramite deflusso superficiale di origine pluviale, Marte avrebbe dovuto avere una spessa e calda atmosfera in grado di supportare intense precipitazioni (Hynek et al., 2003; Masson et al., 2004).

Tramite l'analisi di nuove immagini ad alta risoluzione, THEMIS e HRSC, Masson et al. (2004) riuscí a dimostrare la presenza di valli densamente ramificate e parzialmente sepolte nella regione occidentale di Echus plateau. L'identificazione di una tale ramificazione dendritica, simile a quella Terrestre, con principi di canalizzazione localizzati a differenti quote, fu una nuove prova che Marte, in passato, potesse essere stato caratterizzato da precipitazioni intense. Successivamente, grazie all'analisi dei dati THEMIS ed HRSC, è stata possibile l'individuazione di nuove reti idrologiche

fortemente dendritiche, confutando la consolidata ipotesi secondo la quale le antiche reti fluviali Marziane fossero poco dendritiche rispetto a quelle Terrestri. Secondo Mangold et al. (2004), un alto grado di ramificazione identificato nelle valli Marziane suggerisce un'origine di tipo pluviale. Inoltre, la presenza di alvei interni e la maturità di queste reti ramificate potrebbe indicare che, sulla superficie del pianeta, in passato, vi potesse essere un clima relativamente caldo con acqua liquida che scorreva superficialmente per periodi geologicamente lunghi. In seguito ai precedenti lavori, Ansan et al. (2008), grazie all'utilizzo dei modelli digitali del terreno MOLA e HRSC, la cui risoluzione va dai 460 m fino alla decina di metri, formularono diversi ipotesi per la formazione delle valli identificate nelle regioni fortemente craterizzate situate nell'emisfero meridionale di Marte. Secondo questi studi, una combinazione di deflusso superficiale ed affioramento di acque sotterranee può essere stata l'origine della formazione di queste reti dendritiche.
Come si può evincere da questo breve excursus scientifico, il controverso aspetto riguardante la fonte d'acqua delle reti fluviali Marziane non è ancora stato univocamente identificato.

Un modo per poter indagare i processi responsabili dell'incisione delle reti fluviali Marziane, può essere eseguito attraverso molteplici confronti tra gli alvei fluviali Terrestri e Marziani (Mangold et al., 2004; Ansan et al., 2008; Som et al., 2009; Penido et al., 2013). Vi sono diversi parametri geomorfologici che permettono lo studio di una rete idrografica: uno di questi è la densità di drenaggio (definita come il rapporto tra la lunghezza totale delle aste fluviali caratterizzanti un reticolo idrografico e l'area totale del bacino di drenaggio in esame); oppure l'ordine di Strahler o di Shreve della rete idrografica (Horton, 1945; Strahler, 1952; Schumm, 1956; Shreve, 1966). Il calcolo di tutti i parametri geomorfologici dipende fortemente dalla risoluzione dei dati disponibili e dalla disponibilità di coppie stereo (Ansan et al., 2008; Hoke et al., 2009; Tanaka et al., 2009), infatti la risoluzione delle immagini e del modello 3D del terreno che se ne deriva, può sfavorire sia la possibilità di riconoscere piccole valli dendritiche, indispensabili per il calcolo dell'ordine di Strahler e Shreve, che il calcolo corretto della lunghezza 3D della rete di alvei fluviali, la quale ha un forte impatto sul calcolo del parametro di densità di drenaggio. Risulta pertanto evidente come l'utilizzo di modelli digitali del terreno ad alta risoluzione sia di fondamentale importanza per la comprensione dei sistemi fluviali Marziani. Attualmente, il DEM MOLA copre larghe porzioni della superficie di Marte ad una risoluzione di 460 m (Zuber et al., 1992; Luo et al., 2009). Tale DEM può essere efficacemente utilizzato per eseguire studi idrologici su ampia scala. Infatti, seppur esistono DEM con risoluzione più spinta (ad esempio il DEM HRCS ha una risoluzione superiore al centinaio di metri), tuttavia questi coprono solamente una piccola percentuale della superficie del pianeta.

L'obiettivo del presente lavoro di tesi è stato quello di creare un database dettagliato composto da diverse centinaia di alvei fluviali, individuati nella regione equatoriale della dicotomia Marziana. Nel lavoro vengono ricavati molteplici parametri idrologici come la lunghezza 3D, l'area di drenaggio 3D, la densità di drenaggio, l'ordine di Strahler ed il rapporto di biforcazione R_B secondo la legge di Horton 1945. Per ogni ordine di Strahler è stata calcolata la lunghezza media del ramo fluviale e, tramite la legge di Horton, il rapporto delle lunghezze R_L. Viene inoltre calcolato l'ordine di Shreve. Per ciascuna rete fluviale vengono forniti i valori della quota minima, massima e di pendenza. Particolare attenzione viene rivolta al calcolo della pendenza di ogni singola area di drenaggio. Sulle base di queste quantità, sono stati

quindi eseguiti confronti tra l'area di drenaggio e la pendenza del terreno, la lunghezza globale del reticolo fluviale e la pendenza del letto del fiume, la densità di drenaggio e la pendenza del terreno, gli ordini di Strahler e Shreve con le pendenze del terreno.

Successivamente sono state compiute attente valutazioni sulle passate condizioni climatiche di Marte, al momento in cui tali reti di alvei fluviali incidevano la superficie. Queste analisi hanno permesso di fornire originali indicazioni riguardo al deflusso superficiale fluviale, alla possibile precipitazione che interessava il pianeta e alla distribuzione dell'altitudine dei delta fluviali. Vengono inoltre presentate considerazioni su una possibile antica linea di costa oceanica in corrispondenza della scarpata che separa la regione meridionale Marziana e le pianure settentrionali.

In seguito alle sopracitate analisi, il lavoro si è concentrato sull'individuazione di antichi laghi sulla superficie del pianeta, la loro possibile relazione con un sistema idrologico regionale (Mangold et al., 2006; Schon et al., 2012) e la determinazione dei parametri lacustri che li caratterizzano. Quello dei laghi primitivi è un altro importante tema riguardante la paleoidrologia Marziana. Infatti, la loro presenza è un ulteriore indicazione della presenza stabile di antiche elevate masse d'acqua sulla superficie del pianeta (Matsubara et al., 2011). Sistemi idrologici in grado di sostenere il riempimento dei laghi, introdotti nel contesto più ampio della paleoidrologia Marziana, indicano inequivocabilmente che la fase iniziale della storia evolutiva del pianeta fosse caratterizzata dalla presenza di acqua liquida superficiale. Nel presente lavoro di tesi viene presentato un confronto tra molteplici paleolaghi Marziani e Terrestri, presentando un nuovo approccio riguardante lo spessore di sedimenti stratificati sugli antichi fondali e stimando il grado di maturità relativo di questi sedimenti.

Conclude la tesi un'analisi ed un interpretazione mineralogica della superficie Marziana effettuata attraverso dati spettrali CRISM. In particolare, tramite l'informazione multispettrale da 0.35 a 4 micron, sono state identificate diverse componenti mineralogiche presenti nei letti degli antichi fiumi, nei fondali dei laghi ed i loro affluenti ed emissari.

Contents

Abstract

The investigation of surficial aqueous processes and water bodies on early Mars is a major focus of Mars studies, because environmental conditions suitable for liquid water may have supported life or prebiotic chemistry on Mars (Ori *et al.*, 2000). Much of the geologic record from the first billion years of Earth's history has been lost to erosion, metamorphism and subduction, while on Mars the ancient terrains recording the first billion years of history are found on the southern highland plateau (Milton, 1973; Schultz *et al.*, 1973; Pieri, 1976, 1980; Carr *et al.*, 1981), whereas the northern lowland plains and western equatorial Tharsis volcanic province have been resurfaced since the time widespread valley development ceased (Parker *et al.*, 1993). Valley networks and paleolakes primarily occupy the most heavily cratered regions belonging to the southern hemisphere on Mars but they are not restricted to these areas even if they are much more uncommon on younger northern surfaces (Pieri, 1980; Parker *et al.*, 1993; Carr, 1995).

The most contentious issue regarding valley networks is their water source. The first papers on Martian fluvial landforms compared the common theatre headed valley networks to box canyons with headwall springs in the southwestern United States and Hawaii. The most striking morphological characteristic of the valleys analyzed in Pieri (1980), and in Pieri (1981), was the presence of steep-walled, cuspate terminations at the heads of the smallest tributary valleys. The existence of these terminations suggested head-ward extension sapping by basal undermining and wall collapse (Pieri, 1980, 1981, 1983). In these works no compelling evidence for rainfall erosion in network morphology and topology was observed, while sapping processes and subsurface seepage were considered consistent with observed morphologies, network topology and the location of probable fluid sources. It was derived that dendritic patterns, prevalent on Earth, were absent on Mars, but they were not *a priori* excluded, due to the fact that the resolution of Mariner 9 and Viking images was lower than 100-200 m and such small features could not been resolved. Groundwater sapping depends on spring discharge, which weathers the aquifer material, undermines the surface and extends a valley head-ward. The hypothesis that groundwater alone carved the valley networks gained wide acceptance during and after the Viking missions (Carr, 1995).
To carve valleys by overland flow, Mars would require a thicker, warmer atmosphere capable of supporting more intense rainfall or snowmelt and long-distance flow without freezing (Hynek *et al.*, 2003; Masson *et al.*, 2004). With the analysis of new and high resolution THEMIS and HRSC data, Masson *et al.* (2004) demonstrated the presence of densely branched and buried valleys in the west Echus plateau. A higher ramification with valleys heads at all elevations were proofs that dendritic valleys similar to Terrestrial features of surface runoff due to atmospheric precipitation exist on Mars. THEMIS and HRSC datasets allowed the identification of new valley networks that are strongly dendritic and dismantled the usual considerations that Martian valleys were

poorly dendritic valleys by comparison to Terrestrial river systems. The high fluvial degree of branching favors formation by atmospheric precipitation (Mangold *et al.*, 2004), while the presence of inner channels and the maturity of the branched networks were indicating sustained fluid flows over geologically long periods of time, suggesting a relative warm climate with liquid water stable at the surface. Using both MOLA and HRSC DEM's, Ansan *et al.* (2008) proposed different processes for the formation of the valley networks recognized in the heavily cratered terrain located in the Southern hemisphere of Mars and affirmed that a combination of both runoff and groundwater sapping could be the origin of these dendritic networks. This issue has not yet been resolved, but a combination of the above factors (Ansan *et al.*, 2008) may have contributed to a long-lived or episodic water cycle on early Mars.

In order to shed light on the identification of water supplies responsible for the carving of valley networks, comparisons between Earth and Mars valleys are required (Mangold *et al.*, 2004; Ansan *et al.*, 2008; Som *et al.*, 2009; Penido *et al.*, 2013). The use of the drainage density parameter, derivable from the ratio of the total length of a valley network to the drainage basin area taken into consideration, as well as the Strahler order and Shreve magnitude (Horton, 1945; Strahler, 1952; Schumm, 1956; Shreve, 1966) of the network allow to investigate fluvial processes by making correlations with the physical origin of the system. The quality of the results depends strongly on the resolution of the available data sets and on the availability of stereo pairs (Ansan *et al.*, 2008; Hoke *et al.*, 2009; Tanaka *et al.*, 2009). These data allowed us to derive Digital Elevation Model of the observed area. The resolution of the images and of the derived DEM affects both the possibility to discern small dendritic valleys, which are pivotal in the computation of the Strahler and Shreve order of the valley network, and the correct computation of the 3D length of the valley network, which has a strong impact on the computation of the drainage density parameter. This is the reason why DEM's are essential to the understanding of dendritic systems. Today MOLA DEM's cover large areas of Mars at a moderate resolution of 460 m (Zuber *et al.*, 1992; Luo *et al.*, 2009). This resolution is hardly sufficient to study the dendritic behavior of the smaller scale Martian valleys; some HRSC higher-resolution DEM's are present but they only cover a small percentage of the area we are considering in this work. Nevertheless it is worth noting that the MOLA DEM is still the best global digital elevation model of Mars to date, and it can be effectively used to perform regional hydrological studies, as our work will show, of the Mars drainage networks.

The main goal of this PhD Thesis is to create a detailed database consisting of several hundreds riverbeds, identified in the Martian dichotomy region. Many important hydrological parameter were derived such as the riverbed 3D length, the drainage 3D area, the drainage density of the riverbed network, the Strahler order for each drainage network and its frequency, deriving the bifurcation ratio R_B through Horton (1945) law of stream numbers. We then measured the mean length for each Strahler order deriving the stream length ratio R_L through Horton (1945) law of stream lengths and the Shreve magnitude. We also measured the minimum and maximum elevation value for each drainage area and riverbed. The main value we focused on is the measurement of the slope distribution for each single drainage area and riverbed network. These give us the opportunity to make drainage area-slope, length- slope, drainage density-slope, Strahler order-slope and Shreve magnitude-slope plots. These plots have permitted us to infer considerations on the past Mars climatic conditions, at least at the time when those riverbed networks incised the surface.

The analysis of our riverbeds database has also provided new hints: on the surface runoff; on the past precipitation that was carving the Martian crust; on the deltaic elevation distribution showing the possible presence of an ancient ocean coastline in front of the escarpment that separates the southern heavily cratered the rugged highlands to the northern smooth plains of Mars.

We then focused on the identification of open paleolakes on the surface, their possible relation with a regional hydrological system (Mangold *et al.*, 2006; Schon *et al.*, 2012) and the determination of their lacustrine parameters. This is another important issue of Mars paleohydrology and the presence of multiple paleolakes on the surface of Mars has shown that large bodies of water on the surface were once stable (Matsubara *et al.*, 2011). Hydrological systems capable of sustaining the filling of the lakes, put in the wider paleohydrology frame, unequivocally result in the identification of an early stage of the Martian evolutive history characterized by the presence of liquid water on the surface. We have carried out comparisons between our paleolakes and the Terrestrial ones presenting a new approach on the sediment thickness range layered on their ancient floors, estimating the relative degree of sediment filling maturity.

The final section of this work focuses on the mineralogical analysis and the interpretation of surface features carried out using the CRISM hyper spectral data. We have detected several mineralogical components, within the near-UV, the Visible and the IR wavelength range, on several locations as riverbeds floors, paleolake floors and their tributaries and outlets.

Chapter 1

Mars Paleoriverbeds: Introduction and State of the Art

1.1 Introduction

The study of surficial fluvial morphologies on Mars will provide us with a more complete picture of the past hydrological history of the red planet. Mars appears to have been characterized, in an era yet to be determined, by large quantities of liquid water (Di Achille *et al.*, 2010) sustained by an Earth-like water cycle (Ansan *et al.*, 2006). Since such surficial liquid water may imply that environmental conditions appropriate to sustain organic and prebiotic chemistry were present on Mars, the areas we studied may be considered as potential targets for landing missions searching for past and present life on Mars.

Since Mariner 9 Mars observation, it has been known that widespread valley networks characterize the heavily cratered southern plateau of the planet (Milton, 1973; Schultz *et al.*, 1973; Pieri, 1976, 1980; Carr *et al.*, 1981), while the ancient northern lowlands of Mars have been resurfaced since the time planet-wide valley development ceased (Parker *et al.*, 1993). In particular, the transition region between the southern highlands and the northern plains, characterized by a planet-wide fretted escarpment, shows noticeable valleys patterns and drainage networks (Pieri, 1980; Parker *et al.*, 1993; Carr, 1995).

A number of workers have analyzed Digital Elevation Models (DEMs) with horizontal scales which range from 1 km to few meters (Carr *et al.*, 1981; Baker *et al.*, 1985; Malin *et al.*, 2000; Williams *et al.*, 2001; Hynek *et al.*, 2003; Mangold *et al.*, 2004; Ansan *et al.*, 2006; Mest *et al.*, 2010), in order to detect riverbed networks using Viking (Pieri, 1981), THEMIS (Christensen *et al.*, 2003), MOC (Malin *et al.*, 1998) visible images and THEMIS infrared images (Hynek *et al.*, 2010).

Automated program using MOLA DEMs (Zuber *et al.*, 1992) aiming at the identification of valley drainage networks, as presented in Luo *et al.* (2006, 2009); Stepinski *et al.* (2003, 2004); Molloy *et al.* (2007), were also developed.

As shown by Ansan *et al.* (2008), it is clear that the MOLA spatial resolution of 466 meters is sufficient to map the main valleys, but the small tributaries are hardly de-

tected and they are only visible on the high-resolution imagery; hence higher-resolution DEMs are required. Nevertheless, it is worth noting that the MOLA DEM is still the best global Digital Elevation Model of Mars to date and it can be effectively used to perform regional studies of the Mars drainage networks. Indeed, HRSC DEMs only cover a small percentage of the our analysis area on Mars and its dichotomy boundary, thus not allowing a complete statistical analysis of the riverbed networks on a regional scale. For this reason we focus on, and analyze, MOLA DEM data whose results are validated through the HRSC visible and infrared high-resolution images.

1.2 State of the Art

In the following section we are going to present a brief summary of the most significant works describing the approaches, the methodologies and the analyses and interpretations of Mars paleohydrology. We are going to show the field research flow which begun more than 40 years ago, pointing out how our understanding of Martian riverbeds has developed and sometimes changed over times.

Back to Mariner 9 orbiting Mars in 1971, large and wide valley networks have been seen characterizing the heavily cratered southern plateau of the planet. The first papers dedicated to the Viking data and focusing on the processes of the Martian valleys formation were those by Pieri (1980, 1981, 1983). These works showed that there was no compelling evidence on the recently discovered Martian valleys for rainfall erosion in network morphology and topology, while sapping processes and subsurface seepage were consistent with the observed morphologies, network topology and the location of probable fluid sources. The main results coming from that data are:

- valley systems have been found in all parts of the heavily cratered terrain, the concentration of valleys appears to be greatest in the equatorial zone (10° N-10° S);
- these valleys have high densities of superimposed craters implying very long exposure;
- there is no significant difference between the density of craters in the valleys and in the surrounding terrain, implying that the valleys are roughly as old as the ancient surrounding terrain;
- dendritic patterns, prevalent on Earth, are absent on Mars; diffuse pattern, inefficient at filling space, predominate;
- valleys formed on Mars during an ancient epoch by erosional processes involving not rainfall but the movement of groundwater and its participation as liquid or a solid in the undermining of less competent strata, causing progressive head-ward collapse;
- Martian valleys are distinguished from channels by the absence in the former of the direct evidence of fluid erosion often found in the latter;
- it is possible that inner small riverbeds are too small to be seen in Mariner 9 or Viking images, although features as small as 100 m can be resolved in some Viking Orbiter images of valleys;

- the most striking morphological characteristic is the presence of steep-walled, cuspate terminations at the heads of the smallest tributary valleys, in fact the existence of steep-walled amphitheater terminations suggests head-ward extension sapping by basal undermining and wall collapse;

- valley widths are variable between less then 1 km to 10 km and lengths range from 5 km to 1 000 km;

- ancient thousand-kilometer-long channels suggest almost unimaginably large flows of water;

- even older, widely scattered valley networks, equal in size to or larger than Terrestrial canyon networks and of similar morphology, suggest persistent gound-water erosion.

These results gave birth to a new research field called Martian paleohydrology and most of the above-mentioned results were later confirmed and improved, as in Parker *et al.* (1993) who showed in addition the first possible hint of an ancient sea, or ocean, covering the northern hemisphere and supposed to receive the water coming out from the southern hemisphere riverbeds.

Following the work carried out by Milton (1973); Schultz *et al.* (1973); Pieri (1976, 1980); Carr *et al.* (1981), Carr (1995) distinguished between a fluvial channel and a fluvial valley: a river channel is a conduit that at times is filled or almost filled with water, its width is comparable to the river itself; on the other hand, a river valley is a linear depression that almost always contains river channels, generally much larger than the river itself, and stream channels. They rarely come close to being filled by water. Riverbeds may change their course, thereby causing channels to branch and rejoin, while valleys are fixed but may widen or be encroached upon as a result of competition between adjacent valleys (Carr, 1995). Carr (1995) attempted also to adopt a fourfold classification of the drainage features (but a drainage feature cannot always be unambiguously assigned to one of the four categories):

- outflow channels start several to tens of kilometers wide at discrete sources. They have few, if any, tributaries, but may divide into multiple branches downstream;

- fretted channels branch upstream and increase in size downstream; they differ from the networks in that they have floors several to tens of kilometers across on which longitudinal striations can commonly be observed. The floors are mostly flat and the walls are steep. Debris flows are common at the bases of walls;

- valley networks are composed of narrow (mostly less then 3 km wide), mostly sinuous depressions that generally increase slightly in size downslope and divide into smaller branches upslope; many narrow sinuous depressions with no branches are also included;

- lava channels are long linear channels that occur only in volcanic terrain; they commonly have levees and few, if any, branches.

More than 827 networks and channel data were detected and manually mapped by Carr (1995), confirming Pieri (1980, 1981) results, pointing out that the valley networks are found almost everywhere in the cratered uplands, but drainage densities are orders of magnitude less than on Earth. Both the low drainage density, and the short length

of most networks, combined with the probable long time over which they formed, suggested that whatever processes caused the networks, it was extremely inefficient compared with Terrestrial fluvial processes. The discovered networks have characteristics that suggest some sapping process was involved in their formation, but the occasional very dense network and origin of channels at crater rim crests enhance the process was not simply groundwater sapping.

What Martian paleohydrology shows, is that the most important evidence that water carved the surface of Mars in the distant past and hence the climate was different than today; valley network systems and drainage basin morphometry can then thoroughly used to infer past climatic conditions and the importance of precipitation.

Before the arrival of NASA *Mars Global Surveyor (MGS)*, all Martian geomorphology was based on partial and low resolution digital terrain models, but from 2001, when MGS completed its primary mission, the use of Mars Orbiter Laser Altimeter MOLA-DEM (Zuber *et al.*, 1992) onboard the spacecraft changed the way the paleohydrology field was analyzed. One cornerstone example is Hynek *et al.* (2003), which shows that the new data, complemented by the Mars Orbiter Camera (MOC, (Malin *et al.*, 1998)) wide angle global image mosaic, allow us to discover far more valley systems than previously mapped by Carr (1995). The example is the Arabia Terra area, that was previously characterized by a long trunk segment with a few minor tributaries indicating a poorly integrated and immature drainage basin.

Valley systems identified by Carr (1995) depicted low order systems, including a low number of segments with a consequent incorrect total length, and hence basin drainage densities were so low which were not comparable to the Earth ones. All these results were consistent with an immature drainage basin formed primarily by groundwater processes. Through the use of new data and the MOLA topography, (Hynek *et al.*, 2003) showed that a previous three order riverbed network reaches often a sixth order with many closely spaced tributaries. In total, the length of valley segments can be positively identified, nearly nine times more than previous efforts. Moreover, the calculated drainage density is roughly an order of magnitude larger than evident from earlier data. These drainage densities are comparable to low-end Terrestrial values determined in a similar manner for five varied regions in the United States. Hence an early precipitation and surface runoff may be necessary to explain some of the observed surface features of Mars, and thus the climate must have been significantly different in the past.

Masson *et al.* (2004) presented new observations of valley networks using THEMIS (Mars Odyssey), (Christensen *et al.*, 2003), and HRSC data (Mars Express), (Neukum *et al.*, 2004). THEMIS visible images (18m/px) showed a quite higher ramification with valleys heads at all elevations. All characteristics of these dendritic valleys were similar to Terrestrial features of surface runoff due to atmospheric precipitation. THEMIS dataset allowed to identify new valley networks that are strongly dendritic, instead of the usual considerations indicating poorly dendritic valleys by comparison to Terrestrial river systems.

Mangold *et al.* (2004) improved the results presented by Hynek *et al.* (2003) and by Masson *et al.* (2004) showing evidence for precipitation on Mars from dendritic valleys in the Valles Marineris area. The results indicate that:

- THEMIS images of Valles Marineris region show high fluvial degree of branching, this favoring the formation by atmospheric precipitation;

- the presence of inner channels and the maturity of the branched networks indicate sustained fluid flows over geologically long periods of time;
- these fluvial landforms occur during the Late Hesperian units (2.9 to 3.4 billion years old) when Mars was thought cold. This result suggest a period of warmer condition conducive to hydrological activity;
- most valleys have widths increasing from their sources to their mouth, as seen in Terrestrial valleys;
- the measured drainage density spans between 0.6 and 1.5 km^{-1}: Earth Terrestrial valley networks drainage density goes from 2 to 100 km^{-1}, but if mapped at the Viking resolution have densities of 0.1-0.2 km^{-1}. Densities measured at THEMIS and HRSC resolution, a scale slightly better than Viking mosaics, are equivalent to Terrestrial fluvial valleys mapped at the same scale;
- additional morphometric parameters such as valley order, bifurcation ratio, and valley length ratio give values similar to Terrestrial river networks for the drainages of both regions.

All these characteristics are similar to Terrestrial features of surface runoff due to atmospheric precipitation. They are inconsistent with subsurface seepage induced by hydrothermal activity because water would not seep at the crest of hills. Moreover, no valleys with theater shaped heads are observed as would be the case if sapping had occurred. Mangold *et al.* (2004) proposed that, on Mars, the formation of dendritic valleys likely involves a relative warm climate with liquid water stable at the surface for extended periods of time, and as on the Earth, Martian riverbed become mature only after several tens of thousands of years of activity.

Since the birth of Mars paleohydrology, all riverbed networks and valleys have been detected and manually mapped from different resolution images. With the arrival of MOLA data, digital elevation models spread into this research field, but still in 2007, the vast majority of riverbeds was unmapped, as presented in Molloy *et al.* (2007). Novel automatic drainage delineation algorithms were developed, specially designed for mapping valley networks from digital elevation data, as, for example, Molloy *et al.* (2007); Luo *et al.* (2009). Founding a good agreement between delineated and mapped networks Molloy *et al.* (2007) and Luo *et al.* (2009) pointed out that in the process of comparing manual and delineated networks some shortcomings of manual mapping became apparent. Consequently they argued that delineated networks are indeed of better quality than the networks manually mapped from images. Luo *et al.* (2009) itself derived new maps showing an increase in the total number of discovered valley of 24 941[1].

Ansan *et al.* (2008) summarized the different processes proposed, since 1971 to date, to explain the wide-spread valley networks recognized in the heavily cratered terrain located in the Southern hemisphere of Mars:

- surface runoff (because of their resemblance to the Terrestrial fluvial valley networks), which happens when the water flow occurs at the surface, as the soil is infiltrated to full capacity and excess water from rain, melting of snow or

[1]The unavoidable problem of automatic detecting routines is that manual editing on the results is still clearly necessary in order to remove spurious valley detections (faults, troughs unrelated to fluvial activity)

glaciers; this is often rejected because of the low drainage density and the low degree of valley organization;

- groundwater sapping triggered by geothermal and hydrothermal heating; this process occurs when groundwater exits a bank or hillslope laterally as seeps and springs and erodes soil from the slope. The erosion by sapping is one of the processes involved in the formation of gullies and tends to produce steep-sided V-shaped valleys of fairly uniform width. On Mars this process is supported in few places by regional volcanic and tectonic context.

Ansan *et al.* (2008) made use of the new data, HRSC DEMs with spatial resolution around 50 m/px, to better constrain the geometry of valley networks performed from HRSC visible images. They showed that the derived drainage density increases from MOLA data to HRSC DEM, but is still slightly lower than the value that one obtains in the manual mapping. Through these results it was indicated that the most likely process for the formation of the Martian riverbeds was a combination of both surface runoff and groundwater sapping origin.

Hoke *et al.* (2009) underlined that the determination of stream order, stream length and drainage density is greatly affected by the ability to identify the small, shallow tributaries. The identification of small tributaries depends on the resolution and coverage of the data used to map the valley networks. Combining THEMIS daytime IR and MOLA topographic data the identification of valley networks is improved over THEMIS or MOLA alone, resulting in a superior data set for accurate mapping and analysis of the valley networks on Mars. Within this work they claim that all of the valley networks show characteristics consistent with formation by precipitation, including densely spaced dendritic form with interiors that increase in width and depth downstream. Sinuous main trunks and major tributaries occasionally also exhibit multiple interior channels, braiding, and terracing; as well as tributaries that often reach right up to drainage divides.

Hynek *et al.* (2010) presented an updated global map of Martian valley networks using post-Viking data. Hynek *et al.* (2010) demonstrated that to understand the climate history of Mars as inferred from valley networks, a global approach is necessary. The new data presented are consistent with widespread precipitation and surface runoff on ancient Mars, thus requiring substantially different climatic conditions than at present. Their manual remapping of the valleys on a global scale produced eight times as many valleys on the surface. The computation of the drainage densities are, on average, higher by a factor of 2 with respect to Viking data. These new results are consistent with a warm and wet early climate. Hesperian and Early Amazonian valleys also show signs of formation by precipitation and surface runoff, although at much decreased levels through time.

It is within this frame that we started working on this research field, starting to develop a method to detect and validate Mars riverbeds. Our approach, which is going to be presented in the next chapter, focuses on computation of important hydrological parameters aiming to infer thorough implications for the ongoing arguments on the geomorphic and environmental history of Mars.

Chapter 2

The Extraction of Valley Networks Methodology

2.1 Hydrology Parameters

A stream network can be defined trough several hydrological parameters derivable from a digital elevation model:

- 3D length of all detectable riverbeds (the sum of the lengths distributed on a surface), computed from the source/s to the mouth, belonging to the entire drainage area;
- 3D area of the whole drainage basin, which is the ensemble of the surfaces distributed three-dimensionally;
- Drainage density, derived from the ratio between the total sum of the 3D lengths of all detectable riverbeds and the 3D drainage area of the basin. The drainage density expresses the degree of basin dissection by surface stream. Given a valley network, the closer the riverbed heads are to the drainage divides[1], the greater the total length of the network is. This parameter reflects the interaction between the channelization processes, the ground water resistance and the diffusive infilling processes. It influences the water discharge efficiency from a given area during individual rainfall or water production events;
- Slope of each riverbed and slope of the drainage network area;
- Strahler order and Shreve magnitude, which classify all segments of the riverbed. The Strahler order and the Shreve magnitude (Strahler, 1952; Horton, 1945; Schumm, 1956; Shreve, 1966) are two objective parameters used to define a riverbed on Earth. Assuming no triple junctions, the Strahler parameter attributes order one to the fingertip tributary, which originates from a source. When a junction between two streams of order u occurs, a new stream segment of order $u+1$ is formed. If a junction of two streams of unequal order u and v happens, being v

[1] The drainage divide is the boundary between two adjacent watersheds. The drainage divides are locations where the slope of the landscape changes directions as on ridge crests. Hence water flows on one side of a crest head into a stream, while runoff on the other side of the ridge flows into another stream. See as an example Fig.2.11.

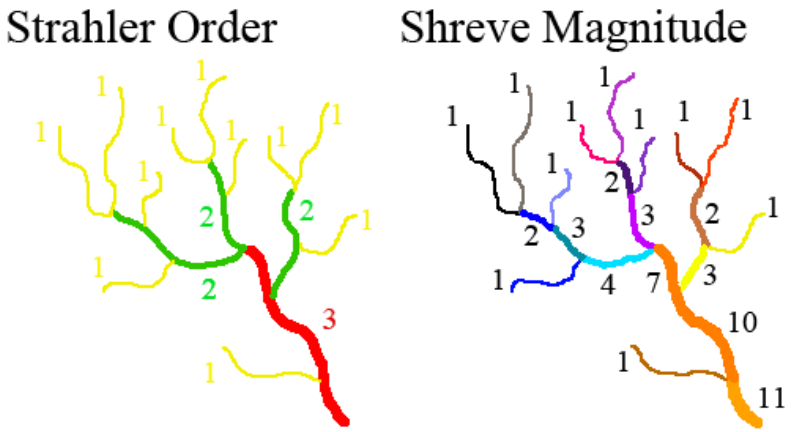

Figure 2.1: The difference between Strahler and Shreve methods in attributing the riverbeds stream order.

greater than u, the downstream segment is considered by Strahler methodology having an order equal to that of the higher order stream v. The computation of how many riverbed sections belonging to Strahler order i, is important to derive the bifurcation ratio R_B from the Horton (1945) law of stream numbers. On the other hand, the Shreve methodology attributes order one to the fingertip tributaries originating at a source; when a junction of two streams of order u and v takes place, the order $u+v$ is given to the new riverbed segment. In the Shreve magnitude method, a stream discharge is considered variable and it is taken into account when a lower-order tributary enters a higher-order stream. A graphic representation of the difference between Strahler and Shreve methods is presented in Fig. 2.1.

2.2 The Drainage Networks Extraction Workflow

Our method to determine valley and riverbed networks involves several different different steps.

The Mars Orbiter Laser Altimeter (MOLA instrument onboard NASA *Mars Global Surveyor* spacecraft (Zuber *et al.*, 1992; Smith *et al.*, 1999)) produced a Digital Elevation Model of Mars (MOLA DEM): a two dimensional elevation grid which is a map of elevations with a fixed x and y spacing/resolution. An example of a specific Mars area of the digital elevation grid derived from our data is presented in Fig. 2.2.

Raw DEM data contain pits, *i.e.* areas where no neighboring grid cell has a lower elevation. There are two types of pits in a digital terrain model: those that represent real depressions such as craters or completely flat areas where water flow cannot be defined; and artificial pits, resulting from data errors or interpolation method (Rieger, 1992). Since pits hinder water flow, it is of fundamental importance to recognize the artificial ones and remove from the DEM.

The pre-processing algorithm we use to fill pits, raising the elevation of the pit until a pour point occurs, is the one presented in Jenson *et al.* (1988). This method ensures hydraulic connectivity within the whole studied watershed and was implemented in

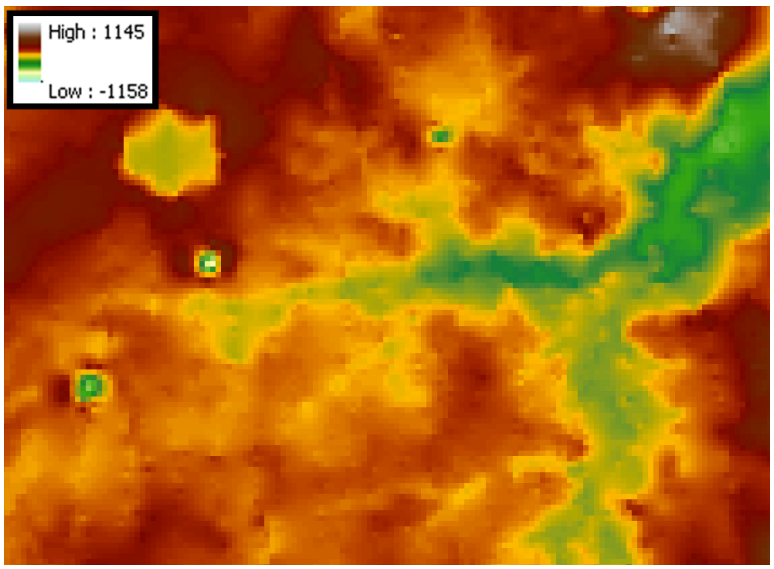

Figure 2.2: An example of MOLA DEM with a scale of 460 m/px. The elevation values in meters are also indicated.

Tarboton (2003) TauDEM software, which we use to clean the MOLA DEM.

After cleaning the raw data we used the Eight Pour Point D8 method developed by Peucker *et al.* (1975) and widely discussed and used by O'Callaghan *et al.* (1984) and Marks *et al.* (1984), which assigns a flow direction to each DEM grid cell based on the neighboring cell with the lowest elevation. The D8 algorithm belongs to the single flow direction, non-dispersive methodology, and was designed to approximate slope lines and to provide a basis for the description of non-dispersive flows essentially driven by gravity. Orlandini *et al.* (2012) compared different flow direction methods, which are evaluated against Terrestrial field observations of overland flow dispersion. The ability of these methods to reproduce the observed flow patterns is analyzed on DEMs having different resolutions. Orlandini *et al.* (2012) stated that the predicted propagation patterns depend critically on the size of grid cells involved. When coarse resolution DEMs are used, the predicted propagation patterns of low degree dispersion method, such as the D8 method, essentially reproduces the results with different flow direction nondispersive methods, where not only 8 flow directions are considered but infinite directions are taken into account (Orlandini *et al.*, 2012).

Using MOLA pixel size of 460 m, the D8 method is then an effective approximation of the directions of drainage flows that carve the Martian surface as shown in Ansan *et al.* (2008). The general flow pattern of the terrain model finally emerges when displaying the trends of a flow direction grid as it is shown in Fig. 2.3. Without removing the above-mentioned pits we would get a misleading flow direction map that would not be representative of the real general flow pattern of the 3D surface.

Once the flow direction grid has been created we need to calculate the flow accumulation grid by counting the number of contributing cells to each cell in the grid (cells crossed by a flow path). Cells that are part of a stream network have a larger flow accumulation value, whereas cells near watershed boundaries, and where overland flow dominates, have a low flow accumulation value.

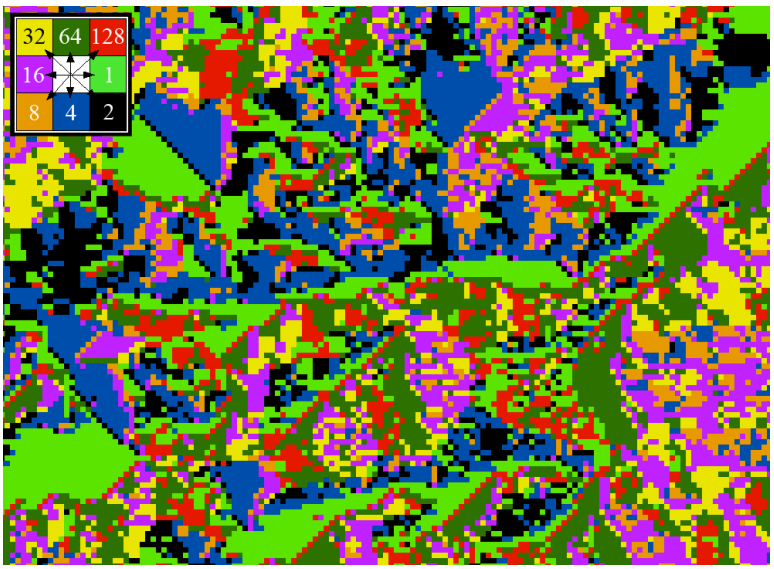

Figure 2.3: The flow direction grid obtained through the Peucker *et al.* (1975) method applied on the DEM presented in Fig 2.2. The 8 values present the direction of the flow for each pixel of the raster data.

In order to define the riverbed networks, a specific threshold of the flow accumulation grid has to be selected. The definition of this flow accumulation value is of great importance because it affects all the following workflow steps. Without assuming mathematical or computational constraints, we decided to use this method to select such threshold range: we superimposed Mars georeferenced High Resolution Stereo Camera images, see Fig. 2.4, (HRSC instrument, (Neukum *et al.*, 2004) onboard ESA *Mars Express* spacecraft), imported as raster layers, on the MOLA DEM (see Fig. 2.5). The HRSC database was selected because its images are the only ones that cover almost the entire[2] surface of Mars, with a high scale ranging from 25.0 up to 12.5 m/px.

We started our analysis by using different thresholds on the flow accumulation chart with a contour map superimposed on the MOLA DEM and HRSC images, see Fig. 2.6. We applied a range of thresholds, between 1000 and 50[3], to several Mars areas belonging to our study region, in order to investigate what is the best threshold range on the flow accumulation chart. In Fig. 2.6 and in Fig. 2.7 we show one of the test case areas we have investigated. We found out empirically that the applicable threshold value on the accumulation maps which confirms the model results with the actual HRSC surface images ranges between 200 and 400. As it is showed in Fig. 2.6 and Fig. 2.7, a threshold value bigger than 400 would not have taken into account the smallest riverbeds visible in the HRSC images and still detectable in the DEM, while a threshold value smaller than 200 (see Fig. 2.7) would have introduced small valley networks that are not present on the HRSC surface of Mars. Lowering too much the threshold introduces random noise into the river analysis, therefore we decided to stop

[2]On February 4, 2013 ESA stated that since 2003 nearly 90% of Mars' surface has been covered with HRSC images.

[3]These values are the numbers of minimum contributing cells flowing inside each cell of the flow accumulation grid.

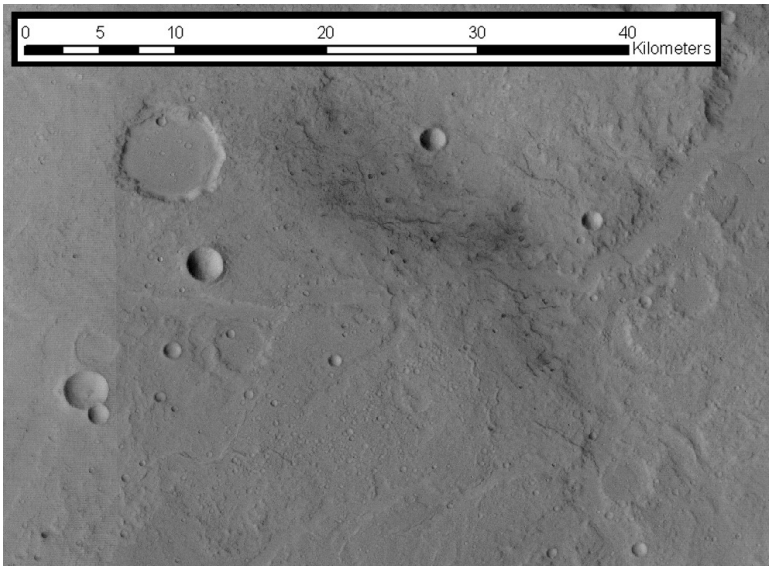

Figure 2.4: HRSC images H4264 and H4242 with a scale of 12.5 m/px covering the example MOLA area presented in Fig. 2.2 and in Fig. 2.3. The scale bar in kilometers is also indicated.

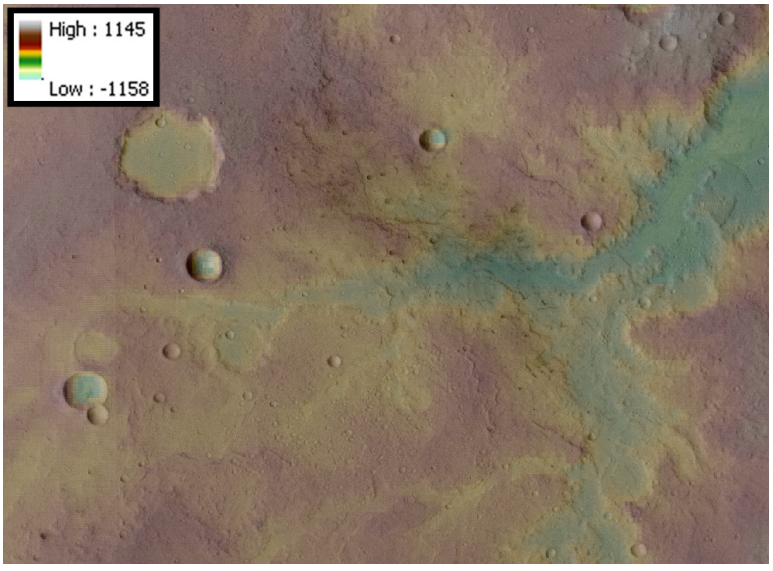

Figure 2.5: The HRSC image presented in Fig. 2.4 georeferenced and superimposed on the MOLA digital elevation model showed in Fig. 2.2. The elevation values indicated are in meters.

at the value of 200.

It is worth noting that the resolution of the MOLA DEM raster is the dominant limitation in detecting the smallest detectable HRSC riverbeds. In some maps, even with the threshold range between 200 and 400, the small networks are only visible in the high-resolution image, but do not appear in the accumulation map derived from the MOLA DEM. The resulting flow accumulation chart derived for the Mars area presented in Fig. 2.2 is shown in Fig. 2.8.

We should point out that the Martian terrains we consider are heavily cratered (Hartmann *et al.*, 2001), and that the delineation of a drainage network on a such a surface is an extremely complex, challenging and difficult task. There are thousands of craters of different size ranging from tens of meters up to hundreds of kilometers, with different ages and hence with different stages of erosion (see Hartmann *et al.* (2001)), which have erased partially or completely various surface features. In addition to these identification difficulties, Mars is an extremely dusty planet. Locally the dust can be accumulated to fill up and hide small craters and riverbeds (Pieri, 1976, 1979, 1980; Szwast *et al.*, 2006). We continuously confirm our workflow results with the high resolution images because one cannot simply consider the depressionless DEM to identify a riverbeds network. To guarantee their integrity, 3D models need to be identified within the high resolution images of the surface.

We emphasize that during the mapping phase four criteria presented in Yamaguchi *et al.* (2009) are taken into account:

- a valley is a generally linear-shaped depression, and it is traceable with its shadow,
- a valley has an observable U- or V-shaped cross section needed to eliminate cliffs,
- the length of a valley is at least twice its width, so that we can avoid mapping horizontally-short depressions,
- a valley length is longer than 2-3 km so that we can smooth out hummocky regions and bumpy areas.

Once the drainage networks are identified, the outlet points of the watershed are determined in order to define the drainage area that belongs to the selected riverbed network, as in Mest *et al.* (2010). This step is of great importance because the flow accumulation map computed on the depressionless surface model, obtained through the TauDEM software, may still include some spurious riverbeds. In order to eliminate any possible misinterpretation or creation of mathematical artifacts, we validate the calculated flow accumulation maps by analyzing the HRSC images and by eliminating those riverbeds that are not identifiable in the high-resolution imagery.

In the course of each successive step, we delineate the sub-watersheds of the above-mentioned area by selecting the sub-basin outlet point inside the drainage area. The Strahler order and the Shreve magnitude of the valley network are then computed from the data raster which contains all the validated riverbed networks (see Fig. 2.9).

After having obtained a clean and validated database we can calculate the 3D stream length of the riverbeds and the 3D area of the watersheds and sub-basins previously identified. This allows us to derive the hydrological drainage density parameter of a network of valleys. The next step consists in identifying the highest and the lowest elevation value of a riverbed network and the elevation range between the drainage divides and the mouth of the river. Then we calculate the slope of the drainage network

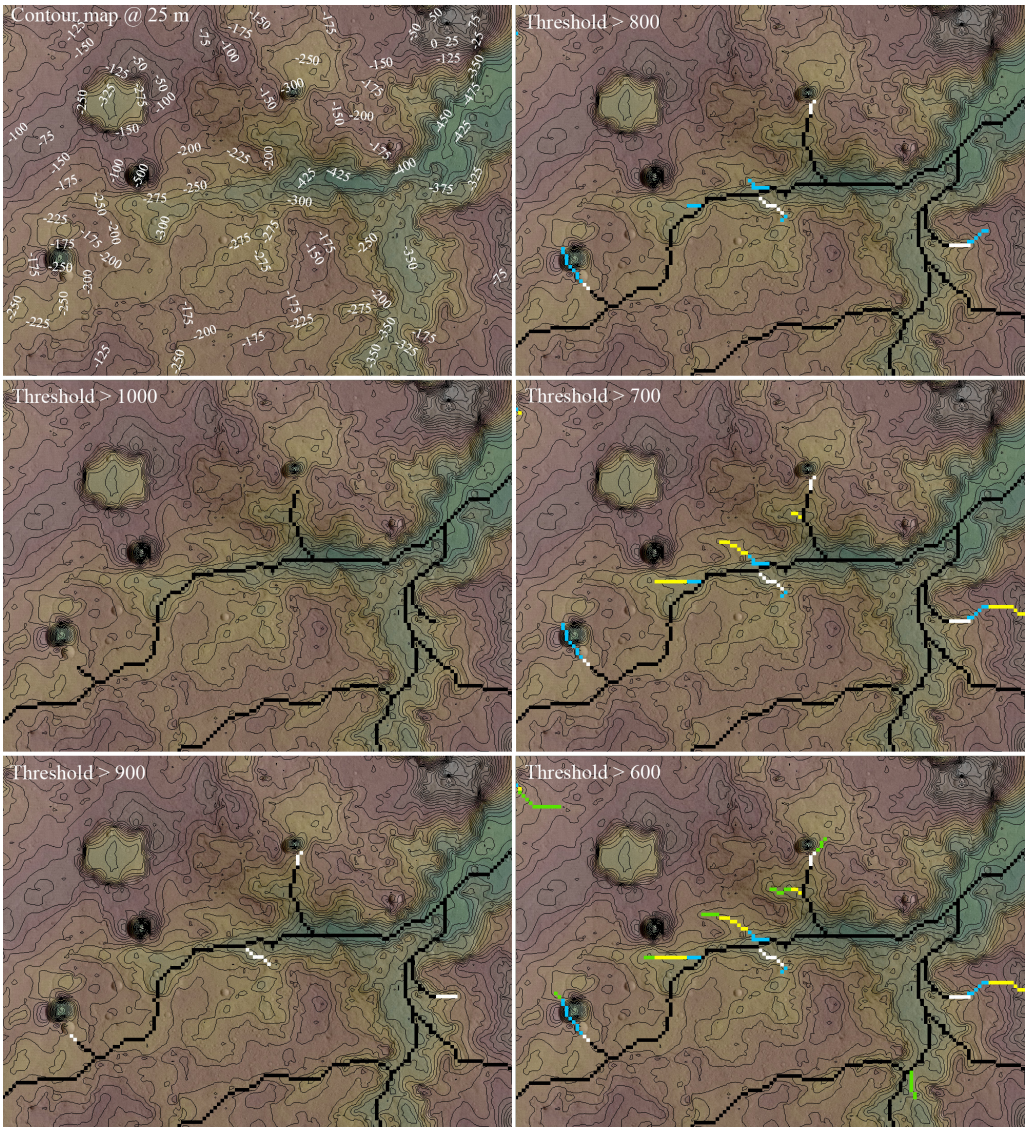

Figure 2.6: Contour map of the study area presented in Fig. 2.2 computed at 25 m and five different sets of threshold values (between 1000 and 600) applied on the flow accumulation chart.

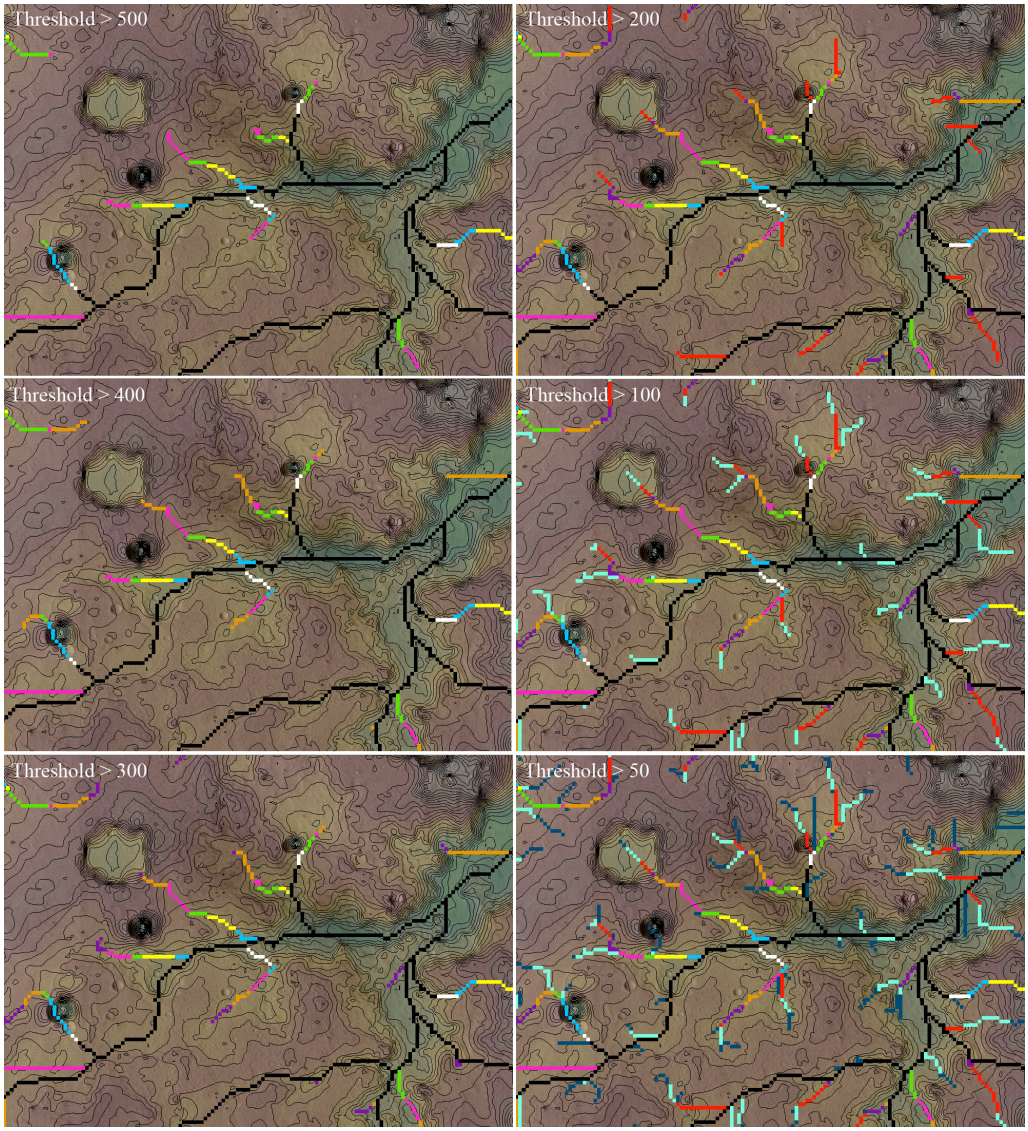

Figure 2.7: Six different sets of threshold values (between 500 and 50) applied on the flow accumulation chart.

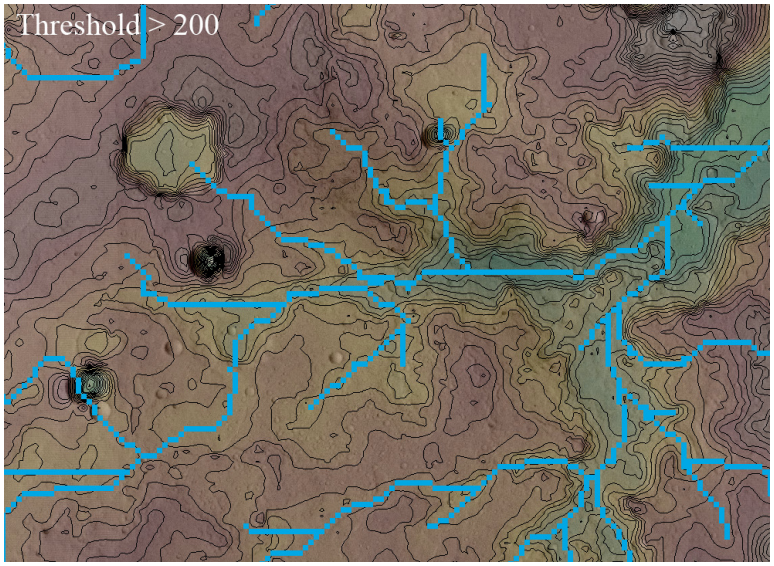

Figure 2.8: Flow Accumulation grid obtained through a threshold bigger than 200 superimposed on the HRSC image, on the MOLA DEM and on the derived contour chart.

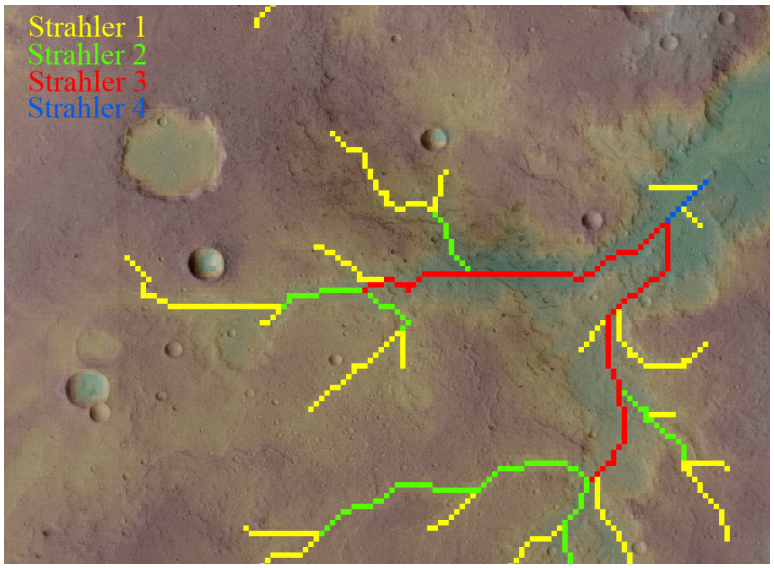

Figure 2.9: The Strahler order derived from the flow accumulation map presented in Fig. 2.8 once the DEM computed network has been double checked with the HRSC images and the spurious paths have been cut out.

and the slope of the drainage area adding these physical parameters to the hydrological interpretation of the watersheds.

2.3 Case study: Four Drainage Networks in Mars Memnonia Quadrangle

What follows is a case study where we applied our methodology to identify and analyze four drainage basins.

2.3.1 Area description

The case study we present here refers to four adjacent drainage areas belonging to the Mars Memnonia quadrangle, identified as MC-16 (Davies *et al.*, 1992). These drainage areas are situated across the equatorial transition region of the Martian hemispherical dichotomy, located between 184° E and 186° E Longitude and between 11° S and 14° S Latitude. This region is situated south of the Lucus Planum, and east of the Ma'adim Vallis watershed. The surveyed area is at the boundary between the Noachian, cratered and hilly region and the Amazonian terrain (Tanaka *et al.*, 1986; Hartmann *et al.*, 2001). A map of this area is presented in Fig. 2.10.

The HRSC images covering this region are the H93240000ND3 and H21280000ND3 at a scale of 12 m/px. Fig. 2.10 shows the MOLA DEM with both HRSC images georeferenced and superimposed in transparency; they are used for the riverbeds identification validation.

2.3.2 Analysis

Using the method described above, we derived the hydrological parameters of the valley drainage networks. This was done after the section of interest of the MOLA dataset was converted to raster format and after the HRSC images covering our case-area were georeferenced. Through the use of the ESRI Software ArcGIS10 and Python routines, we obtained the flow direction grid of each area and the flow accumulation with an applied threshold around 200. We cleaned the flow accumulation grid as described above.

After having derived the contour map with elevation steps of 100 meters we identified four riverbeds. For each riverbed we computed its 3D length and derived its Strahler order and Shreve magnitude. We identified the drainage area and computed the 2D and the 3D area of each basin deriving its drainage density parameter (see Tab. 2.1).

We consequently focused on the computation of the percent slope layer (45 degree slope = 100%) for each drainage area, as it is displayed for example in Fig. 2.12. This map served as an important guide in the detection of both the rims of the several craters present on the surface, and the boundaries of the valleys and riverbeds of the drainage network. It also allowed us to cross check and validate their identification. We also computed the slope for each pixel belonging to the riverbed path. After the mapping was complete, we derived the mean and the standard deviation of the slope distribution both for the drainage areas and for the riverbed networks. The histograms we obtained are presented in Fig. 2.12, Fig. 2.13, Fig. 2.14 and in Fig. 2.15. We computed also the median, the first and the third quartile of the slope distribution and its skewness. These physical and statistical parameters are presented in Table 2.1.

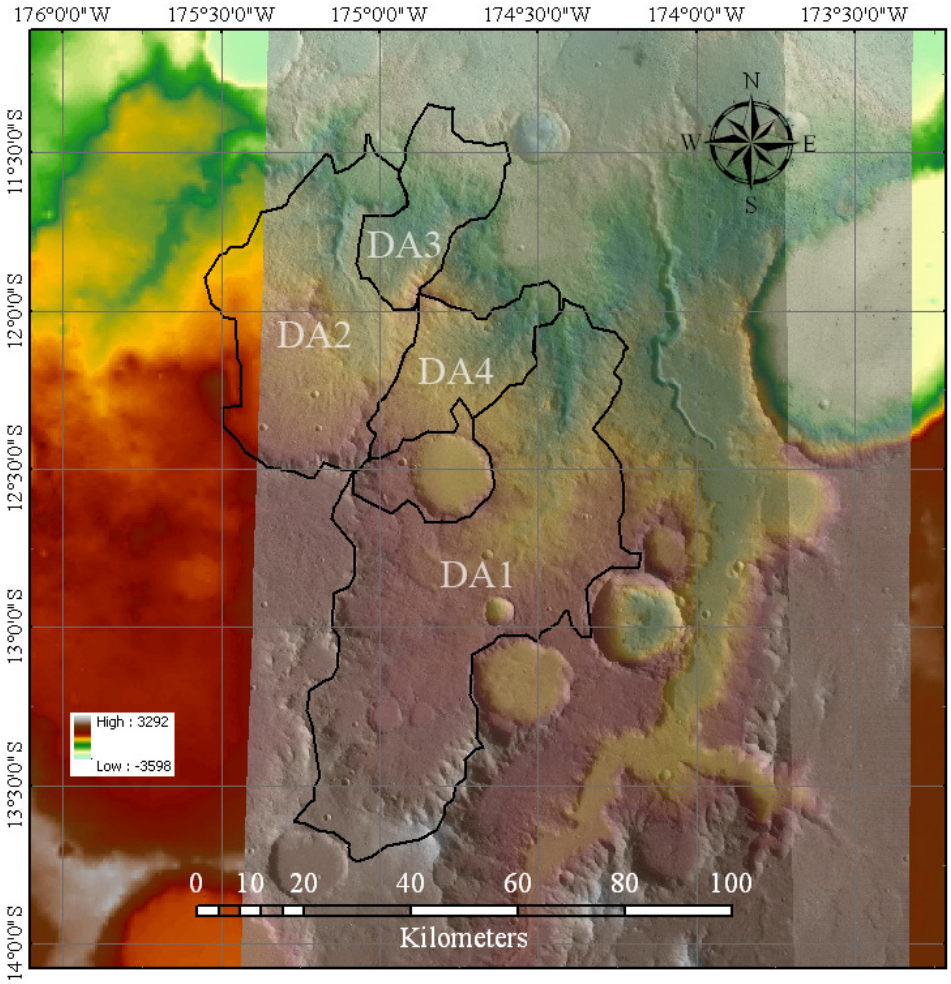

Figure 2.10: Overview of the case study area, with latitude and longitude grids, scale bar in Kilometers and elevation value in meters.

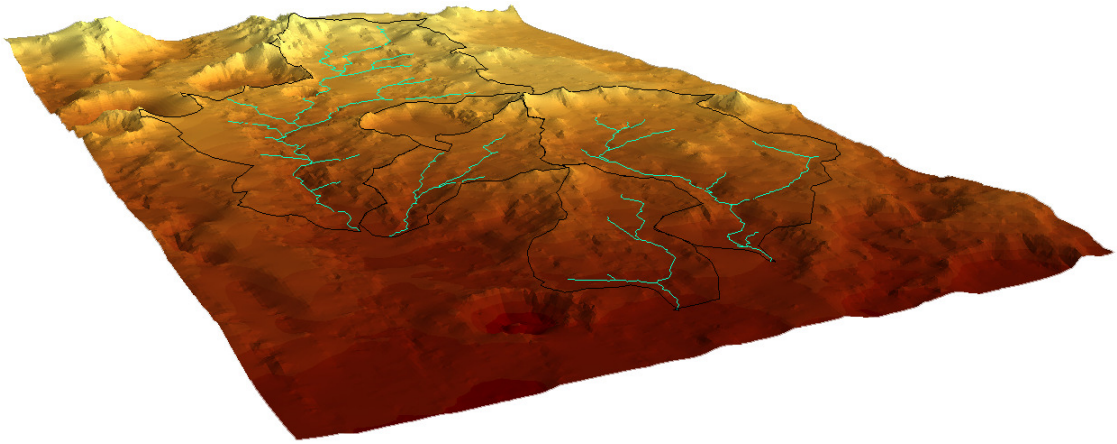

Figure 2.11: 3D view of the four drainage basin we have identified in the Memnonia quadrangle. The riverbed are depicted with a light blue line while the drainage divides are presented with black lines. The surface elevation values are the same of those presented in Fig. 2.10.

2.3.3 Results and Discussion

We derived a total riverbed network length ranging from 59 to 303 kilometers and a drainage area from 512 to 2 906 km^2. The derived drainage density we obtain for the four networks spans from 0.104 to 0.125 km^{-1}. The maximum Strahler order is 3 while the maximum computed Shreve magnitude is 17. In Fig. 2.11 we show the 3D view of the drainage divides for the four adjacent watersheds, where the riverbed networks are depicted in light blue and the drainage divides, identified through ARCGIS hydrology tool, are in black. This 3D map is important because it depicts the real landscape surface and validates our definition of the drainage network as derived from our workflow process described here. The drainage areas and riverbeds slope distribution of the four areas are presented in Fig. 2.12, Fig. 2.13, Fig. 2.14 and in Fig. 2.15.

In order to avoid outliers that affects the mean value computation of a physical parameter, we use the median value of such distributions to define the slope of the entire drainage network. As seen from figures 2.12 - 2.15 the drainage area slope median value ranges between 5.01% to 5.82%, which means between 2.87° and 3.33°, while the riverbed median slope ranges between 2.77% and 4.49%, *i.e.* 1.58° and 2.57°. On Earth such slope values refers to high reliefs related to rapids and cascades stream types (Rosgen, 1994). In the riverbed slope histograms we find also slope values ranging between 0 and 2%, this meaning that in these locations gentle-gradient riffle/pool stream types are found and they are typically closer to the riverbeds mouth.

We hence suggest that the median value of the drainage area slope distribution for area-slope comparisons would be a useful common standard for researchers, along with the median value of the drainage network slope in length-slope plots.

To understand the meaning of the physical and hydrological values presented in Table 2.1 in context with previous Mars hydrological studies, we strongly suggest the reader to give particular attention to the following analysis chapter.

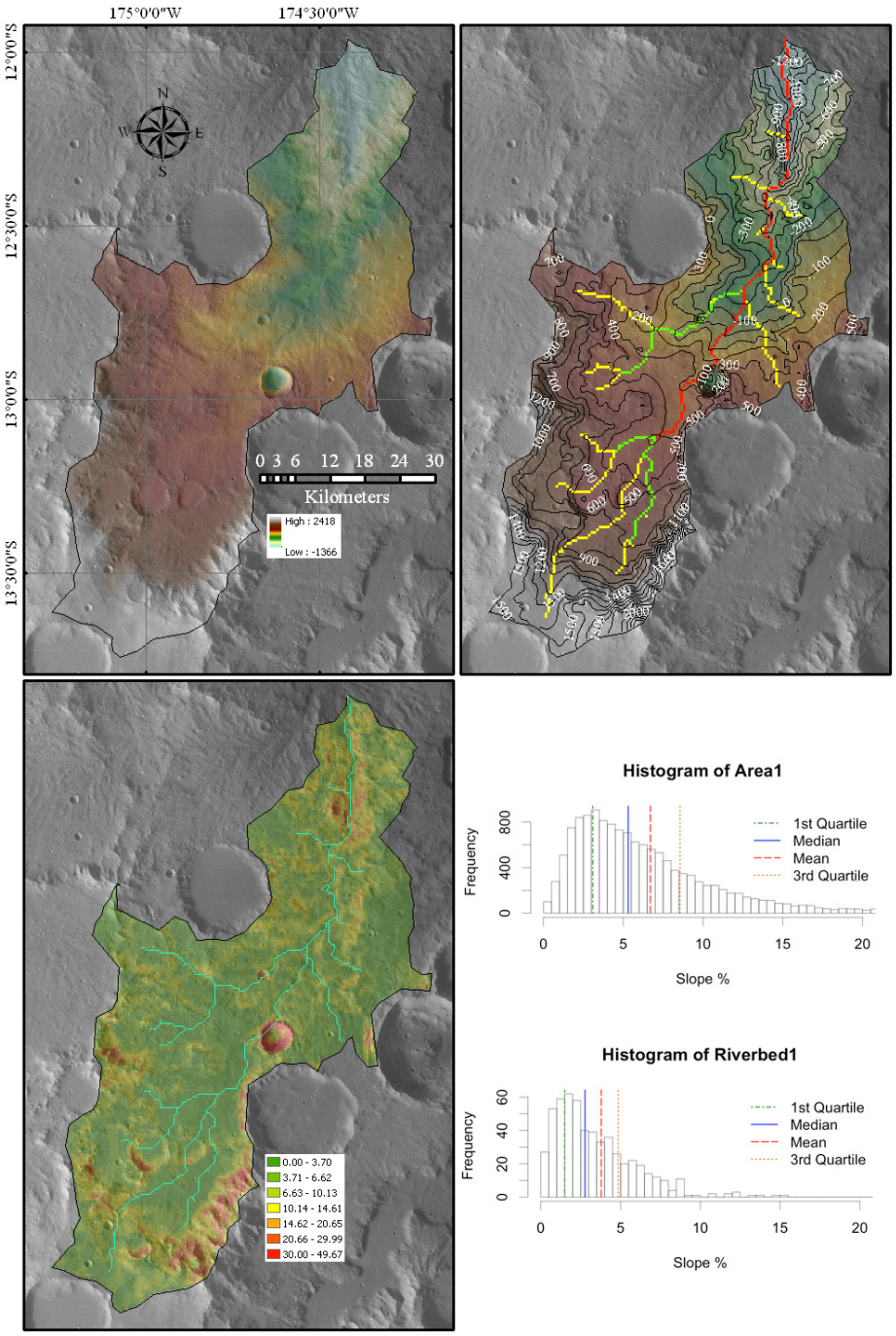

Figure 2.12: The case study area number 1. The upper-left image shows the location, the scale bar in kilometers, the elevation values in meters superimposed on the HRSC image. The upper-right image shows the contour map with 100 meters step and the Strahler order of the identified riverbed 1 network. Lower-left the slope map is depicted with the values expressed in percentage. Two histograms are presented, the one showing the slope distribution values of the whole drainage area; the second one is the slope distribution histogram of the riverbed network path.

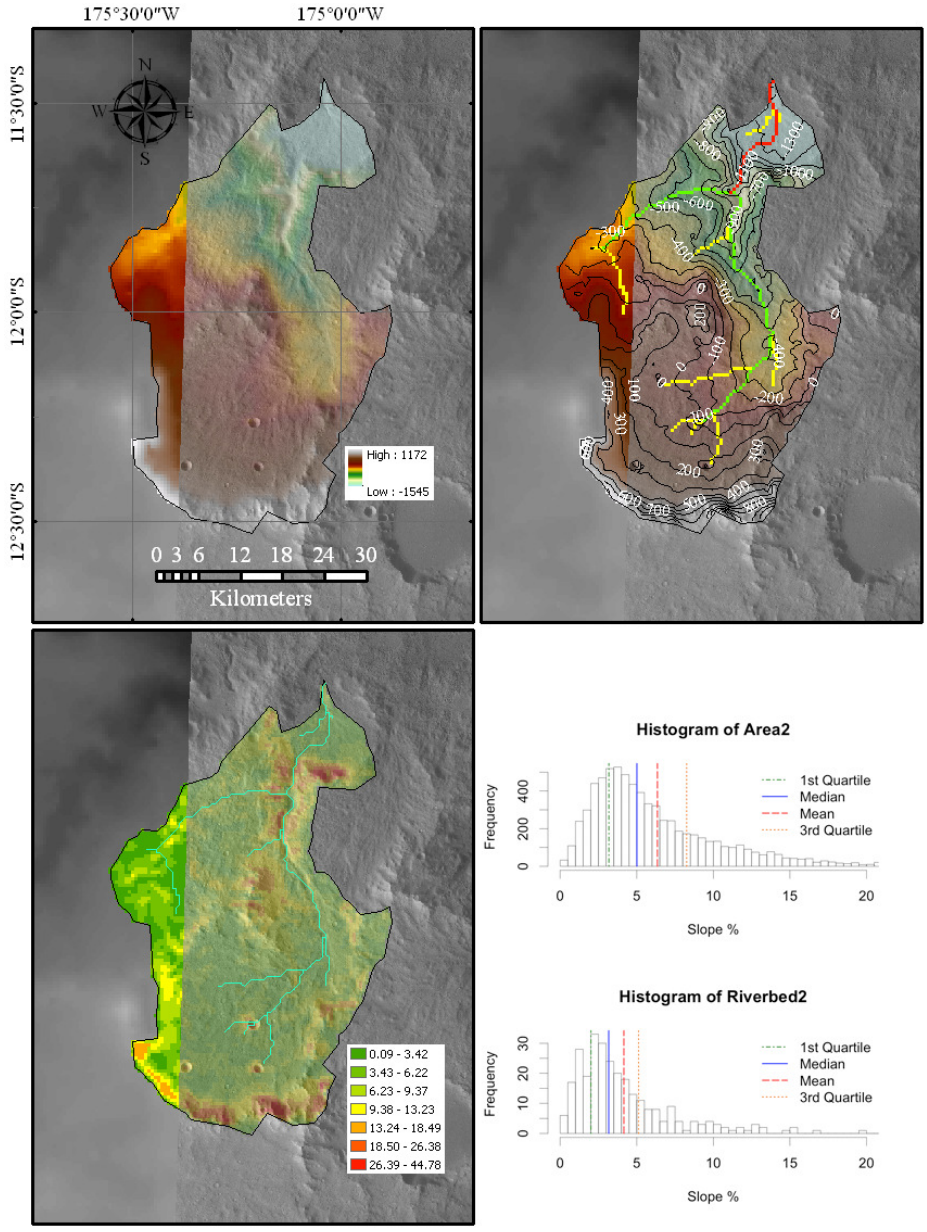

Figure 2.13: The case study area number 2. The upper-left image shows the location, the scale bar in kilometers, the elevation values in meters superimposed on the HRSC image. The upper-right image shows the contour map with 100 meters step and the Strahler order of the identified riverbed 2 network. Lower-left the slope map is depicted with the values expressed in percentage. Two histograms are presented, the one showing the slope distribution values of the whole drainage area; the second one is the slope distribution histogram of the riverbed network path.

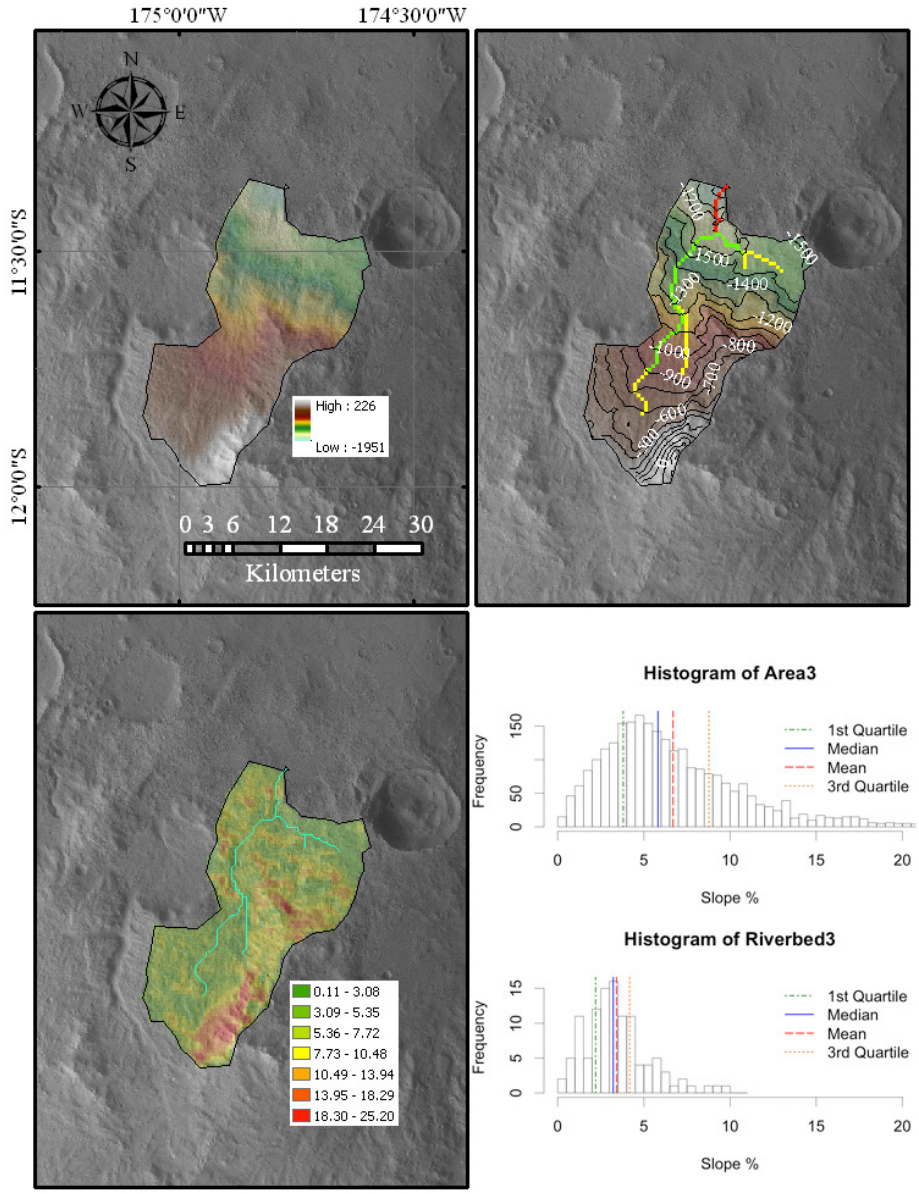

Figure 2.14: The case study area number 3. The upper-left image shows the location, the scale bar in kilometers, the elevation values in meters superimposed on the HRSC image. The upper-right image shows the contour map with 100 meters step and the Strahler order of the identified riverbed 3 network. Lower-left the slope map is depicted with the values expressed in percentage. Two histograms are presented, the one showing the slope distribution values of the whole drainage area; the second one is the slope distribution histogram of the riverbed network path.

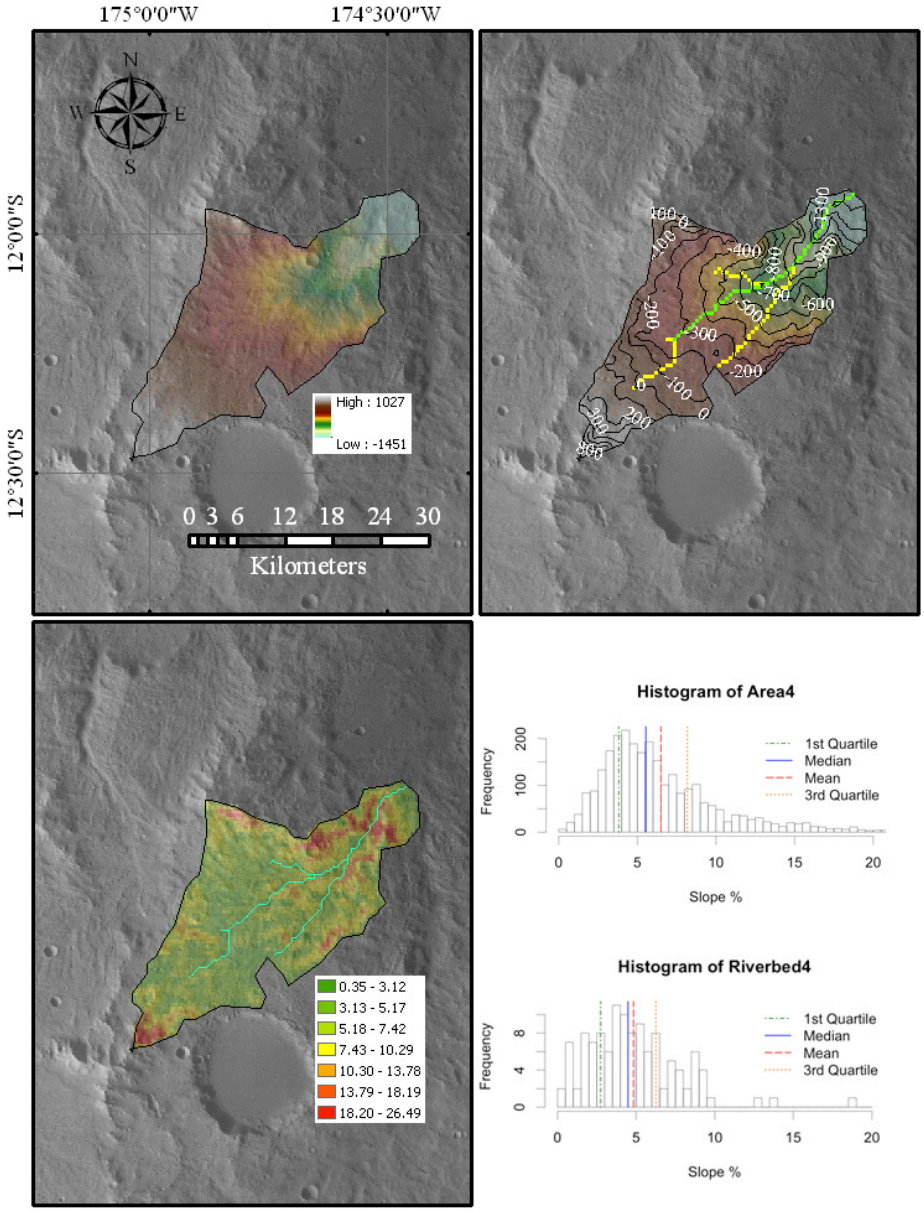

Figure 2.15: The case study area number 4. The upper-left image shows the location, the scale bar in kilometers, the elevation values in meters superimposed on the HRSC image. The upper-right image shows the contour map with 100 meters step and the Strahler order of the identified riverbed 4 network. Lower-left the slope map is depicted with the values expressed in percentage. Two histograms are presented, the one showing the slope distribution values of the whole drainage area; the second one is the slope distribution histogram of the riverbed network path.

	Case study 1	Case study 2	Case study 3	Case study 4
3D length (km)	302.93	154.79	58.72	67.81
2D drainage area (km^2)	2892.70	1472.29	510.20	539.57
3D drainage area (km^2)	2906.20	1477.88	512.18	541.64
Drainage density (km^{-1})	0.104	0.105	0.115	0.125
Riverbed elev max (m)	1330	101	-687	-2
Riverbed elev min (m)	-1366	-1545	-1951	-1451
Area elev max (m)	2418	1172	226	1027
Area elev min (m)	-1366	-1545	-1951	-1451
Strahler order	3	3	3	2
Strahler 1 no.	17	10	5	4
Strahler 2 no.	3	2	2	1
Strahler 3 no.	1	1	1	0
Mean Strahler 1 length (km)	9.13	7.09	4.97	8.83
Mean Strahler 2 length (km)	20.34	31.34	13.49	32.48
Mean Strahler 3 length (km)	86.70	21.26	6.88	0
Shreve magnitude	17	10	5	4
Area Slope min (%)	0.00	0.09	0.11	0.35
Area Slope 1st Qu. (%)	3.09	3.18	3.80	3.82
Area Slope median (%)	5.31	5.01	5.82	5.54
Area Slope mean (%)	6.70	6.35	6.69	6.5
Area Slope standard dev (%)	5.40	4.67	4.11	3.94
Area Slope skewness	2.25	1.95	1.14	1.50
Area Slope 3rd Qu. (%)	8.56	8.26	8.77	8.18
Area Slope max (%)	49.67	44.78	25.3	26.49
Riverbed Slope min (%)	0.05	0.24	0.36	0.36
Riverbed Slope 1st Qu. (%)	1.50	2.01	2.20	2.74
Riverbed Slope median (%)	2.77	3.17	3.22	4.49
Riverbed Slope mean (%)	3.79	4.16	3.41	4.83
Riverbed Slope standard dev (%)	4.29	3.38	1.85	2.94
Riverbed Slope skewness	4.94	1.91	0.97	1.26
Riverbed Slope 3rd Qu. (%)	4.85	5.12	4.17	6.25
Riverbed Slope max (%)	40.74	21.28	9.65	18.62

Table 2.1: Physical values of the four case study riverbeds and drainage areas.

Chapter 3

Paleoriverbeds Analysis, Results and Discussion

3.1 Introduction and Area Contextualization

Our paleoriverbeds study is entirely based on the *Mars Global Surveyor* MOLA DEM, (Zuber *et al.*, 1992), which at the Mars equator presents a spatial resolution of 466 m and a vertical resolution of about 0.5 m. As indicated in Ansan *et al.* (2008), the MOLA resolution is sufficient to map the main valleys and riverbeds and can be sometimes used for the small tributaries, even if they are hardly detected and mostly visible only on the high-resolution imagery (this is the reason why we continuously validated our results with the HRSC (Neukum *et al.*, 2004) 12.5 m resolution images). Nevertheless it is worth noting that the MOLA DEM is still the best global digital elevation model of Mars to date, and it can be effectively used to perform regional hydrological studies, as our work will show, of the Mars drainage networks.

The Mars area we decided to study is the one located between the equator and -38° S in latitude and between 142° E and 164° W in longitude, fully inside the Martian dichotomy, see Fig. 3.1. The HRSC DEMs only partially covers our considered area and its dichotomy boundary, thus not allowing a complete statistical analysis of the riverbed networks on a regional scale, which, instead, MOLA permits.
Mars is characterized by a heavily cratered rugged southern hemisphere presenting wide highlands, covering 2/3 of the entire surface, and a smooth northern hemisphere, covering the remaining 1/3 of the surface, which is relatively flat and presents occasional impact craters (Smith *et al.*, 2001). The south pole has a higher elevation with respect to the north pole of about 6 kilometers (Smith *et al.*, 2001): the boundary between the southern rugged terrain and the wide and smooth northern basin is quite complex in places, starting around 10° S close to the Tharsis region and reaching 40° N between Isidis Planitia and Arabia Terra. The southern highlands degrade towards the northern accumulation region, on top of this elevation gradient many large riverbeds called Megafloods have incised their paths, but they are not the only paleohydrological presence in this area, because also several medium and small riverbed networks are recognizable: these paleoriverbeds are the main subject of this PhD thesis.

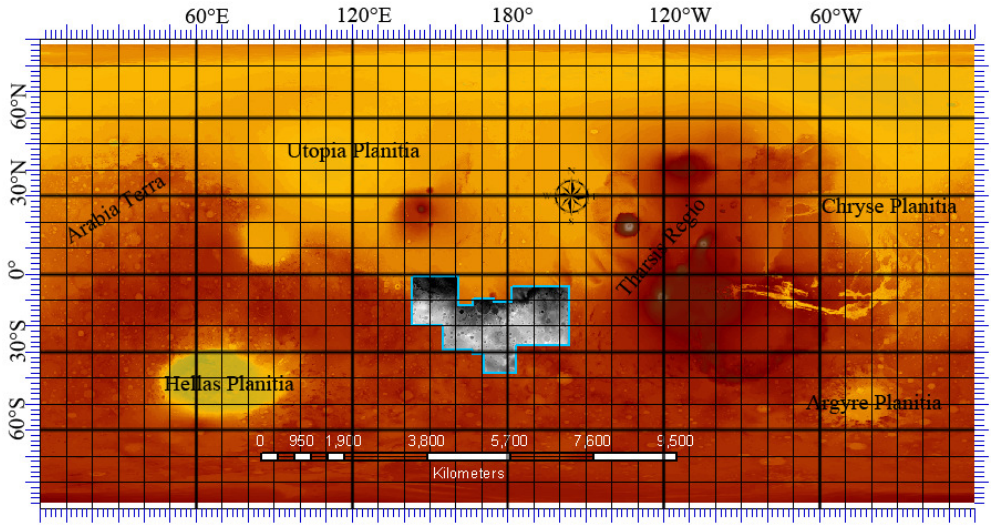

Figure 3.1: MOLA map of Mars showing some surface features and our analyzed dichotomy area.

3.2 Our paleoriverbeds database

We intensively used the extraction methodology described in the previous chapter on the area presented in Fig. 3.2: the elevation difference between the highest peaks and the deepest depressions of our area is quite high, reaching a difference of about 7400 meters on a surface which is 3600 km wide and 2000 km long. This is the "cliff area" which connects the southern highlands to the northern plains.

The deep use of the riverbeds extraction methodology made possible the identification of 546 paleoriverbeds, see Fig. 3.3. As it is possible to see from this figure, the paleoriverbeds presence is scattered over almost the entire considered area, avoiding only two areas, the one between -22° S and -30° S and 154° E - 166° E, and the second between -16° S and -28° S and 172° W - 162° W where we could not identify any presence of ancient paleoriverbeds neither on the MOLA DEM nor on the HRSC images.

Our paleoriverbeds database covers mainly the Aeolis (MC-23) and Memnonia (MC-16) Mars quadrangles, Davies *et al.* (1992), but also some sections of the Eridania (MC-29) and Phaethontis (MC-24) quadrangles.

At first sight, our 546 riverbeds database, can be considered small with respect to the one derived by Hynek *et al.* (2010), who found several thousands riverbeds on the entire surface of Mars (around 40% of the riverbeds found in our work corresponds to those found in the cited study), but the main difference between our data and those of Hynek *et al.* (2010) consists on the fact that Hynek *et al.* (2010) identified his database using high-resolution images and depicted the observed riverbeds on top of the imagery; consequently he derived through the MOLA DEM the drainage density and the Strahler order. In our study we extended this approach, deriving the riverbeds network from the MOLA DEM, validating them through the imagery taken at different phase angles, in order not to be misguided from surface shades; consequently we measured

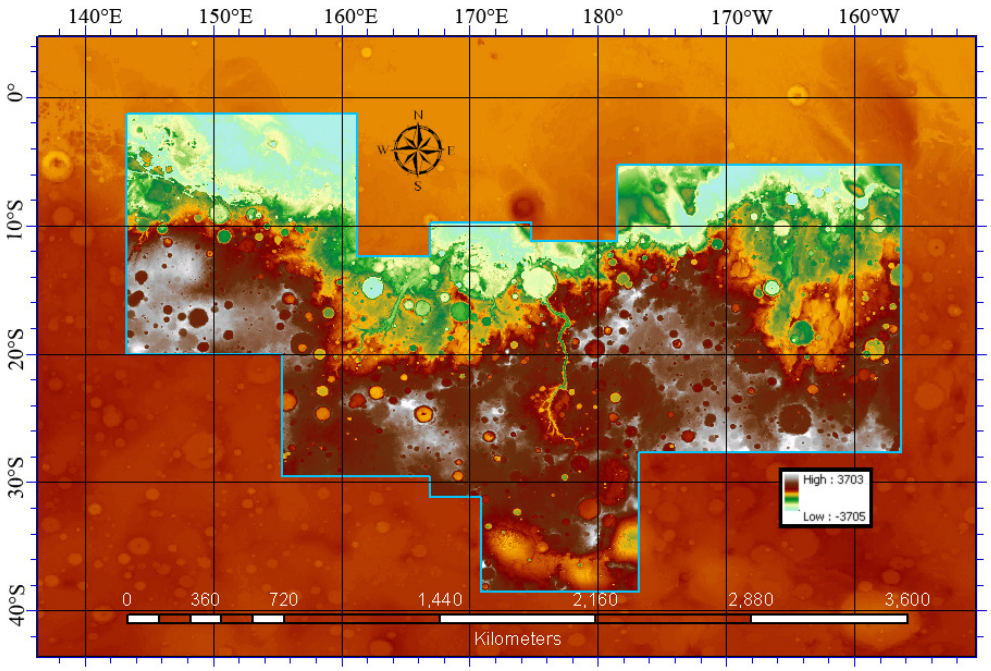

Figure 3.2: MOLA DEM section covering our considered area.

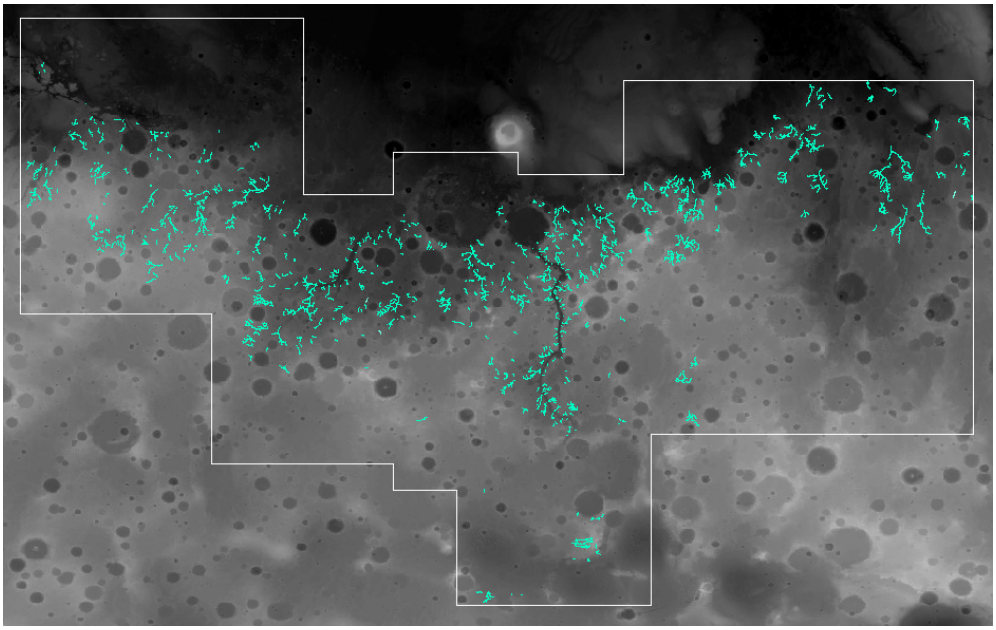

Figure 3.3: Overview of the riverbeds database we created though this work, superimposed on the MOLA grey-colored DEM.

not only the 3D length and 3D area and hence the drainage density, but also the Strahler order for each drainage network and its frequency, deriving the bifurcation ratio R_B through Horton (1945) law of stream numbers. We then measured the mean length for each Strahler order deriving the stream length ratio R_L through Horton (1945) law of stream lengths and the Shreve magnitude. We consequently measured the minimum and maximum elevation value for each drainage area and riverbed. The most important value we derived with our database consisted on the measurement of the slope distribution for each single drainage area and riverbed network, giving us the opportunity to make drainage area-slope, length-slope, drainage density-slope, Strahler order-slope and Shreve magnitude-slope plots. The specific case of drainage density-slope plots permitted us to infer considerations on the past Mars climatic conditions, at least at the time when those riverbed networks incised the surface. We can therefore infer that our database is a highly detailed riverbed database, presenting some of the most important hydrological parameters required to understand the surface flow and the weather conditions that lead to the formation of the Martian paleoriverbeds.

3.2.1 The global statistics

The first approach we followed in order to understand the meaning of our global dataset has been to plot the slope versus drainage area and the slope versus riverbed network's length, presented in Fig. 3.4. In the first plot, Fig. 3.4 I, the slope presented is the one computed on the entire drainage area, while for the second one, Fig. 3.4 II, the slope value is the one computed of the riverbed path.
As previously mentioned, the slope data we are presenting indicate the first quartile, the median, the mean and the third quartile of the slope distribution with the same color code used in the previously showed histograms. Through this way we give an idea of the slope distributions characterizing whether the drainage area or the riverbed network. This is an improvement with respect to previous studies, as the one of Som *et al.* (2009) or Penido *et al.* (2013) which typically use in their statistics the mean slope value for such data. On the contrary, we stress out that with such distributions as presented in Fig. 2.12, 2.13, 2.14 and 2.15, which we found similar for all 546 riverbeds, the median value is the correct one in defining the slope of the terrain avoiding outliers that affects the mean value computation. Theoretically, the mode value for those distribution would be even better identifying the more frequent slope value of the distribution, but we decided not to focus on this because it is strongly dependent on the bin selection used for the histogram, fact this which does not affect the median value.

In Fig. 3.4 II, we see three different slope values identified by dashed lines at 2%, 4% and 10%. Rosgen (1994) published an important classification of natural Earth rivers based on the slope value where the riverbed carved its path; the dominant bed slope range strongly relates to the various stream types:

- low slope riverbeds with a bed slope range between 0% and 1% can present pools;
- riffles are characterized by a bed slope which ranges from around 1% and 2-3%;
- riverbeds are called rapids when the dominant bed slope is in a range between 2% and 4%;
- cascades bed slope ranges between 3% up to 7-8%;

- the step riverbeds slope ranges from 4% up to 40%.

As a simplified classification presented in Rosgen (1994) we can say that on Earth the stream types with a slope greater than 10% are very steep with frequently spaced, vertical drop/scour-pool bed features, tending to be high debris transport streams and waterfalls. Riverbeds with a dominant bed slope between 4% and 10% are steep, with cascading and step-pool bed features. When the slope is about 2-4% riverbeds streams are typically riffle dominated with rapids and infrequently spaced scour-pools at bends or areas of constriction. Slopes smaller than 2% are characterized by gentle-gradient riffle/pool stream types. Finally riverbeds below 0.1-0.01% presents braided channels streams with convergence/divergence processes leading to localized, frequently spaced scour/depositional bed forms. Through Rosgen (1994) classification it is then fast and easy to understand in what kind of hydrological regime the 546 Mars riverbeds are when compared with the Terrestrial ones.

We then decided to compute the coefficient of determination[1], R^2 for four different fits we performed on the data, the linear-law, the power-law, the exponential-law and the logarithmic law fit. With such low values for the R^2 (with R^2 equal to 1.00 being the best replication of the measured outcomes replicated by the model and R^2 equal to 0.00 the worst case replication), we can say that the four models hardly represent the discrete distribution that we found; the explanation for this behavior is clear, in one single plot we are showing so many different kind and types of paleoriverbeds which formed in totally different geomorphological regions, that is it difficult to make a global comparison between them, trying to derive a significant global fit. It would be as comparing on the Earth the Amazon river and the Nile together with Alps riffles and cascades and trying to understand between such morphologically and geographically different riverbeds a common trend.

Nevertheless a meaningful and important global result has to be presented: the global frequency distribution of the drainage density values which we found through our database, see Fig. 3.5. In this figure we see that the drainage density values which we derived span between 0.04 km^{-1} and 0.6 km^{-1} with a peak around 0.12 km^{-1} and a cumulative percentage which reaches the 94% at a value of 0.2 km^{-1}, see Tab. 3.1.

Carr (1997) presented a paper on Martian drainage densities showing the results he derived, which were typically 2-3 orders of magnitude lower than typical Terrestrial densities as measured from Landsat 4 images. Within this work Carr (1997) indicated a table showing different drainage densities computed on some of the United States, as Arizona, Nebraska, New York, Texas and Washington and he underlined that the lowest drainage density value found on his Earth database was that on Nebraska with a value of 0.06 km^{-1}, while the maximum was in Washington with a value of 0.209 km^{-1}. Hynek *et al.* (2003) found a value of drainage density of 0.06 km^{-1} in his first database, and the highest drainage density he derived in 2010 was 0.14 km^{-1} on an extended statistic of 82 217 riverbeds. The Carr (1997) 0.06 km^{-1} value is indicated as a Terrestrial reference in Hynek *et al.* (2010) Martian work. This result lead Hynek *et al.* (2010) to affirm that the new data support some degree of surface runoff and by inference precipitation on Mars. It is also indicated that surface runoff is the simplest explanation for the integrated drainage basins, valley heads near the top of the divides and a drainage density comparable to Terrestrial values seen in *Mars Global Surveyor* data.

[1] It provides a measure of how well observed outcomes are replicated by the model, as the proportion of total variation of outcomes explained by the model (Steel *et al.*, 1960).

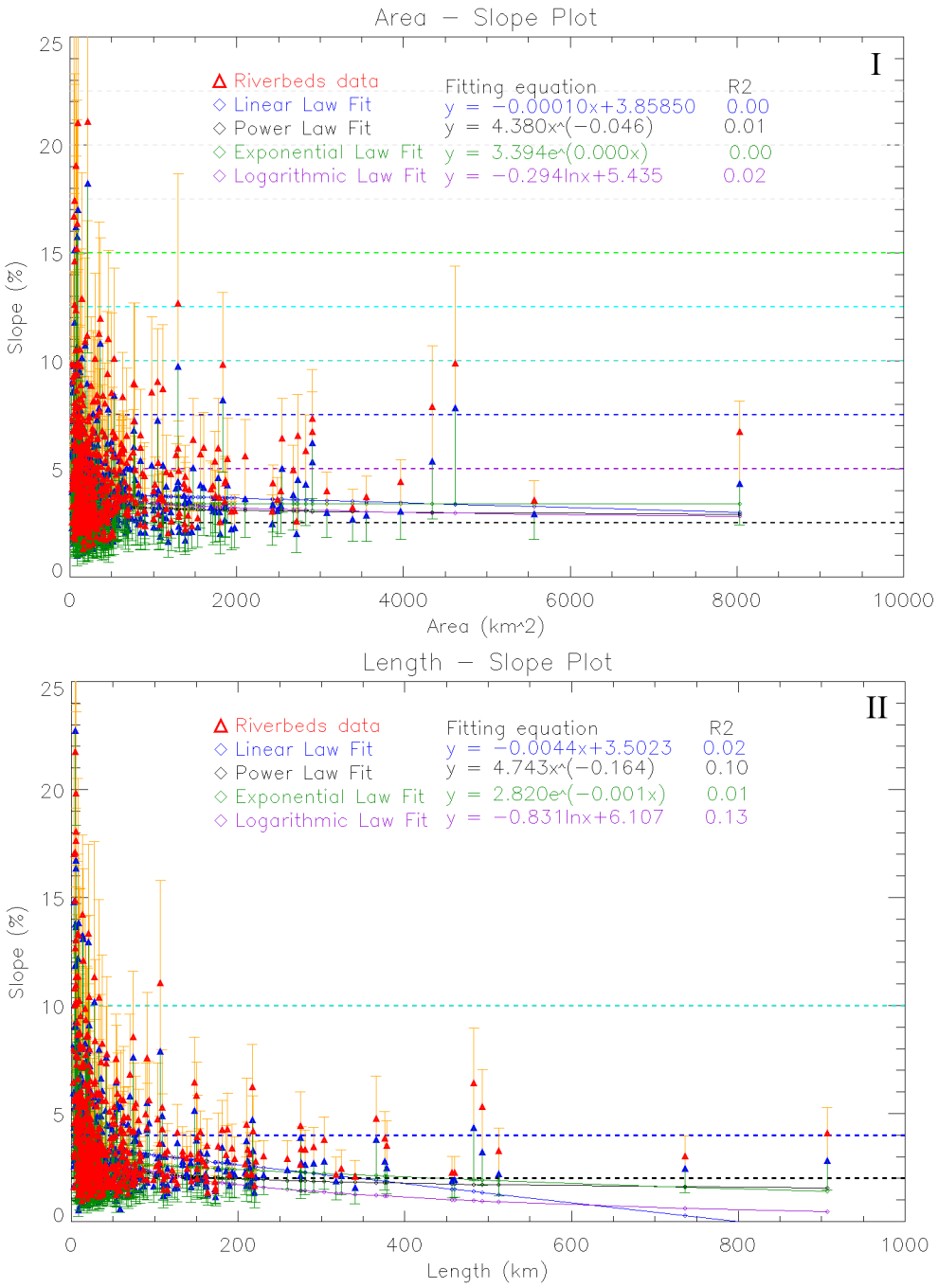

Figure 3.4: I: 3D area versus slope plot. II: 3D length versus slope plot. Both plots use the same color code for the error bars used in Fig. 2.12. The R^2 value is computed on the median value for each distribution.

The values which we derive, as from Fig. 3.5 and Table 3.1 are extremely important because only 2.20% of our data, *i.e.* 12 paleoriverbeds, are below a drainage density of 0.06 km^{-1}, while the remaining 97.8% is bigger than that. Our data are similar to the maximum values derived by Hynek *et al.* (2010) and as he presented in his work such results are consistent with a warm and wet early climate that incised the crust, with "early" being used also in our case because our riverbeds lie mostly in the Noachian and Hesperian units (Tanaka *et al.*, 1986). Our drainage density values are then comparable to low-end Terrestrial values and are also comparable to the results found in Masson *et al.* (2004).

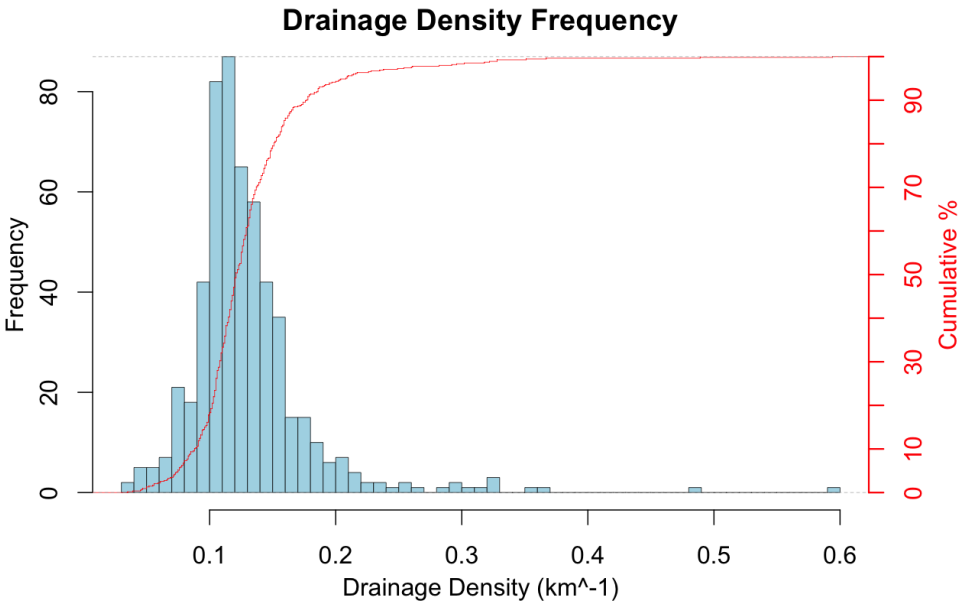

Figure 3.5: Drainage density frequency distribution based on our 546 riverbeds database. Note on the right side of the plot the cumulative distribution reaching 94% at a value of 0.2 km^{-1}.

Drainage Density (km^{-1})	Percentage %	# Riverbeds
0.04	0.37	2
0.06	2.20	12
0.08	6.78	37
0.10	18.32	100
0.12	47.10	257
0.14	71.79	392
0.16	85.35	466
0.18	91.39	499
0.20	94.32	515
0.22	96.34	526
0.24	97.07	530
0.26	97.44	532
0.28	97.80	534
0.30	98.35	537

Table 3.1: Drainage density distribution over the 546 paleoriverbeds.

The 1802 Playfair's law (Fairbridge, 1968) says: "On Earth every river appears to

consist of a main trunk, fed from a variety of branches, each running in a valley proportioned to its size, and all of them together forming a system of valleys connecting with one another, and having such a nice adjustment of their gradients that none of them join the principal valley either on too high or too low a level; a circumstance which would be infinitely improbable if each of these valleys were not the work of the stream which flows in it". What we find in our database is this connection of riverbed/valley networks which as from Playfair's law would be a low probable circumstance if each of these valleys was not the work of the stream which was flowing in it. Contextualizing this law with Carr (1997); Hynek *et al.* (2003); Masson *et al.* (2004); Ansan *et al.* (2006); Hynek *et al.* (2010) work and our results, we can affirm that the valley network systems which falls in the category showing a drainage density above 0.06 km^{-1} are believed to reflect a substantial contribution of precipitation and subsequent surface runoff.

Following with the global analysis, we plotted the Strahler order versus slope and the Shreve magnitude versus slope, see Fig. 3.6 I and II; what we derived is something expected as happens on Earth, generally the higher the slope of the drainage terrain, the lower the dissection degree (both Strahler and Shreve) appears. This can be explained in the following way: the higher the slope of the drainage area is, the lower is the possibility to create a higher-order degree of a dendritic network, because the water flow has a high velocity which does not allow to incise a sinuous pattern joining together with close riverbeds. The junction angle between tributaries will consequently be very low and the resultant pattern would result in a more digitate pattern instead of dendritic behavior (Pieri, 1979, 1980). Nevertheless this global behavior can be locally modified if topographic control is present, as it will be showed later. The maximum Strahler order which we found in our database is 4 while the maximum Shreve magnitude we computed is 65.

Once derived the number of streams for each Strahler order, we plotted the law of stream numbers which is derived plotting the number of streams of a specific Strahler order versus the Strahler order itself. By fitting the resultant values with an exponential law a value for the bifurcation ratio, R_B, of 6.794 is given. After plotting the average length for each Strahler segment order on the entire database versus the Strahler order itself, we derived a stream length ratio, R_L, of 1.702 through the law of stream lengths. The R_B value falls slightly out of the typical Earth bifurcation ratio (Horton, 1945) of 3 - 6, where values 5 and 6 are considered happening on hilly and mountainous areas, while the stream length ratio R_L we derived is well between the expected Earth ranges of 1.5 - 3.5. This is anyway an indication that the considered database is constituted by different riverbed morphologies and a similar geomorphological selections have to be performed before computing the bifurcation ratio and the stream length ratio parameter. Only the selection of continuous paleorivebeds, which we think have formed together through the same climatic conditions and morphologies, will give significant and more meaningful values for both R_B and R_L parameters.

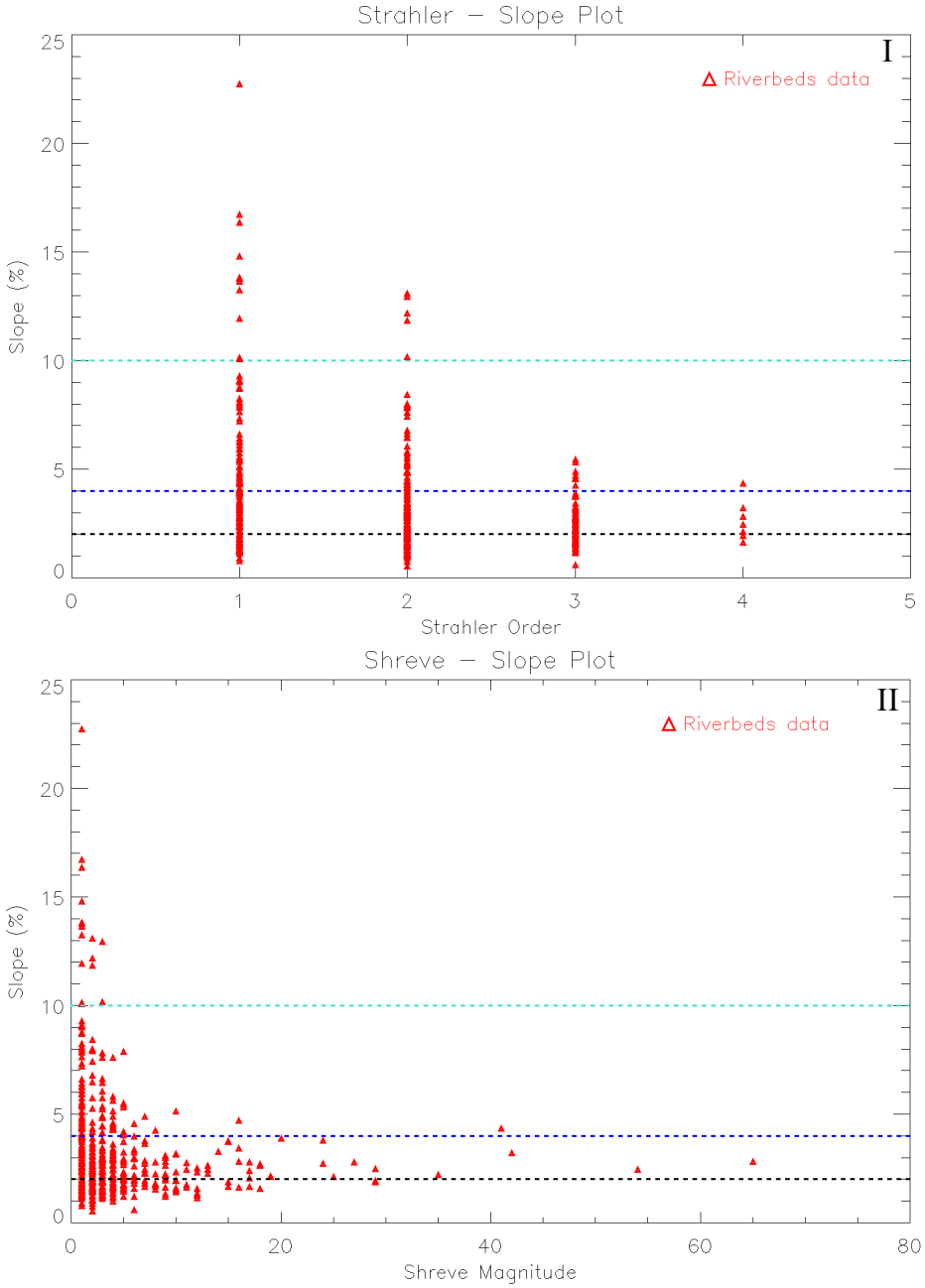

Figure 3.6: I: Strahler order versus slope plot. II: Shreve magnitude versus slope plot. Note the slope classification as presented in Rosgen (1994).

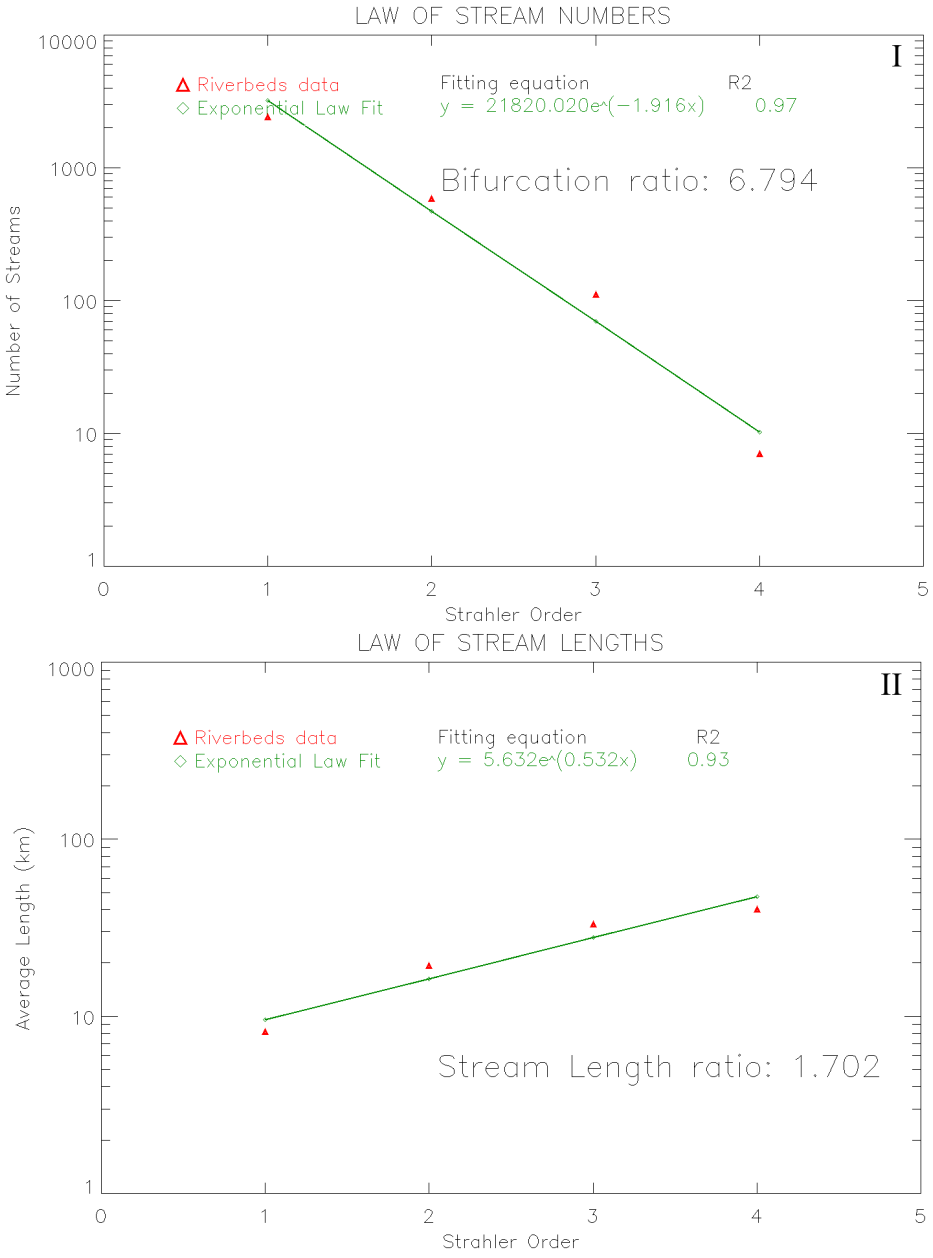

Figure 3.7: I: the law of stream numbers giving the bifurcation ratio R_B value. II: the law of stream lengths giving the stream length ratio R_L value.

3.2.2 Two specific case units

In order to get significant trends between our hydro-morphological variables, we decided to select specific drainage areas and basins which are geographically close. This criterium originates from the fact that it is expected that the proximity regions presenting similar morphological variations and latitude, have been likely characterized by similar weather and climatic conditions. Hence meaningful selections can help to understand the Martian paleohydrology in providing new insights in the climatic conditions at the time the water flows incised the crust.

Over the entire presented database we found out 25 different regions. We point out that not all 546 riverbeds belong to these regions, but within the 25 selections which contains almost 200 riverbeds, close morphological behaviors are found.
In the following pages two specific cases are presented, whose trends have to be considered as reference trends which are found in the remaining 23 selections.

Selection #1

The first area is located between 176°30'0"W and 173°0'0"W longitude and between 11°0'0"S and 14°0'0"S latitude. On this area, presented in Fig. 3.8, we identified 10 different riverbeds reaching a maximum Strahler order of 4 and identifying more than 130 riverbed tributaries characterized by a Strahler order of 1, 29 riverbed trunks with a Strahler order of 2 and 8 riverbeds with a Strahler order of 3. The drainage density found spans between 0.098 km^{-1} and 0.125 km^{-1}, while the drainage area range found in this selection spans between 500 km^2 and 4 600 km^2, and the total length of the drainage networks ranges between 80 and 520 km. The difference in elevation on this area is about 5 400 m.

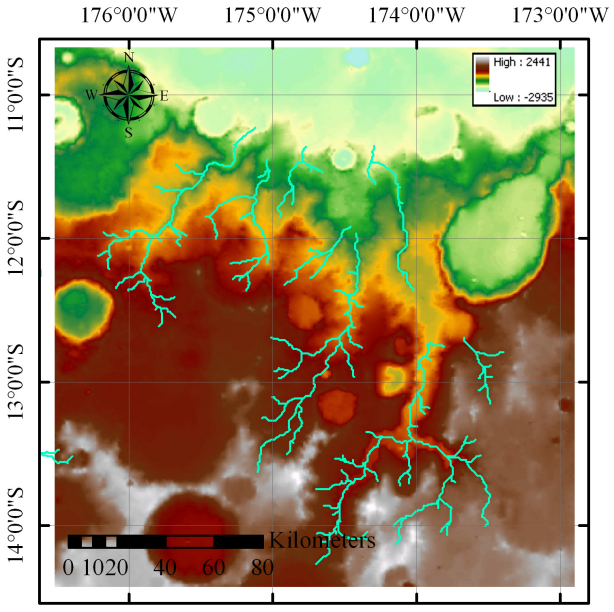

Figure 3.8: Context map of the selection area #1, with the riverbeds indicated with light blue polylines.

Once the plot slope versus drainage density is presented, see Fig. 3.9 I, an interesting behavior is found out: the higher the slope of the terrain is, the higher the drainage density (which is a synonym of riverbed maturity) becomes. As presented in Yamaguchi *et al.* (2009), a systematic increase in the drainage density with the mean slope suggests that the maturity of the valley networks depends largely on the local slope: this is called topographic control on the drainage density. In Yamaguchi *et al.* (2009) is also indicated that only if water is supplied by precipitation at much the same rate, the mean slope of the precipitated area generally controls the velocity of the resultant surface runoff, which largely influences the efficiency of erosion and eventually determines the maturity of the drainage density. In other words such drainage density behavior cannot be explained neither by having local water sources for the formation of the valley networks nor groundwater undermining the terrain and permitting collapses, because the hydraulic head on both cases does not necessarily depend on the mean slope. On the contrary such topographic control should be considered as one important hint indicating that on the surface of Mars was raining at the time these valleys were forming.

For the sake of completeness note from Fig. 3.9 I two specific aspects: the first one is that the regime which is characterizing the considered riverbeds spans from low-slope and riffle to rapids, while the second aspect is the R^2 value which in all 4 fits can be considered consistent, not pointing towards a selection of a better fit with respect to another, but, instead, indicating that the increase of the drainage density together with the slope is realistic.

In Fig. 3.9 II, the area versus length trend for the considered area is indicated. The higher the surficial area is, the bigger the total length of the riverbed network hosted in the drainage basin is. This trend is found linear for the entire statistics based on the 546 riverbeds and for each possible sample selection. This behavior shows that an increasing length of a riverbed requires an increasing drainage area dimension: this is another hint pointing towards a possible rainfall and surface runoff origin of the selected riverbeds. On the contrary, a sapping riverbed origin does not need any increase of the drainage discharge area along with the riverbed length, simply because it does not need to collect any water flows from the surroundings to be fed.
This topographic control on the drainage density is found on 6 over the 25 selections we made.

After we plot the law of stream numbers and the law of stream lengths (see Fig. 3.10 I and II) we derive from this selection, what we derive is that both the bifurcation ratio and the stream length ratio fall well inside the Earth ranges, presenting a value of 4.973 for the R_B and a value of 1.923 for the R_L. Both values indicate that the area we are considering is globally hilly-mountainous, which is confirmed from the slope regime presented in Fig. 3.9 and the difference in elevations found in each drainage area.

This area is an example that shows how from our database of 546 riverbeds, smaller meaningful selections can be obtained indicating specific and peculiar trends between the hydrological parameters that from the global trend are not thinkable and derivable. This improvement is made possible thanks to the wealth of parameters we computed for each drainage area and riverbed network.

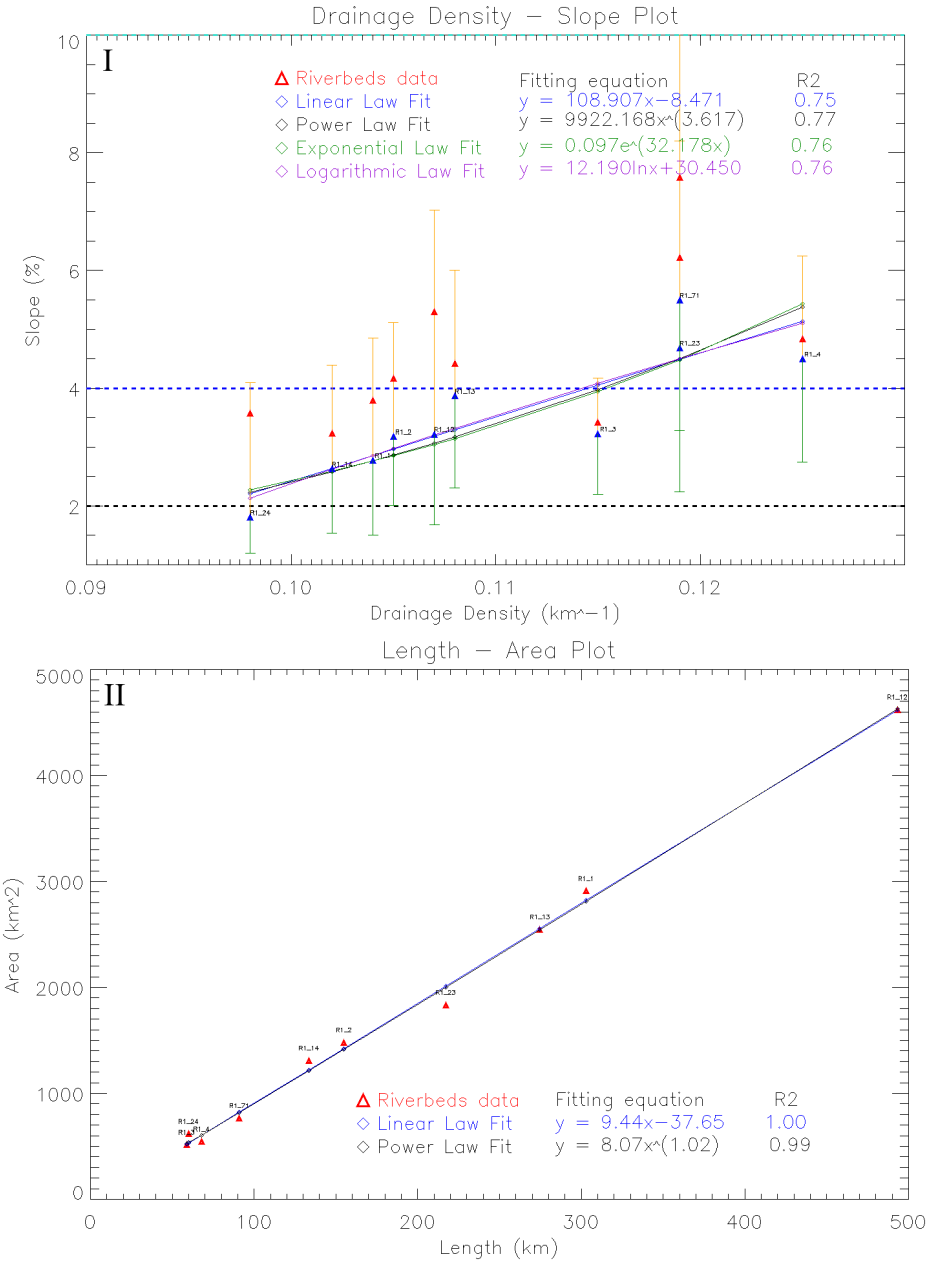

Figure 3.9: I: Drainage density versus slope plot. II: 3D length versus 3D area plot.

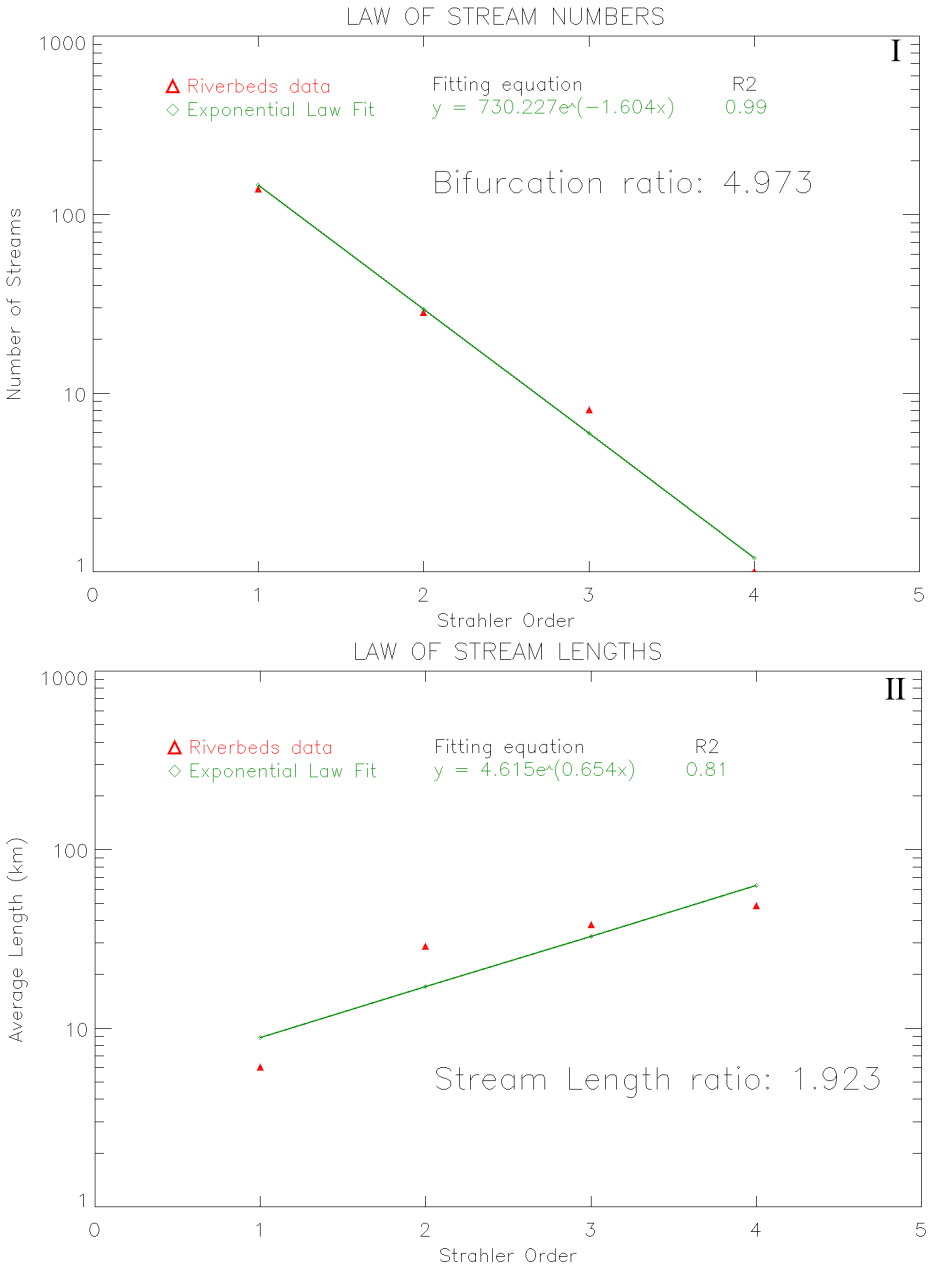

Figure 3.10: I: the law of stream numbers giving the bifurcation ratio R_B value. II: the law of stream lengths giving the stream length ratio R_L value.

Selection #2

The second area we identified, is the one presented in Fig. 3.11 inside the black polygon. The area ranges between 176°0'0"E and 178°50'0"E longitude and between 16°20'0"S and 18°0'0"S latitude. It is 140 km long and 60 km wide. Within this terrain 13 riverbeds incised the surface falling down into the main canyon, which is the Ma'adim vallis, the one flowing inside the Gusev crater, NASA's rover Spirit landing site. This site presents a global topography with violent discrepancies in altitude due to the major cut of the Ma'adim canyon, and hence the principal hydrological regime for the considered riverbeds ranges from the Step/Cascades one to the Rapids one, with just a small component of riffles and low slope riverbed sections.

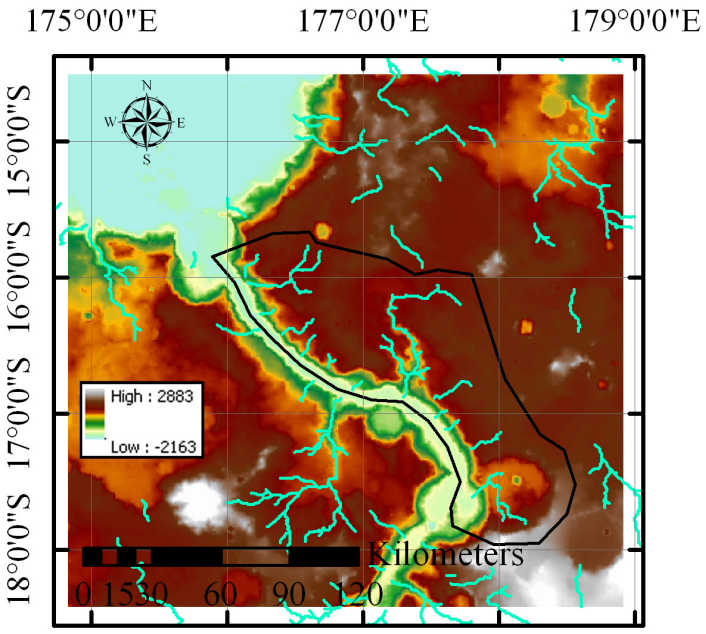

Figure 3.11: Context map of the selection area #2, with the considered riverbeds indicated with light blue polylines inside the black polygon.

The maximum Strahler order measured on this area is 3, we have 50 riverbeds trunks with a Strahler order of 1 and 10 riverbeds characterized by a Strahler order of 2.

If we now take into account the plot presented in Fig. 3.12 I, what we can derive is a trend which is intimately different with the one presented in Fig. 3.9 I. Nevertheless this is a trend which we think is much more intelligible with respect to the one characterized by the topographic control on the drainage density: the lower the slope of the terrain is, the higher the drainage density becomes. This trend is repeated similarly in 19 over the 25 selections we made, especially on terrains presenting a smaller global slope with respect to this area. In this case the drainage density versus slope behavior is explained by the fact that the lower the slope of the terrain is, the higher the possibility for the river to start meandering is (and the higher the possibility for riverbed branches to connect is), increasing the total length of the network with respect to the same drainage area. This is possible when no topographic control is affecting the drainage density;

the same behavior is commonly observed on the Earth.

The measured length for the selected riverbeds ranges from small steep riverbeds around 5-10 km, to a bigger network of about 150 km, with areas ranging from 50 km^2 up to 1 000 km^2. When the area versus slope is plotted, see Fig. 3.12 II, a linear fit is favored with respect to the power law one, which still keeps a high R^2 value. If we compare the two angular coefficients for the linear fits of Fig. 3.9 II and 3.12 II, we see that the second one is lower with respect to the first one. If we consider an equal riverbed that incises the terrain presenting the same length for both regions, within the second case a smaller drainage area is expected/required to fed it. We think that this is related to the global slope of the entire region which for the second area is bigger than the first one, as validated by the hydrological regimes. Considering the rainfall and the consequent surface runoff as the possible origin for these paleoriverbeds, a higher original slope of the terrain being incised typically favors a Strahler order degree that is lower with respect to the one presenting a lower slope: this is the trend we observe, *i.e.* a maximum Strahler order 4 for the previous region, while we have a maximum Strahler order of 3 for this one.

We point out that this area has to be considered as an upper limit case of a high slope terrain, while the resultant 23 selections range in the middle between this case and the previous selection #1 presented.

Once we plot the law of stream numbers and the law of stream lengths of this selection, we derive a bifurcation ratio and a stream length ratio which are slightly out of the Terrestrial ranges, pointing toward a particular steep and mountainous morphology, with a high global slope, as enhanced in the drainage density slope plot.

As this case has demonstrated, together with the previous one, the slope measurement of the drainage area and the riverbed network itself, is completely necessary to understand the trend we see and the relations intervening between the measured parameters, as the drainage density, the Strahler order and the Shreve magnitude, the bifurcation ratio and the stream length ratio. Taking into account the topography of a terrain throughout the digital elevation model and computing the slope of the considered drainage areas, highly improves the understanding of the inter connections intervening between the hydrological parameters. This provides, as results, new hints pointing towards a more similar climatic behavior between the past wet and humid Mars atmosphere and the actual Earth one.

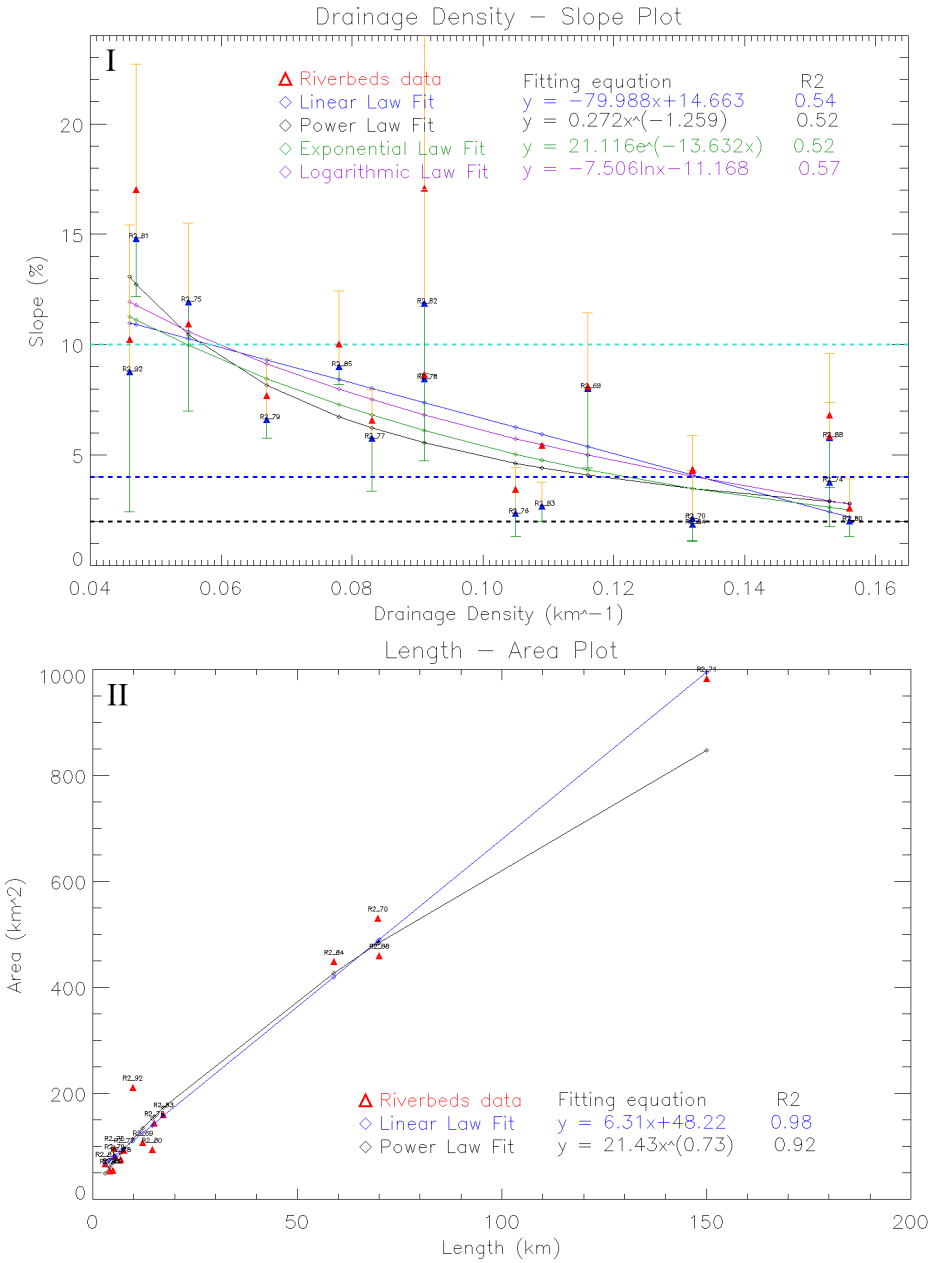

Figure 3.12: I: Drainage density versus slope plot. II: 3D length versus 3D area plot.

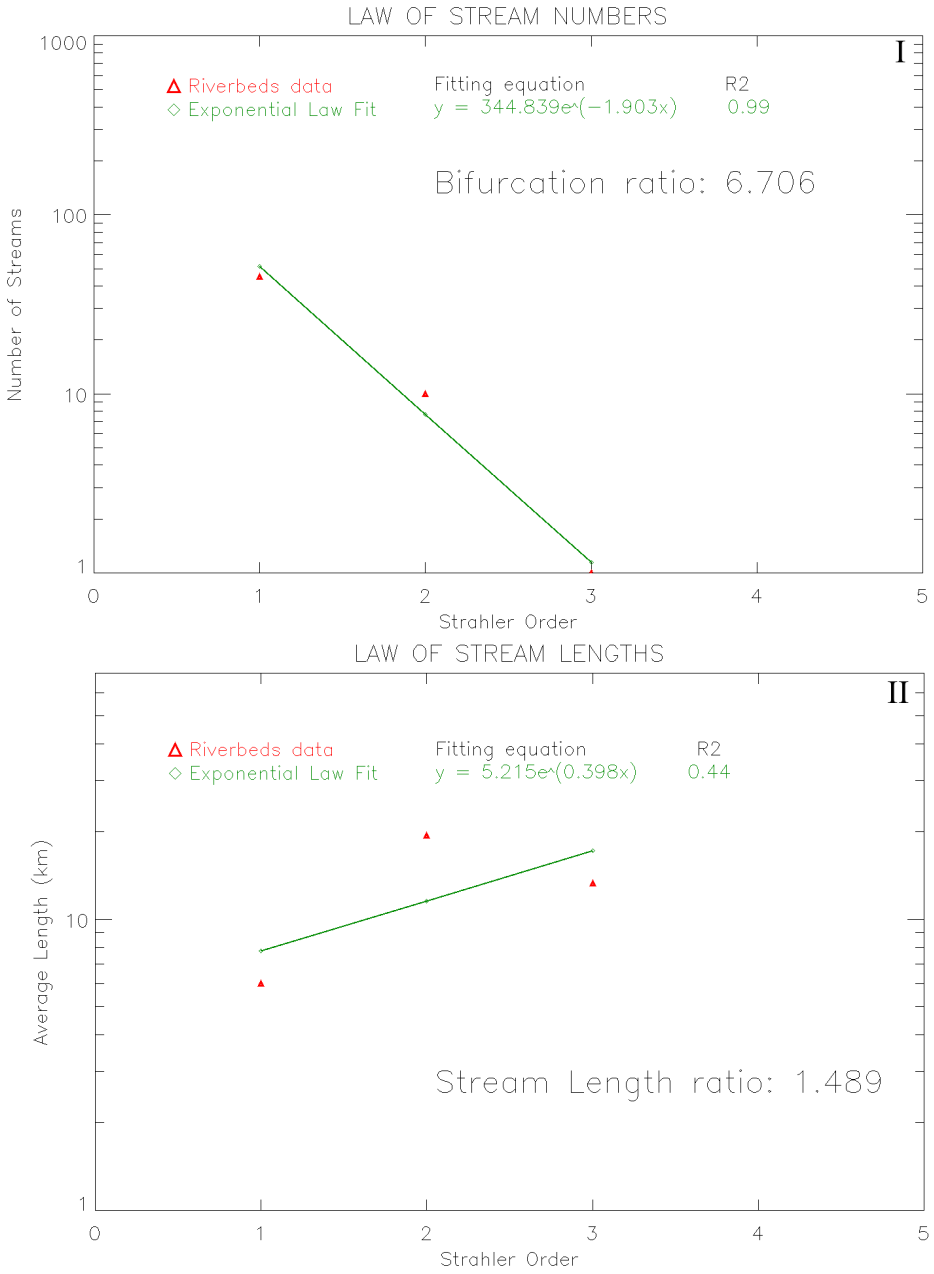

Figure 3.13: I: the law of stream numbers giving the bifurcation ratio R_B value. II: the law of stream lengths giving the stream length ratio R_L value.

3.2.3 Hints of a Martian past surface runoff and precipitation

The following analysis we made on our database has been to start performing a set of statistics in order to show more deeply the possible presence of Martian past surface runoff and by inference the presence of past precipitation.

For completeness, note that as from Carr (2006): "since Mars has no oceans and hence no sea level, an arbitrary zero-elevation level as to be defined in order to map the surface. It has been then arbitrarily decided that this zero level for Mars is defined in terms of a constant atmospheric pressure, which during the *Mariner 9* mission, this was chosen as 610.5 Pa, *i.e.* 6.105 mbar, considering that below this pressure liquid water can never be stable[2]".

In Fig. 3.14 we plotted the histogram of the distribution of the maximum elevation peak measured for each drainage area on our database. The mean of this distribution is at 733 m; 25% of the entire database is below 0 m, while the other 25% of the entire database is above 1 400 m. The median of this distribution is at 791 m. The cumulative distribution resembles the one of a gaussian distribution. The elevation values are derived from the MOLA topography, which has a vertical resolution of 0.5 m at the considered latitude range.

Thanks to the high resolution of the HRSC images (12.5 m), we had the opportunity to identify on each riverbed network, where the channelization processes started, *i.e.* the point on the surface where the riverbed network started to appear. This point is completely independent from the digital elevation model and it is observed on the high-resolution images. After this identification has been done, the elevation of this point is then computed through the digital model. Once we derived the 546 channelization locations, one for each basin, we attempted to plot the same histogram as the one for the maximum areas elevation. The result is presented in Fig. 3.15. The mean of the distribution lies at 335 m, while the median at 391 m, the 25% of the database is below -450 m while the other 25% is above 981 m. What is extremely important of these two histograms is their comparison: they seem similar and this interpretation is also confirmed by the same trend of the cumulative distribution. The major aspect which is different between the two distributions is that the one representing the riverbed maximum elevations seems to be shifted of about 400 meters in elevation. What is the meaning of this behavior?

In order to quantify properly this difference, we decided to plot the histogram representing the distribution of the distances between the maximum elevation peaks of the drainage areas, *i.e.* the drainage divides, and the channelization points identified through the HRSC images. The aim of this is to understand if there is a specific elevation distance from the drainage divides where the channelization processes starts or not. This provides two major implications:

- if we find out that there is not a specific elevation distance from the drainage divides where the channelization process starts, this would justify a sapping or groundwater origin of the paleoriverbeds, which can be present and happen at each altitude with respect to the drainage divides;
- if we derive a random distribution, this would result in a direct proof that the surface runoff was present on the Martian surface and by inference there was precipitation.

[2]The triple point of water is at this pressure. Note that this means that below this elevation, were the temperature exceeds 273.16 K the water can be found in liquid form.

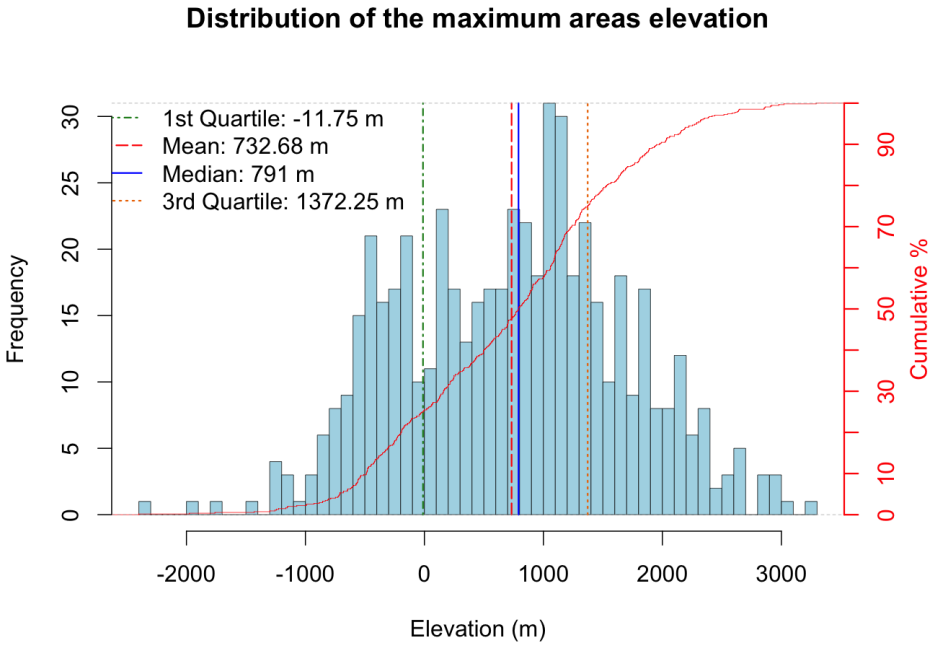

Figure 3.14: The distribution of the maximum elevation peak of each drainage basin of our database.

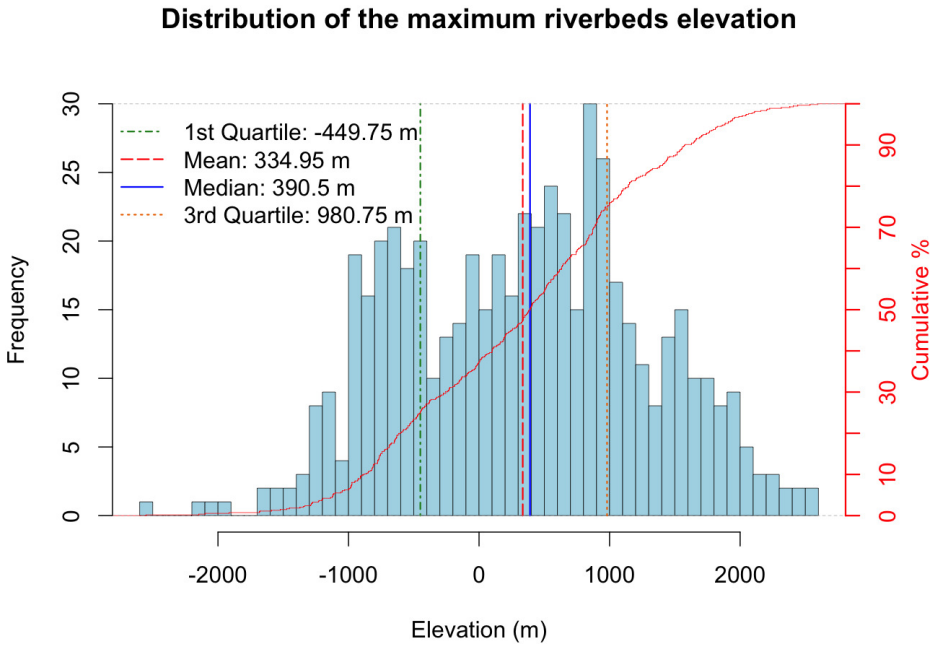

Figure 3.15: The distribution of the maximum riverbed elevation from each drainage network of our database.

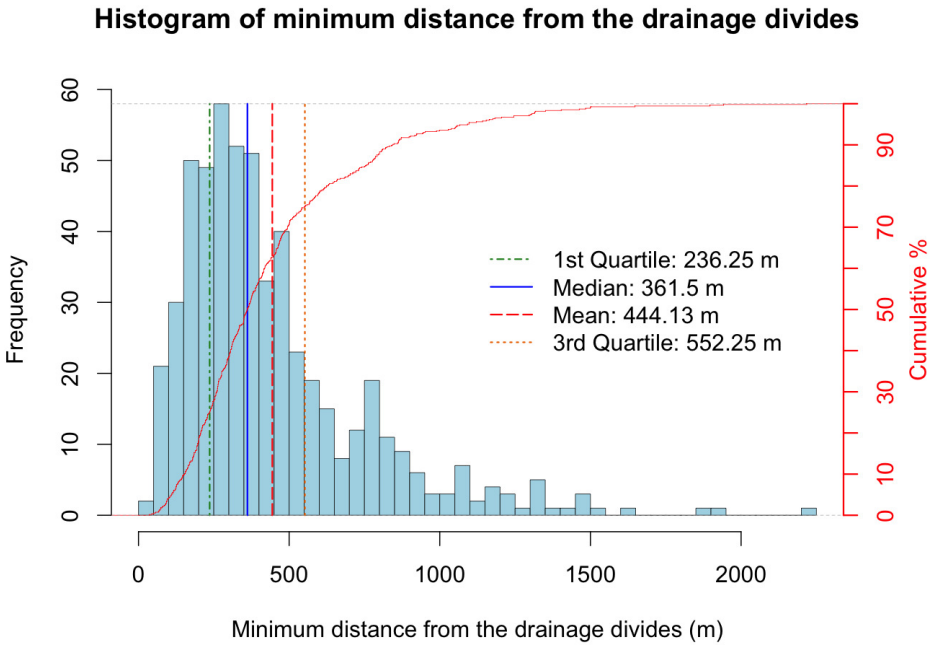

Figure 3.16: Distribution of the minimum elevation distances in meters of the riverbed networks from the drainage divides.

From Fig. 3.16, the major result we derived from our analysis is presented: a non random distribution with a median at 362 m, and a mean at 444 m is obtained. The 75% of our database lies below 552 m, while the tail of the distribution reaches up to 2 300 m. If we would have derived a random distribution between 0 m and thousands of meters below the drainage divides, this could have supported the fortuity of the sapping processes, which can happen at whatever elevation value far from the peaks of the drainage areas. Instead, what we obtained from our work is that an elevation distance of about 450 meters is typically required in order for the channelization process to happen and been visible from the high-resolution images.
Groundwater sapping is the process when groundwater exits a bank or hillslope laterally, as seeps and springs and erodes soil from the slope; this typically happens when the groundwater, pressurized by the gravity, encounters an underlying impermeable layer of soil and it is then forced to found a laterally or an overlying path to exit. The sapping process happens when the water table, *i.e.* the boundary surface between the unsaturated zone and the water saturated zone, encounters the surface terrain, see 3.17 I and II. In Fig. 3.17 I the water table level of the saturated zone reaches the hillslope way before being laterally pushed by the presence of the underlying impermeable layer of rock, while in Fig. 3.17 II the water saturated zone is laterally directed by the presence of an impermeable layer of rock which forces the pressurized water to spring out from the bank. In both cases this process is independent from the elevation distance from the drainage divides, and it appears at whatever altitude, because it does not need a collection area as the surface runoff requires to start the channelization process. Nevertheless we point out that also these sapping processes require precipitation to recharge the groundwater flow which can originate the riverbed streams.

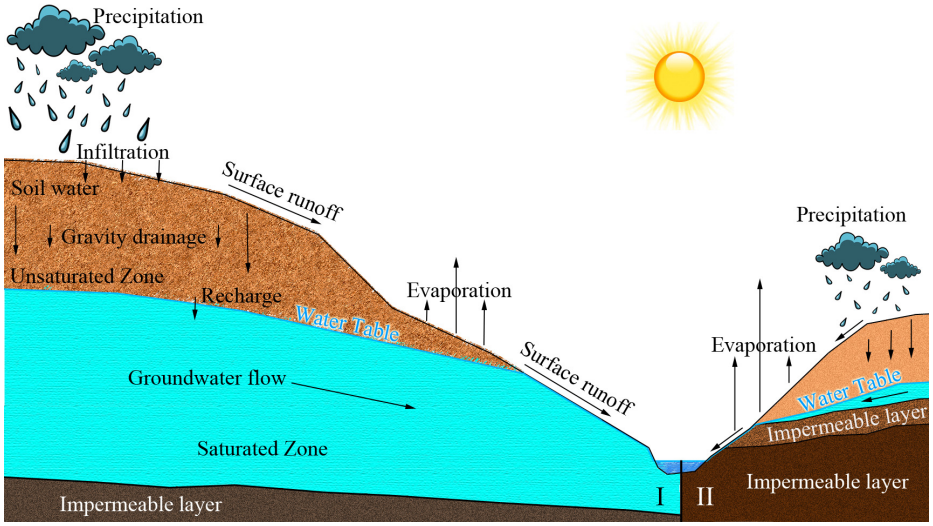

Figure 3.17: Schematic explication how surface runoff, groundwater flow and sapping work.

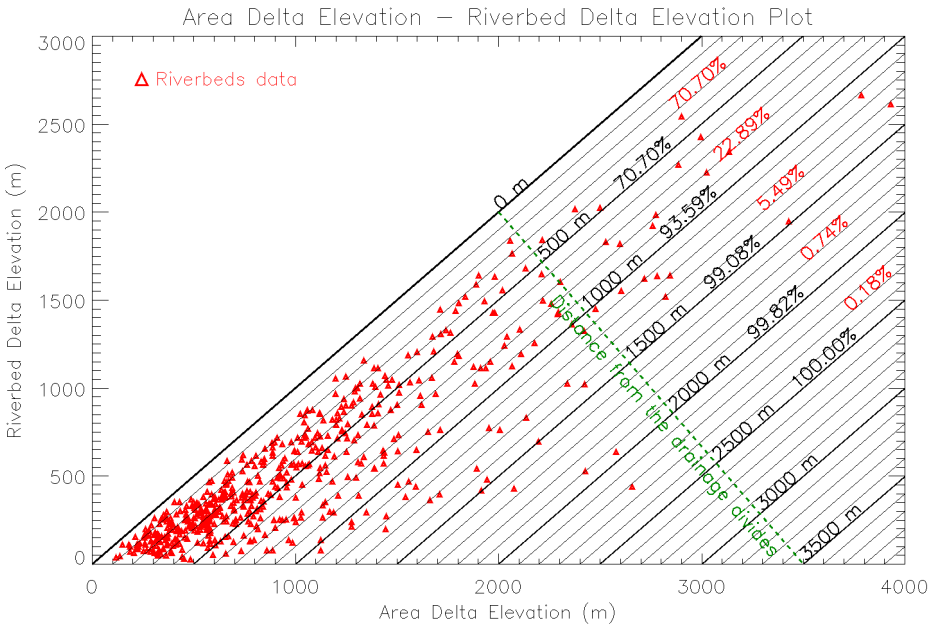

Figure 3.18: Elevation distances from the drainage divides derived from the maximum elevation peak belonging to a drainage area and the maximum elevation value computed when a riverbed starts to channelize, as observed through the HRSC images.

What we suggest we have derived through the Fig. 3.16 is the direct evidence that on the considered Mars region it was raining and consequently there was surface runoff at the time these paleoriverbeds incised the terrain. This major result together with the drainage density values presented in the previous chapters strongly point towards a wet and humid climate on Mars with an active water cycle.

In Fig. 3.18, we are showing a plot with the entire 546 riverbeds data located at different distances from the drainage divides where the channelization processes begin. As it is possible to observe, the 70.70% of our database is less then 500 m distant from the drainage divides, *i.e.* channelizes before reaching an elevation altitude of 500 m below the peaks of the drainage areas, the 22.89% is between 500 m and 1 km, the 5.49% is between 1 km and 1.5 km, the 0.74% is between 1.5 and 2.0 km, and the remaining 0.18% is between 2.0 and 2.5 km. We strongly think that our entire database cannot be simply constituted from riverbeds which formed through precipitation and surface runoff, because the tail of the distribution presented in Fig. 3.16 would justify also a sapping origin, but we suggest that the main bulk of our database does point towards a humid and rainy formation validating the warm and wet early climate that incised the crust presented by Masson *et al.* (2004); Ansan *et al.* (2006); Hynek *et al.* (2010).

3.2.4 Hints towards a past northern sea through the coastline distribution

The following analysis we performed on our database has been the identification of the distribution of all 546 outlet elevations. Through the HRSC 12.5 m resolution images, we identified the location of the deltas and outlets of our paleoriverbeds, after that we measured the elevation of all identified outlets through the MOLA DEM, which presents a vertical resolution of 0.5 m, and then we plotted the histogram of their frequency versus the measured altitude. The aim of this approach has been the identification of specific frequent outlet altitudes which could justify the presence of a possible sea/ocean coastline stopping the development of riverbeds while flowing into it. In Fig. 3.19 we can see the main results of this analysis:

- the outlet elevation distribution spans between -2 600 m and 2 000 m;
- above 1 500 m we have a fast cut off of higher elevation outlets;
- there is a main distribution with random, but similar elevations between -1 350 m and 1 000 m, not identifying specific elevations with higher frequency with respect to others;
- on top of the main histogram, a peak located around -1 350 m is present, identifying a possible second outlets elevation distribution;
- 447 outlet elevations, *i.e.* the 81.87%, are higher than -1 357 m;
- 99 outlet elevations, *i.e.* the 18.13%, are lower than -1 357 m;
- below -1 350 we have a rapid counts drop which goes to zero at an elevation between -2 550 and -2 600 m.

We compared our results with the work of Di Achille *et al.* (2010), that indicated the presence of an ancient northern ocean on Mars supported by the global distribution

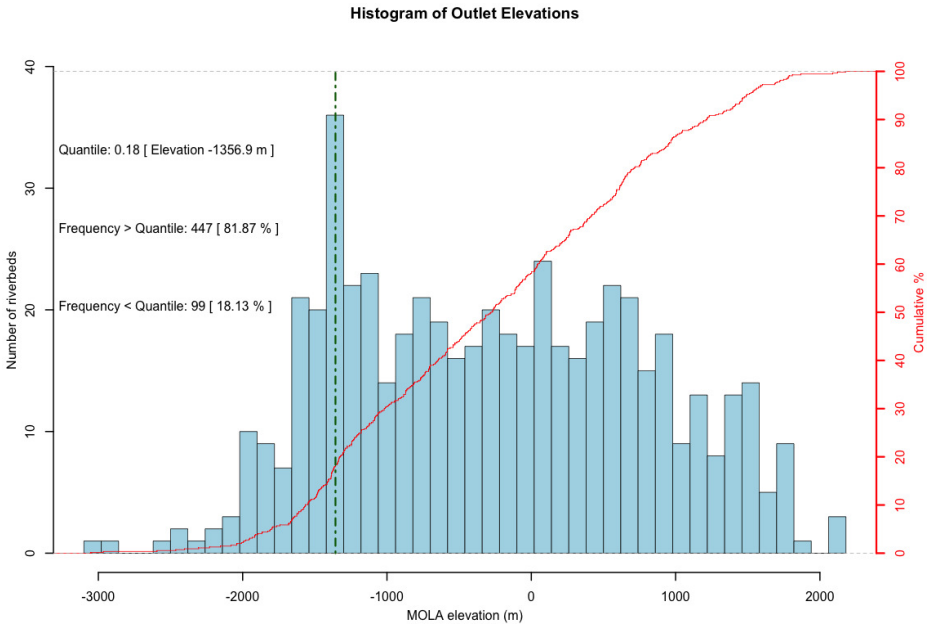

Figure 3.19: Distribution of the outlet elevations measured from our database.

of deltas and valleys. Through this analysis Di Achille *et al.* (2010) indicated the elevation level of -2 540 $\pm$ 177 m as the one of the putative ocean covering the entire northern Martian hemisphere. To derive this measure, Di Achille *et al.* (2010) focused entirely on the elevation of 52 deltaic deposits and the valleys database presented by Hynek *et al.* (2010).

If we look carefully at Fig. 3.19, we can actually see that less then 0.5% riverbeds present an outlet elevation which is lower than -2 540 m: we can then affirm that first result appears to confirm Di Achille *et al.* (2010) results. We suggest anyhow that the statistics we derive from our data is indicating something more: the peak located at -1 350 m could identify a possible higher ocean water level, probably older then the one identified by Di Achille *et al.* (2010), see Fig. 3.20. The likely explanation of this results is that the ancient ocean could have experienced different phases of evolution and evaporation, and hence different coastline elevation values with consequent different riverbed outlets elevations, alternated by stability periods.
This idea could be justified in terms of the Mars wobbling axis measure as presented by Laskar (2005, 2008), which indicated a possible Mars obliquity oscillation from 25 to 45 degrees only in the past 10-5 Myr. In both cases, *i.e.* that the ocean level was only at -2 540 m or also at -1 350 m, a completely different atmosphere with a bigger pressure and temperature, with respect to the actual one, is required to justify the stable presence of an ocean on the surface of Mars. This analysis, completely different with respect to the previous hydrological ones presented in the previous chapters, shows another important hint pointing towards a wetter and more humid atmosphere of Mars, likely similar to the one which is present nowadays on the Earth favoring a water cycle recharging rivers, lakes, seas and oceans.

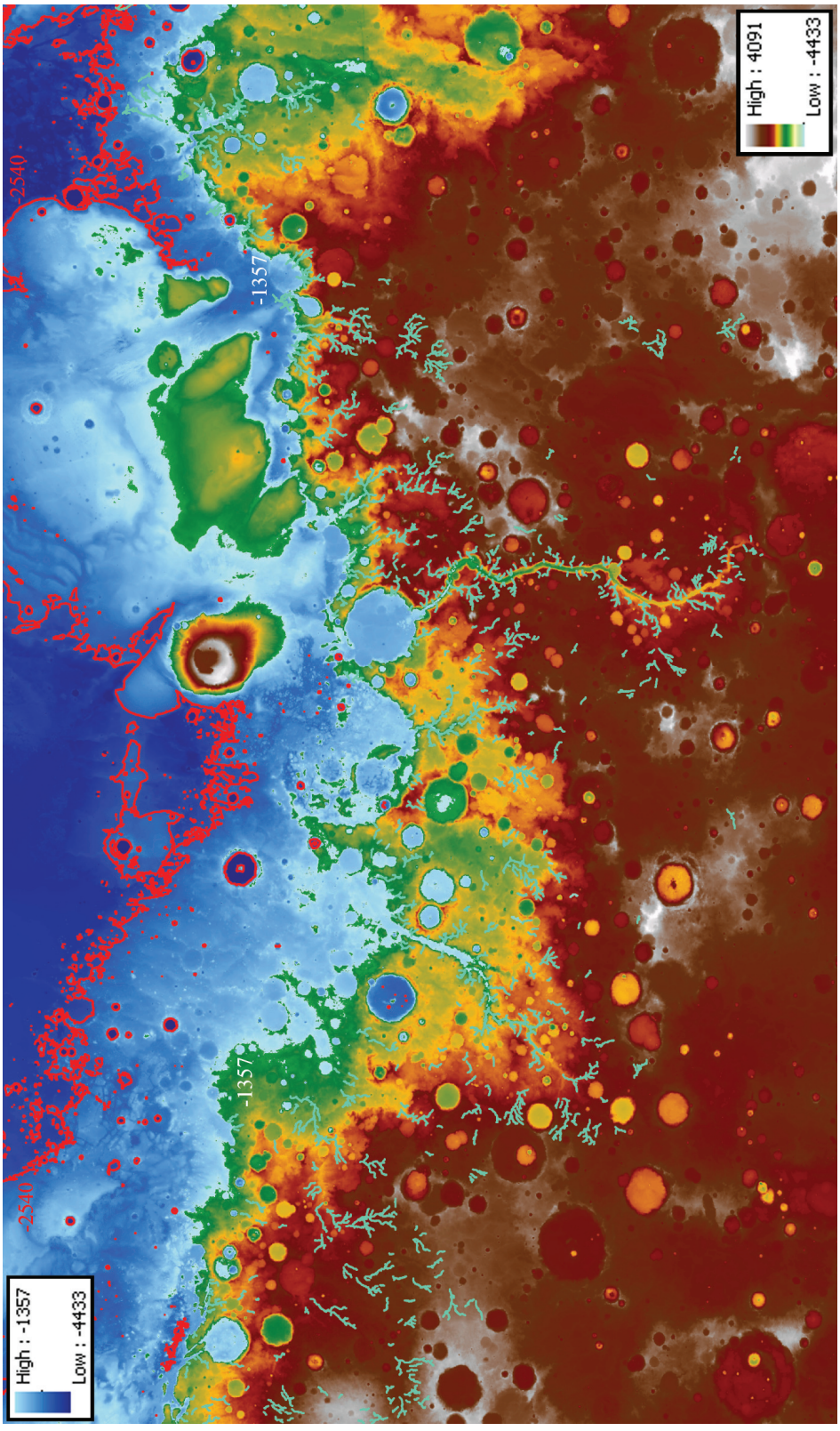

Figure 3.20: Elevation map showing our entire riverbeds database, our coastline elevation at -1 357 m and the Di Achille *et al.* (2010) coastline in red at -2 540 m. The depths of the Martian ocean are presented, together with the inland altitudes.

Chapter 4

Mars Paleolakes: Introduction, Issues and Methodology

4.1 Paleolakes Introduction

The ancient Mars terrains are found on the southern highland plateau (Milton, 1973; Schultz *et al.*, 1973), whereas the northern lowland plains and western equatorial Tharsis volcanic province have been resurfaced since the time widespread valley development ceased (Parker *et al.*, 1993). The most heavily cratered regions belong to the southern hemisphere on Mars. This hemisphere shows evidences of multiple paleolakes connected through valley networks and drainage riverbeds (Pieri, 1976; Carr *et al.*, 1981; Goldspiel *et al.*, 1991).

Multiple candidate paleolakes have been discovered through the Viking data (Goldspiel *et al.*, 1991; Cabrol *et al.*, 1999, 2001) recognizing valley networks as sources of water entering topographic low where water would have ponded. The first global surveys focusing on the presence of lake basins on Mars were developed before the realization of the Mars global topography by MOLA (Smith *et al.*, 1999). With the works of De Hon *et al.* (1992); Cabrol *et al.* (1999, 2001) it was demonstrated that both valley network and outflow channel resulted in ponding of water and lake formation. Outflow channels formed catastrophically and later in Martian history (Baker *et al.*, 1974), while valley network-fed lakes are likely to have been longer-lived and closer to equilibrium with the surface environment when they formed (Fassett *et al.*, 2008a).

Fassett *et al.* (2008b) work, is the first example of an analysis and paleolakes survey, using new topographic information, as MOLA (Zuber *et al.*, 1992), as well as high-resolution image data from *Mars Global Surveyor*, *Mars Odyssey*, *Mars Express* and *Mars Reconnaissance Orbiter*, to study the population of candidate lakes that once existed on the surface of Mars. Fassett *et al.* (2008b) directed their focus on candidate lakes characterized by clearly observed outlet valleys. They interpret as having been once open basins, in contrast to closed basins with valley sources but no outlet valleys. The advantage of studying possible lakes where outlets are observed, is that through this analysis, strong, direct evidence that lakes must have existed at these sites is given.

4.2 Issues

Several issues are related to the study of Mars ancient paleolakes: the detection, the georegistration between elevation models and remote sensing imagery (Matsubara *et al.*, 2011), the 3D morphology, the hydrological study and the relationship between the input valley networks and the connected lakes (Fassett *et al.*, 2008b). Nevertheless the most contentious issues are the identification of possible relation with a regional hydrological system (Mangold *et al.*, 2006; Grant *et al.*, 2011; Schon *et al.*, 2012), the assessment of relative age of the paleolakes, i.e., relative age of the terrains that contain them, through crater counts (Tanaka *et al.*, 1986; Hartmann *et al.*, 2001) and the estimation of the minimum volume of ponding water in the basin using the present topography (Fassett *et al.*, 2008b; Schon *et al.*, 2012).

Our specific study regards paleolakes with outlets, which provide direct evidence that the water, in the past, needed to have ponded to great enough depth in the basin to form an outlet and breach the basin boundary.

Addressing these issues about open-basin lakes, results in providing constraints on the surface environment at the time they were active, identifying uniquely a TBD time on the Martian evolutive history characterized by the presence of liquid water on the surface and of a hydrological system capable of sustaining the filling of the lakes.

4.3 Methodology and Goals

The main way to make comparisons between Mars and Earth lakes is merging the previous issues with the paleolake parameters we manage to derive. In order to get a thorough understanding of the Mars paleolakes, we focus on a methodology that allows us to derive the following lacustrine parameters:

- the water level, W_L, derived from the elevation value of the outlet riverbed;
- the lake surface, A_0, computed at the W_L;
- the 3D area, A_{3D}, of the paleolake basin hosted by the impact crater;
- the water volume, W_V;
- the mean elevation of the paleolake floor, $\bar{Z}$ which corresponds to the mean elevation of the crater floor;
- the water mean depth $W_{\bar{D}}$;
- the lake minimum elevation z_{min}, equal to the crater minimum elevation;
- the mean elevation of the crater rim and its radius, essential to compute the sediment thickness range;
- the sediment thickness range, derived from the depth (d) − diameter (D) relationship, $d = 0.36D^{0.49}$, presented by Garvin *et al.* (2003). As from Schon *et al.* (2012), by using the Garvin *et al.* (1998, 2000, 2003), law on the crater hosting the paleolake, the depth of the crater is predicted. Subtracting the expected depth to the elevation difference from the rim's mean value and the $\bar{Z}$, the sediment thickness range filling the crater is derived;

- the relative depth, Z_R, which is the ratio of the minimum elevation of the lake z_{min} in kilometers, as a percentage of the mean diameter of the lake at the surface:

$$Z_R = \frac{50 z_{min}\sqrt{\pi}}{\sqrt{A_0}},$$

(Hutchinson, 1957; Wetzel *et al.*, 1991);

- the shoreline length, S_L;

- the shoreline development, D_L, which is the ratio of S_L to the length of the circumference of a circle of area A_C equal to A_0:

$$D_L = \frac{SL}{2\sqrt{\pi A_C}}.$$

(Hutchinson, 1957);

- the volume development, D_V, that is a measure of departure of the shape of the lake basin from that of a cone:

$$D_V = 3\frac{\bar{z}}{z_{min}},$$

(Hutchinson, 1957).

The quality of the results depends strongly on the resolution of the available Digital Elevation Model of the observed paleolake (Mangold *et al.*, 2004; Masson *et al.*, 2004; Ansan *et al.*, 2008; Fassett *et al.*, 2008b; Hynek *et al.*, 2010). The resolution of the images and of the derived DEM affects both the possibility to discern the elevation value of the outlet riverbed, which is pivotal in the computation of the minimum value for water to overflow and the correct computation of the volume of water once filling the paleolake. In order to derive the above-mentioned lacustrine parameters, we use both MOLA (Zuber *et al.*, 1992) DEMs that cover large areas of Mars at a moderate resolution of 460 m and, when possible, HRSC (Neukum *et al.*, 2004) DEMs which have a resolution of 75 m. Through the use of both MOLA and HRSC DEMs, we produce a detailed study of various Mars paleolakes, contextualized with Earth lacustrine parameters. These results are helpful for future analysis aiming to use new DEM with higher resolution observations.

Chapter 5

Paleolakes Analysis, Results and Discussion

In this chapter we are applying the above-mentioned methodology deriving the lacustrine parameters on three paleolakes we have discovered on the considered Mars analysis area. The first two paleolakes (I, II) belongs to the same hydrological network and are located in Mars Memnonia quadrangle between 164°0’0”W and 169°0’0”W longitude and between 7°0’0”S and 12°0’0”S latitude.

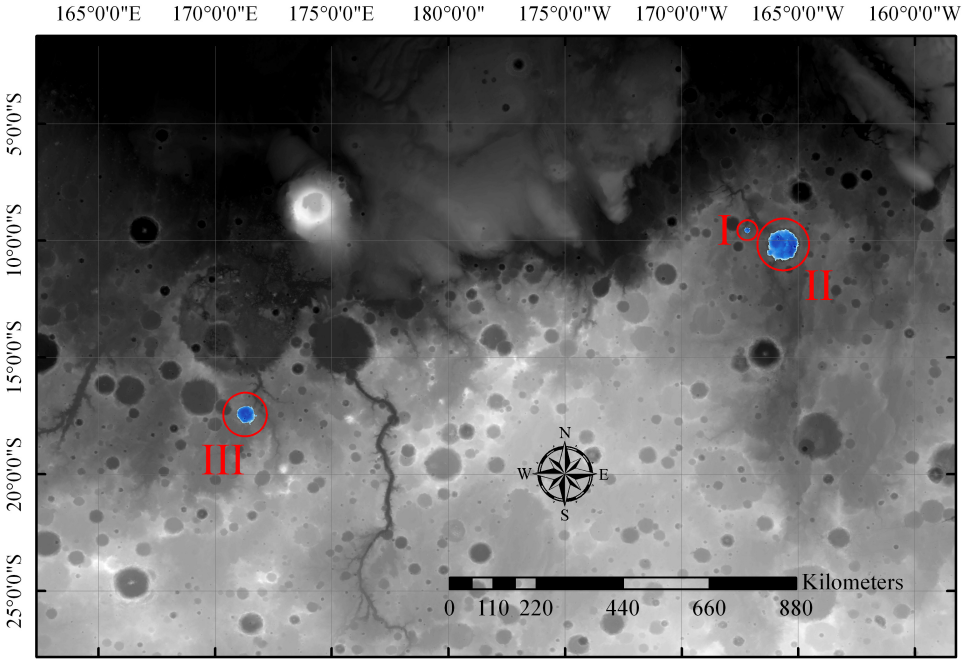

Figure 5.1: The location, on Mars, of the three considered paleolakes I, II, and III.

The third paleolakes is 1430 km far from paleolake II and belongs to the Durius Vallis drainage network, located between 170°50’0”E and 171°50’0”E longitude and

between 17°0'0"S and 18°0'0"S latitude, in Mars Aeolis quadrangle. The context global map showing the location of the three paleolakes with respect to our study area is presented in Fig. 5.1.

5.1 Contextualization of study area #1

The first case study area where we identified two paleolakes is presented in Fig. 5.2. It is located in the Mars Memnonia quadrangle, or MC-16 (Batson *et al.*, 1979), between 164°0'0"W and 169°0'0"W longitude and between 7°0'0"S and 12°0'0"S latitude. As from Fig. 5.2, the terrain elevation difference is of about 6700 meters. This region lies in the transition region between the southern highlands and the northern lowlands, known as the Mars dichotomy region. The area we are considering belongs to the Noachian age and confines on the north with the Amazonian surface (Tanaka *et al.*, 1986; Hartmann *et al.*, 2001). The two paleolakes we are presenting are identified on the map in Fig. 5.2 with two red circles. The elevation values we are showing in this map are the MOLA ones with a scale of 460 m/px, while the HRSC images used in this work are those presented in Tab. 5.1 with a scale of 12.5 m/px.

It is worth noting that the MOLA DEM is still the best global Digital Elevation Model of Mars to date and it can be deeply used to perform Mars hydrological regional studies. Indeed, HRSC DEMs cover only a small percentage of our case study area of Mars and its dichotomy region, not allowing a complete statistics of the riverbed networks and lakes on a regional scale. Nevertheless two HRSC DEMs fall inside our region of interest, the H31850000DA4 and the H3207000DA4; the first DEM has a spatial scale of 75 m/px, while the second DEM has a scale of 125 m/px. We focused on the first DEM due to the slightly better scale and because it covers entirely the Paleolake I and hence its tributary and outlet, and the west side of the Paleolake II sampling both the tributary and the outlet which are located west on the crater rim (see Fig. 5.2). The remaining side of the Paleolake II is covered only by MOLA data.

ID no.	Max. Lat (°)	Min. Lat (°)	West. Lon (°W)	East. Lon (°W)	Map scale (m/px)
H20620000ND3	3.1	-10.3	169.3	168.3	12.5
H20730000ND3	3.3	-12.4	170.0	168.9	12.5
H31850000ND3	4.1	-11.6	167.8	165.8	12.5
H32070000ND3	3.6	-11.0	169.1	166.9	12.5
H84070000ND3	-10.4	-22.7	167.3	165.7	12.5
H84950000ND3	-10.6	-22.9	169.2	166.9	12.5
H93310000ND3	-10.4	-23.3	170.7	168.3	12.5
H93380000ND3	-2.8	-25.7	166.9	164.2	12.5
H93450000ND3	-2.9	-19.9	165.6	163.3	12.5

Table 5.1: Identification number, maximum and minimum latitude, westernmost and easternmost longitude and map scale of each HRSC image used in the context map of our area of interest.

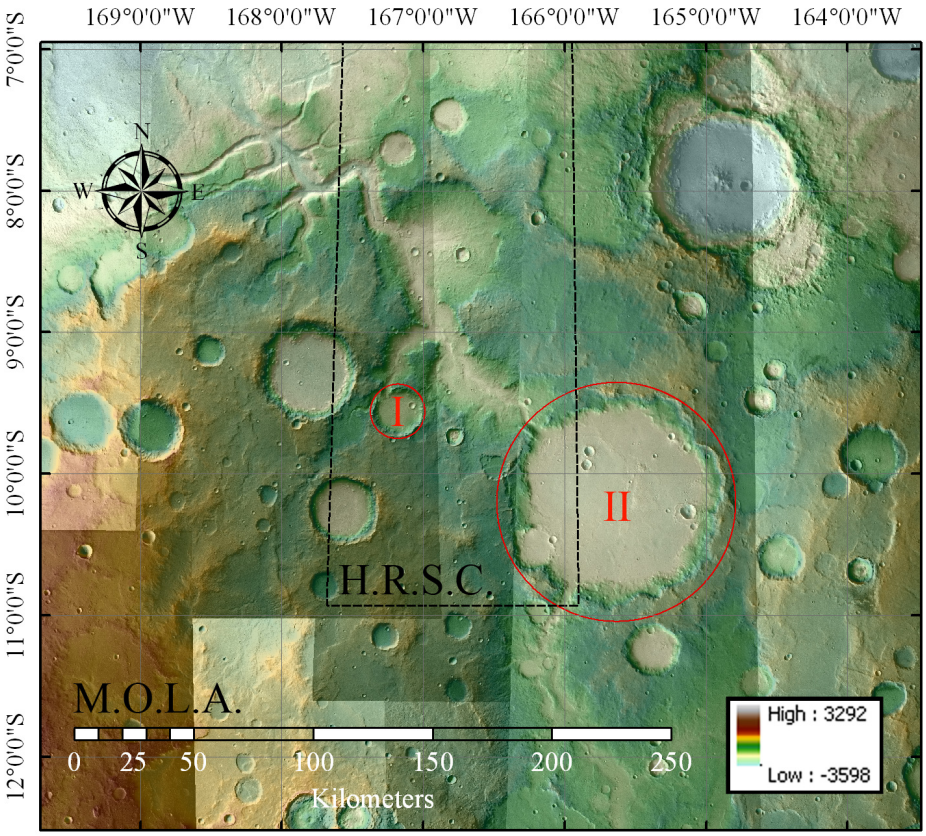

Figure 5.2: Context map of the case study area showing MOLA DEM elevation values in meters, the latitude and longitude grid and a scale bar reference. HRSC images are also showed in transparency and the boundaries of the HRSC H3185000DA4 DEM with black dashes, together with the location of the paleolakes I and II presented in this study.

5.2 Paleolake I (9°34’00”S-167°11’00”W)

5.2.1 Paleolake description and analysis

The first paleolake we consider is located at 9°34’00”S latitude and 167°11’00”W longitude. The highest peak of the surrounding area is at an elevation of -486 m located north west of the tributary riverbed, while the deepest point is the crater located north east inside the paleolake itself, see Fig. 5.3 A. The steepest slopes are on the south east side of the inner rim of the crater hosting the paleolake and reaching a value up to 65%, while the majority of the paleolake floor has a slope not exceeding 4%, see Fig. 5.3 B. We identified the rim of the crater positioning the observer in the center of the paleolake floor. The rim edge is then identified as the maximum height of the observable skyline. The highest elevation of the crater rim is at -624.3 m, while the lowest is at -998.8 m. As we can see from Fig. 5.3 C, the dashed side of the rim is completely erased, and it cannot be considered representative for the elevation computation. The median value of the elevation of the rim is -796.3 m, the mean value we derived is -805.7 m with a

standard deviation of 103.0 m (see Fig. 5.4). Once the crater's rim was identified we computed the intern and the extern osculatrix circles, obtaining a radius of 9.57 km for the inner circle, and a value of 11.39 km as the extern radius, see Fig. 5.3 C. The 2D area of the crater spans consequently between 290.0 and 408.9 km^2. A significative set of physical properties of the impact crater hosting paleolake I is presented in Table 5.2.

We created a contour map of the entire crater and the surrounding area identifying the elevation value of the outlet W_L (*i.e.* the water level): -1 409 m, see Fig. 5.5 A. The outlet elevation is the minimum value for water to overflow. We then derived the depth map of the paleolake I, as shown in Fig. 5.5 B, where 20 meters bathymetric lines are indicated. In Fig. 5.3 A, the north east crater located inside the paleolake is presenting a young and not eroded topography, hence we considered it as a crater that occurred after the lake was no longer filled and present. The computed 2D area of this crater is 4.9 km^2, its 3D area value is 5.30 km^2 and its volume is 1.14 km^3. Assuming that the paleolake before such impact covered this area, and the depression volume of the successive crater has not to be considered, we derived a paleolake 2D area, A_0, of 164.7 km^2 at the water level W_L of -1 409 m, a 3D basin area, A_{3D}, of 165.4 km^2 below the water level, and a total water volume, W_V, of 10.9 km^3. Once the depth of the small crater inside the paleolake was excluded from the computation, we computed the paleolake floor mean elevation $\bar{Z}$, deriving a value of -1 480.4 m, and a root mean square of 30.6 m, giving a water mean depth, $W_{\bar{D}}$, of 71 m. The minimum elevation of the paleolake, z_{min}, is -1 563.0 m. The elevation difference from the mean rim value and the paleolake depth is then 675 m. In Fig. 5.5 C we show the location of the elevation profiles presented in Fig. 5.6. Note the sudden change in slope of the crater's terrain at the expected W_L elevation: we think this is related to the water erosion and redeposition processes acting on the crater's interior rim. The close elevation value of the water level and the surface redeposition processes gives weight to our interpretation that the water level was at -1 409 m.

Garvin *et al.* (1998, 2000, 2003) systematically studied the depth-diameter relationship for Mars impact craters, characterizing more than 6 000 impact craters with MOLA topography. The refined power-law relationship derived through Garvin *et al.* (2003) study is:

$$d = 0.36D^{0.49},$$

where d is the crater depth in kilometers, and D is the diameter in kilometers. As a reference, this law was already used in Schon *et al.* (2012), studying the sediments thickness filling the paleolake inside the Jezero crater. By using the Garvin *et al.* (2003) law on the crater hosting the paleolake I, the crater depth, $depth_{max}$, of 1.67 km is predicted, considering the extern osculatrix circle diameter of 22.78 km. The inner circle diameter is 19.14 km, with a predicted depth, $depth_{min}$, of 1.53 km. If we subtract the expected depth with the elevation difference from the rim and the bottom of the paleolake we derive a value that ranges between 850 m and 990 m: this is the sediment thickness range which we expect has filled the crater's floor.

The relative depth (Z_R) (Hutchinson, 1957; Wetzel *et al.*, 1991) is the ratio of the minimum elevation of the lake z_{min} in kilometers, as a percentage of the mean diameter of the lake at the surface:

$$z_R = \frac{50 z_{min} \sqrt{\pi}}{\sqrt{A_0}},$$

where A_0 is the 2D area computed at the water level of -1 409 m. The value of Z_R we derive is 10.9%, close to the one derived from Crater Lake in Oregon(Hutchinson, 1957; Wetzel *et al.*, 1991).

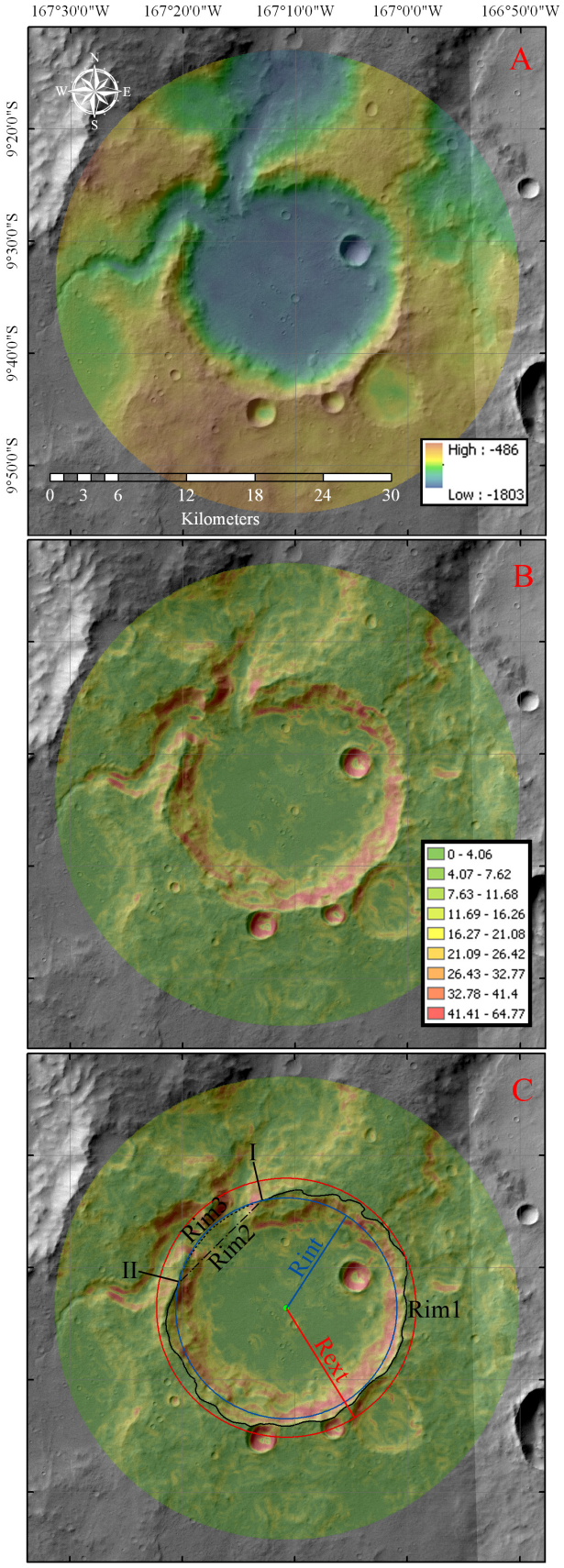

Figure 5.3: A: HRSC DEM showing the elevation values in meters, the scale bar and the latitude and longitude grid. B: Slope map with values in percentage. C: Identification of the intern and the extern osculatrix circles of the crater's rim. Rim 1, 2 and 3 are presented in Fig. 5.4.

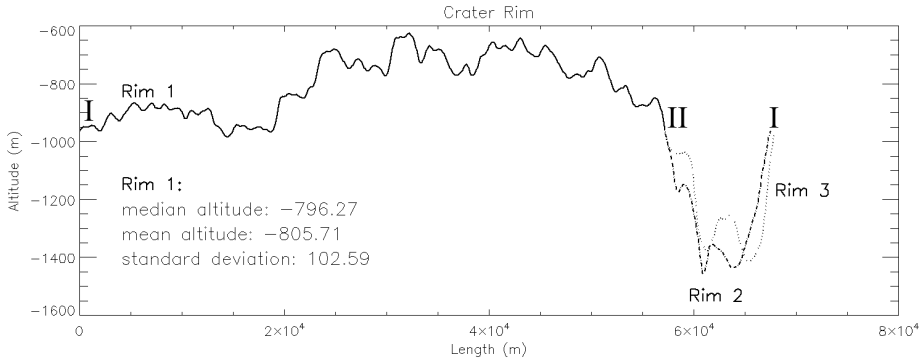

Figure 5.4: Crater rim based on the HRSC topography. Rim 1, 2 and 3 are those presented in Fig. 5.3 with the same clockwise direction from I to II.

We computed the shoreline length (SL) at the outlet elevation value, i.e. -1409 m, deriving a length of 59.74 km. We used this value to compute the shore line development, D_L, presented by Hutchinson (1957), which is the ratio of the length of the shoreline (SL) to the length of the circumference of a circle of area A_C equal to that of the lake A_0:

$$D_L = \frac{SL}{2\sqrt{\pi A_C}}.$$

Our D_L value is 1.33, close to the value derived from Crater Lake in Oregon (Hutchinson, 1957) which approaches the circular shape, i.e. $D_L = 1$. On Earth many sub circular and elliptical lakes have a value of D_L around 2, while D_L becomes large for lakes of flooded river valleys. D_L increases as lakes become more elongated and the shore line development is interpreted in terms of origin of the lake basin, having lakes in volcanic craters or caldera and meteors craters, small ratios.

We then computed the development of volume D_V presented by Hutchinson (1957). D_V is a measure of departure of the shape of the lake basin from that of a cone:

$$D_V = 3\frac{\bar{z}}{z_{min}},$$

where $\bar{Z}$ is the mean lake floor elevation and z_{min} is the minimum elevation of the considered paleolake. Our D_V is 2.84, being the value of 1 the ideal conical depression. As presented in Hutchinson (1957) in caldera lakes, graben lakes and crater lakes D_V is expected greater than 1.5.

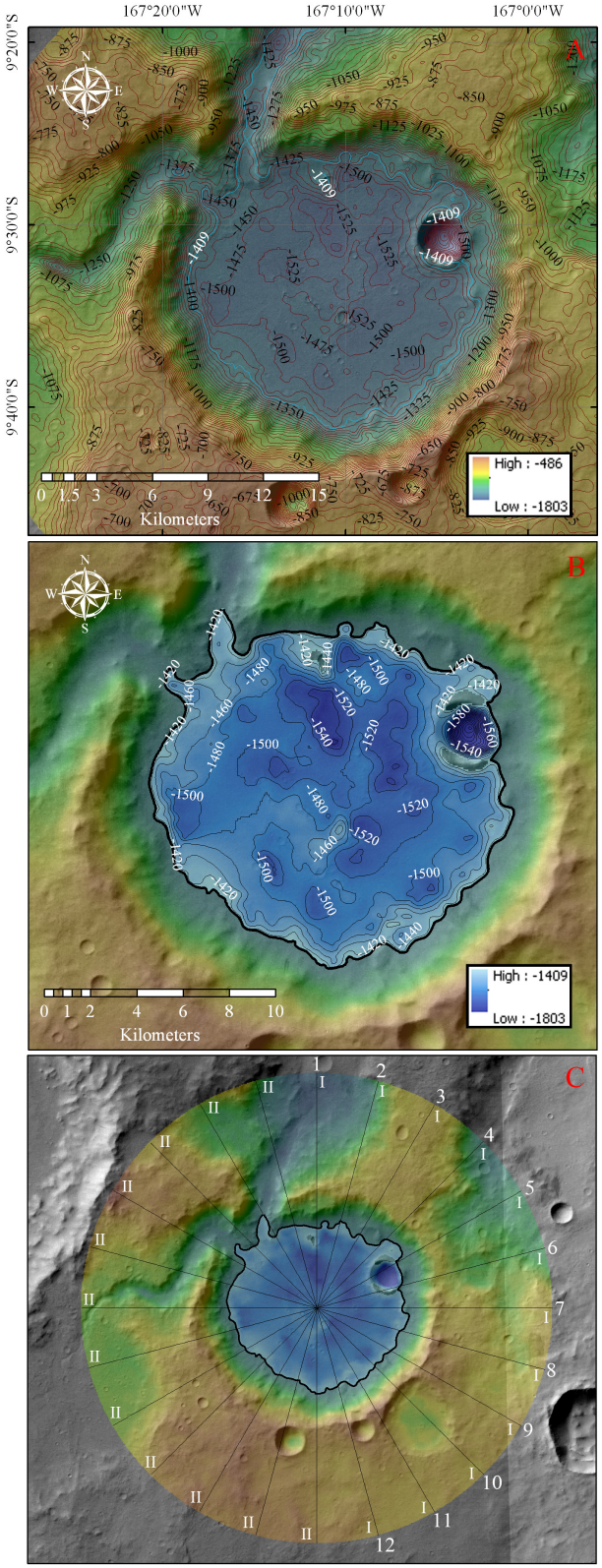

Figure 5.5: A: Contour map at 25 meters on the HRSC elevation values. The light blue polyline taken at an elevation of -1409 m shows the shoreline of the paleolake. B: Paleolake's depth contour map at 20 meters superimposed on the HRSC elevation values. C: Map showing the location of the elevation profiles presented in Fig. 5.6. The profiles are indicated with the same name of Fig. 5.6 and are extracted in the clockwise direction.

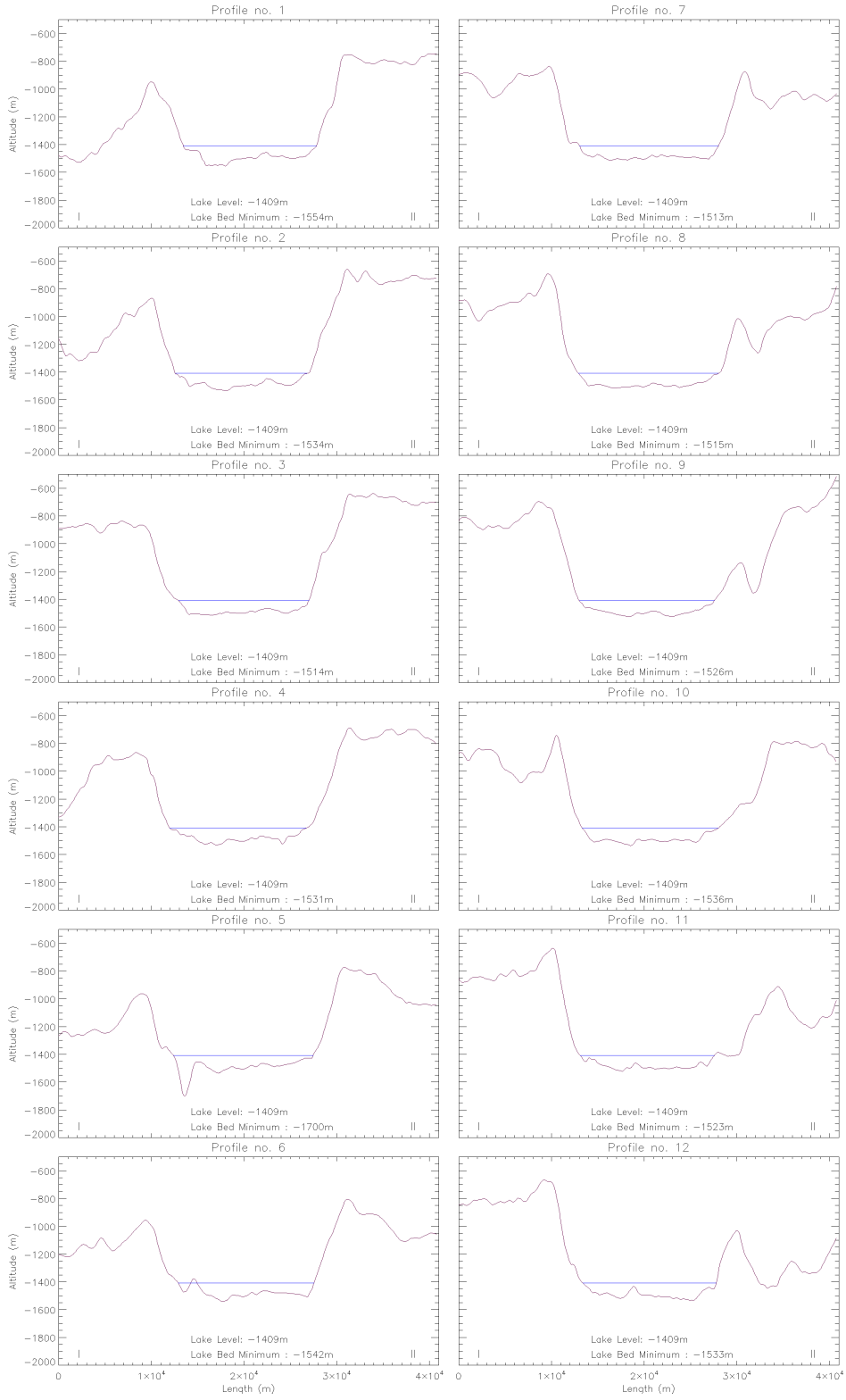

Figure 5.6: The twelve elevation profiles presented in Fig. 5.5 C. For each one the water level heigh and the maximum depth of the profile is presented.

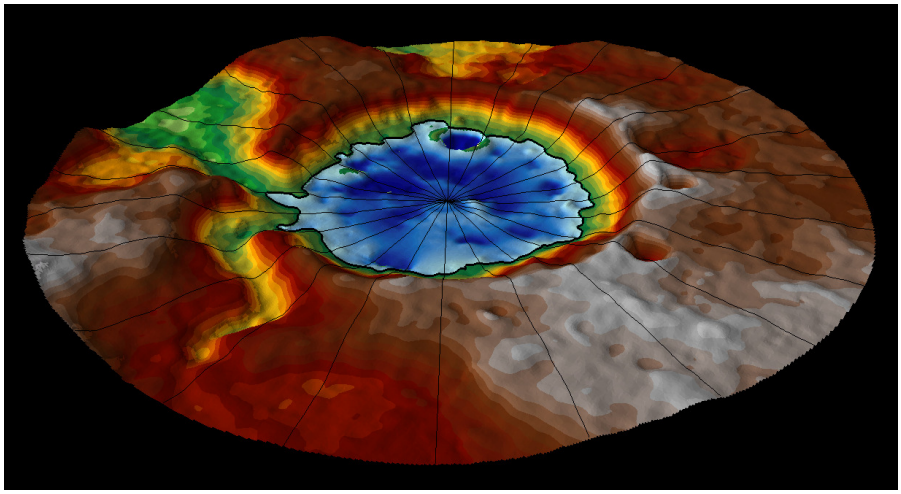

Figure 5.7: The HRSC 3D representation of the paleolake I. The 12 elevation profiles are also depicted together with the paleolake water depth. The elevation values for the terrain and the paleolake are the same of Fig. 5.3 A and Fig. 5.5 B.

	Crater I
Center latitude	9°34'00"S
Center longitude	167°11'00"W
Maximum radius r_{max} (km)	11.39
Minimum radius r_{min} (km)	9.57
Maximum diameter D_{max} (km)	22.78
Minimum diameter D_{min} (km)	19.14
Rim mean value rim_{mean} (m)	-805.7
Rim standard deviation value rim_{stdev} (m)	103.0
Rim median value rim_{median} (m)	-796.3
Expected max $depth_{max}$ (km)	1.67
Expected min $depth_{min}$ (km)	1.53

Table 5.2: Physical properties of the impact crater hosting paleolake I.

5.3 Paleolake II (10°12'00"S-165°38'00"W)

5.3.1 Paleolake description and analysis

The second considered paleolake is located at 10°12'00"S latitude and 165°38'00"W longitude.

The highest peak of the surrounding area is at an elevation of -330 m located north east of the crater's rim hosting paleolake II. The deepest depression [reaching -2 179 m] is the crater located east inside the paleolake itself (see Fig. 5.8 A). The steepest slopes presented in Fig. 5.8 B are on the inner side of the crater's rim: the maximum value is 54%. Inside the crater floor, the most frequent slopes are in a range between 0% and 8%. Once we identified the rim of the crater as we did for paleolake I, we measured the crater's rim maximum at an elevation of -343.5 m. MOLA DEM covers the entire rim's length: we plotted the crater's rim in Fig. 5.9 starting from I (Fig. 5.8 C) in the clockwise direction. We over plotted also HRSC DEM elevation values that are only available from II to I. From Fig. 5.9 we can see that MOLA and HRSC elevations mostly agree, with the important difference of the tributary and outlet altitude: this is the reason why in the following computations we measured the outlet altitude only from HRSC data, which has a bigger DEM resolution (75 m instead of 460 m). The median value of the elevation of the rim is -747.6 m (we do not consider the tributary and the outlet elevation values), the mean value we derived is -759.2 m with a standard deviation of 144.95 m (see Fig. 5.9). In Fig. 5.8 C we indicate the intern and the extern osculating circles we derived from the craters rim, giving a minimum radius of 41.31 km and a maximum of 49.70 km. The 2D area of the crater spans between 5 355.9 and 7 756.1 km^2. We also present in Fig. 5.8 C the tributary T, and the outlet O of the paleolake II. A set of physical properties of the impact crater hosting paleolake II is presented in Table 5.3.

We created a contour map of the entire crater and the surrounding area identifying the HRSC elevation value of the outlet: -1 420 m, see Fig. 5.10 A. On the superimposition area, the shoreline difference between the MOLA and the HRSC contour line at -1 420 is negligible, as it is visible with the two different light blue polylines. The biggest difference is in the location of the outlet, which in the HRSC DEM is 3.5 km further from the paleolake and the location of the tributary inside the paleolake. On the tributary, the HRSC contour line at -1420 is still open lacking data coverage. Hence we could only use the contour line derived from the MOLA DEM. The depth map with 25 meters steps bathymetric lines is in Fig. 5.10 B.

In Fig. 5.8 A, we can identify at least 13 recent craters that impacted the floor of the lake. They all present a young and not eroded topography. We considered them as craters, which occurred after the lake was no more filled and present. The computed 2D area of these craters is 72.24 km^2, their 3D area value is 73.95 km^2 and their volume is 24.59 km^3. As for paleolake I, we assume that the paleolake before such impacts covered the crater areas, but that the depression volume of the 13 craters is not considered. We derived a paleolake 2D area, A_0, of 4 734.6 km^2 at the water level of -1 420 m, a 3D basin area, A_{3D}, of 4 740.6 km^2 below the water level, and a total water volume, W_V, of 1 264.7 km^3. Once the depths of the 13 craters inside the paleolake were excluded from the computation, we computed the lake floor mean elevation $\bar{Z}$, deriving a value of -1 695.7 m, and a root mean square of 82.3 m, giving a water mean depth $W_{\bar{D}}$ of 276 m. The minimum elevation of the paleolake, z_{min}, is -1 913.0. m. The elevation difference from the mean rim value and the paleolake depth is then 937 m.

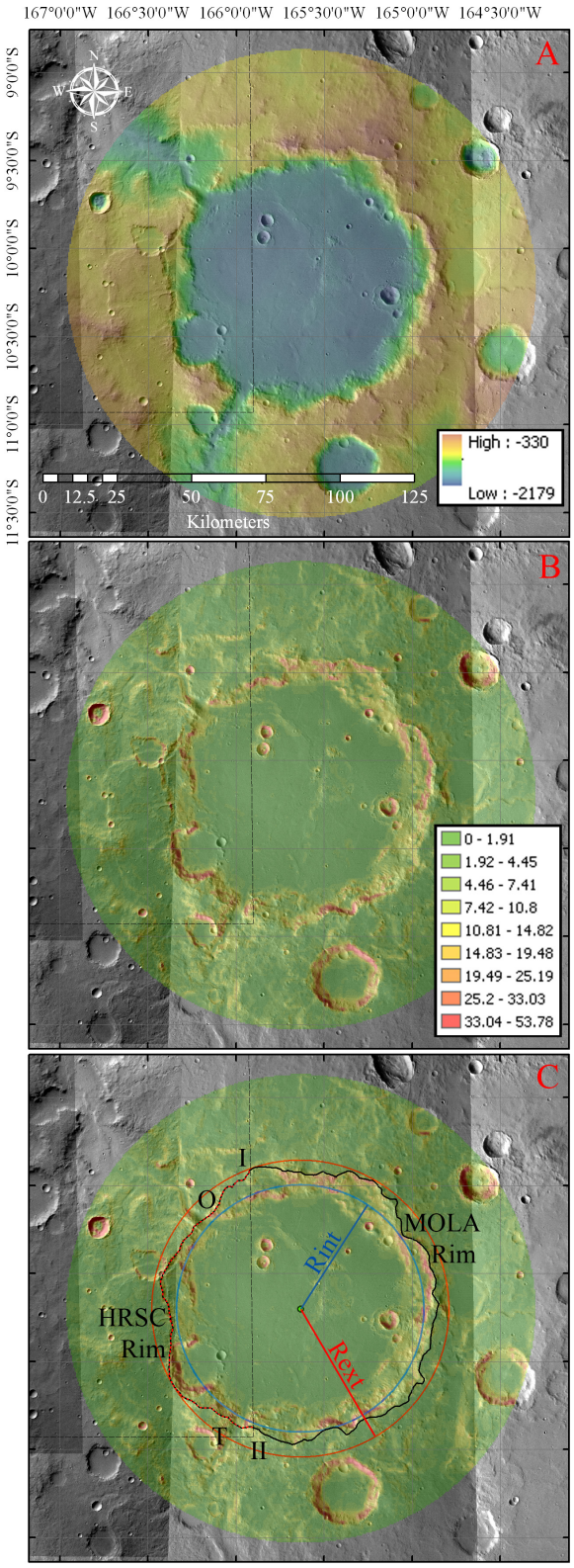

Figure 5.8: A: MOLA DEM showing the elevation values in meters, the scale bar and the latitude and longitude grid. The dashed line shows HRSC DEM coverage. B: Slope map with values in percentage. C: Identification of the intern and the extern osculatrix circles of the crater's rim. MOLA rim is indicated in black and covers the entire crater while HRSC rim is in red and cover from II to I in clockwise direction, as presented in Fig. 5.9. T is the paleolake tributary, O is the outlet.

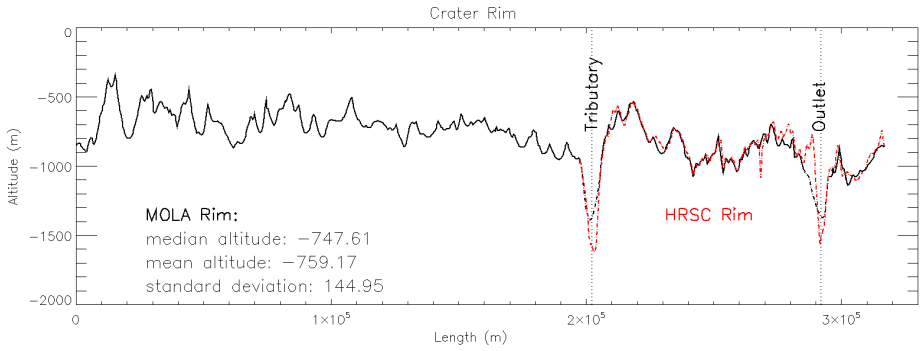

Figure 5.9: Crater rim based on the MOLA (black) and HRSC (red) topography. The rims are those presented in Fig. 5.8 with the same clockwise direction from I passing through II. The tributary and the outlet topographies are also indicated.

	Crater II
Center latitude	10°12'00"S
Center longitude	165°38'00"W
Maximum radius r_{max} (km)	49.70
Minimum radius r_{min} (km)	41.31
Maximum diameter D_{max} (km)	99.40
Minimum diameter D_{min} (km)	82.62
Rim mean value rim_{mean} (m)	-759.2
Rim standard deviation value rim_{stdev} (m)	145.0
Rim median value rim_{median} (m)	-747.6
Expected max $depth_{max}$ (km)	3.43
Expected min $depth_{min}$ (km)	3.13

Table 5.3: Physical properties of the impact crater hosting paleolake II.

By using the Garvin *et al.* (2003) law on the crater hosting the paleolake II, the crater depth of 3.43 km is predicted, considering the extern osculating circle diameter of 99.40 km. The inner circle diameter is 82.60 km, with a predicted depth of 3.13 km. Subtracting the expected depth with the elevation difference from the rim and the bottom of the paleolake we derive a value that ranges between 2 190 and 2 490 m: this is the sediment thickness range which we expect has filled the crater floor.

The relative depth Z_R derived for paleolake II is 2.5%, the measured shoreline S_L is 305.84 km. The shoreline development D_L is 1.25, while the volume development D_V we obtained is 2.66.

The resulting lacustrine parameters we derived applying the above-mentioned methodology to paleolakes I and II, are presented in Table 5.4.

As seen from Fig. 5.2, paleolake I & II belong to the same drainage network. The outlets coming from both paleolakes connect together at 9°00'00"S and 167°02'00"W form in an inner riverbed which points in the north-west direction. A comparison between the lacustrine parameters of the two paleolakes is given in Table 5.4.

	Paleolake I	Paleolake II
Center latitude	9°34'00"S	10°12'00"S
Center longitude	167°11'00"W	165°38'00"W
Water level W_L (m)	-1 409	-1 420
2D area A_0 (km^2)	164.7	4 734.6
3D area A_{3D} (km^2)	165.4	4 740.6
Water volume W_V (km^3)	10.9	1 264.7
Lake floor mean elevation $\bar{z}$ (m)	-1 480	-1 696
Water mean depth $W_{\bar{D}}$ (m)	71	276
Lake minimum elevation z_{min} (m)	-1 563	-1 913
Sediment thickness range (m)	850 - 990	2 190 - 2 490
Relative depth Z_R (%)	10.9	2.5
Shoreline length S_L(km)	59.74	305.84
Shoreline development D_L	1.33	1.25
Volume development D_V	2.84	2.66

Table 5.4: Lacustrine parameters as derived through the application of the methodology on paleolake I and II.

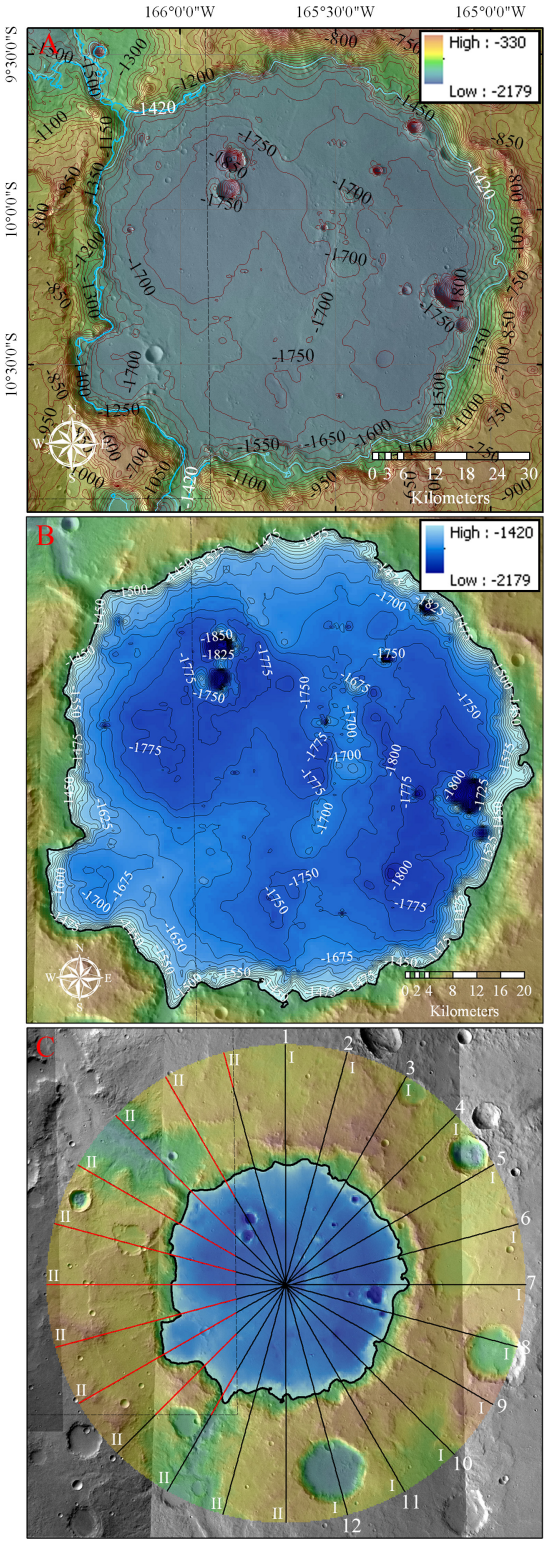

Figure 5.10: A: Contour map at 50 meters on the MOLA elevation values. The light blue polyline taken at an elevation of -1420 m shows the shoreline of the paleolake. Note that MOLA and HRSC (when present) topography are similar with the main difference in the tributary elevation values, see Fig. 5.11 profile no. 3. B: Paleolake depth contour map at 25 meters superimposed on the MOLA elevation values. C: Map showing the location of the elevation profiles presented in Fig. 5.11. The profiles are indicated with the same name of Fig. 5.11 and are extracted in the clockwise direction. Note that HRSC topography is extracted from the red polylines.

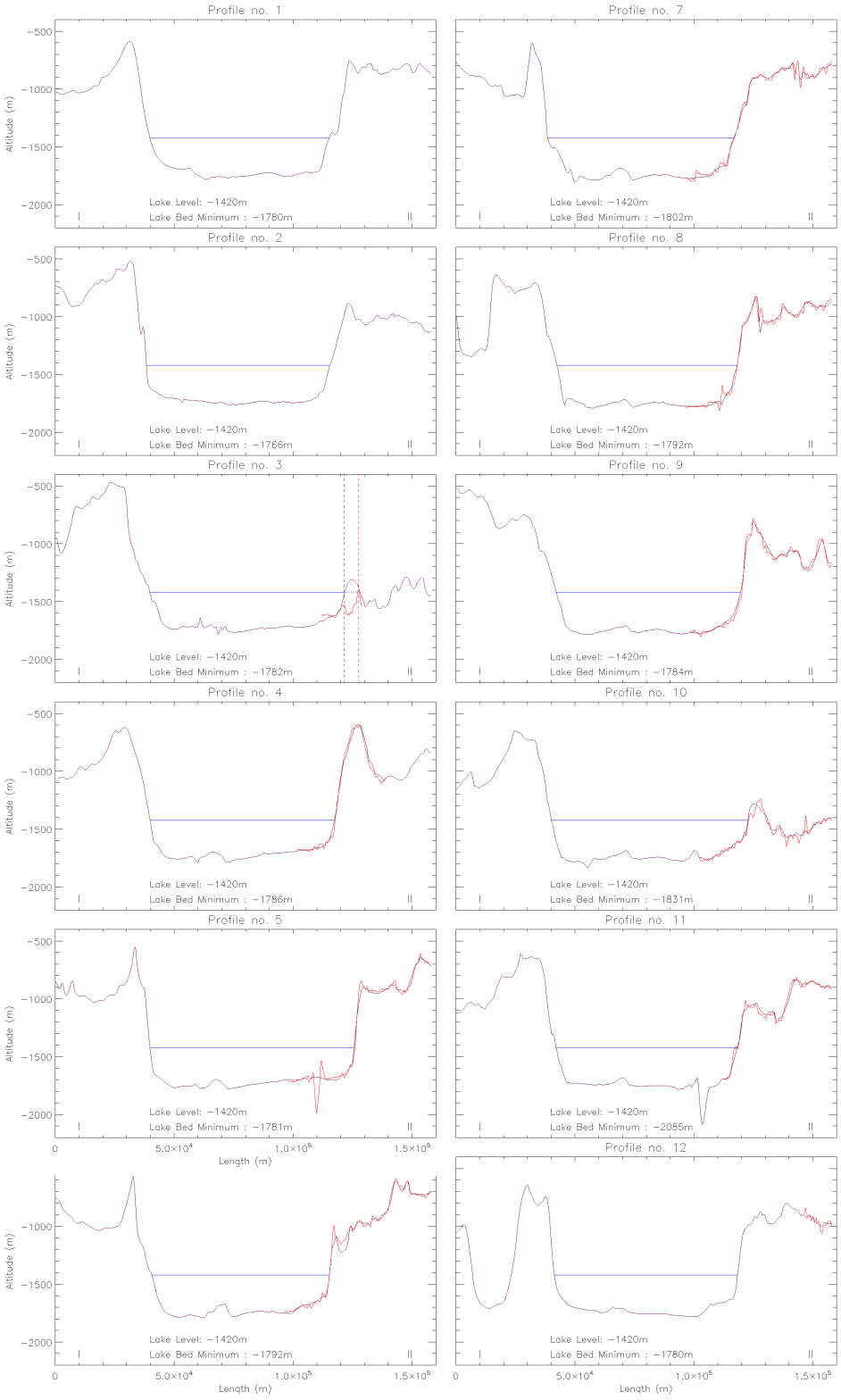

Figure 5.11: The twelve elevation profiles presented in Fig. 5.10 C. For each one the water level heigh and the maximum depth of the profile is presented. When possible, HRSC profiles are also extracted and compared with the MOLA ones. Note the main difference between MOLA and HRSC data at the tributary riverbed in profile no. 3.

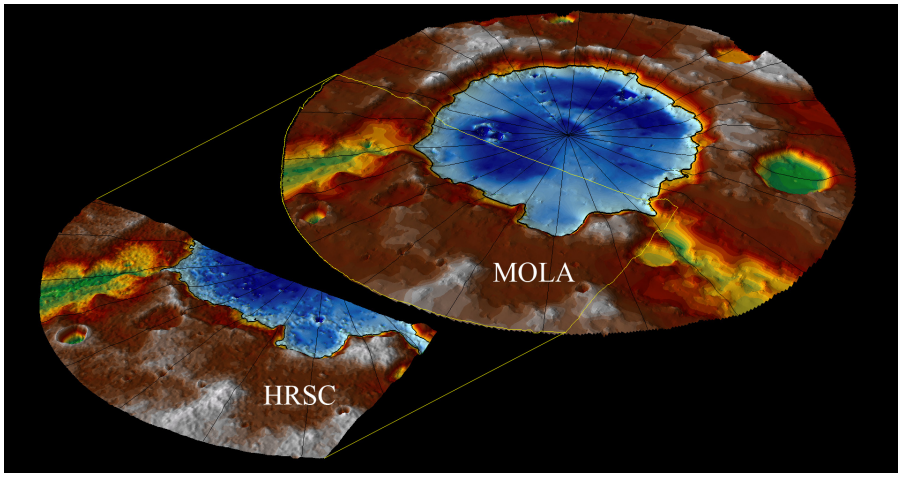

Figure 5.12: The MOLA and HRSC 3D representation of the paleolake II. The 12 elevation profiles are also depicted together with the paleolake water depth. The elevation values for the terrain and the paleolake are the same of Fig. 5.8 A and Fig. 5.10 B.

5.4 Study area #2 and Paleolake III (17°32'00"S-171°19'00"E)

The third paleolake we are presenting is located at 17°32'00"S latitude and 171°19'00"E longitude in the Mars Aeolis quadrangle, or MC-23 (Batson *et al.*, 1979); it belongs to the Durius Vallis drainage network whose connection is ensured by the paleolake outlet. The HRSC images used in this work are those presented in Tab. 5.5 with a scale that ranges between 12.5 and 25 m/px.

ID no.	Max. Lat (°)	Min. Lat (°)	West. Lon (°E)	East. Lon (°E)	Map scale (m/px)
H18790000ND3	-9.7	-42.3	172.3	179.6	25.0
H19010000ND3	-11.1	-38.4	170.7	176.3	25.0
H19120000ND3	3.7	-27.7	170.3	173.7	12.5
H42420000ND3	-7.8	-19.6	169.2	170.7	12.5

Table 5.5: Identification number, maximum and minimum latitude, westernmost and easternmost longitude and map scale of each HRSC image used in the context map of our area of interest.

In Fig. 5.13 A there is the contextualization map of the close surroundings of paleolake III. The highest peak of this area is at an elevation of 204 m located north of the crater's rim hosting paleolake III, while the area's deepest depression is located outside the paleolake's floor inside the Durius Vallis: - 1 770 m. The steepest slopes of the crater's inner rim, presented in Fig. 5.13 B, are on the northern and eastern side, reaching a value of 40%. Inside the crater floor, the most frequent slopes are in a range between 0% and 9%, with the exception of the small crater located south west inside of the paleolakes floor, whose values overcome 42.5%. Once we identified the rim of the crater as we did for paleolake I and II, we measured the crater's rim maximum at an elevation of 101.0 m. MOLA DEM is the only digital terrain model available here, it covers the entire rim's length: we plotted the crater's rim in Fig. 5.14 starting from I (Fig. 5.13 C) in the clockwise direction.

The median value of the elevation of the rim is -224.6 m (we do not consider the tributary and the outlet elevation values, nor the elevations of craters A and B, see Fig. 5.14), the mean value we derived is -219.5 m with a standard deviation of 169.41 m. In Fig. 5.8 C, as for paleolakes I & II, we indicate the intern and the extern osculatrix circles we derived from the craters rim, giving a minimum radius of 21.90 km and a maximum of 29.70 km. The 2D area of the crater spans consequently between 1 506.0 and 2 770.0 km^2. We also present in Fig. 5.8 C the tributary T, and the outlet O of the paleolake III. A set of physical properties of the impact crater hosting paleolake II is presented in Table 5.6.

We created a contour map of the entire crater and the surrounding area identifying the MOLA elevation value of the outlet: -646 m, see Fig. 5.15 A.

The depth map with 20 meters steps bathymetric lines is in Fig. 5.15 B showing the depth levels of the paleolake. In Fig. 5.15 C we show the location of the MOLA transversal profiles, which are presented then in Fig. 5.16. In Fig. 5.8 A, throughout the DEM, we can identify at least 6 recent craters that impacted the floor of the lake.

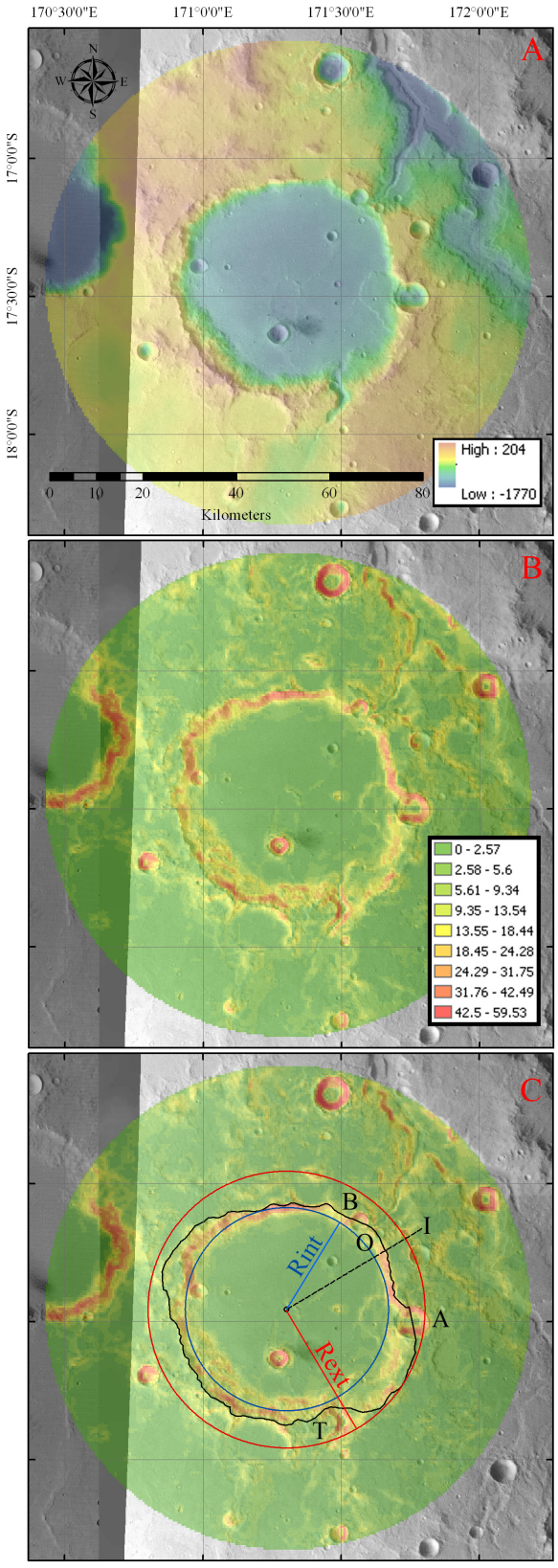

Figure 5.13: A: MOLA DEM showing the elevation values in meters, the scale bar and the latitude and longitude grid. The dashed line shows HRSC DEM coverage. B: Slope map with values in percentage. C: Identification of the intern and the extern osculating circles of the crater's rim. MOLA rim covers the entire crater. T is the paleolake's tributary, O is the outlet. A and B are two craters on the rim.

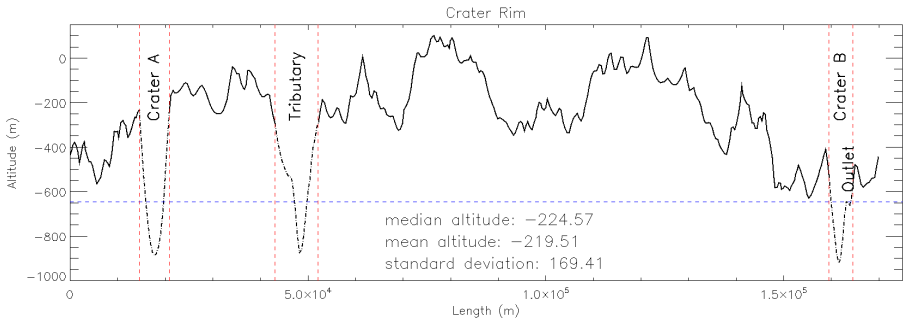

Figure 5.14: Crater rim based on the MOLA topography. The rims are those presented in Fig. 5.13 with the same clockwise direction from I. The tributary and the outlet topographies are also indicated together with the elevation values of crater A and crater B.

They all present a young and not eroded topography. Hence, we could consider them as craters which occurred after the lake was no more filled and present.

The computed 2D area of these craters is 75.45 km^2, their 3D area value is 76.81 km^2 and their volume is 31.84 km^3. As for paleolake I and II, we assume that the paleolake before such impacts covered the crater areas, but that the depression volume of the 6 craters is not considered. We derived a paleolake 2D area, A_0, of 1 564.0 km^2 at the water level of -646 m, a 3D basin area, A_{3D}, of 1 569.1 km^2 below the water level, and a total water volume, W_V, of 559.1 km^3.

Once the depths of the 6 craters inside the paleolake were excluded from the computation, we computed the lake floor mean elevation $\bar{Z}$, deriving a value of -1 011.1 m, and a root mean square of 128.3 m, giving a water mean depth $W_{\bar{D}}$ of 365 m. The minimum elevation of the paleolake III, z_{min}, is -1 176.0 m. The elevation difference from the mean rim value and the paleolake depth is then 791 m.

By using the Garvin *et al.* (2003) law on the crater hosting the paleolake III, the crater depth of 2.66 km is predicted, considering the extern osculating circle diameter of 59.40 km. The inner circle diameter is 43.80 km, with a predicted depth of 2.30 km. Subtracting the expected depth with the elevation difference from the rim and the bottom of the paleolake we derive a value that ranges between 1 506 and 1 873 m: this is the sediment thickness range which we expect has filled the crater's floor.

The relative depth Z_R derived for paleolake III is 1.4%, the measured shoreline S_L is 177.58 km. The shoreline development D_L is 1.27, while the volume development D_V we obtained is 2.58.

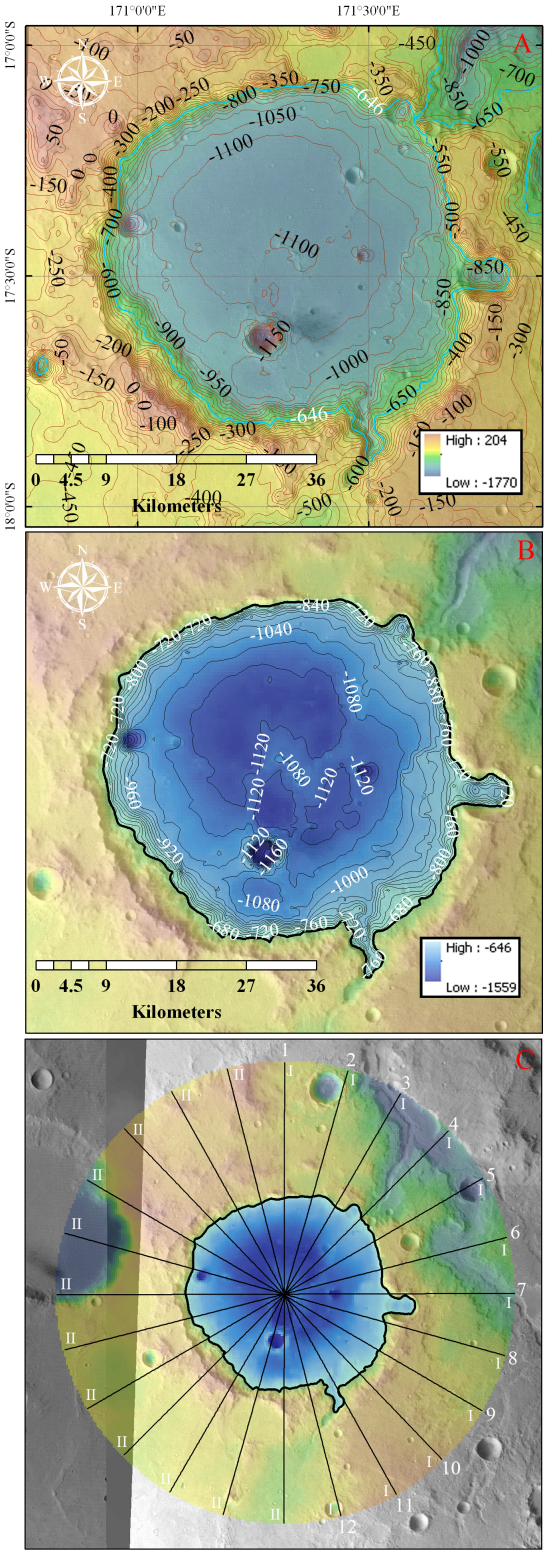

Figure 5.15: A: Contour map at 50 meters on the MOLA elevation values. The light blue polyline taken at an elevation of -646 m shows the shoreline of the paleolake. B: Paleolake depth contour map at 20 meters superimposed on the MOLA elevation values. C: Map showing the location of the elevation profiles presented in Fig. 5.11. The profiles are indicated with the same name of Fig. 5.11 and are extracted in the clockwise direction.

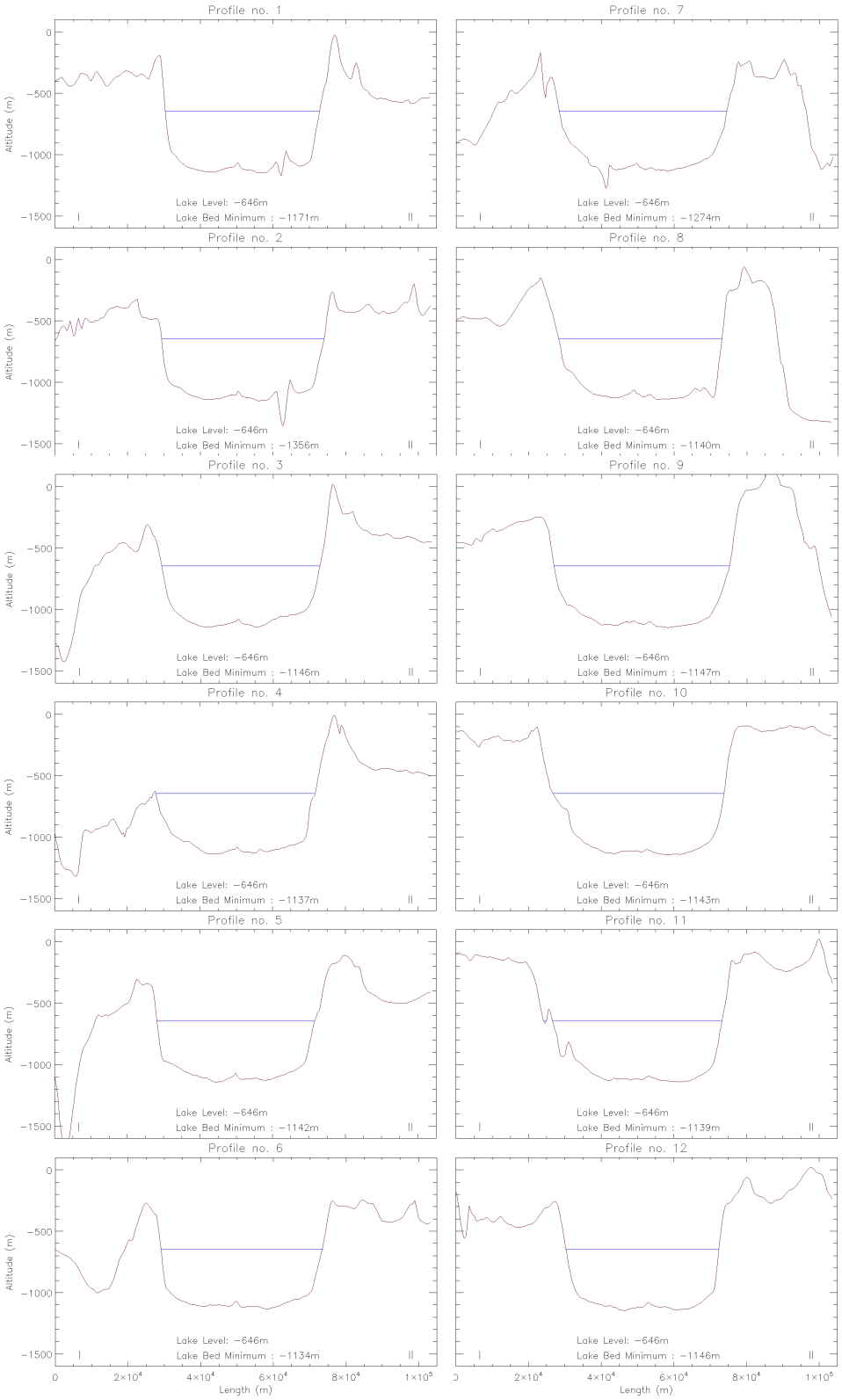

Figure 5.16: The twelve elevation profiles presented in Fig. 5.15 C. For each one the water level heigh and the maximum depth of the profile is presented.

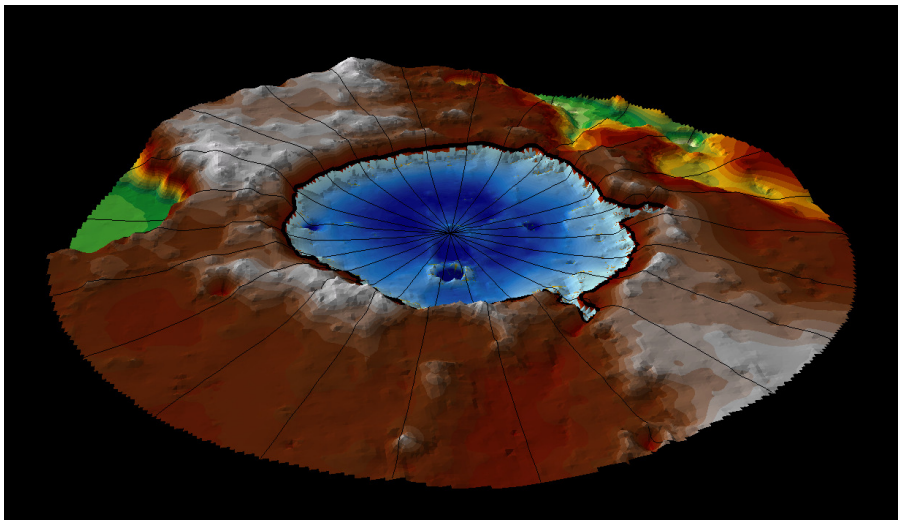

Figure 5.17: The MOLA 3D representation of the paleolake III. The 12 elevation profiles are also depicted together with the paleolake water depth. The elevation values for the terrain and the paleolake are the same of Fig. 5.13 A and Fig. 5.15 B.

	Crater III
Center latitude	17°32'00"S
Center longitude	171°19'00"E
Maximum radius r_{max} (km)	29.70
Minimum radius r_{min} (km)	21.90
Maximum diameter D_{max} (km)	59.40
Minimum diameter D_{min} (km)	43.80
Rim mean value rim_{mean} (m)	-219.5
Rim standard deviation value rim_{stdev} (m)	169.4
Rim median value rim_{median} (m)	-224.6
Expected max $depth_{max}$ (km)	2.66
Expected min $depth_{min}$ (km)	2.30

Table 5.6: Physical properties of the impact crater hosting paleolake III.

5.5 Paleolakes Comparisons, Discussion and the Hypsographic curves

Once we have derived the above-mentioned lacustrine parameters for the three Martian paleolakes, we made a comparison to understand what are the differences and the similarities between them (see Table 5.7). The first one has a radius which spans between 9.6 and 11.4, the second one between 41.3 and 49.5 km, while the third one ranges between 21.9 and 29.7 km. These side differences obviously affect parameters such as the surface area, the water volume and the shoreline length.

	Paleolake I	Paleolake II	Paleolake III
Center latitude	9°34'00"S	10°12'00"S	17°32'00"S
Center longitude	167°11'00"W	165°38'00"W	171°19'00"E
Water level W_L (m)	-1 409	-1 420	-646
2D area A_0 (km^2)	164.7	4 734.6	1 564.0
3D area A_{3D} (km^2)	165.4	4 740.6	1 569.1
Water volume W_V (km^3)	10.9	1 264.7	559.1
Lake floor mean elevation $\bar{z}$ (m)	-1 480	-1 696	-1 011
Water mean depth $W_{\bar{D}}$ (m)	71	276	365
Lake minimum elevation z_{min} (m)	-1 563	-1 913	-1 176
Sediment thickness range (m)	850 - 990	2 190 - 2 490	1 506 - 1 873
Relative depth Z_R (%)	10.9	2.5	1.4
Shoreline length S_L(km)	59.74	305.84	177.58
Shoreline development D_L	1.33	1.25	1.27
Volume development D_V	2.84	2.66	2.58

Table 5.7: Lacustrine parameters as derived through the application of the methodology on the three Martian paleolakes.

In order to make a meaningful comparison between them, we decided to apply the following technique: we computed the hypsographic curves of the three paleolakes. Hypsographic curves are plots of stratum surface area versus depth. Representing these curves as the percent of the total lake volume lying above a particular percentage depth, we enhance the sediment thickness differences between various paleolakes. We measured the 2D surface area at different paleolake depths, with a step of 10 meters starting from the surface water level; from 0 to -150 m for paleolake I, from 0 to -390 m for paleolake II and from 0 to -530 m for paleolake III. If we now plot the percent of the surface area lying above a particular percent depth, we create a meaningful method to compare the degree of sediment filling for each paleolake.

What we see from the hypsograhic curve of paleolake I, is that the first trend is totally different with respect to paleolakes II and III, which appear to behave more closely. Paleolake I reaches an area value of 50% when the depth is 50%, while this is not the case for paleolakes II and III where a percentage area of 50% is only reached at a depth of 76-78%. A trend change between concavity and convexity appears on paleolake II and III only when the percent area is less than 5%.

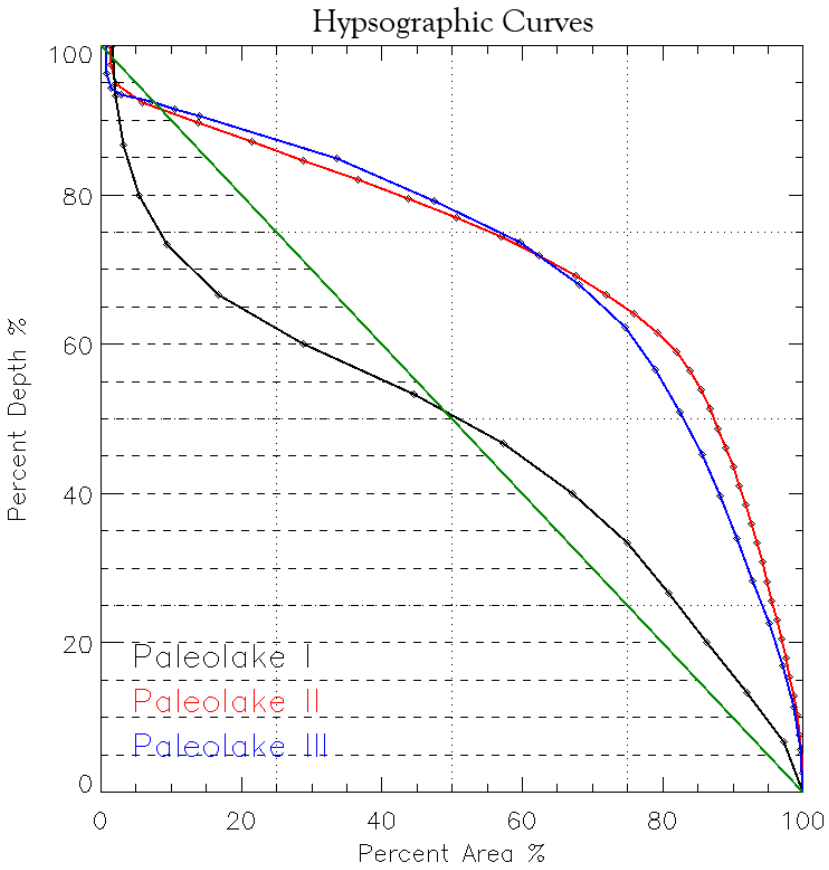

Figure 5.18: The three hypsographic curves derived from paleolake I, II and III.

We think that the meaning of the presented hypsographic curves relates to the sedimentary maturity degree of the paleolake floor. The absolute value of sediment thickness range would indicate that the paleolake which is "more" filled is the second one, but if we consider what the hypsometric plot shows, we see that the paleolake I floor has undergone a more mature sedimentation with respect to the dimension of the crater hosting the paleolake. The quantity of sediments layered on paleolakes II and III floors show that a percent area of 80% is only reached at a depth of 55%, while for paleolake I is at a depth of 25%. As from Schon *et al.* (2012), the impact crater shape is related to its depth within the the Garvin *et al.* (2003) depth-diameter relationship, unless it is a complex crater which formed through an impact on another existing crater or prominent cliff (Garvin *et al.*, 1998, 2000, 2003). Craters I, II and III are regular craters and hence what we would have expected for the craters hosting paleolakes II and III is that if they could have reached the same degree of sediment maturity of paleolake I, the plots' trend would have followed more closely paleolake I trend. Nevertheless the sediments filling would have reached a bigger value reaching a higher elevation towards the crater's rim.

Chapter 6

The Paleoriverbeds and Paleolakes Mineralogy

This chapter is divided in four sections: the first one describes the CRISM instrument which we use to detect minerals on the surface of our drainage networks and paleolakes; the second one provides the workflow pipeline used to correct CRISM raw data into scientific products; the third one is a brief summary of the main minerals that can be found on the surface of Mars; finally the last section contains a mineralogical description of the studied areas.

6.1 The CRISM Instrument

The *Compact Reconnaissance Imaging Spectrometer for Mars*, CRISM, aboard the *Mars Reconnaissance Orbiter* (*MRO* (Zurek *et al.*, 2007)) is a visible/short-wave infrared (VIS/SWIR) hyperspectral camera.

The main goals of this instrument are (Murchie *et al.*, 2007):

- characterizing seasonal variations in dust and ice aerosols and water content of surface materials, recovering science lost with the failure of the *Mars Climate Orbiter*, *MCO*;
- searching for evidence of aqueous and/or hydrothermal activity;
- mapping and characterizing the composition, geology, and stratigraphy of surface deposits;
- providing information on the atmosphere complementary to the *MCO* investigations;
- identifying new sites with high science potential for future investigation.

The camera provides two modes of operation: in the multispectral mapping mode the instrument acquires multispectral images with a scale of 100 to 200 m px^{-1} at 72 different wavelengths, covering absorptions bands corresponding to key mineralogical features; these multispectral data cover approximately 60% of the surface of the planet. In the "targeted" mode the instrument acquires radiative energy coming from

the planet within 362-3920 nm using 544 spectral bands and it can operate systematically in multi-angle mode from space; this mode is characterized by a quasi-nadir hyperspectral image, 15×15 km wide with a spatial resolution of 15-19 m.

In addition to these observations ten additional images are captured before and after the main image, or central scan, providing hyperspectral measurements of the same site with different emergence angles, up to 70°. The multi-angle information of a single targeted CRISM observation is primarily analyzed to address atmospheric studies, such as the observation of water vapor, carbon monoxide and dust aerosols. These angular capabilities can also be used to separate the atmospheric contribution from the surface information (Seelos *et al.*, 2011).

The CRISM atmospheric correction (Morgan *et al.*, 2011) makes possible the retrieval, from orbit, of photometric properties of the surface according to observation geometry and wavelength. These results are essential to understand the physical state of Martian materials as well as to distinguish between different types of terrains. To date, CRISM has complemented the results of OMEGA (Bibring *et al.*, 2004) instrument, searching for mineralogical clues of past and present water on the surface of Mars. CRISM multiplied the detections of hydrated minerals (Carter *et al.*, 2013; Noe Dobrea *et al.*, 2013) on Mars, and it has also carried out the first orbital detections of opal (Bishop *et al.*, 2008), carbonate (Jain *et al.*, 2013) and serpentine (Ehlmann *et al.*, 2009a,b) on the Martian surface.

6.2 From Raw CRISM Data into Scientific Products

6.2.1 The Photometric and Atmospheric Corrections

The CRISM instrument team (Murchie *et al.*, 2007) provides the Mars CRISM public data online at *http://crism-map.jhuapl.edu*, see *e.g.* Fig. 6.1.

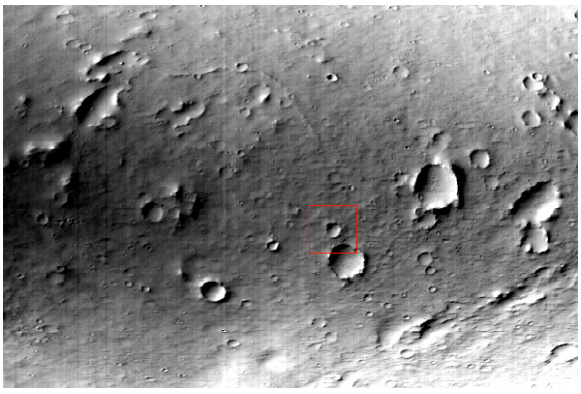

Figure 6.1: An example of a CRISM targeted mapping mode image of Mars, located between 165°57'30"W and 166°10'00"W longitude and between 9°55'00"S and 10°5'00"S latitude. The red box is the area where the spectra of Fig. 6.2 are derived.

The calibrated raw downloadable products need to be processed through the CRISM Analysis Tool (CAT). The workflow from the raw data into scientific data cubes requires two standard corrections (Morgan *et al.*, 2011): a basic photometric Lamber-

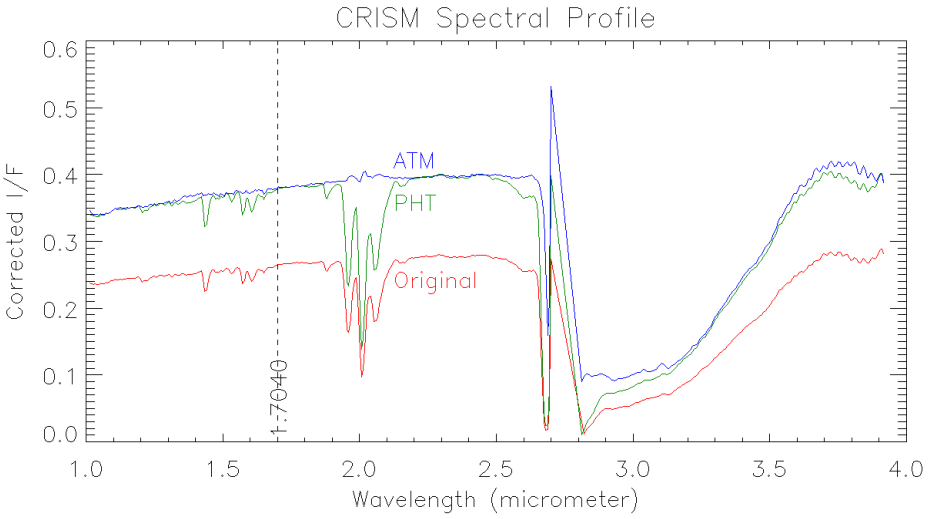

Figure 6.2: The raw/original spectral profile, the photometrically corrected (PHT) and the atmospheric corrected (ATM) spectral profile of the specific area selected in the red box in Fig 6.1 and 6.3. The vertical line shows the selected wavelength (1.7040 μm) of Fig 6.1 and 6.3. Some of the gaps on the spectral behavior or peaks such as between 2.6-2.8 μm derive from the considered "bad bands" of the instruments associated, for example, with boundaries between detectors or corrupted optical filters mounted on the detectors. See *e.g* Fraeman *et al.* (2012). Note both the difference in the corrected I/F after the photometric correction has been applied on the original data and the absence of the CO_2 band around 2 μm after the atmospheric correction has been performed.

tian correction and an atmospheric correction which uses an empirically derived atmospheric transmission spectrum to characterize and remove a CO_2 spectral structure.
The first step is needed to standardize the observation geometry; a first order correction is applied to radiance for non-normal solar incidence, dividing by the cosine of the incidence angle (the sunlight incidence angle at the 3D surface is computed from the DDR ancillary data file). The Lambertian photometric correction assumes the simplest reasonable bidirectional surface reflectance function and operates corrections by referring the whole data set to a normal illumination geometry, thus, allowing observations acquired at varying incidence angles to be more readily compared, see Fig. 6.2.
The second step is applied only on the IR data. It consists in applying atmospheric corrections required to remove from the surface spectrum the CO_2 absorption in the 2 μm spectral region, see Fig. 6.2. The CRISM team has processed 7 Volcano scans so far. A volcano scan is a special observation, containing atmospheric CO_2 absorption, viewing nadir on traverse across Olympus Mons. Through the volcano scans the team estimates the atmospheric transmission by dividing the volcano base spectrum by the volcano summit spectrum.

The following step required to perform atmospheric corrections consists in cleaning the scene spectrum in the proximity of two wavelengths situated near the CO_2 2 μm band. The first of those wavelengths is the one at 2007 nm near the absorbtion peak; the second one is at 1980 nm in the wing of the absorption band. These wavelengths were selected to reduce the systematic error in presence of broad mineralogical absorptions

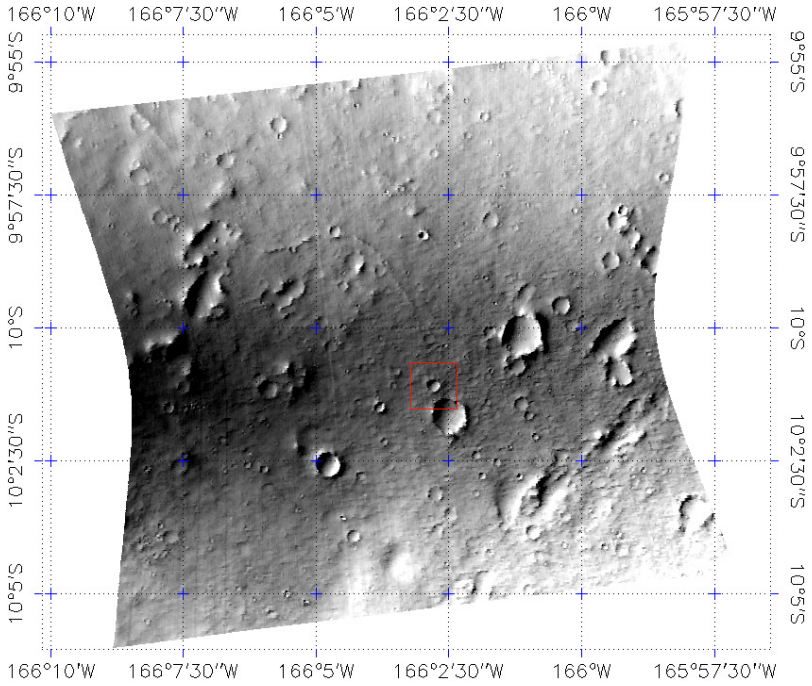

Figure 6.3: The projected CRISM targeted mapping mode image of Mars presented in Fig. 6.1.

near 2 μm (the so called McGuire 2-wavelength (2007/1980) recommended-by-the-team scaling correction). Once the transmission is scaled to match the absorption in the scene spectrum, it is divided to remove the atmosphere. In Fig. 6.2 the raw/original, the photometrically corrected (PHT) and the atmospheric corrected (ATM) spectral profiles are presented.

The above-described methodology was released by the CRISM team and presented during the March 22, 2009, first MRO/CRISM workshop at the 40th Lunar and Planetary Science Conference (LPSC) in Houston, Texas, and at the second CRISM Data Users Workshop held on March 18, 2012, The Woodlands, Houston, Texas.

6.2.2 The Map Projection and the Spectral Summary Parameters

After the photometric and the atmospheric corrections have been used on the data cube, the scientific product can be projected on a Latitude and Longitude map, see Fig. 6.3. This is important because the georeferenced image can be superimposed on our ARCGIS hydrological analysis.

To find and visualize the occurrences of mineral exposures, the CRISM team has created synthetic images that parameterize diagnostic, indicative, or informative spectral structure which are called summary parameters. These products are based on Pelkey *et al.* (2007) work and are derived from reflectances in key wavelengths for every CRISM observation.

Table 6.1 shows the key VNIR and IR spectral summary parameters, we use in this work. One of the most common spectral analysis presented by Pelkey *et al.* (2007), is

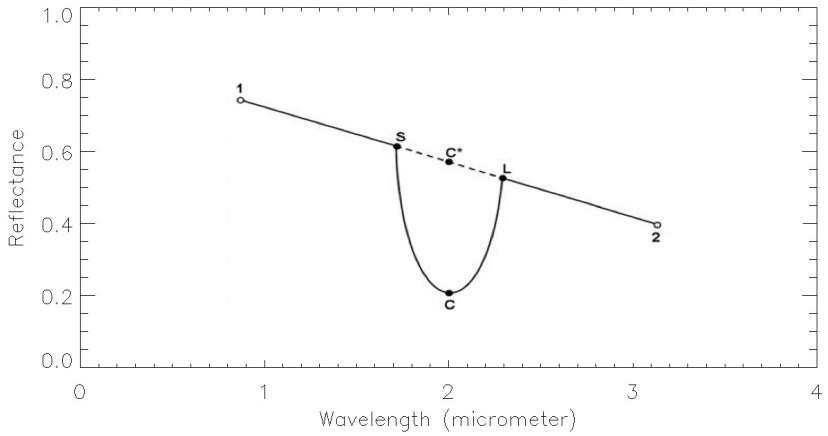

Figure 6.4: Schematic example of mineral detection obtained by superimposing an absorption band to a sloped continuum.

the detection of a specific mineral by looking at an absorption band superimposed on a sloped continuum.

Fig 6.4 shows the above-mentioned case. In the figure the reflectance at the wavelengths indicated by points 1 and 2 (*i.e.*, at λ_1 and λ_2) is indicated as R_1 and R_2. The spectral slope refers to the slope of the spectral continuum, *i.e.* the shape of a spectrum without a specific absorption/absorptions. It is computed through the $\Delta R/\ \Delta\lambda$ ratio, hence in this case it is found by (R1-R2)/(λ_1-λ_2). The absorption's depth, or band depth, is computed as 1-Rλ/R$^*\lambda$, where Rλ is the reflectance at the wavelength of the center of the absorption, and R$^*\lambda$, is the interpolated continuum reflectance at the same wavelength. The continuum level is created from a linear fit between two wavelengths (λ_1 and λ_2) from either side of the absorption that are at least local continuum levels. The band depth is 1-R_C/R_{C*}, where R_C is the reflectance at the center of the band, and R_{C*} is derived from the continuum fit across the band and is equal to (a*R_S + b*R_L), where a = 1 - b and b = (λ_C-λ_S)/(λ_L-λ_S).

6.3 General description of the main mineralogical components of the Martian surface

The main goal of this section is a general overview of the main mineralogical components found so far on the surface of Mars. This is required to give a contextualization for the following work of analysis based on CRISM spectra. A detailed analysis on the origin of rocks, minerals and their spectroscopy, not the aim of this section, can be found, for example, in Clark (1999).

6.3.1 Igneous Silicate Minerals

The igneous rocks are formed through the cooling and the solidification of magma. They may form either below the surface, the so-called intrusive/plutonic rocks, or on the surface as extrusive/volcanic rocks. The silicate minerals are classified according

Name	Description	Derivation	Higher values detect:
VNIR			
R770	Reference VNIR brightness image	Reflectance at 770 nm	Brighter materials or sunward facing slopes
RBR	Slope of VNIR "red edge"	770/440 nm reflectance ratio	Dustier surface
BD530	530-nm band depth	Relative to continuum between 440 & 709 nm	Greater content or larger particles of ferric oxide
SH600	Height of 600-nm "shoulder"	Relative to continuum between 530 & 709 nm	Dust coatings on dark rock, or olivine
BD920	Depth of 920-nm band	Relative to continuum between 800 & 984 nm	Crystalline Fe minerals (e.g. hematite, pyroxene)
BDI1000VIS	Integrated depth of 1-μm band at VNIR wavelengths	Area between spectrum and horizontal line tangent to peak reflectance	Stronger 1 μm band due to Fe in pyroxene, olivine
IR			
IRA	Reference IR brightness image	Reflectance at 1330 nm	Brighter materials or sunward facing slopes
OLINDEX	Strenght of broad Fe absorption with shoulder at 1.7μm	Area between spectrum and line fit to wavelengths 1700-2500 nm	Olivine and/or Fe- containing phyllosilicates
LCPINDEX	Indicator of low-Ca pyroxene	3-point curvature index (1050, 1330, 1815 nm)	Pyroxene, favors low-Ca type
HCPINDEX	Indicator of high-Ca pyroxene	3-point curvature index (1050, 1470, 2067 nm)	Pyroxene, favors high-Ca type
ISLOPE	NIR spectral slope	Slope evaluated between 1815, 2530 nm	Ferric coating on dark rock, or atmospheric aerosols
BD1435	1435 nm CO2 ice band depth	Relative to continuum between 1370 & 1470 nm	CO2 frost on surface
BD1500	1500 nm H2O ice band depth	Relative to continuum between 1367 & 1808 nm	H2O ice on surface or in atmospheric aerosols
BD1900	1900 nm H2O band depth	Relative to continuum between 1875 & 2067 nm	Bound H2O in hydrated phyllosilicate, zeolite, sulfate, carbonate, silica
BD2100	2100 nm shifted H2O band depth	Relative to continuum between 1930 & 2250 nm	Monohydrated sulfate
BD2210	2210 nm Al/Si-OH band depth	Relative to continuum between 2140 & 2250 nm	Al-phyllosilicates and hydrated silica
D2300	Dropoff into 2300 nm band	Relative to reflectance at 2140-2210 nm	Fe/Mg phyllosilicates, Mg carbonate
SINDEX	Convexity due to bands at 1900-2100 & 2400 nm	3-point curvature index (2100, 2290, 2400 nm)	Mono- and poly-hydrated sulfates
BDCARB	Depth of overtone bands in Ca/Fe carbonate	Sqrt of product of depth of bands at 2330 and 2500 nm	Ca/Fe carbonate
BD3000	3000 nm H2O band depth	Relative to continuum extrapolated from 2210 & 2530 nm	Adsorbed and bound H2O
CINDEX	1-sided depth of 3890 nm carbonate band	Relative to continuum extrapolated between 3630 & 3750 nm	Carbonate
BD2350	Depth of 2350 nm band	Relative to continuum between 2290 & 2430 nm	Serpentine, chlorite
IRR2	NIR continuum	2530/2210 reflectance ratio	Ice vs. dust clouds, surface dust / dust-bearing deposits

Table 6.1: Key VNIR and IR Spectral Summary Parameters (from Pelkey *et al.* (2007)) and the 2012 CRISM workshop (Seelos F., Murchie S. and the CRISM SOC). Most of these parameters are derived through the spectral technique showed in Fig. 6.4.

to different ratios of silicon and oxygen they can contain in their silicate group.

The nesosilicates, as the olivine group, have isolated $[SiO_4]^{4-}$ tetrahedra connected only by interstitial cations. The inosilicates, divides in single chain inosilicates as the pyroxene group, and in double chains silicates as the amphibole group. They have interlocking chains of silicate tetrahedra with either SiO_3, 1:3 ratio, for single chains or Si_4O_{11}, 4:11 ratio, for double chains.

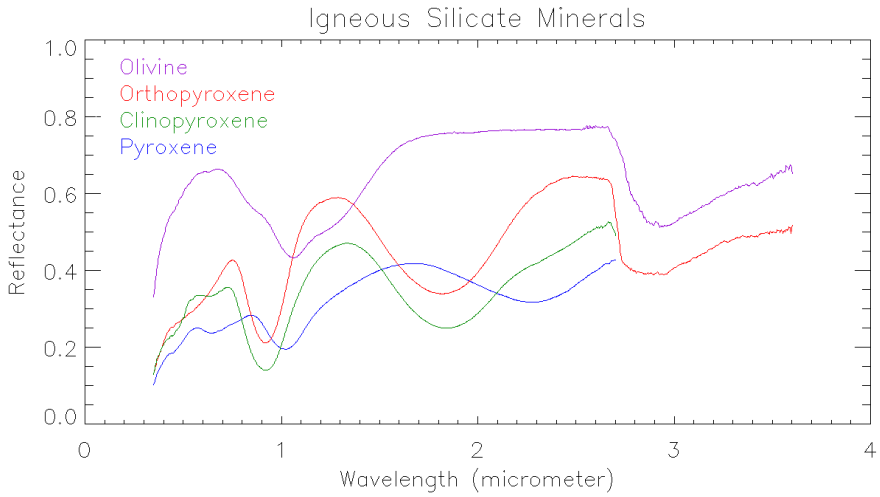

Figure 6.5: Spectral profiles of four igneous silicate minerals: olivine, orthopyroxene, clinopyroxene and pyroxene. Data source CRISM Analysis Tool on ENVI USGS Spectral Library.

The OMEGA and CRISM instruments (Bibring *et al.*, 2004; Murchie *et al.*, 2007) demonstrated that the main minerals making up igneous rocks on Mars are olivine and two kinds of pyroxene, *i.e.* orthopyroxene and clinopyroxene:

- the olivine is a magnesium iron silicate with the formula $(Mg^{+2}, Fe^{+2})_2SiO_4$. The ratio of magnesium and iron varies between the two endmembers of the solid solution series: forsterite (Mg-endmember: Mg_2SiO_4) and fayalite (Fe-endmember: Fe_2SiO_4). Compositions of olivine are commonly expressed as molar percentages of forsterite (Fo) and fayalite (Fa) (e.g., $Fo_{70}Fa_{30}$);
- the orthopyroxenes have a general formula $(Mg,Fe,Ca)(Mg,Fe,Al)(Si,Al)_2O_6$, but natural compositions are dominated by two major end member components: enstatite, $Mg_2Si_2O_6$, and ferrosilite, $Fe_2Si_2O_6$;
- the clinopyroxenes have a general formula $(Ca,Mg,Fe,Na)(Mg,Fe,Al)(Si,Al)_2O_6$. Most clinopyroxenes in igneous and metamorphic rocks can be thought of as $(Ca,Mg,Fe)_2Si_2O_6$, with small amounts of Al, Mn and Na substituting for other elements. The most significant clinopyroxene end member is diopside, $CaMgSi_2O_6$. Its Fe equivalent, $CaFeSi_2O_6$ is hedenbergite.

As a main spectroscopic feature, these minerals have absorptions near 1 μm and 2 μm, respectively, and their exact wavelengths and relative strengths indicate the mineral composition of the rock (see Fig. 6.5).

6.3.2 Oxidized Iron Minerals

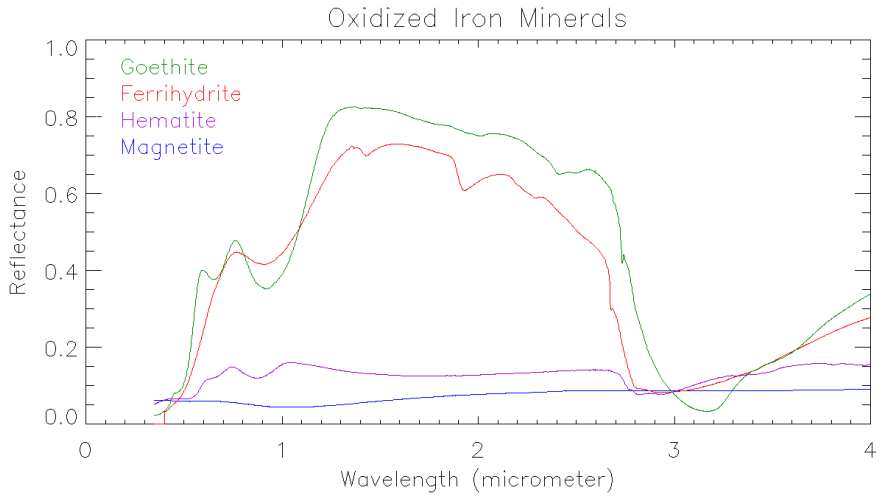

Figure 6.6: Spectral profiles of four oxidized iron minerals: goethite, ferrihydrite, hematite and magnetite. Data source CRISM Analysis Tool & ENVI USGS Spectral Library.

The oxidized iron minerals, as oxides, hydroxides and oxide-hydroxides, derives from the weathering of igneous rocks:

- the iron oxides are chemical compounds composed of iron and oxygen;
- the iron hydroxides are compounds composed of iron and the diatomic anion, called hydroxide, OH^-;
- the iron oxide-hydroxide are composed of an iron oxide and the OH^-. They may occur in anhydrous (FeO(OH)) or hydrated ($FeO(OH)\cdot nH_2O$) forms, where n is the number of water molecules present in the compounds.

Some examples of iron oxides are the mineral magnetite, Fe_3O_4, and hematite, Fe_2O_3, while a couple of examples of oxides/hydroxides are the goethite, FeOOH, and the ferrihydrite $5Fe_2O_3\cdot 9H_2O$.

These minerals are most distinguished by the relative strengths of absorptions at visible wavelengths (0.4-0.7 μm) and in the infrared out to 1 μm.

In Fig. 6.6 we present some oxidized iron minerals reflectance spectra. As an example, hematite has a narrower absorption at a slightly shorter wavelength than goethite; note, however, that a coarse-grained hematite has a broader absorption, approaching the position and width of a fine-grained goethite (or a thin- film goethite) (Clark, 1999).

6.3.3 Phyllosilicate (Clay) Minerals

Phyllosilicates, also called sheet Silicate minerals, are formed by parallel sheets of silicate tetrahedral structures with Si_2O_5, a 2:5 ratio. The phyllosilicates are an impor-

tant group of minerals that includes the micas, chlorite, serpentine, talc, and the clay minerals.

The basic structure of the phyllosilicates is based on interconnected six member rings of $[SiO_4]^{4-}$ tetrahedra that extend outward in sheets. Three out of the 4 oxygens from each tetrahedra are shared with other tetrahedra. This leads to a basic structural unit of $[Si_2O_5]^{2-}$.

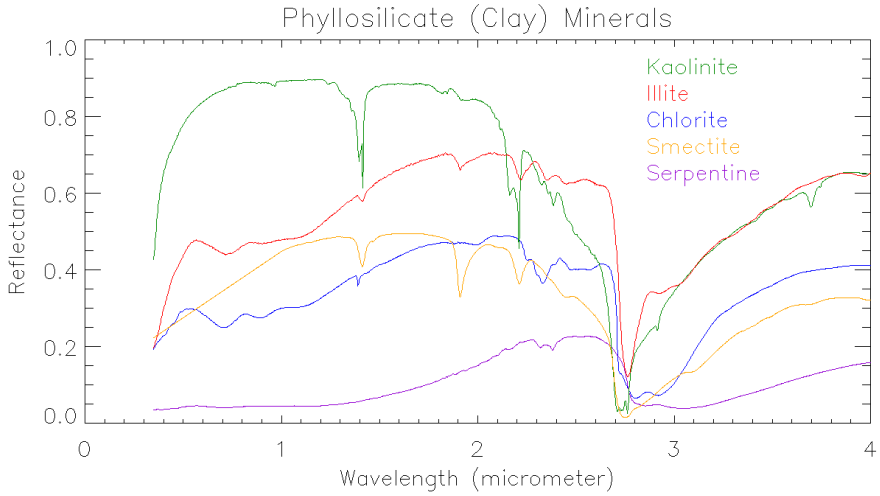

Figure 6.7: Spectral profiles of five phyllosilicate clay minerals: kaolinite, illite, chlorite, smectite and serpentine. Data source CRISM Analysis Tool & ENVI USGS Spectral Library.

The phyllosilicate minerals indicate a prolonged, wet environment, and oftentimes a warm and wet environment:

- the micas have the general formula $X_2Y_{4/6}Z_8O_{20}(OH,F)_4$ in which X is K, Na, or Ca or less commonly Ba, Rb, or Cs; Y is Al, Mg, or Fe or less commonly Mn, Cr, Ti, Li, etc.; Z is chiefly Si or Al, but also may include Fe^{3+} or Ti. Some examples of micas are biotite, muscovite, lepidolite;

- the chlorite can have a rather complicated formula $(Mg,Fe,Al)_3(Si,Al)_4O_{10}(OH)_6$; it is a common mineral in low grade metamorphic rocks, where it occurs in association with minerals like actinolite, epidote, and biotite. It also forms as an alteration product of pyroxenes, amphiboles, biotite, and garnet in igneous as well a metamorphic rocks;

- the serpentine group of minerals has the formula $Mg_3Si_2O_5(OH)_4$. It is found as an alteration product of Mg-rich silicates like pyroxene and olivine. It results due to hydration;

- the talc has the chemical formula $Mg_3Si_4O_{10}(OH)_2$, and like serpentine, it requires an environment rich in Mg. It is therefore found in low grade metamorphic rocks that originated as ultrabasic to basic igneous rocks;

- the clay minerals are hydrous aluminium phyllosilicates, sometimes with variable amounts of Fe, Mg, alkali metals, alkaline earths, and other cations. They are characterized by sheet units with a chemical composition of $(Al,Si)_3O_4$. Clays form flat hexagonal sheets similar to the micas. They are common weathering products (including weathering of feldspar) and low temperature hydrothermal alteration products. Clay minerals include for example the kaolin group, the smectite group, the illite group.

Clay-like minerals are recognized by absorptions near 1.4, 1.9 and 2.2-2.4 μm due to water or hydroxyl that is trapped in the minerals' crystal structure, see Fig. 6.7.

6.3.4 Sulfate Minerals

The sulfate minerals are characterized by the sulfate ion $[SO_4]^{2-}$ within their structure. The sulfate minerals indicate a relatively acidic environment and occur commonly in primary evaporite depositional environments, as minerals in hydrothermal veins and as secondary minerals in the oxidizing zone of sulfide mineral deposits.

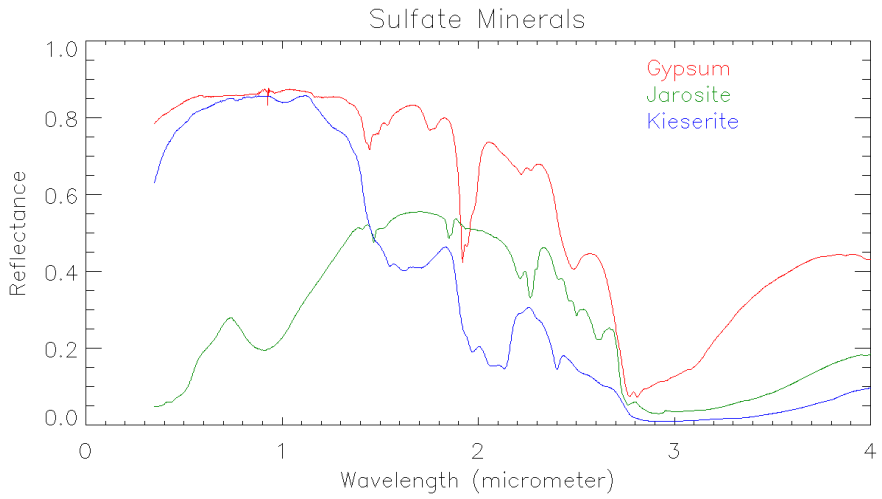

Figure 6.8: Spectral profiles of three sulfate minerals: gypsum, jarosite, kieserite. Data source CRISM Analysis Tool & ENVI USGS Spectral Library.

There are many varieties of sulfates that differ in the amount of water they contain, and they can be distinguished by the shapes and wavelengths of the absorptions:

- Jarosite, $KFe^{3+}{}_3(OH)_6(SO_4)_2$, is a basic hydrous sulfate of potassium and iron formed in ore deposits by the oxidation of iron sulfides. Jarosite has a diagnostic absorption at 2.27 μm due to a combination OH stretch and Fe-OH bend. However, this feature is weaker than the electronic absorptions in the visible and is often masked by clay or alunite (jarosite often occurs in hydrothermal deposits with alunite). The features near 1.475 μm and 1.8 μm are OH related and are commonly seen in sulfate spectra;

- Gypsum is a soft sulfate mineral composed of calcium sulfate dihydrate, $CaSO_4 \cdot 2H_2O$. It is a common mineral on Earth, with thick and extensive evaporite beds in association with sedimentary rocks. Gypsum is deposited from lake and sea water, as well as in hot springs, from volcanic vapors, and sulfate solutions in veins. Hydrothermal anhydrite in veins is commonly hydrated to gypsum by groundwater in near-surface exposures;
- Kieserite is a magnesium sulfate mineral ($MgSO_4 \cdot H2O$). It forms in marine evaporite deposits where sea water has been concentrated and exposed to prolonged evaporation. Evaporite minerals are geologically important because they clearly are related to the environmental conditions that existed at the time of their deposition, namely coastal arid. The more hydrated version of kieserite is epsomite, with the formula $MgSO_4 \cdot 7H2O$. This forms both as encrustations on cavern walls and in beds as evaporite layers.

In general, as showed in Fig. 6.8, these minerals sulfates are recognized from numerous absorptions from 1 to 2.5 microns due to water in the minerals' crystal structures.

6.4 Areas of Interest and Discussion of the results

6.4.1 Area #1

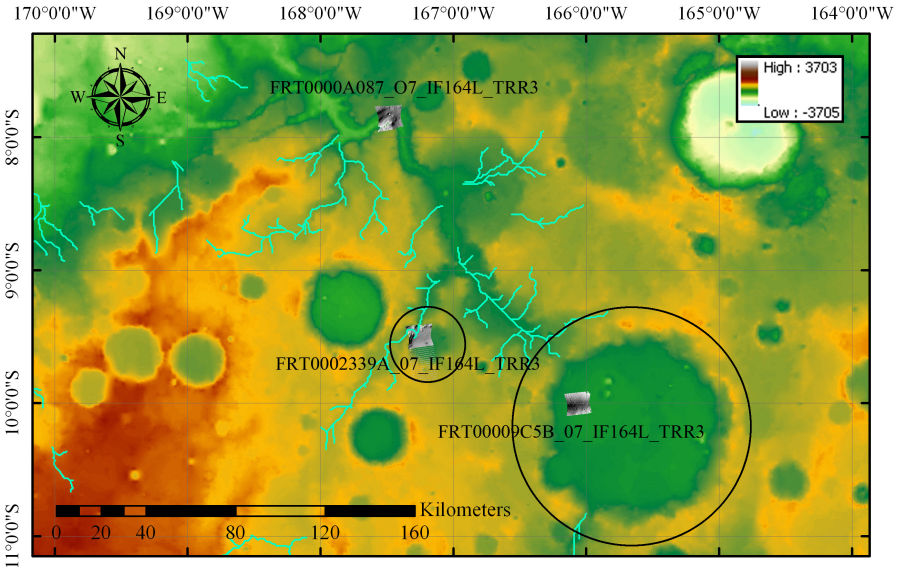

Figure 6.9: Map of the first analyzed Mars region, belonging to the Memnonia quadrangle, where the three considered CRISM data cubes are indicated. The black circles correspond to the paleolake I (the smaller one) and paleolake II (the bigger black circle) previously studied.

The first area we have studied on the surface of Mars is located between 170°00'00"W - 164°00'00"W and 7°00'00"S - 11°00'00"S, as presented in Fig. 6.9. Within this area

we have identified three CRISM datacubes which lie on a paleoriverbed floor, at the tributary and outlet of paleolake I, and on the paleolake II floor. The georeferenced CRISM datacubes are indicated in Fig. 6.9: they cover the wavelength range between 1.0 μm and 3.9 μm. As presented in the work of Ehlmann *et al.* (2009b), we focused on the IR wavelength range between 1.0 and 2.6 μm, avoiding the range between 2.6 - 3.9 μm for a main reason: there are no wide ranges characterized by CRISM bad bands in this wavelength coverage which can affect the spectral matching we want to perform. With the only exception of the 2 μm atmospheric correction residual, the 1.0-2.6 μm coverage is the one with the wider unaffected range observed by CRISM, useful to perform our mineralogical interpretation.

CRISM datacube FRT0000A087

The first datacube is located between 167°36'W - 167°24'W and 7°45'S - 7°57'S. This CRISM cube covers a section of a riverbed bend characterized by a width of 5 km, see Fig. 6.10 I-V. We performed the above-mentioned photometric and the atmospheric correction, and then we used the LCPINDEX on the data cube in order to identify possible regions of interest, ROIs, showing low-Ca pyroxene type (Fig. 6.10 II). We identified seven different ROIs on the base of the different LCPINDEX values (Fig. 6.10 III-IV). Afterwards we computed the maximum, the minimum, the ± 1 sigma spectrum and the mean spectrum for each ROI. The georeferenced cube is presented in Fig. 6.10 V.

We then compared each ROI's mean spectrum: the resulting plot is presented in Fig. 6.11. It is worth noting a couple of things from Fig. 6.11: some of the 2 μm atmospheric correction residual is still present, and the three wavelengths indicated at 1.050 μm, 1330 μm and 1815 μm are showing the three values where the LCPINDEX 3-point curvature is computed. The mean plots show different absorptions' depth and spectral slopes; in order to compare them we removed the spectral continuum as described in section 7.2, showing through this way clear shoulders for each band and their percentage absorption's depth. What we derived is presented in Fig. 6.12. The seven ROIs spectra show three different absorption bands: the first one located around 1.05 μm, the second one with a minimum close to 1.20 - 1.25 μm, while the third one is a wide band with shoulders at 1.35-1.40 and 2.60 μm centered close to 2 μm.

We followed the same procedure presented by the LCPINDEX using the OLINDEX, a spectral parameter which indicates the strength of the broad Fe absorption with the shoulder at 1.7 μm, see Tab. 6.1. This parameter is aimed to give higher values when olivine and/or Fe-containing phyllosilicates are detected. We identified three ROIs to see possible spectral differences with respect to the spectra identified by the LCPINDEX; two of them, *i.e.* ROI 1 and 2 had already been selected in the LCPINDEX ROIs selection as a low and mean LCPINDEX value regions, while ROI 3 has been selected as a high OLINDEX area, with a value of 0.011. The resulting spectra are plotted in Fig. 6.14, being the high-OLINDEX spectra located in the upper part of the plot and low-OLINDEX spectra in the lower side of the plot. From Fig. 6.11 note both the difference in slope between ROI 3 and the other ROIs and its band located around 1.2 μm which is not so deep or present in the two other spectra. When eliminating the continuum, the differences between the third ROI and the other two is clear: the band centered at 1.2 μm is not present in the previous spectra, while a signature of the wide band with shoulders around 1.3 and 2.6 μm is still present, see Fig. 6.15. The behavior of the blue spectrum around 1.8 μm is different, where there is an increase of 2% of I/F with respect to the other spectra.

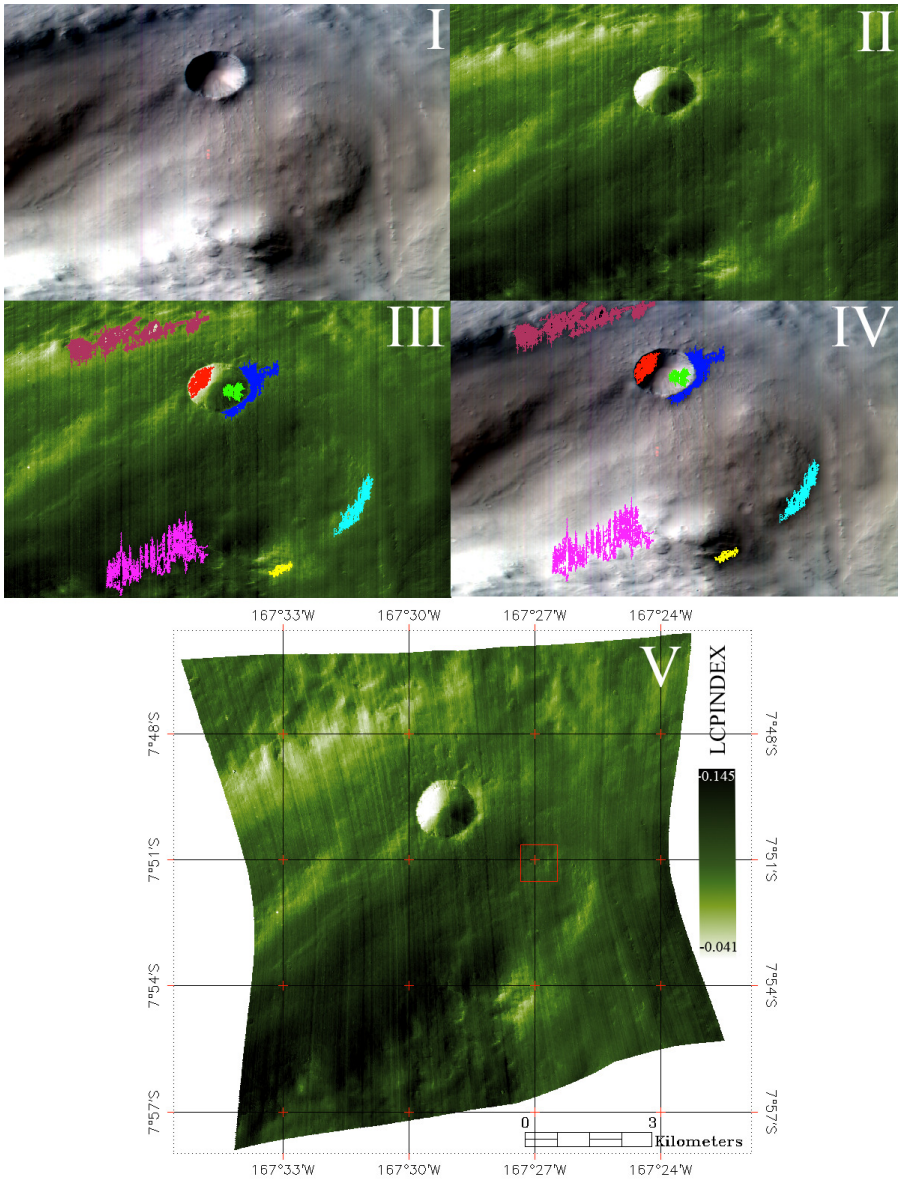

Figure 6.10: I: original CRISM data cube. II: LCPINDEX applied on the datacube with an enhancing green colorbar. III: ROIs identified by using the LCPINDEX spectral parameter. IV: extraction of the maximum, minimum, the ± 1 sigma spectrum and the mean spectrum for each ROI from the original cube. V: georeferenced CRISM cube map with the LCPINDEX values found on the considered area.

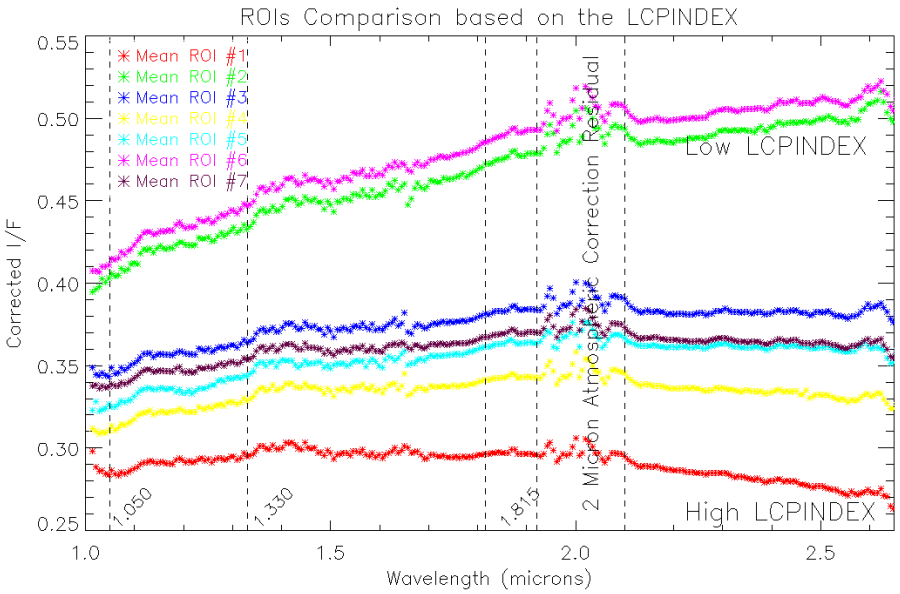

Figure 6.11: Mean ROIs surface spectra derived from CRISM cube after the LCPINDEX has been applied. Note that the 2 μm atmospheric correction residual is still present, while the three wavelengths indicated at 1.050 μm, 1330 μm and 1815 μm are the three wavelength values where the LCPINDEX 3-point curvature is computed. The color code is the same of the ROIs identified in Fig. 6.10. The low LCPINDEX spectra, with values close to -0.145 are located in the upper part of the plot and show a higher slope, while those with a high LCPINDEX, *i.e.* a value of -0.041, are located in the lower side of the plot and are typically flat or with a negative slope.

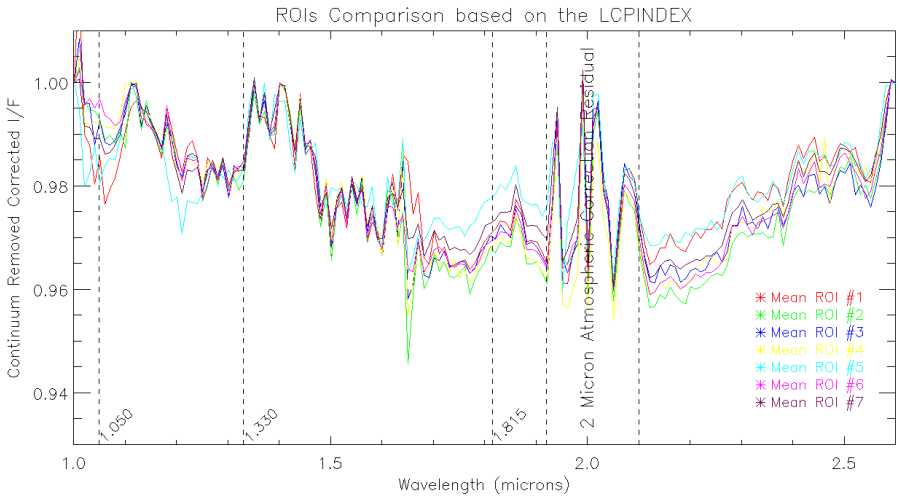

Figure 6.12: The same ROIs spectra, as presented in Fig. 6.11, but with the spectral continuum removed, as indicated in section 6.2. Note the wide absorption from 1.3 to 2.6 μm.

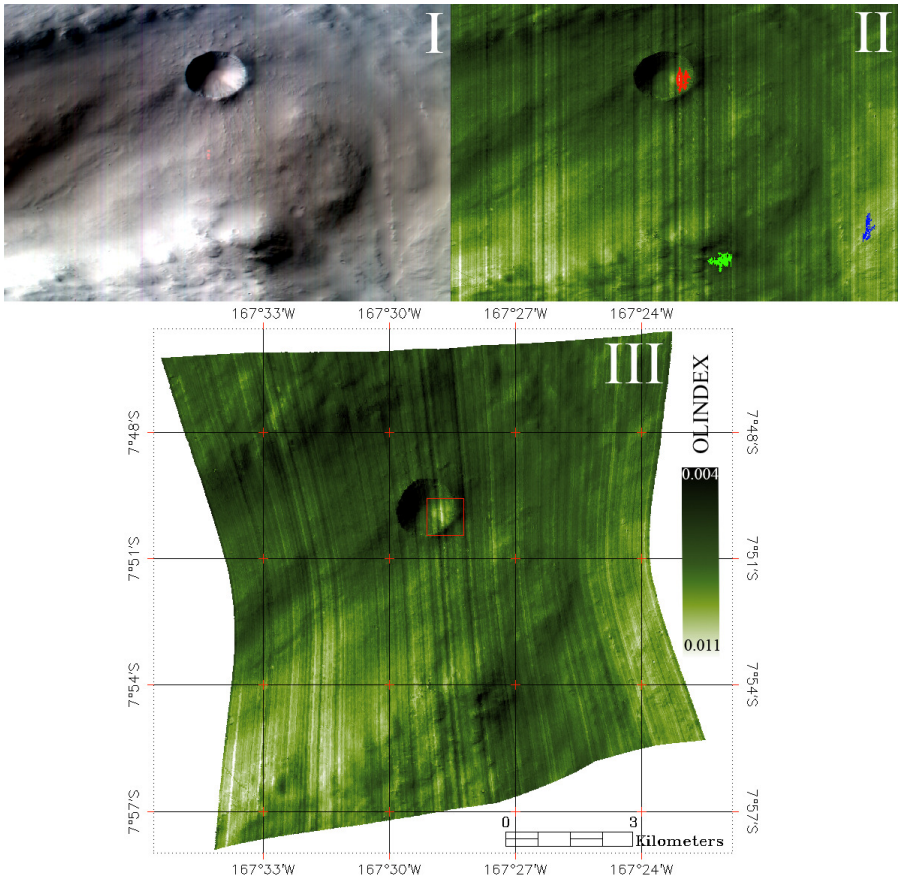

Figure 6.13: I: original CRISM data cube. II: OLINDEX applied on the datacube and the three ROIs identified by using this parameter. III: georeferenced CRISM cube map with the OLINDEX colorbar values.

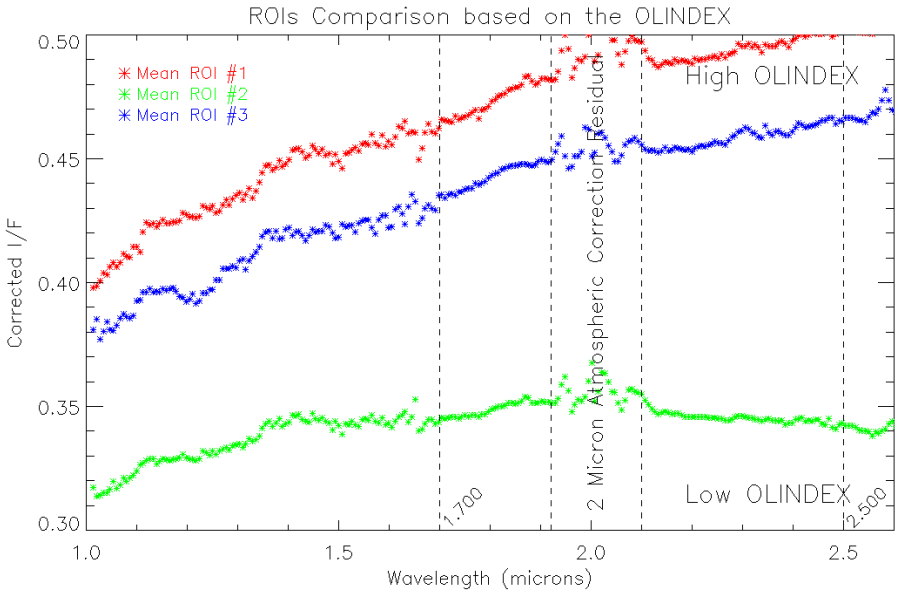

Figure 6.14: Mean ROIs surface spectra derived from CRISM cube after the OLINDEX has been applied. Note that the 2 μm atmospheric correction residual is still present, while the two wavelengths indicated at 1.700 μm and 2500 μm are the ones used by the spectral parameter to get the strength of board Fe absorption with shoulder at 1.7 μm.

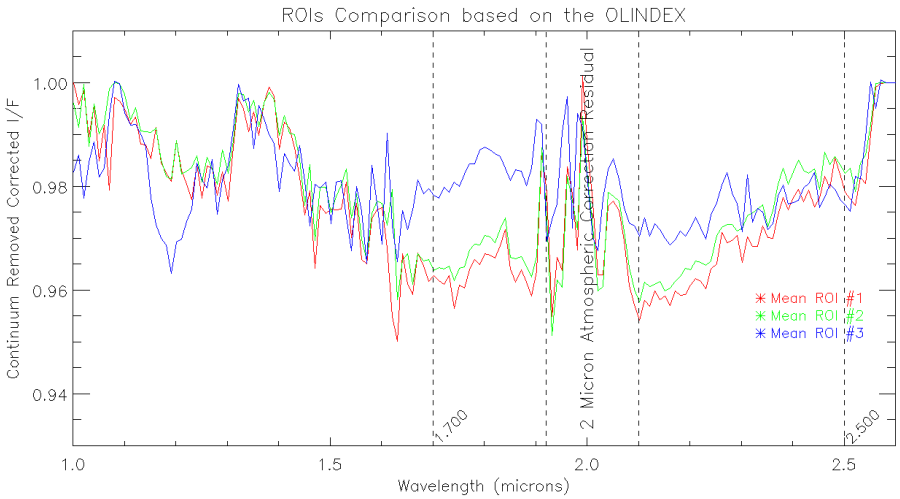

Figure 6.15: The same ROIs spectra, as presented in Fig. 6.14, but with the spectral continuum removed. Note that ROIs 1 and 2 were present also in the LCPINDEX analysis, while the strong difference with respect to the previous spectra comes from the third spectrum that shows a different spectral behavior around 1.2 μm and 1.8 μm.

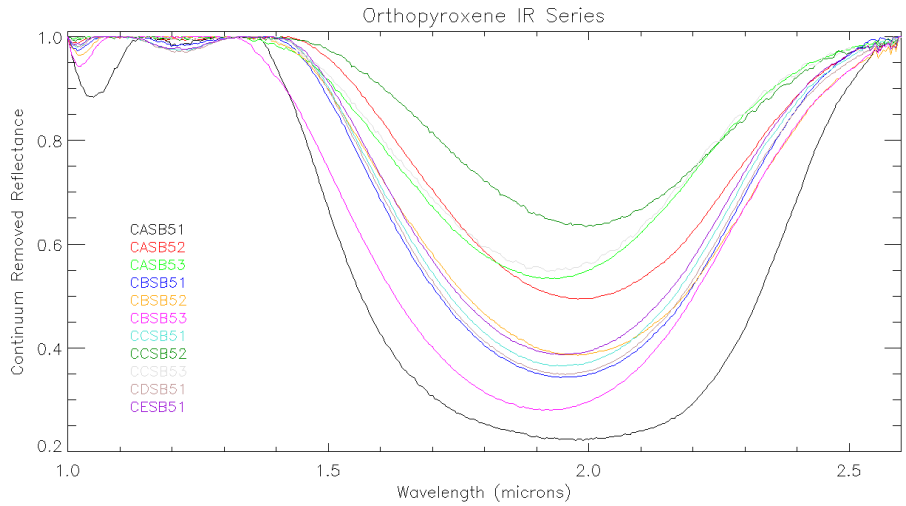

Figure 6.16: Spectral continuum removed profiles of eleven minerals belonging to the orthopyroxene series. Data source CRISM Analysis Tool & ENVI USGS Spectral Library.

In order to understand what kind of minerals could have produced the spectral behavior presented in Fig. 6.12 and 6.15, we decided to eliminate the spectral continuum, for the same wavelength range of the above-mentioned plots, for a set of comparison minerals spectra. We consequently performed the spectral matching between the CRISM results and these reference spectra. In Fig. 6.16 and 6.17 we plotted the orthopyroxene and the ortopyroxene/bronzite, ortopyroxene/enstatite and the ortopyroxene/hypersthene series respectively. The orthopyroxene series belong to the family of igneous silicate minerals, specifically called inosilicates. If we take into account the seven mean ROIs spectra of Fig. 6.12 and the two first ROIs of Fig. 6.15, we can see that the three bands at 1.050 μm, 1.250 μm and the wide band with shoulders around 1.3 and 2.6 μm strongly agree with the spectral behavior of the pure orthopyroxene series. The small differences, as the presence of small absorption bands, inside the three bands, can be due to the realistic case of different mixture of minerals, as we are expecting on the surface of Mars, while the difference in the absorption's depth can be due to the different grain sizes of the mineralogical material on the surface of the planet. Nevertheless it is worth noting that the main overtone characterizing these spectra is the one of the orthopyroxene mineral. This can be observed from the fact that the ortopyroxene/bronzite, ortopyroxene/enstatite and the ortopyroxene/hypersthene series show a wider band between 1.3 and 2.6 μm, they present the band at 1.05 μm, but there is no hint showing the 1.2 μm band we are observing on our data. A specific mineral is identified on the surface of a body by the presence of absorption bands at the same wavelength expected from the reference laboratory spectra; a different depth can be explained by the different size of surface grains, but if an expected band is absent then a different mineralogical composition has to be conceived.

The spectral behavior of the third ROI of Fig. 6.15 shows that the presence of orthopyroxene is still strong, as from the band between 1.35 and 2.6, but we think that the strong absorption band (about 4%) at 1.2 μm can be due to the presence whether

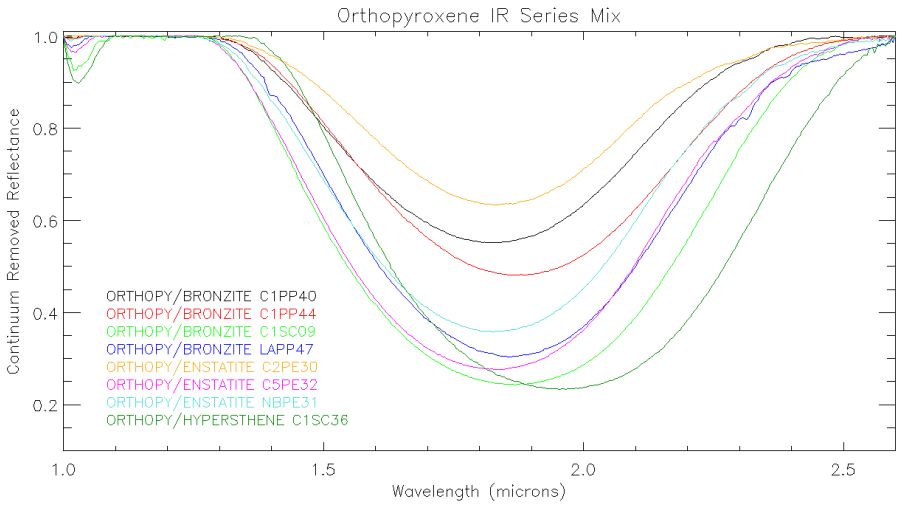

Figure 6.17: Spectral continuum removed profiles of eight different minerals belonging to the orthopyroxene series. Data source CRISM Analysis Tool & ENVI USGS Spectral Library.

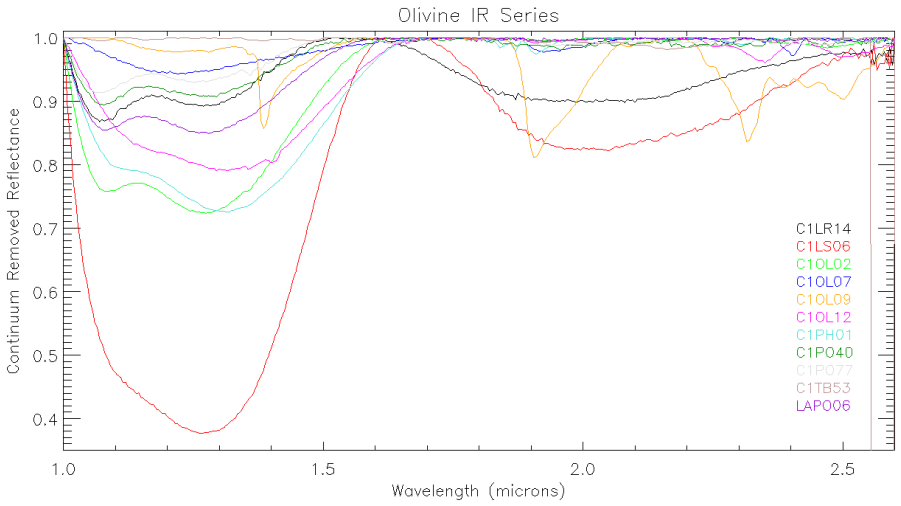

Figure 6.18: Spectral continuum removed profiles of elven different minerals belonging to the olivine series. Data source CRISM Analysis Tool & ENVI USGS Spectral Library.

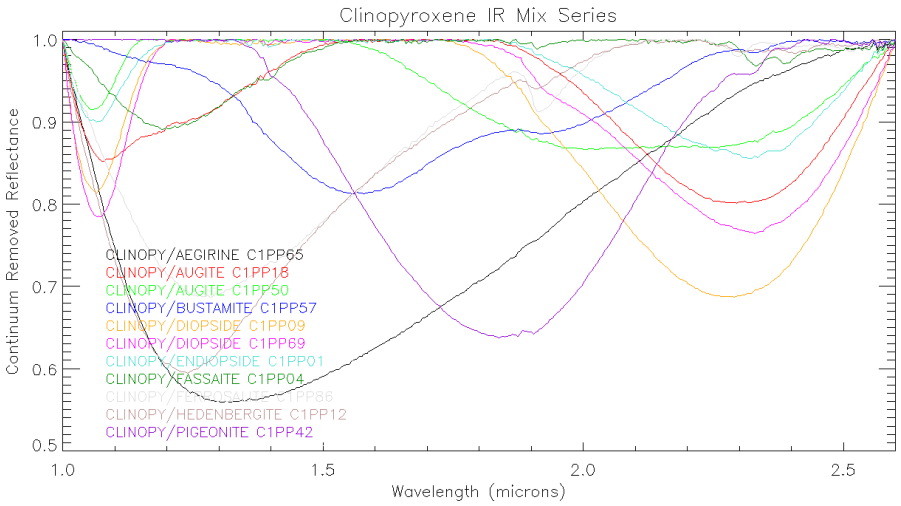

Figure 6.19: Spectral continuum removed profiles of eleven different minerals belonging to the clinopyroxene series. Data source CRISM Analysis Tool & ENVI USGS Spectral Library.

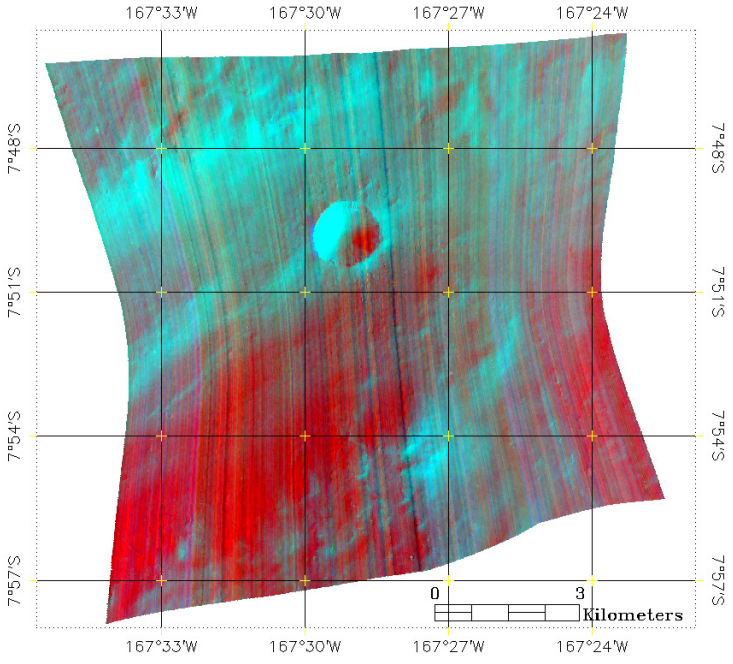

Figure 6.20: RGB map made possible assigning the OLINDEX map to the red R channel, the LCPINDEX map to the green G channel and HCPINDEX to the blue B channel. Within this RGB image the bluish areas indicates the presence of hi-Ca pyroxene, the greenish areas indicate low-Ca pyroxene, while the light blue is a mixture of possible both low- and hi-Ca pyroxene type. This color scale attributes dull red to Fe-phyllosilicate, while red areas show the presence of olivine.

of olivine , see Fig. 6.18 or clinopyroxene (as the case of clinopyroxene/fassaite), see Fig. 6.19 which both could explain the behavior around 1.8 μm with an increase of 2% of I/F. We think that the most likely explanation here is that a mixture with a bigger percentage of these components with respect to the orthopyroxene present in the other cases can be real.

The third map we produced is the one presented in Fig. 6.20. This is a RGB map created assigning the OLINDEX map to the red R channel, the LCPINDEX map to the green G channel and HCPINDEX to the blue B channel. Within this RGB image the bluish areas indicate the presence of hi-Ca pyroxene type, the greenish areas indicate low-Ca pyroxene type, while the light blue is presenting a mixture of possible both low- and hi-Ca pyroxene types. This color scale attributes dull red to Fe-phyllosilicate, while red areas likely show the presence of olivine.

CRISM datacube FRT00009C5B

The second CRISM datacube is located between 166°90'W - 165°57'W and 9°54'S - 10°60'S. This is an area 9 km wide and $\sim$9 km long located in the west upper side inside the paleolake II floor. In this case the morphology is completely different with respect to the previous riverbed case: from MOLA and HRSC DEMs elevation values, we can say that the topography is flatter, with the exception of some 1 km wide craters.

After performing the photometric and the atmospheric corrections, we applied the LCPINDEX on the data cube, see Fig. 6.21 I and II. We used an exponential green colorbar with the same limits of Fig. 6.10 II to see the small surface features. The first notable difference with respect to the previous area is that the LCPINDEX mineralogy is not showing wide and well defined outcrops: there are few craters' rims with values close to -0.041, but nothing else appears. Nevertheless we identified 7 ROIs and then we computed the maximum, the minimum, the $\pm$1 sigma spectrum and the mean spectrum for each ROI. The georeferenced cube and the LCPINDEX colorbar are presented in Fig. 6.21 V. The resulting mean spectra we derived are indicated in Fig. 6.22 while the removed continuum spectra are in Fig. 6.23. With the exception of ROI 5, we find out that the spectral behavior from 1.0 to 2.6 μm of all ROIs is similar with the one of the ROIs spectra identified through the LCPINDEX in the first riverbed region. The likely presence of orthopyroxene on the selected area showing the same absorption bands with different percentage depths can be the explanation of this spectral behavior, but the mean spectrum derived from ROI 5 is showing something different.

The spectral trend shows a minimum around 1.20 μm with a positive slope from 1.20 μm to 2.60 μm. This cannot be explained by the exclusive presence of pure orthopyroxene. The realistic presence of a mixture of Martian minerals as orthopyroxene and magnetite, which has a spectral trend very similar in the 1.0 - 1.7 μm range (Fig. 6.24), might be significant to reproduce this spectral behavior. ROI 5 spectrum still presents an increasing peak at 1.4 μm, *i.e.* the typical signature of orthopyroxene spectra, but the global spectral trend between 1.20 μm to 2.6 μm is also increasing, as for the magnetite case. The combination of both behaviors consequently lead to our spectral interpretation.

In the previous cases the presence of orthopyroxene was identified through the spectral matching technique, we understand that in this case a deeper and detailed theory of minerals mixture is required: this meaning that a spectral modeling of the Martian surface should be undertaken, which is not the purpose of this thesis. Despite the limitations of the spectral matching technique, we think that the central wavelength of the mineralogical absorption bands showed in the continuum removed spectra are

significant, at least to identify the main components of the suggested mineralogical mixtures.

We consequently used the OLINDEX spectral parameter on the CRISM cube and the results we obtained are presented in Fig. 6.25. The resulting spectra of the three ROIs are indicated in Fig. 6.26 and 6.27: the three spectra can be explained in the same way used in describing the previous LCPINDEX spectra.

The most significant comparison between the first CRISM cube and this one is presented in Fig. 6.28, where the intensity of the R, G and B color is the same of the one used in Fig. 6.20. Through this technique we can make a comparison of the mineralogical distribution between the two sites. The paleolake floor mineralogy is, as expected, more homogeneous with respect to the riverbed floor and its rims. This is demonstrated by the absence of a intense red or blue region on the surface, on the contrary, a similar reddish/bluish color is scattered on the surface not tending to specific mineralogical sites.

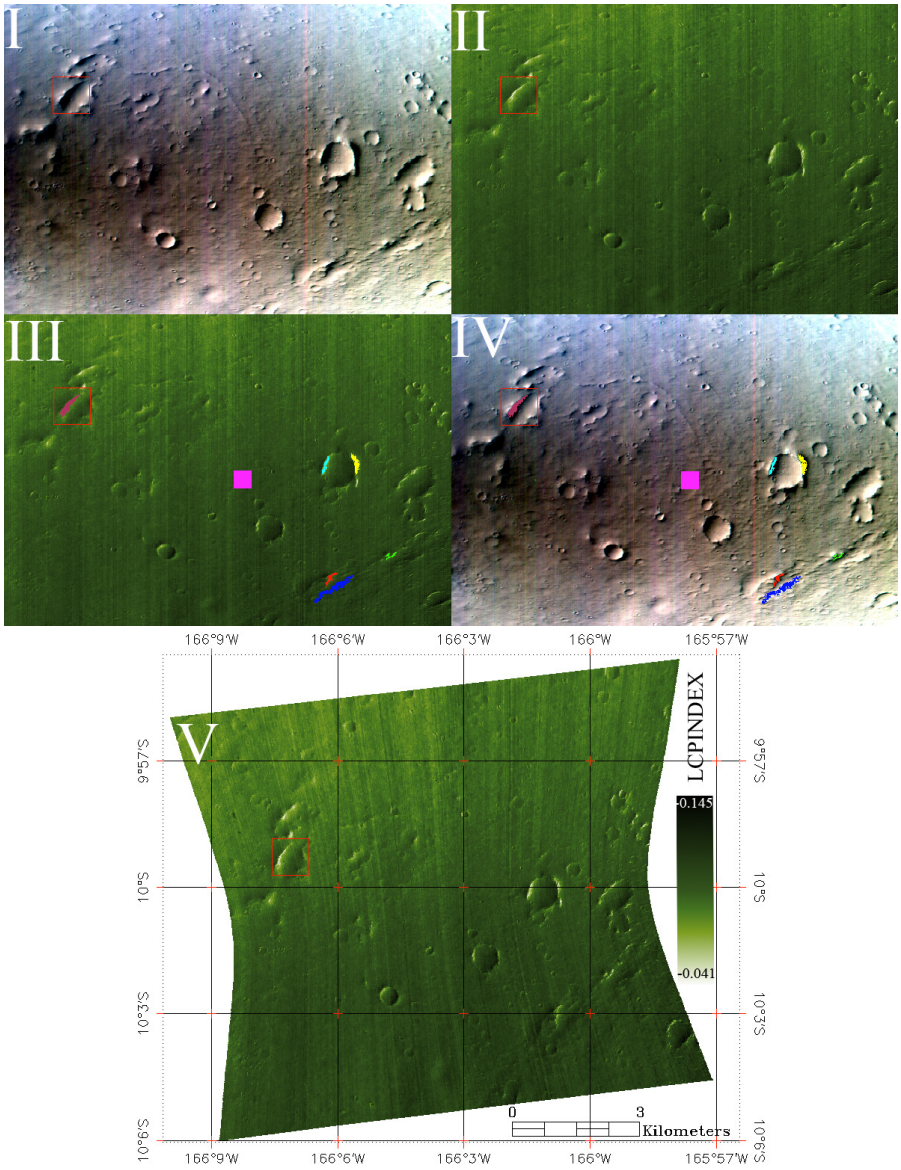

Figure 6.21: I: original CRISM data cube. II: LCPINDEX applied on the datacube with an enhancing green colorbar. III: ROIs identified by using the LCPINDEX spectral parameter. IV: extraction of the maximum, minimum, the ± 1 sigma spectrum and the mean spectrum for each ROI from the original cube. V: georeferenced CRISM cube map with the LCPINDEX values found on the considered area.

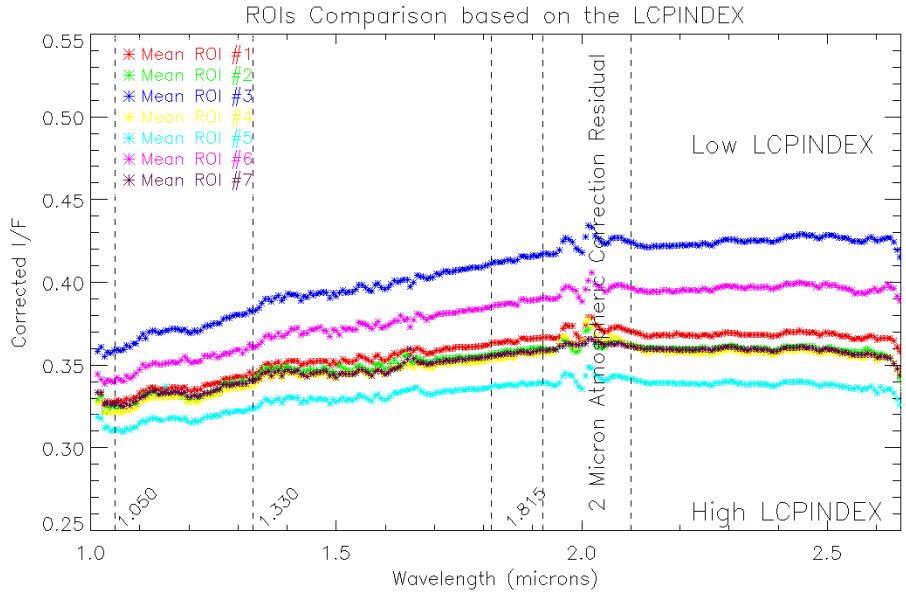

Figure 6.22: Mean ROIs surface spectra derived from CRISM cube after the LCPINDEX has been applied. As for Fig. 6.11 note that some of the 2 μm atmospheric correction residual is still present.

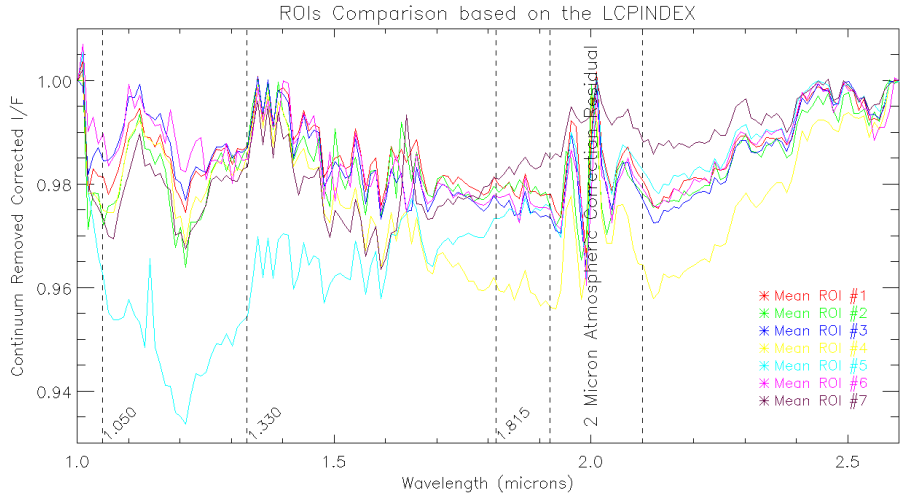

Figure 6.23: The same ROIs spectra, as presented in Fig. 6.22, but with the spectral continuum removed, as indicated in section 6.2. The wide absorption found in the previous CRISM cube, from 1.4 and 2.6 μm, is still present, but a different spectral signature is found on the ROI 5.s

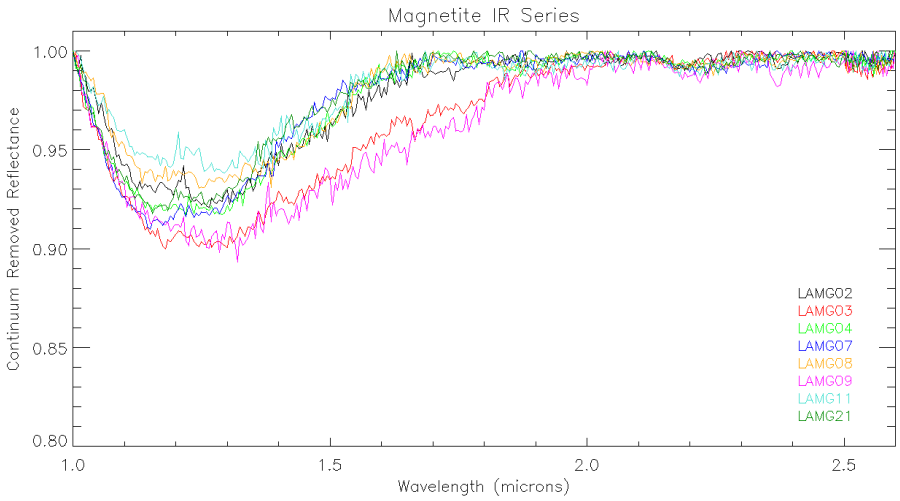

Figure 6.24: Spectral continuum removed profiles of eight different minerals belonging to the Magnetite series. Data source CRISM Analysis Tool & ENVI USGS Spectral Library.

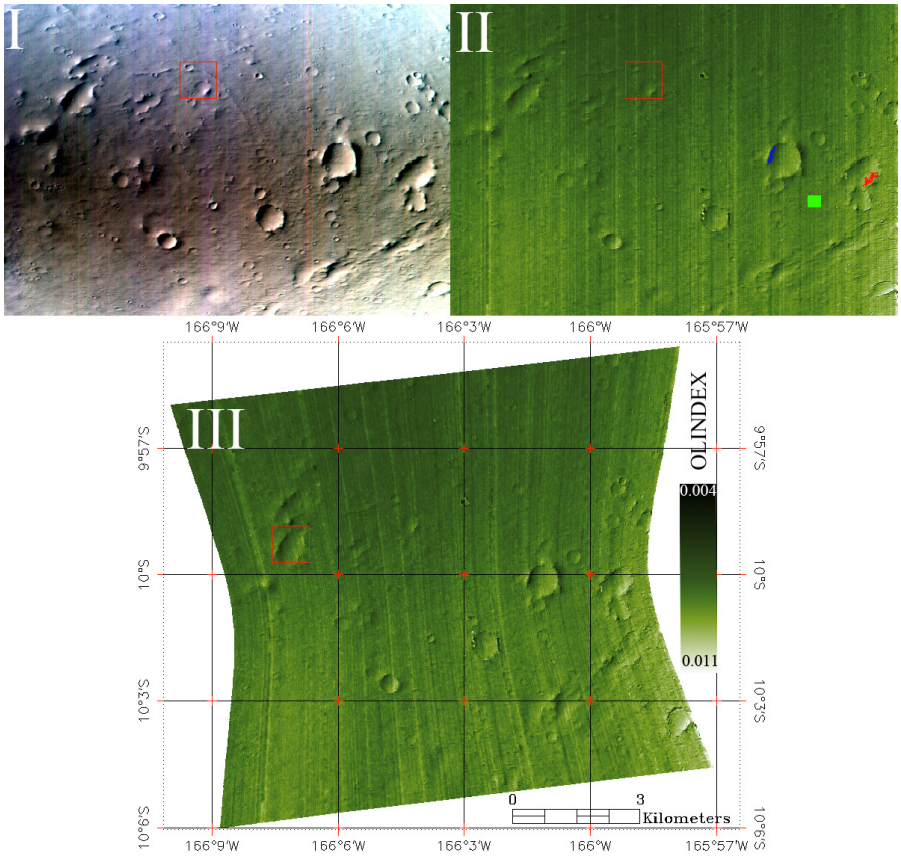

Figure 6.25: I: original CRISM data cube. II: OLINDEX applied on the datacube and the three ROIs identified by using this parameter. III: georeferenced CRISM cube map with the OLINDEX values presented in the colorbar.

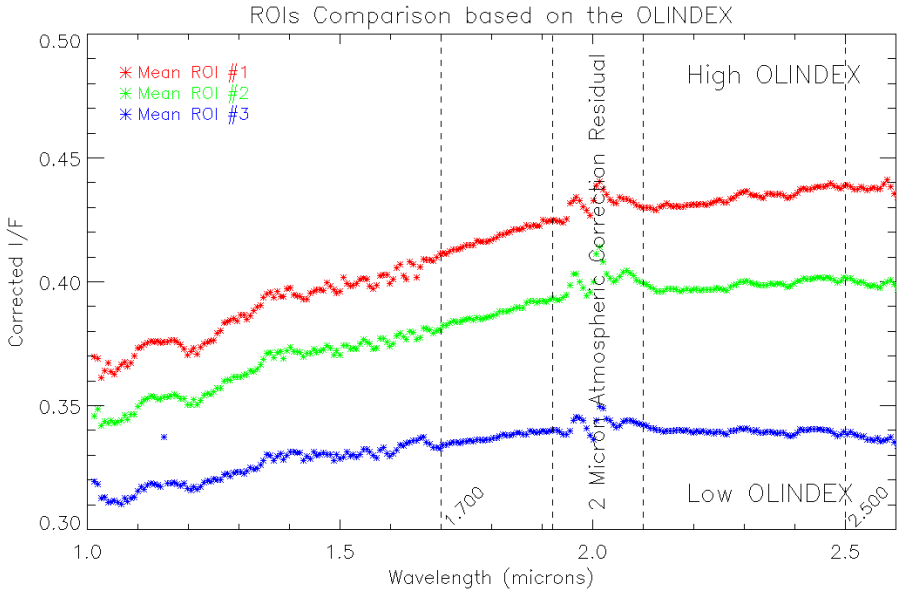

Figure 6.26: As from Fig. 6.14 the mean ROIs surface spectra derived from CRISM cube after the OLINDEX has been applied.

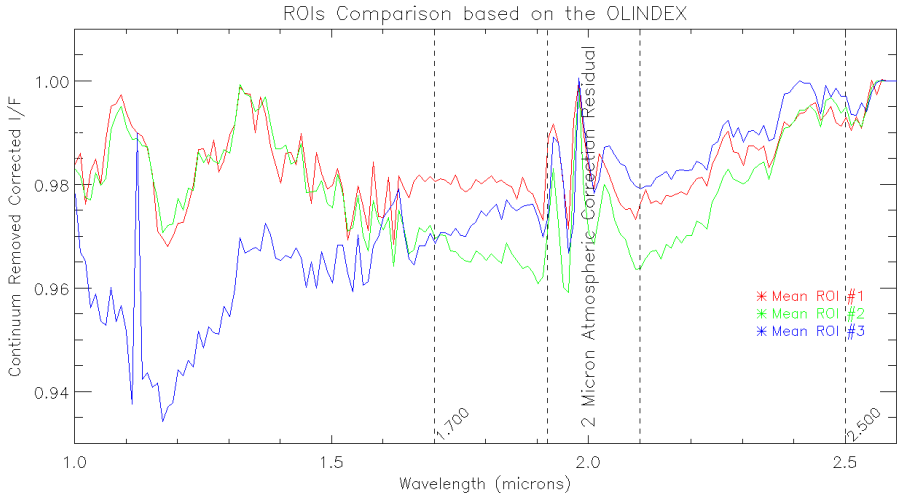

Figure 6.27: The same ROIs spectra, as presented in Fig. 6.26, but with the spectral continuum removed. Note the different spectral behavior of ROI 3 with respect to ROIs 1 and 2.

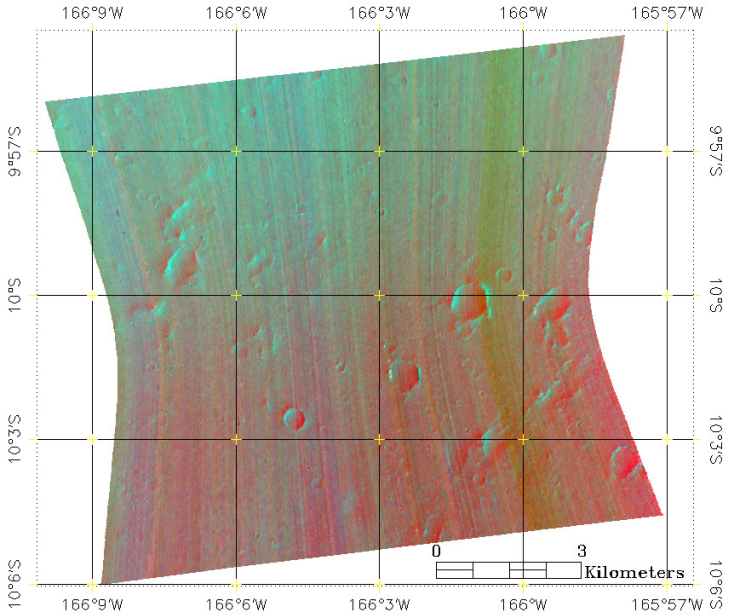

Figure 6.28: RGB map made possible assigning the OLINDEX map to the red R channel, the LCPINDEX map to the green G channel and HCPINDEX to the blue B channel. The intensity of the R, G and B color is the same of that one used in Fig. 6.20: this allows us a comparison of the mineralogical distribution between the two sites. The paleolake floor mineralogy is, as expected, more homogeneous with respect to the riverbed floor and its rims. This is demonstrated by the absence of a red or blue region on the surface, instead a similar color is present on the presented surface.

CRISM datacube FRT0002339A

The third CRISM datacube is located at the entrance of paleolake I tributary and it covers a section of the riverbed outlet too. The area coverage goes from 167°21'W - 167°90'W and 9°24'S - 9°36'S over a surface which is roughly 10 km wide and 9 km long.

After performing the photometric and the atmospheric corrections, we applied both the LCPINDEX and the HCPINDEX on the datacube, see Fig. 6.29 I and II. With both maps in hand, we decided to consider a different approach for this dataset instead of using the above LCPINDEX and the OLINDEX mentioned technique. This was suggested by the fact that the OLINDEX map is, in this case, corrupted. We subtracted the HCPINDEX to the LCPINDEX map, attempting to enhance areas where only possible high-Ca mineralogical response is present. The resulting map is presented in Fig. 6.29 III where we applied an exponential red color scale, this ranges from -0.041 to 0.098 (a different color with respect to the exponential green color scale which here was not good enough to show small surface differences). We derived 7 different ROIs considering areas with different HCPINDEX minus LCPINDEX values. The resultant spectra are presented in Fig. 6.30 and 6.31. From Fig. 6.31 we see clearly the absorption's band between 1.35-1.40 and 2.6 (ROIs 1, 5 and 6) that we noticed in the spectra of the first CRISM data cube. For this three ROIs we can also see the two bands located at

1.2 and 1.05 μm typical of the Orthopyroxene series presented in Fig. 6.16.

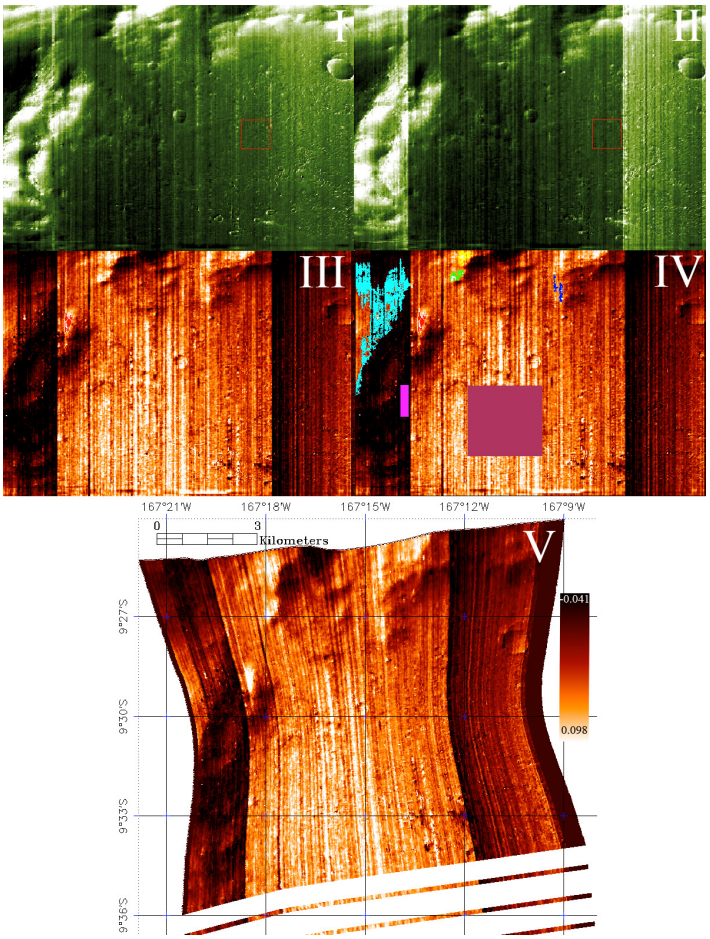

Figure 6.29: I: LCPINDEX applied on the datacube with an enhancing green colorbar. II: HCPINDEX applied on the datacube with an enhancing green colorbar . III: HCPINDEX minus LCPINDEX applied on the datacube with an enhancing red colorbar. IV: ROIs identification and extraction of the maximum, minimum, the ± 1 sigma spectrum and the mean spectrum for each ROI from the original cube. V: georeferenced CRISM cube map with the HCPINDEX minus LCPINDEX values found on the considered area.

The resultant ROIs present a difference with the previous spectra: the bands located at 1.2 and 1.05 are somehow very shallow or not even present. We think that this behavior can be explained by the fact that the present surface mineralogy is a mixture of both pure orthopyroxene (Fig. 6.16 presenting the band between 1.35 and 2.6 μm) and orthopyroxene mixed with bronzite, enstatite and/or hypersthene which widen the above-mentioned band to 1.25 - 1.30 μm (see the spectra in Fig. 6.17) together with pyroxene material, see Fig. 6.32, which shows a couple of possible spectra, as C1XP04 and C1LS12, that do not present the band at 1.2 but only a small feature at 1.05 μm.

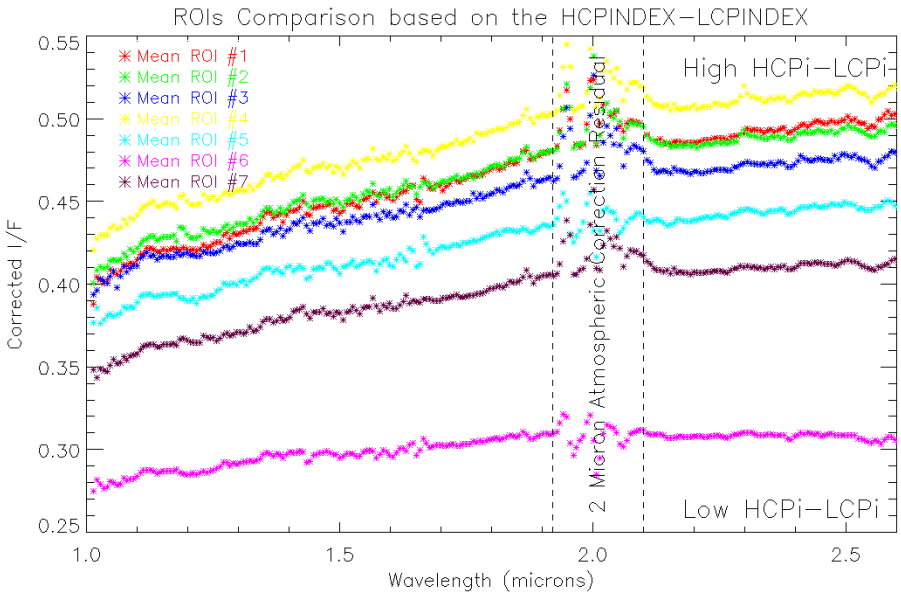

Figure 6.30: Mean ROIs surface spectra derived from CRISM cube after the HCPINDEX minus LCPINDEX has been applied. Note that some of the 2 μm atmospheric correction residual is still present.

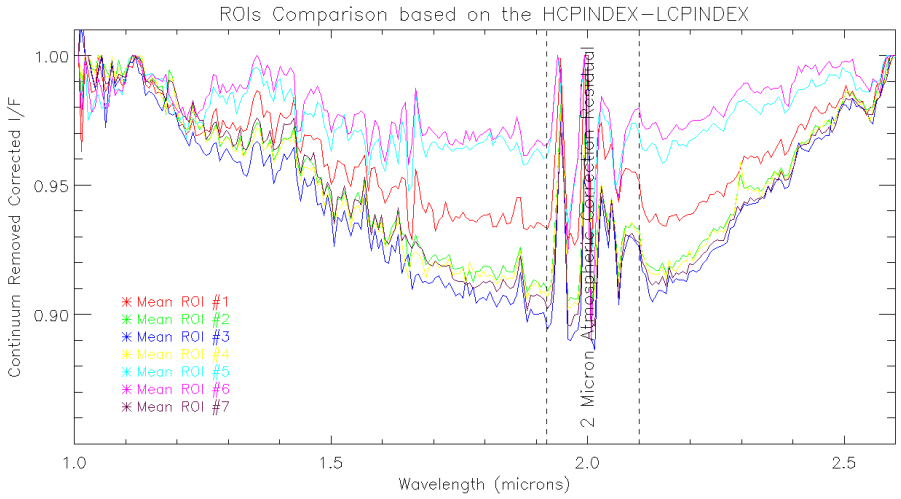

Figure 6.31: The same ROIs spectra, as presented in Fig. 6.30, but with the spectral continuum removed, as indicated in section 6.2. Note the wide band from 1.3 to 2.6 μm, and the similarity between all spectra, the difference being the absorption's depth.

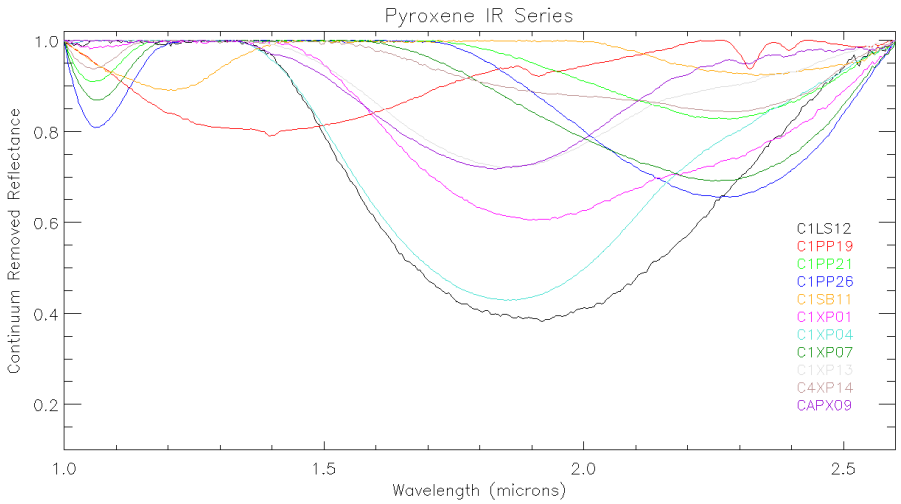

Figure 6.32: Spectral continuum removed profiles of eleven different minerals belonging to the pyroxene series. Data source CRISM Analysis Tool & ENVI USGS Spectral Library.

This case is the one which shows more difficulties to understand the mineralogical mixture characterizing the surface. The spectral matching technique, here, helps in defining the possible main components constituting the surface layers but we are aware that a deeper and detailed theory of minerals mixture would be required to model the spectral behavior.

6.4.2 Area #2

The second area we have considered is located between 168°30'00"E - 173°00'00"E and 16°00'00"S - 18°00'00"S, as presented in Fig. 6.33. Three different CRISM datacubes have been analyzed, the first one located between the junction of two riverbeds belonging to the Durius vallis drainage area, the second one is right in the middle of the paleolake III floor, while the third one is on a rim located between two craters 100 km far west from paleolake III.

The first data cube covers two different wavelength ranges, the visible one between 0.35 - 1.00 μm and the IR section between 1.00 and 3.90 μm, the paleolake III CRISM cube is only covering the visible range, while the third data cube covers the same wavelength range of the first spectral cube.

CRISM datacube FRT000099EE

The first CRISM datacube is located between 171°45'E - 171°54'E and 16°45'S - 16°54'S, see Fig. 6.34 I. The considered area is inside the Durius Vallis drainage basin, at the junction of two distinct riverbeds, one, the bigger, 750 m wide, while the second is 250 m wide. On the right side of the junction there is the remnant of an ancient crater characterized by a radius of 4 km whose rim is just present on the east - north east side. The remaining part of the crater's rim has been eroded, probably by the activity of the main riverbeds which is cutting this terrain at 171°47'E and 16°49'S.

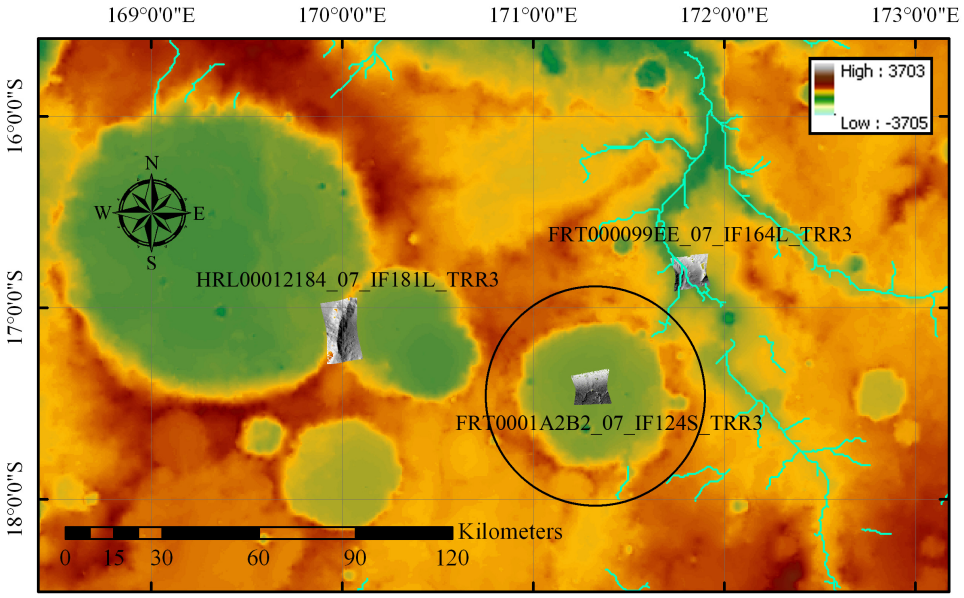

Figure 6.33: Map of the second considered Mars region, belonging to the Aeolis quadrangle, where the three indicated CRISM data cubes are analyzed. The black circle corresponds to the paleolake III previously presented.

The first spectral cube covers the visible and near IR range between 0.35 and 1.00 μm. Within this wavelength range, no atmospheric CO_2 correction is required, only the photometric correction has to be applied. We then used several spectral parameters presented in Table 6.1. The one which gave the strongest morphologically localized value was the BD530, *i.e.* the one identifying the greater content of the presence of larger particles of ferric oxide. Focusing on the BD530 values, we identified seven ROIs located, as example, on the crater rim, inside the main riverbed's floor or on both riverbed's sides, see Fig. 6.34 II. We then derived the mean ROIs spectra and plotted them all together to see their mutual differences. The resulting plot is presented in Fig. 6.35, where we can see that no different spectral bands appear from ROI 1 to 7 and the spectral trend is very similar. This spectral behavior is confirmed after the continuum is removed from the spectra, Fig. 6.36, where the wide and deep absorption band between 0.4 and 0.63 μm is clearly visible; the only difference between the seven ROIs are small differences in this band depth.

As a first possible mineralogical interpretation we made a comparison between our 7 ROIs spectra and the goethite visible reference spectra, see Fig. 6.37. The goethite series shows three characteristic bands, one from 0.35 to 0.58 μm, the second from 0.60 to 0.76 μm and the third from 0.78 to 1.0 μm. The CRISM data show a different behavior especially from 0.6 to 1.0 μm, where a possible narrow band from 0.63 to 0.7 μm is present. The presence of this feature is controversial because it falls right in the middle of CRISM bad bands coverage, so it has not to be considered. From 0.7 μm to 1.0 μm there is the main difference between goethite and our spectra, which do no show a deep absorption, but mainly a flat behavior. The second attempt we made to find an iron oxide mineralogical reference for our spectra has been the hematite series.

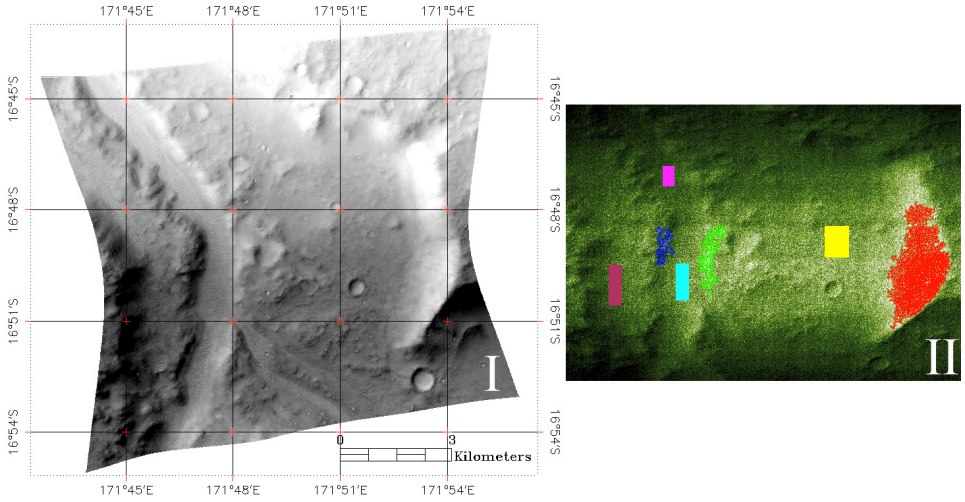

Figure 6.34: I: georeferenced CRISM datacube. II: BD530 applied on the datacube with an enhancing green colorbar and ROIs identification and extraction of the maximum, minimum, the ± 1 sigma spectrum and the mean spectrum for each ROI from the original cube.

From Fig. 6.38, we see that the general spectral trend from 0.4 to 1.0 μm is heavily different, whether in the 0.4 - 0.65 μm range or in the 0.75 - 1.0 μm.
The third attempt was made with the magnetite series, and it gave more robust results: the first magnetite band located between 0.4 and 0.63 μm matches with our results even if we find a deeper band. The reflectance behavior long wards 0.7 μm matches with our results too. The important question we have to answer here is how the difference in depth for the 0.5 μm band is explained. We know that the Mars surface is normally characterized by mineralogical mixtures and just locally shows pure minerals. Considering the width of the ROIs we have selected, we think that the spectral reflectance we are looking at, could be characterized by a magnetite overtone, but with possible presence of hematite which could deepen the 0.5 μm centered band and flatten the spectra behavior long wards 0.7 μm. A possible presence of goethite is not even *a priori* excluded.

In Fig. 6.40 we present the spectral maps we derived from this cube: the above-mentioned BD530, then the SH600, which identifies dust costings on dark rocks or the presence of olivine, then the BD920 indicating crystalline Fe minerals as hematite or pyroxene, and BDI1000VIS showing minerals characterized by the strong 1 μm band due to Fe as in pyroxene or olivine. The main feature we can see throughout the four maps is that ferric oxides seems to be located in the east rim of the main riverbed and the ancient crater, where the SH600 map shows low levels of olivine, indicated also by the distribution of the BDI1000VIS spectral parameter. On the other side, the BD920 map shows no specific localization of hematite or pyroxene on this area.

Using other two maps presented in Fig. 6.41, we can see that where in the FEM map there are red/pink areas, we are looking at crystalline ferric oxides confirmed also by the reddish/yellowish colors on the FM2 map, while the bluer areas on both maps identify cleaner or more mafic surfaces.

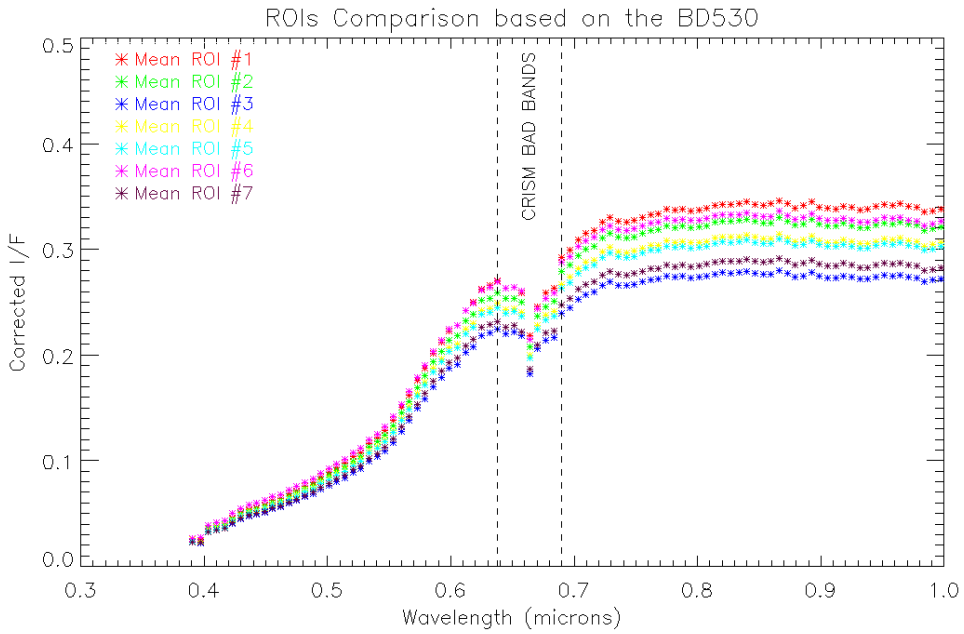

Figure 6.35: Mean ROIs surface spectra derived from CRISM cube after the BD530 has been applied.

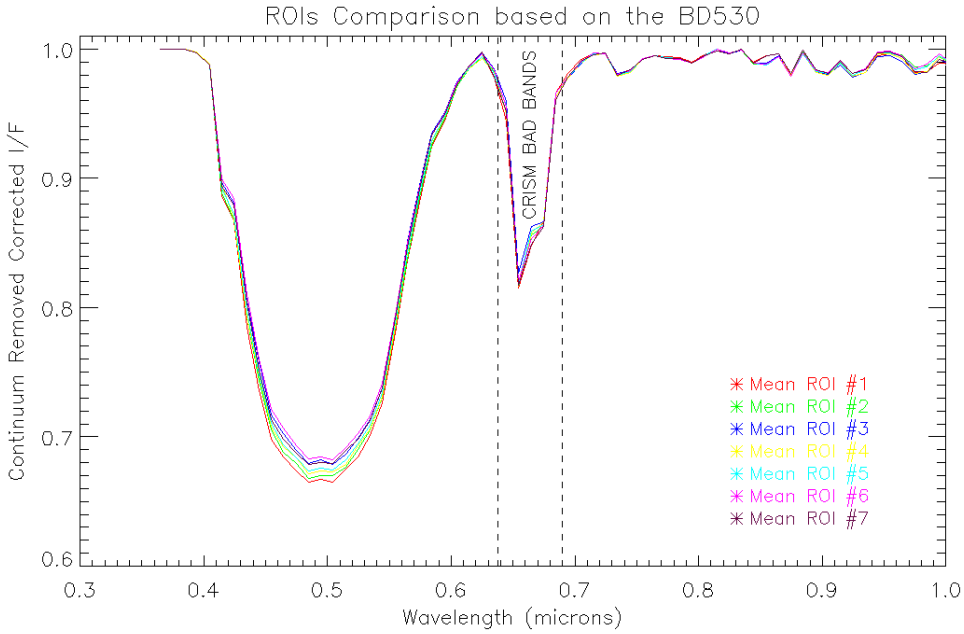

Figure 6.36: The same ROIs spectra, as presented in Fig. 6.35, but with the spectral continuum removed, as indicated in section 6.2. Note the deep band from 0.40 to 0.63 μm.

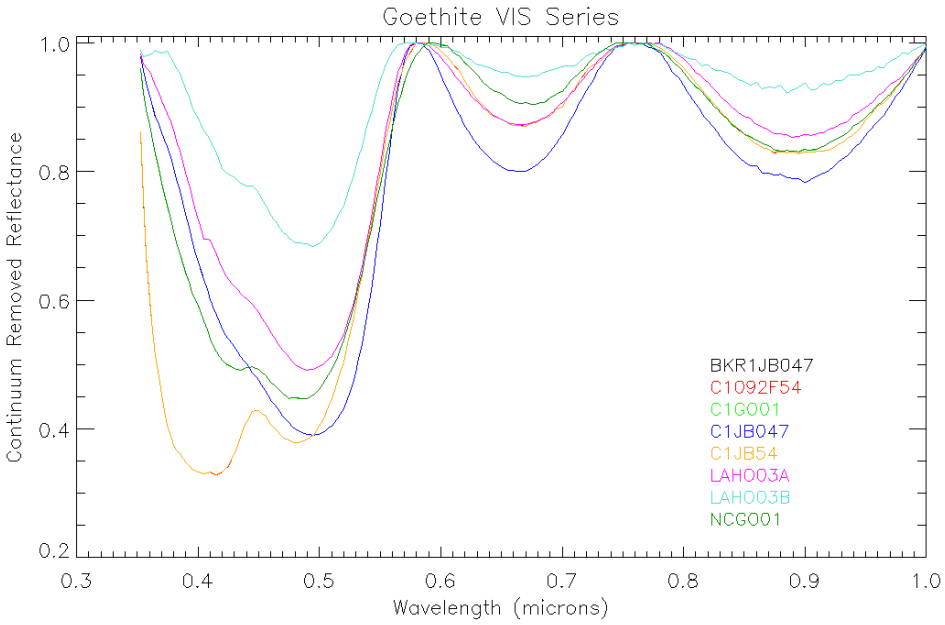

Figure 6.37: Spectral continuum removed profiles of eight different minerals belonging to the goethite series. Data source CRISM Analysis Tool & ENVI USGS Spectral Library.

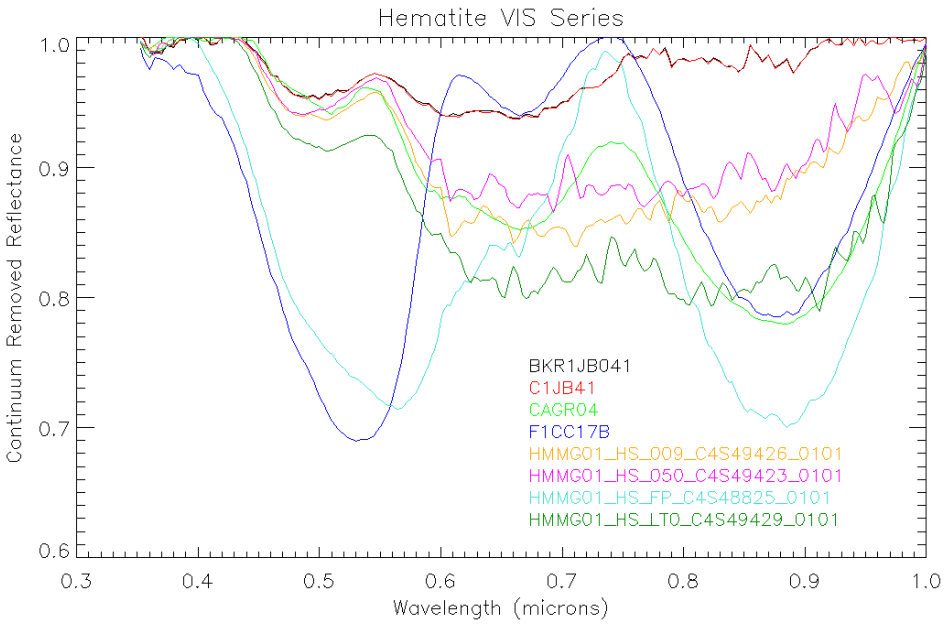

Figure 6.38: Spectral continuum removed profiles of eight different minerals belonging to the hematite series. Data source CRISM Analysis Tool & ENVI USGS Spectral Library.

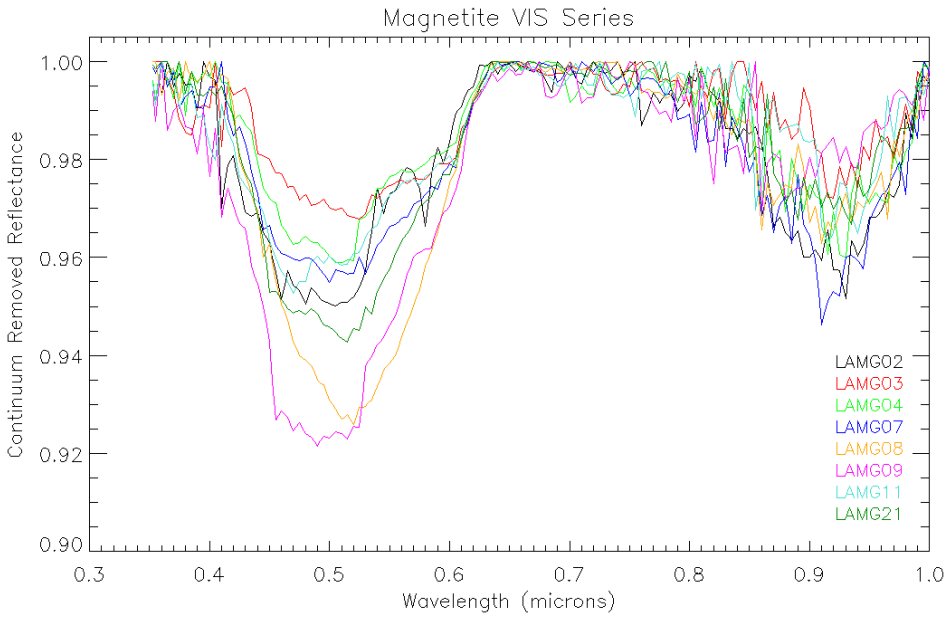

Figure 6.39: Spectral continuum removed profiles of eight different minerals belonging to the magnetite series. Data source CRISM Analysis Tool & ENVI USGS Spectral Library.

After the analysis of the visible range has been performed, we decided to study also the IR range of the CRISM data cube covering this area. We decided to use the same ROIs identified with the BD530 visible parameter in the IR cube for two reasons: the first one is the excellent VNIR-IR registration performed by the CRISM instrument and the second one is the possibility to understand if the IR wavelength coverage is justified by the same mineralogical material found in the same areas for the visible range. We then derived the mean ROIs spectra indicated in Fig. 6.42. The continuum removed spectra of the same ROIs are plotted in Fig. 6.43. The spectral behavior of the seven ROIs shows the main overtone of orthopyroxene presented in Fig. 6.16, with the wide band between 1.35 and 2.6 μm and the two bands centered at 1.2 and 1.05 μm, as the case of ROIs 1, 2 and 4. The possible different behavior of the remaining ROIs can be explained by the surficial presence of magnetite, see Fig. 6.24 as reference, confirmed by the visible spectral matching showed in Fig. 6.36 and 6.39. A mixture of orthopyroxene and magnetite is the likely explanation for all 7 spectra. This confirms that what is observed in the visible range of the spectrum, is showed also by the IR wavelength coverage.

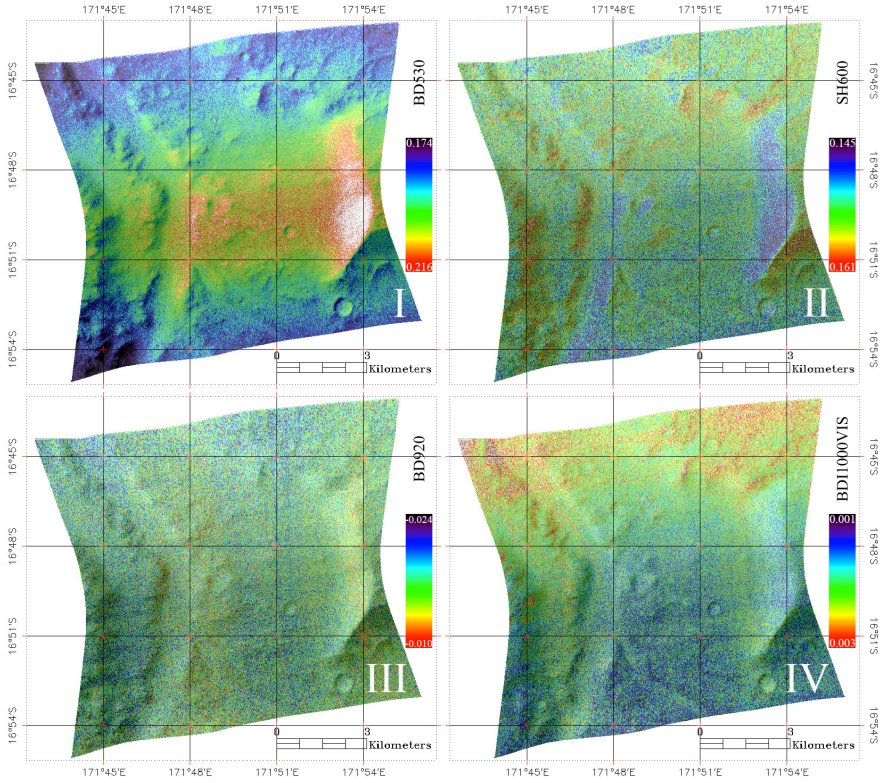

Figure 6.40: I: BD530 map identifying the presence of larger particles of ferric oxide; II: SH600 spectral parameter mapping the presence of olivine,; III: BD920 map indicating crystalline Fe minerals as hematite or pyroxene; IV: BDI1000VIS map showing minerals characterized by the strong 1 μm band due to Fe as in pyroxene or olivine.

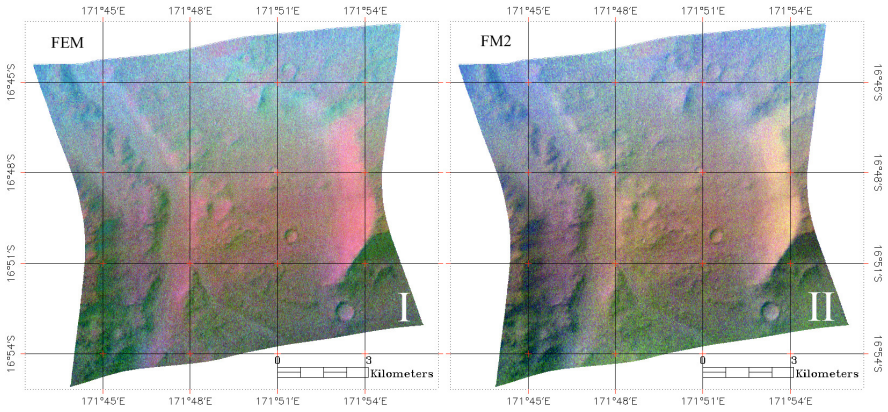

Figure 6.41: I: FEM map obtained using the BD530 as the R channel, the SH600 for the green one, and BDI1000VIS for the blue channel. II: FM2 map obtained using the BD530 as the R channel, the BD920 for the green one, and BDI1000VIS for the blue channel.

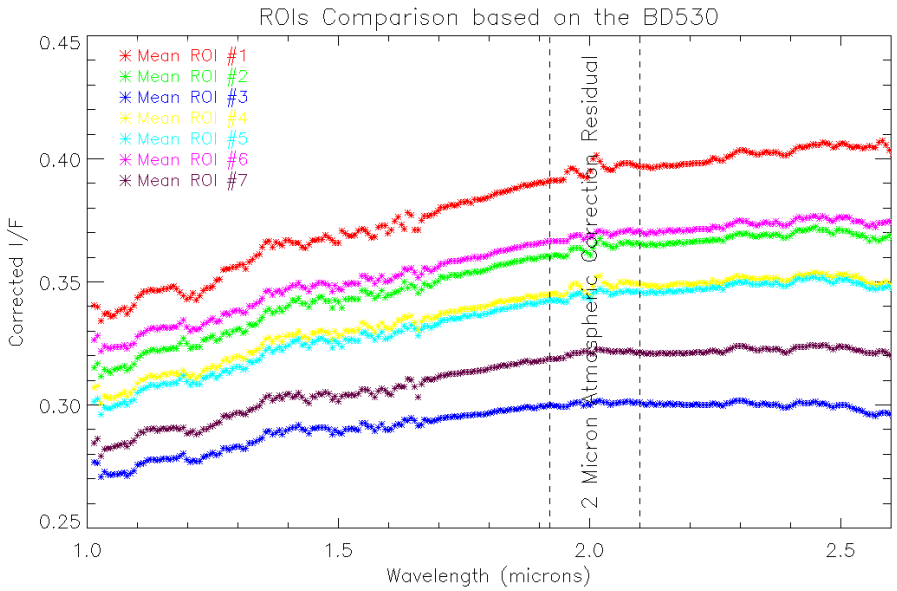

Figure 6.42: Mean ROIs surface spectra derived from CRISM IR cube using the ROIs identified through the BD530 Visible spectral parameter. Note that, as for the first three datacubes in the first area, some of the 2 μm atmospheric correction residual is still present.

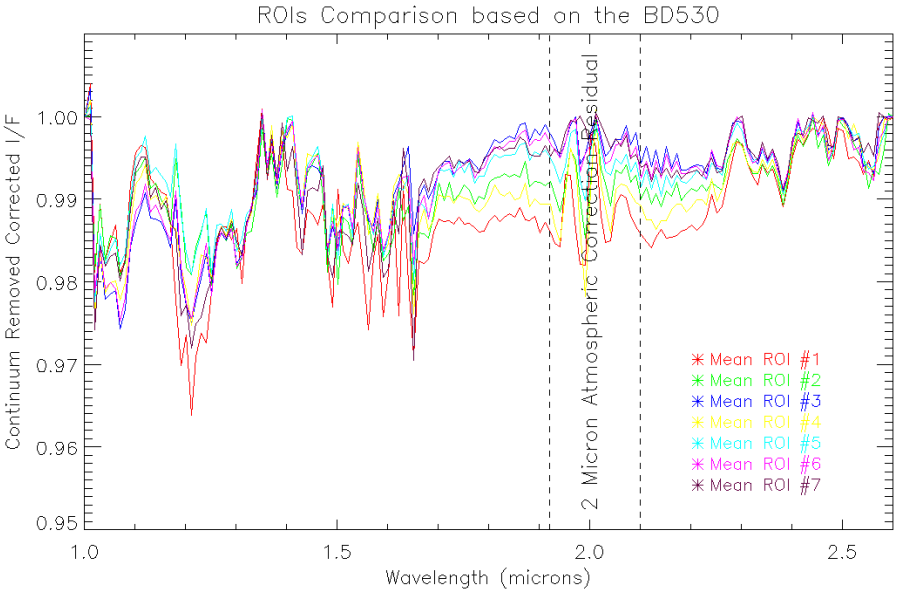

Figure 6.43: The same ROIs spectra, as presented in Fig. 6.42, but with the spectral continuum removed, as indicated in section 6.2.

CRISM datacube FRT0001A2B2

The second datacube is located between 171°12'E - 171°24'E and 17°21'S - 17°30'S, see Fig. 6.44 I. It is fully located in the middle of paleolake III floor. The only wavelength coverage of this area is between 0.35 and 1.0 μm, no IR data between 1.0 and 3.9 is currently available. Nevertheless we can compare the results we get from this region with the previous one, at least in the visible and near IR range.

We followed the same workflow, as presented in data cube FRT000099EE visible range georeferencing the CRISM map, Fig. 6.44 I, selecting the 7 ROIs on the base of the BD530 results and extracting the localized mean spectra, Fig. 6.44 II and Fig. 6.45. The removed continuum spectra are presented in Fig. 6.46. From this plot we can see that the visible spectral behavior inside the paleolake III floor is similar to the one presented inside the Durius Vallis drainage basin, showing a deep band centered at 0.5 μm and a flatter trend above 0.7, with the exception of a more recognizable band from 0.8 to 1.0 μm of about 3%. This feature appears both for the goethite series and the hematite series, but the common presence of this band together with the one located at 0.5 μm highly favors the presence of magnetite.

As for the previous cube, in Fig. 6.47 we present the spectral maps we derived: the BD530, the SH600, the BD920 and the BDI1000VIS. The considered area is inside the paleolake III floor, it is then expected the lack of areas with strong mineralogical differentiation; what these 4 maps are showing is that there is a spread layer of oxides on top of the entire surface. This is confirmed by Fig. 6.48, which show a similar area color coverage.

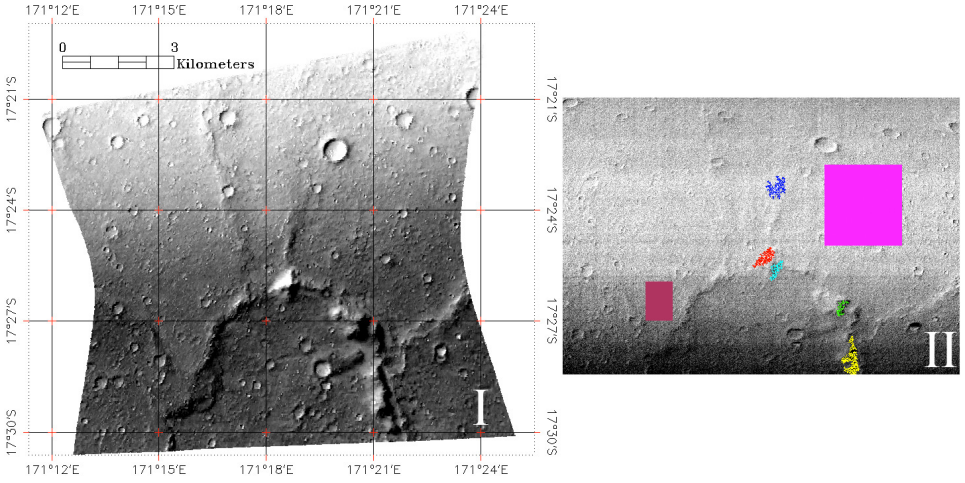

Figure 6.44: I: georeferenced CRISM datacube. II: BD530 applied on the datacube with an enhancing b/w colorbar and ROIs identification and extraction of the maximum, minimum, the ± 1 sigma spectrum and the mean spectrum for each ROI from the original cube.

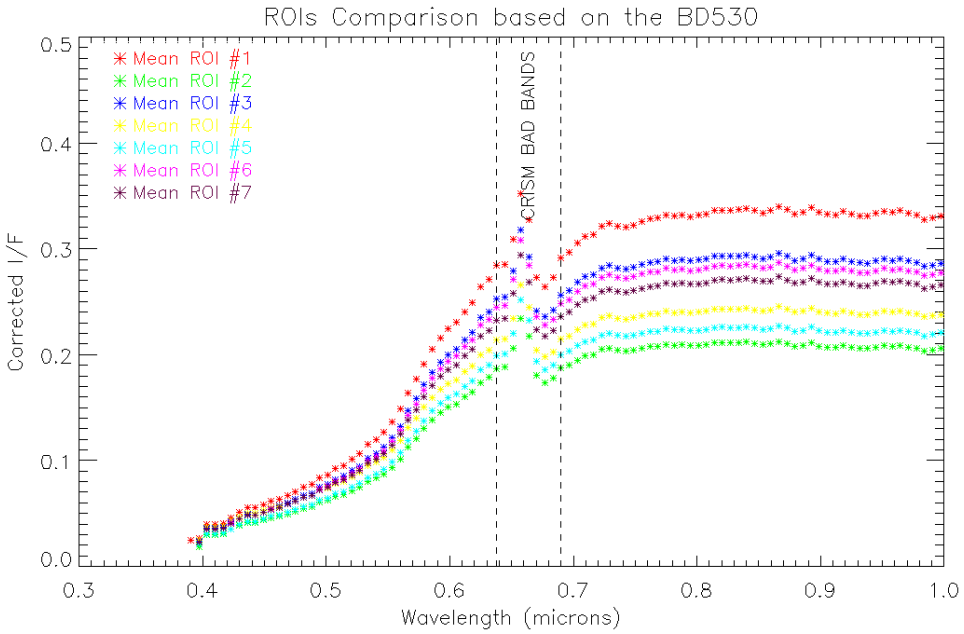

Figure 6.45: Mean ROIs surface spectra derived from CRISM cube after the BD530 has been applied.

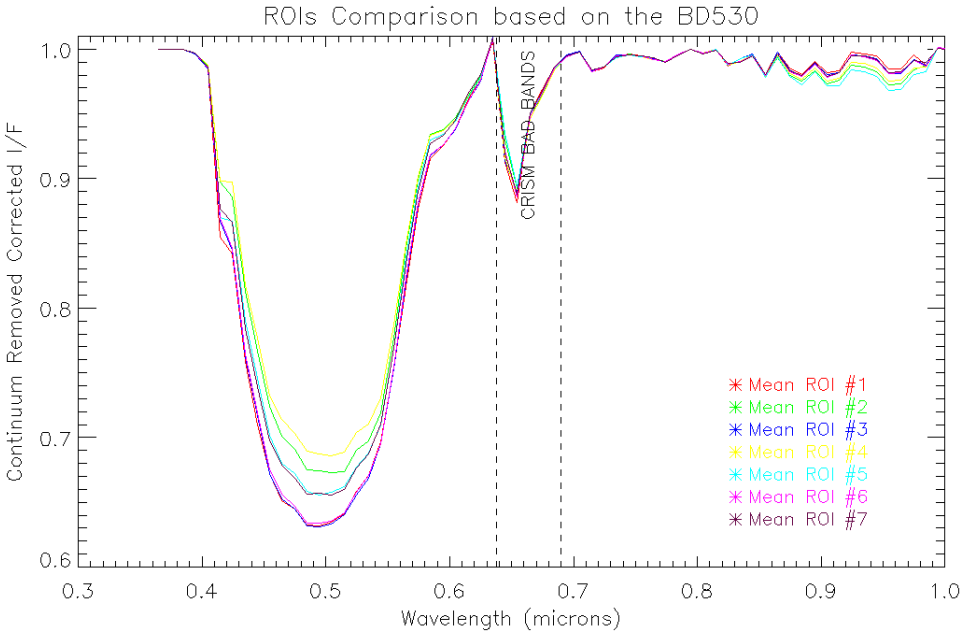

Figure 6.46: The same ROIs spectra, as presented in Fig. 6.45, but with the spectral continuum removed, as indicated in section 6.2. Note the deep band from 0.40 to 0.63 μm.

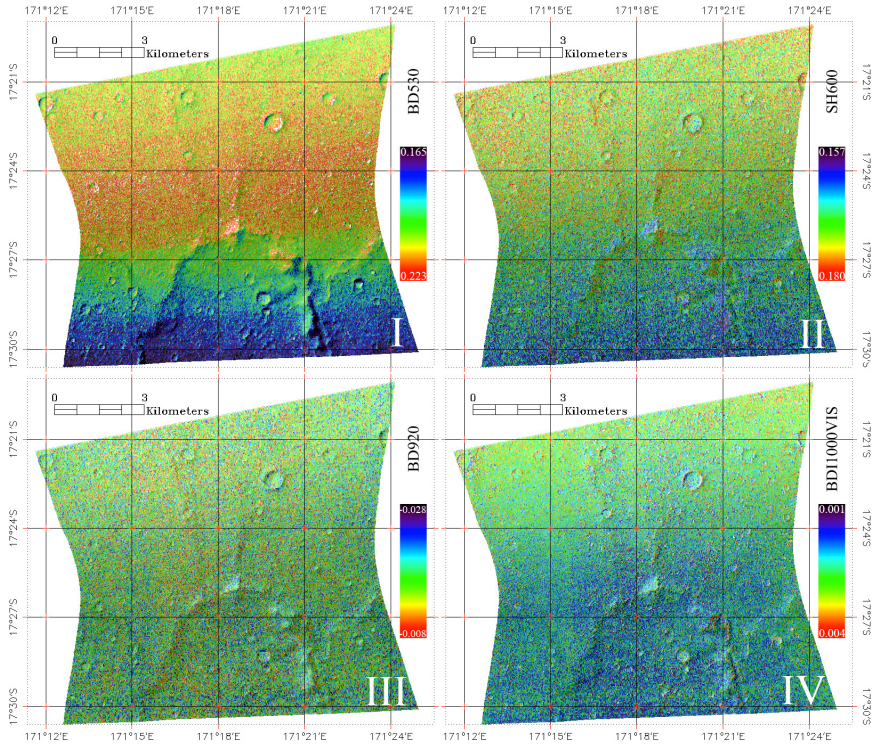

Figure 6.47: I: BD530 map identifying the presence of larger particles of ferric oxide; II: SH600 spectral parameter mapping the presence of olivine,; III: BD920 map indicating crystalline Fe minerals as hematite or pyroxene; IV: BDI1000VIS map showing minerals characterized by the strong 1 μm band due to Fe as in pyroxene or olivine.

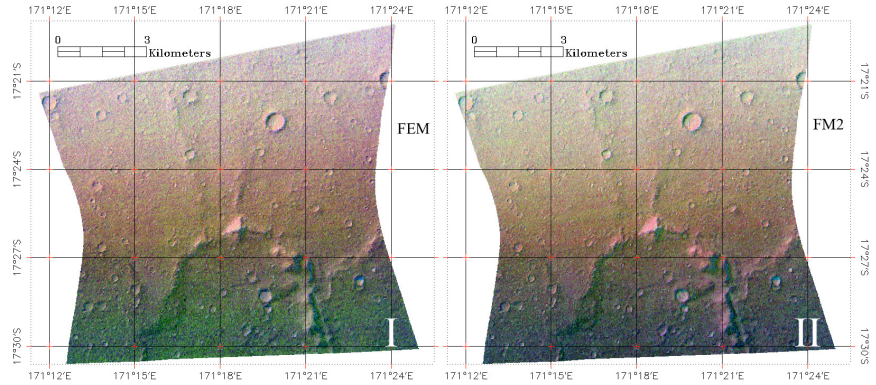

Figure 6.48: I: FEM map obtained using the BD530 as the R channel, the SH600 for the green one, and BDI1000VIS for the blue channel. II: FM2 map obtained using the BD530 as the R channel, the BD920 for the green one, and BDI1000VIS for the blue channel.

CRISM datacube HRL00012184

The third area we considered is located between 169°54'E - 170°60'E and 16°57'S - 17°18'S, see Fig. 6.49 I. This section is lying on the rim located between two craters, one with a diameter of about 30 km, partially superimposed on a second one presenting a diameter of 90 km. We chose this data cube to make comparisons with the two previous analyzed areas, which were specifically characterized by the presence of past surficial water.

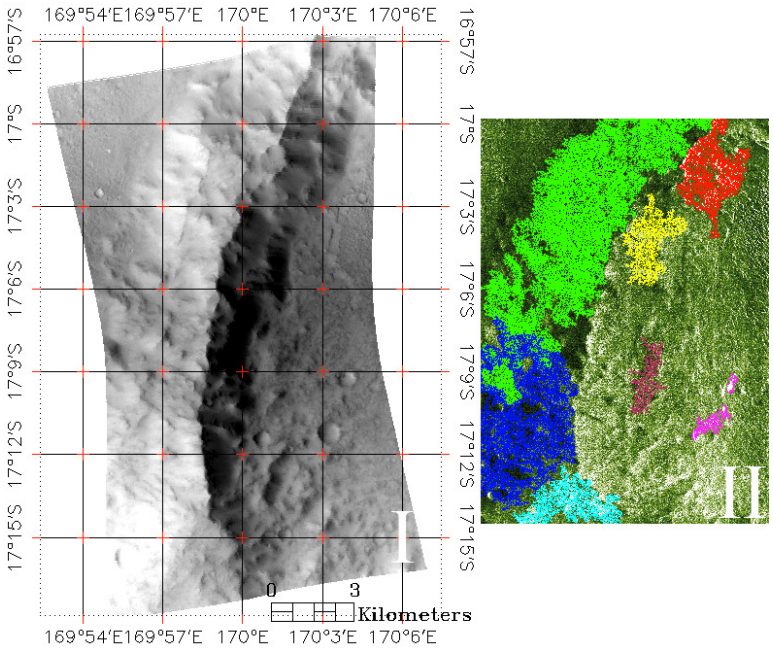

Figure 6.49: I: georeferenced CRISM datacube. II: BDI1000VIS applied on the datacube with an enhancing green colorbar and ROIs identification and extraction of the maximum, minimum, the ± 1 sigma spectrum and the mean spectrum for each ROI from the original cube.

We have a CRISM spectral coverage from 0.35 to 3.9 μm. As for the first data cube belonging to this region, we only applied the photometric correction to the visible part of the spectrum. After we georeferenced the cube, Fig. 6.49 I, we decided to use a different spectral parameter, BDI1000VIS, to identify ROIs with possible minerals showing the strong 1 μm band as pyroxene or olivine, see Fig. 6.49 II. The resulting plots are presented in Fig. 6.50 and 6.51. The spectral trend we are getting is close to the one identified in Fig. 6.36, with the exception of a minimum of the 0.50 μm band around 0.70 and not 0.73. This means that at least the same surfical layer which covers the riverbeds area is covering this area as well.
Looking at the four maps presented in Fig. 6.52, we actually see that there is a stronger localization of the iron oxides on the west side of the rim, where there is the possible lack of olivine or pyroxene, as presented by the SH600 and the BDI1000VIS and confirmed by the reddish areas and yellowish areas on Fig. 6.53 I and II. Through the BD920 map we see that the presence of hematite is ubiquitous on the surface.

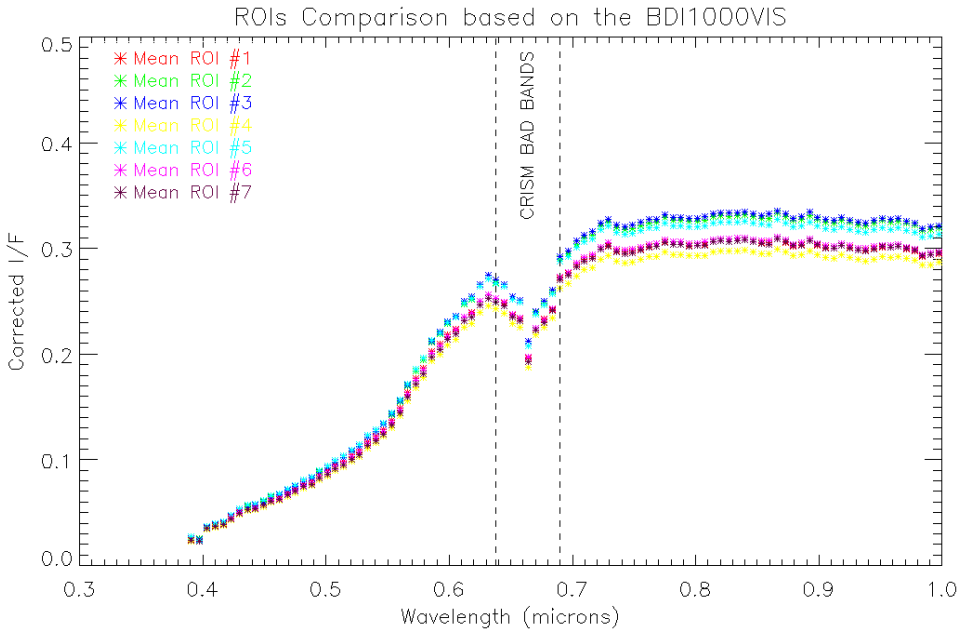

Figure 6.50: Mean ROIs surface spectra derived from CRISM cube after the BDI1000VIS has been applied.

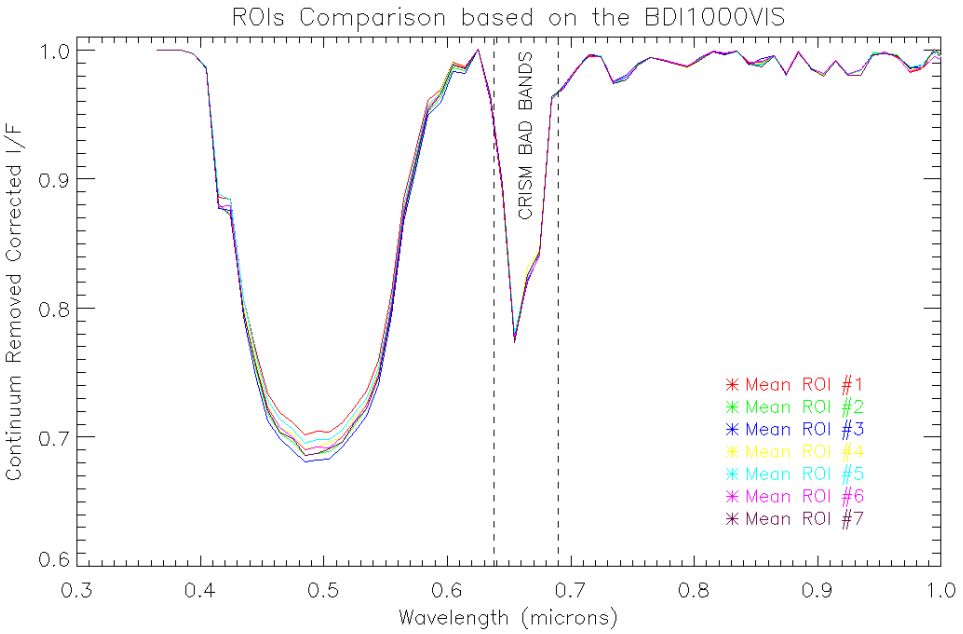

Figure 6.51: The same ROIs spectra, as presented in Fig. 6.50, but with the spectral continuum removed, as indicated in section 6.2. Note the deep band from 0.40 to 0.63 μm.

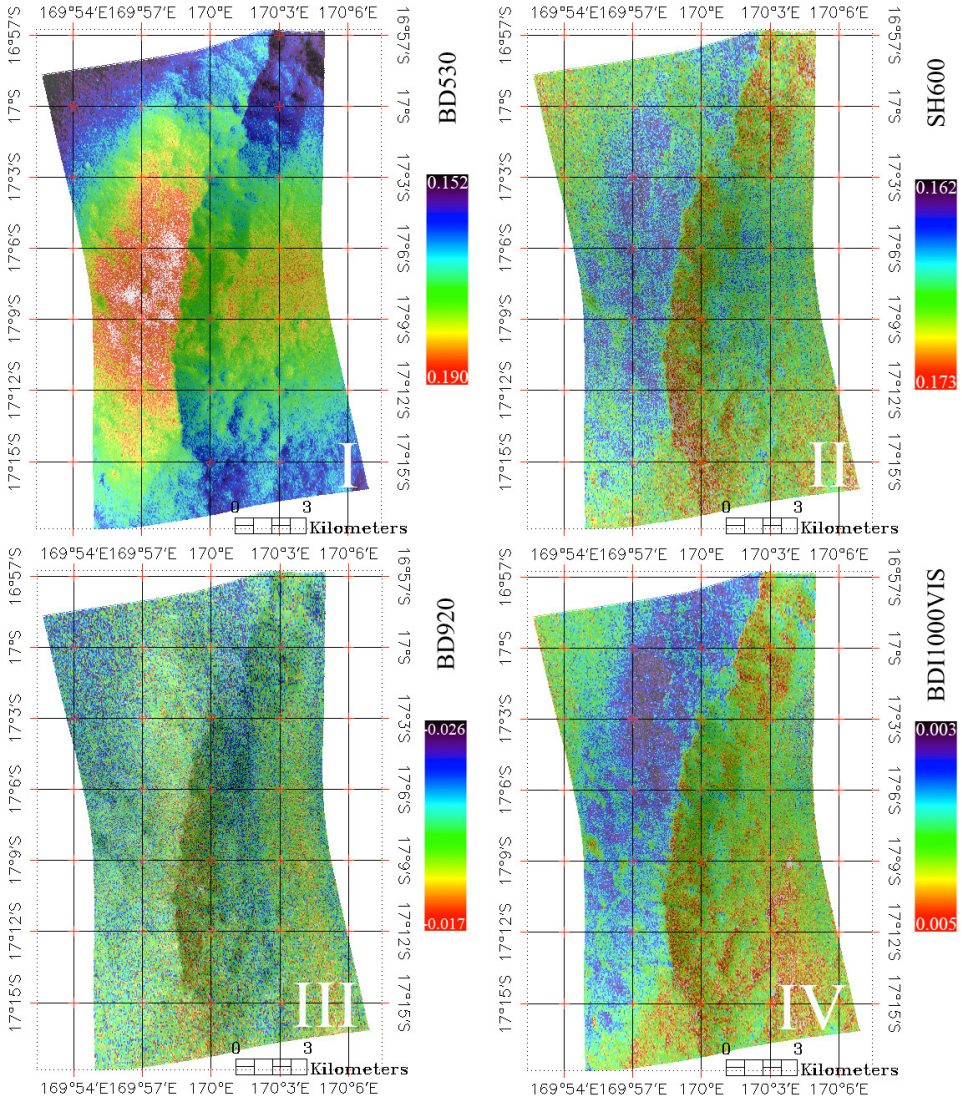

Figure 6.52: I: BD530 map identifying the presence of larger particles of ferric oxide; II: SH600 spectral parameter mapping the presence of olivine,; III: BD920 map indicating crystalline Fe minerals as hematite or pyroxene; IV: BDI1000VIS map showing minerals characterized by the strong 1 μm band due to Fe as in pyroxene or olivine.

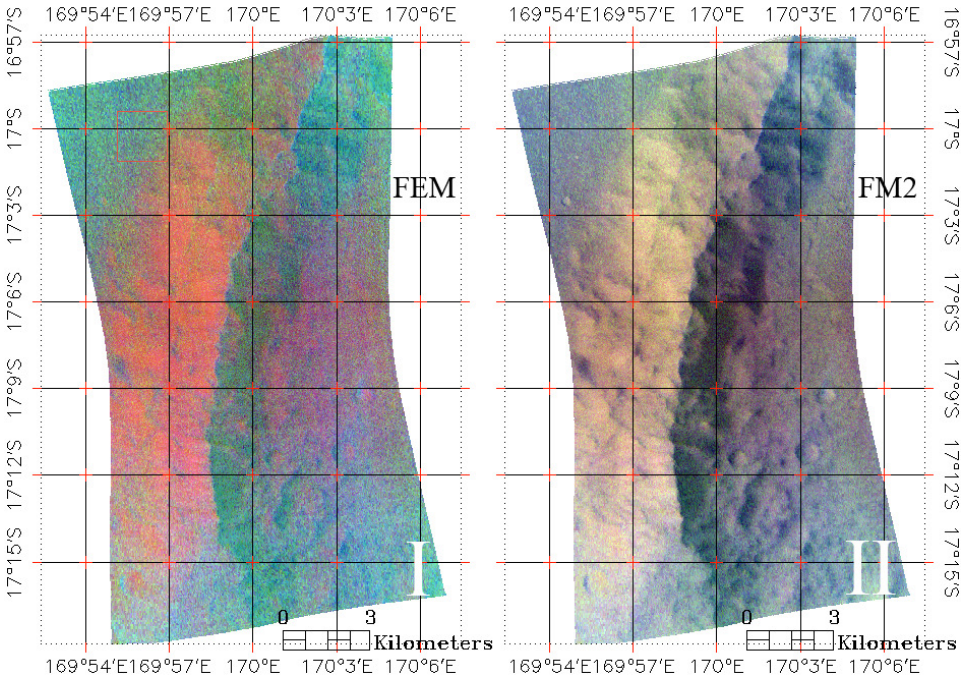

Figure 6.53: I: FEM map obtained using the BD530 as the R channel, the SH600 for the green one, and BDI1000VIS for the blue channel. II: FM2 map obtained using the BD530 as the R channel, the BD920 for the green one, and BDI1000VIS for the blue channel.

As the case for the CRISM cube FRT000099EE, there is also the CRISM IR spectral coverage. We performed the photometric and atmospheric corrections and consequently derived the mean spectra for seven ROIs, which are the same identified by the BDI1000VIS parameter in Fig. 6.49. The resulting spectra are presented in Fig. 6.54 and 6.55. As for the first cube, the spectral behavior presented here can be the explained by the presence of Magnetite on top of the selected ROIs, as the spectral trend between 1.0 and 2.0 μm shows.

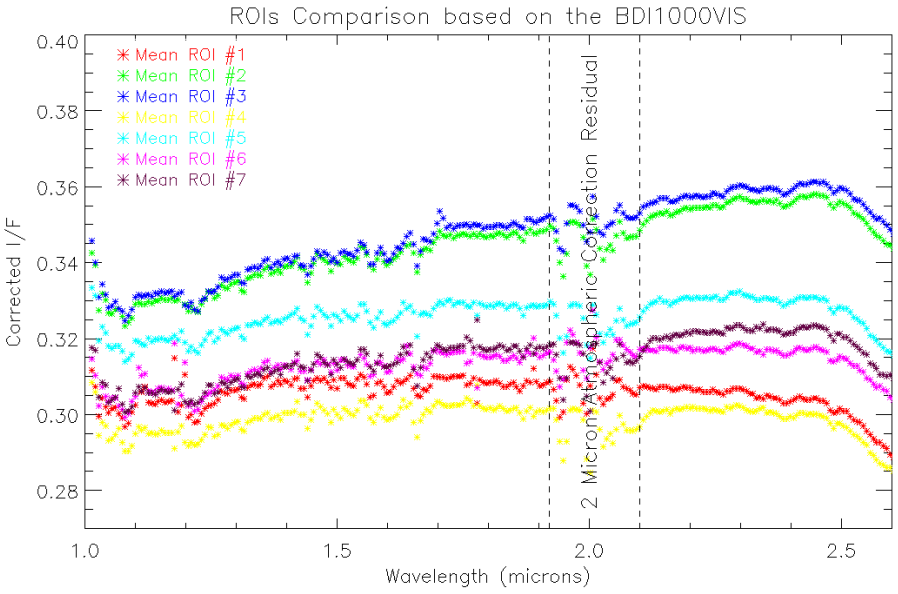

Figure 6.54: Mean ROIs surface spectra derived from CRISM IR cube using the ROIs identified through the BDI1000VIS Visible spectral parameter. Note that, as for the first three datacubes in the first area, some of the 2 μm atmospheric correction residual is still present.

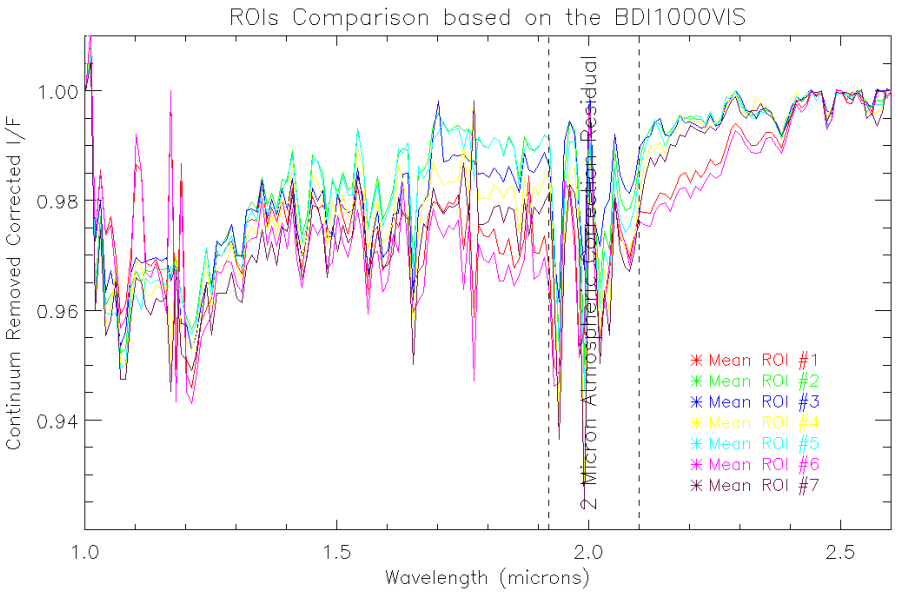

Figure 6.55: The same ROIs spectra, as presented in Fig. 6.54, but with the spectral continuum removed, as indicated in section 6.2.

A summary of the main mineralogical results

Despite the different geomorphological and hydrological origins which characterize the areas we have selected, we found two different mineralogical components on the Martian surfaces:

- on one side we identified minerals belonging to the igneous silicate family as the orthopyroxene, with different percentage of calcium and magnesium, then possibly olivine and also pyroxene. As above-mentioned, these rocks derives from the cooling and the solidification of magma whether below the surface (which then can resurface due to the erosion of the underlying layers), or on the surface itself;

- on the other side we found out a spread coverage of oxidized iron minerals, as magnetite, goethite and hematite, which derives from the weathering of the above-mentioned igneous rocks.

The identification of minerals formed through prolonged warm and wet environment, as one could expect from the morphology we showed in the paleoriverbeds and paleolakes chapters, has not been found. We did not recognize on the above spectra neither clay minerals nor sulfate minerals, which both would have required depositional and wet environments, as the one we suggested through our paleohydrological analysis.
There are several explanations that can likely justify the behavior we found.

First of all the CRISM instrument, as is the case for the OMEGA instrument, is a spectrometer that is remotely sensing only the first microns of the surface of the planet and derives the spectral behavior of these layers. As is the case of the three discovered paleolakes, hundreds of meters of sediments are expected on their floors, deposited by the ancient tributaries, but if on top of these thick layers a few-microns thin dust layer is superimposed, there is no way to derive the spectral signature of the sediments underneath[1]. Mars is a dusty and windy planet with frequent dust storms covering the surface, there is then no surprise if dusty material is found on the surface.
The analysis performed by NASA *Spirit Mars Exploration Rover* on Gusev crater indicated that most of the rocks, observed throughout the mission, contain a fine coating of dust, typically one millimeter thick (Christensen *et al.*, 2004), which covers all surfaces and was found to be magnetic (Gelbert *et al.*, 2004). Spirit demonstrated that magnetism was caused by the presence of great quantities of the mineral magnetite which is considered to be the main component of the Martian dust (Bertelsen *et al.*, 2004): this is the material which we found in the visible spectra on our analyzed areas. The typical mineralogical composition of the rocks laying on the plains of the Gusev crater is pyroxene, olivine, plagioclase and magnetite (McSween *et al.*, 2004; Arvidson *et al.*, 2004); these rocks have been very slightly altered by the presence of water despite their location, which is considered an ancient paleolake where the Ma'adim vallis was flowing in (Cabrol *et al.*, 2003; Irwin *et al.*, 2009). Spirit found the evidence of slight weathering on Gusev plains, but no direct evidence, as on the contrary was expected (Irwin *et al.*, 2004), that a lake was there. However it is believed that the Gusev

[1]This aspect is the reason why for the Mars Exploration Rovers (Squyres *et al.*, 2004a) and for the Mars Science Laboratory rover (Grotzinger *et al.*, 2012), it has been inserted, as a fundamental tool, a driller/brush to clean rocks and samples superficially, which are then mineralogically analyzed. The next step in the identification of hydrated and deposited minerals is the one undertaken by the European Space Agency, which foresees a Martian rover for the 2018, with capabilities to drill and collect samples down to a depth of two meters (Vincenzo *et al.*, 2008; Cabane, 2010; Vago *et al.*, 2010).

crater may have held a lake in the past, but it has since then been covered by igneous materials: this question remains still open. On the contrary, the NASA *Opportunity Mars Exploration Rover* on the Meridiani Planum, discovered spherules covering the surface of the interior of the crater where it landed, and it was indicated that these were hematite iron-rich concretions that formed inside deposits soaked with groundwater (Squyres *et al.*, 2004b; Soderblom *et al.*, 2004). This detailed analysis was possible thanks to the direct observation of the rover.

Nevertheless, thanks to the spatial and spectral resolutions reachable through remote sensing, specific sites, observed through the CRISM instrument, have indicated the presence of hydrothermal clay-carbonate as in Brown *et al.* (2010), or have demonstrated the presence of hydrated silicate-bearing outcrops as in Loizeau *et al.* (2012) or also have showed spectral signatures of hydrated silicate minerals as in Ehlmann *et al.* (2009b). This shows that the identification of hydrated-minerals locations on the surface of Mars is still open and accessible through orbiting satellites and can be extensively confirmed and widen through the *in situ* analysis.

As demonstrated by the Spirit rover, despite accepted geomorphological and hydrological proofs of a Martian past climate characterized by large quantities of water which formed the observed paleoriverbeds and paleolakes, there is a problematic lack of corresponding high quantities of hydrated minerals and carbonates on the Mars surface. This is the same aspect which we found out through our analysis.
A possible cover of successive volcanic extrusions, volcanic ashes or dust covering the surface, which we expect to be sediment layered from our hydrological analysis, can be the first explanation of the spectral behavior we find. It is also possible that the regions of interest we localized are too big (hundreds of meters) to identify small surface outcrops showing hydrated minerals and when getting the mean ROIs spectra we could have hidden their spectra. But the most accredited interpretation we give to our results is the fact that the only spectral matching may be not sufficient to identify possible mixtures of materials as it is expected on Mars, but only the main spectral overtones (remember the presence of small absorptions that is typically observed on our spectra). We then suggest that future deep spectral modeling could wide the mineralogical interpretation we give in this PhD Thesis, possibly identifying hydrated minerals on our above-mentioned plots.

Chapter 7

Summary and Conclusions

This PhD Thesis focused on three main topics: the Martian paleoriverbeds extraction and analysis; the identification of open paleolakes on the surface of the planet including the determination of their lacustrine parameters; and the identification of the main mineralogical components, through high-resolution reflectance spectra, of specific paleoriverbeds and paleolakes identified in the previous two sections.

The Martian Paleoriverbeds:
Through the use of the extraction methodology, 546 paleoriverbeds have been identified covering mainly the Aeolis and the Memnonia Mars quadrangles but also some sections of the Eridania and Phaethontis quadrangles. The area that we analyzed is 3600 km wide and 2000 km long and it is located between 0° and -38° S latitude and 156° E - 156° W longitude. Our region covers the "cliff" which connects the southern heavily cratered and rugged highlands to the northern smooth plains of Mars: on top of this elevation gradient an ancient hydrological activity incised the crust shaping the 546 paleoriverbed networks we identified.

The MOLA DEM allowed us to identify each riverbed network, while the high resolution HRSC imagery taken at different phase angles (in order not to be misguided by surface shades) was used for validation. Consequently, we measured not only the 3D length and 3D area, and hence the drainage density, but also the Strahler order for each drainage network and its frequency, deriving the bifurcation ratio R_B through Horton (1945) law of stream numbers. We then measured the mean length for each Strahler order, deriving the stream length ratio R_L through Horton (1945) law of stream lengths and the Shreve magnitude. We also measured the minimum and maximum elevation value for each drainage area and riverbed. The most important value we derived in our database consisted on the measurement of the slope distribution for each single drainage area and riverbed network, giving us the opportunity to make drainage area-slope, length-slope, drainage density-slope, Strahler order-slope and Shreve magnitude-slope plots.
We identified Mars paleoriverbeds showing several different hydrological regimes and we compared them with the Terrestrial analogues. We verified that they span from low slope rivers, presenting pools and incipient riffles, to step rivers and cascades, passing through the rapids regime.

The first main result we obtained through our detailed database derived from the global frequency distribution of the riverbed drainage density values: this histogram showed that the drainage density values span between 0.04 km^{-1} and 0.6 km^{-1} with

a peak around 0.12 km^{-1}, presenting a cumulative percentage which reaches the 94% at a value of 0.2 km^{-1}. Carr (1997) presented a paper on Martian drainage densities showing the results he derived, which were typically 2-3 orders of magnitude lower than typical Terrestrial densities as measured from Landsat 4 images. Within this work Carr (1997) indicated a table showing different drainage densities derived from a number of regions in the United States: Arizona, Nebraska, New York, Texas and Washington state. He underlined that the lowest drainage density value found on his Earth database was that on Nebraska with a value of 0.06 km^{-1}, while the maximum was in Washington state with a value of 0.209 km^{-1}. Hynek *et al.* (2003) found a value of drainage density of 0.06 km^{-1} in his first Mars riverbeds database, and the highest drainage density he derived in 2010 was 0.14 km^{-1} on an extended statistic of 82 217 riverbeds. The Carr (1997) 0.06 km^{-1} value was indicated as a Terrestrial reference in Hynek *et al.* (2010) Martian work. The above-mentioned result led Hynek *et al.* (2010) to affirm that their data were supporting some degree of surface runoff and, by inference, precipitation on Mars. It was also indicated that surface runoff was the simplest explanation for the integrated drainage basins, valley heads near the top of the divides and a drainage density comparable to Terrestrial values seen in the *Mars Global Surveyor* data. The values we obtained are hence extremely important because only 2.20% of our data, *i.e.* 12 paleoriverbeds, are below a drainage density of 0.06 km^{-1}, while the remaining 97.8% is bigger than that. Our data are similar to the maximum values derived by Hynek *et al.* (2010) and, as they state, such results are consistent with a warm and wet early climate responsible for the incision of the crust. "Early" can be used also in our case because our riverbeds lie mostly in the Noachian and Hesperian units (Tanaka *et al.*, 1986). Our drainage densities are comparable to low-end Terrestrial values and confirm Carr (1997); Hynek *et al.* (2003); Masson *et al.* (2004); Ansan *et al.* (2006); Hynek *et al.* (2010). We can consequently affirm that those valley network systems showing a drainage density above 0.06 km^{-1} are believed to reflect a substantial contribution of precipitation and subsequent surface runoff.

Our database is characterized by different paleoriverbeds that formed in totally different geomorphological regions: it is then difficult to make a global comparison between them, trying to derive a significant global fit. This would be like comparing the Amazon river and the Nile together with Alps riffles and cascades and trying to understand between such morphologically and geographically different riverbeds a common trend. In order to get meaningful trends between our hydromorphological variables, we then decided to select geographically close drainage areas and basins. This criterion originated from the assumption that the neighboring regions showing similar morphological variations and located at similar latitudes were likely characterized by similar weather and climatic conditions in the past. Hence, meaningful selections would help understanding the Martian paleohydrology by providing new insights of the climatic conditions at the time the water flows incised the crust.

Over the entire presented database we found out 25 different regions. Not all 546 riverbeds belong to these regions, but within the 25 selections that contain almost 200 riverbeds, close morphological behaviors were found. Two main selections, one located 176°30'0"W - 173°0'0"W longitude and 11°0'0"S - 14°0'0"S latitude and the other located 176°0'0"E - 178°50'0"E longitude and 16°20'0"S - 18°0'0"S latitude, were used as main references representing the remaining 23 selections. In the first area we identified 10 different riverbeds reaching a maximum Strahler order of 4 alimented by more than 130 riverbed tributaries characterized by a Strahler order of 1, 29 riverbeds with a Strahler order of 2 and 8 riverbeds with a Strahler order of 3. The drainage density found spans between 0.098 km^{-1} and 0.125 km^{-1}, while the drainage

area range found in this selection spans between 500 km^2 and 4 600 km^2; the total length of the drainage networks ranges between 80 and 520 km. The difference in elevation on this area is about 5 400 m. The slope versus drainage density plot presents an interesting behavior: the higher the slope of the terrain is, the higher the drainage density (which is a synonym of riverbed maturity) becomes. As presented in Yamaguchi *et al.* (2009), a systematic increase in the drainage density with the mean slope suggests that the maturity of the valley networks depends largely on the local slope: this is called topographic control on the drainage density. In Yamaguchi *et al.* (2009), it is suggested that only if water is supplied by precipitation at much the same rate, the mean slope of the precipitated area generally controls the velocity of the resultant surface runoff. This largely influences the efficiency of erosion and eventually determines the maturity of the drainage density. In other words such drainage density behavior could not be explained neither by having local water sources for the formation of the valley networks nor groundwater undermining the terrain and permitting collapses, because the hydraulic head on both cases does not necessarily depend on the mean slope. On the contrary, such topographic control should be considered as one important indicator that it was raining on Mars at the time these valleys formed.

When plotting the area versus length for the considered area we found that the higher the surficial area was, the bigger the total length of the riverbed network hosted in the drainage basin was. This behavior showed that an increasing length of a riverbed required an increasing drainage area dimension: this is another evidence that rainfall and surface runoff are likely responsible for the selected riverbeds. On the contrary, a sapping riverbed origin does not need any increase of the drainage discharge area along with the riverbed length, simply because it does not need to collect any water flows from the surroundings to be fed. This topographic control on the drainage density was found on 6 over the 25 selections we made.

When we apply the law of stream numbers and the law of stream lengths to our selected regions, we find that both the the bifurcation ratio, R_B, and the stream length ratio, R_L, fall well inside the Earth ranges, presenting a value of 4.973 for the R_B and a value of 1.923 for the R_L. Both values indicated that the area we were considering is globally hilly-mountainous, which is confirmed from the slope regime and the difference in elevations found in each drainage area.

The second area is 140 km long and 60 km wide. Within this terrain, 13 riverbeds incised the surface flowing into the main canyon, Ma'adim vallis, that once flowed inside the Gusev crater. This site presents a global topography with violent discrepancies in altitude due to the major cut of the Ma'adim canyon, and hence the principal hydrological regime for the considered riverbeds ranges from the Step/Cascades to Rapids, with just a small component of riffles and low slope riverbed sections. The maximum Strahler order measured on this area is 3. We have 50 riverbeds trunks with a Strahler order of 1 and 10 riverbeds characterized by a Strahler order of 2. The slope versus drainage density trend we found here is completely different from the one presented in the previous area: the lower the slope of the terrain the higher the drainage density becomes. This trend is similarly found in 19 of the 25 selections made, especially on terrains presenting a smaller global slope [with respect to this area]. In this case the drainage density versus slope behavior is explained by the fact that the lower the slope of the terrain, the higher the possibility for the river to start meandering is (and the higher the possibility for riverbed branches to connect), increasing the total length of the network with respect to the same drainage area. This is possible when no topographic control is affecting the drainage density; the same behavior is commonly observed on the Earth. The measured length for the selected riverbeds ranges from

small steep riverbeds around 5-10 km, to a bigger network of about 150 km, with areas ranging from 50 km^2 up to 1 000 km^2. Plotting the area versus slope a linear fit is evident. We should note that the linear fit of the second area is smaller: this means that the drainage area of the second region is smaller, as confirmed by the hydrological regime of highly sloping regions. Should rainfall and consequent surface runoff be the likely origin for these paleoriverbeds, a higher slope of the terrain implies a lower Strahler order degree. This is indeed the trend we observe: a maximum Strahler order 4 for the first region, and a maximum Strahler order of 3 for this one. The law of stream numbers and the law of stream lengths of this selection provide a bifurcation ratio and a stream length ratio that are slightly out of the Terrestrial ranges. This implies a particularly steep and mountainous morphology, with a high global slope, as shown in the drainage density slope plot.
The two cases just analyzed demonstrate that the slope measurements of both the drainage area and the riverbed network itself, were absolutely necessary to understand general trends and relations intervening between the measured parameters such as the drainage density, the Strahler order, the Shreve magnitude, the bifurcation ratio and the stream length ratio. Taking into account the topography of a terrain throughout the digital elevation model and computing the slope of the considered drainage areas, highly improves the understanding of the inter connections intervening among hydrological parameters. This results in the identification of new hints pointing towards climatic behavior of a past wet and humid Mars similar to the Earth today.

We subsequently plotted the histogram of the distribution of the maximum elevation peaks measured for each drainage area of our database. Thanks to the high resolution of the HRSC images (12.5 m), we had the opportunity to identify the beginning of the channelization process, *i.e.* the point on the surface where the riverbed network started to appear, on each riverbed network. We derived 546 channelization locations, one for each basin, and we plotted an histogram similar to the one for the maximum areas elevation. Both histograms have a similar extent around 4 000 meters as also confirmed by the same trend of the cumulative distribution. The only difference between the two distributions consists in a shift of about 400 meters in elevation. In order to understand this difference, we plotted the histogram representing the distribution of the distances between the maximum elevation peaks of the drainage areas, *i.e.* the drainage divides, and the channelization points identified through the HRSC images. Indeed, we tried to understand if there was a specific elevation distance from the drainage divides, where the channelization processes started. We obtained a non random distribution with a median at 362 m, and a mean at 444 m. The 75% of our database lies below 552 m, while the tail of the distribution reaches up to 2 300 m. If had obtained a random distribution, it would support the fortuity of the sapping processes, which can happen at whatever elevation value far from the peaks of the drainage areas.
Groundwater sapping is a process of lateral exit of the water from a bank or hillslope, as it seeps and springs and erodes soil from the slope. This typically happens when the groundwater, pressurized by the gravity, encounters an underlying impermeable layer of soil and it is then forced to found a lateral or an overlying path to exit. When the water table, *i.e.* the boundary surface between the unsaturated zone and the water-saturated zone, encounters the surface terrain, we have a sapping process. Sapping is independent from the elevation distance from the drainage divides, and it appears at whatever altitude, because it does not need a collection area as the surface runoff. Instead, what we obtained from our analysis is that an elevation distance of about 450 meters is typically required in order for the channelization process to happen and been visible from the high-resolution images. This can be considered as a direct evidence

that on the considered Mars region it has been raining and consequently there was surface runoff at the time these paleoriverbeds incised the terrain. This major result, together with the drainage density values previously presented, strongly point towards a wet and humid climate on Mars characterized by an active water cycle.

We also derived and plotted the distribution of all 546 outlet elevations. Through the HRSC 12.5 m resolution images, we identified the location of the deltas and/or outlets of our paleoriverbeds and we measured the elevation of all identified outlets through the MOLA DEM. Finally, we plotted the histogram of their frequency versus the measured altitude. Our goal was the identification of a possible sea/ocean coastline stopping the further development of riverbeds flowing into it. We found out that the outlet elevation distribution ranges between -2 600 m and 2 000 m; between -1 350 m and 1 000 m we notice a random distribution of the outlet elevations, but at exactly -1 357 m we find a discontinuty; above 1 500 m we have a fast cut off. 447 outlet elevations, i.e. the 81.87%, are higher than -1 357 m, while 99 outlet elevations, i.e. the 18.13%, are lower than -1 357 m, going to zero at an elevations ranging between -2 550 and -2 600 m.

We compared our results with the work of Di Achille *et al.* (2010), who postulate the presence of an ancient northern ocean on Mars supported by the global distribution of deltas and valleys. They propose the elevation level of -2 540 $\pm$ 177 m as the one of the putative ocean covering the entire northern Martian hemisphere. To derive this measure, Di Achille *et al.* (2010) focused entirely on the elevation of 52 deltaic deposits and the valleys database presented by Hynek *et al.* (2010). Through our statistics, we can actually confirm that less then 0.5% riverbeds present an outlet elevation which is lower than -2 540 m, in apparent agreement with Di Achille *et al.* (2010). However, our data is showing something more: the peak located at -1 350 m could identify a possible higher ocean level, probably older then the one identified by Di Achille *et al.* (2010). Our proposed explanation is that the ancient ocean could have experienced different phases of evolution and evaporation, and hence different coastline elevation values with consequent different riverbed outlets elevations, alternated by stability periods. This idea could be justified in terms of wobbling of the Mars axis as presented by Laskar (2005, 2008). He calculated a possible Mars obliquity oscillation from 25 to 45 degrees only in the past 10-5 Myr. Whatever the ocean level was, a completely different atmosphere with a higher pressure and temperature is required to justify the stable presence of an ocean on the surface of Mars. This analysis, completely different with respect to the previous chapters shows another important evidence of a wetter and more humid Mars, characterized by a water cycle recharging rivers, lakes, seas and oceans.

The Martian Paleolakes:

In the course of our assessment of the Martian riverbeds we bumped on a number of ancient open paleolakes hosted by impact craters, presenting tributaries and outlets cutting their rims.

We focused our attention to three specific paleolakes, two connected through a complex drainage network, and located at 9°34'00"S - 167°11'00"W and at 10°12'00"S - 165°38'00"W, respectively, the third one located at 17°32'00"S - 171°19'00"E in the Durius Vallis region.

In order to carry out a thorough and accurate comparisons between Martian and Terrestrial lakes and/or paleolakes, we managed to derive multiple lacustrine parameters: the ancient water level, W_L, derived from the elevation value of the outlet riverbed, the lake surface, A_0, computed at the W_L, the 3D area, A_{3D}, of the paleolake basin hosted

by the impact crater and the water volume, W_V.
We also obtained: the mean elevation of the paleolake floor, $\bar{Z}$ that corresponds to the mean elevation of the crater floor, the water mean depth $W_{\bar{D}}$, the lake minimum elevation z_{min}, equal to the crater minimum elevation, the mean elevation of the crater rim and its radius, essential to compute the sediment thickness range and the sediment thickness range itself, derived from the depth (d) − diameter (D) relationship, $d = 0.36D^{0.49}$, obtained by Garvin *et al.* (1998, 2000, 2003).
We then computed the relative depth, Z_R, which is the ratio of the minimum elevation of the lake z_{min} in kilometers, as a percentage of the mean diameter of the lake at the surface (Hutchinson, 1957; Wetzel *et al.*, 1991); the shoreline length, S_L, the shoreline development, D_L, which is the ratio of S_L to the length of the circumference of a circle of area A_C equal to A_0 (Hutchinson, 1957) and the volume development, D_V, that is a measure of departure of the shape of the lake basin from that of a cone (Hutchinson, 1957).

The three considered paleolakes present different morphological characteristics: the first one, called paleolake I, is hosted by a crater with a radius that ranges between 9.57 km and 11.39 km, its identified water level is located at an elevation of -1 409 m and the 2D measured surface is 164.7 km^2. The shoreline length is 59.75 km, while the expected sediment thickness range is 850 - 990 m. The second one, called paleolake II, belongs to the same hydrological system, it is hosted by a crater with a radius that ranges between 41.31 km and 49.70 km, its identified water level is located at an elevation of -1 420 m and the 2D measured surface is 4 734.6 km^2. The shoreline length is 305.84 km, while the expected sediment thickness range is 2 190 - 2 490 m. The last one, paleolake III, is characterized by morphological values which place it in the middle between the two previous cases: it is hosted by a crater with a radius that ranges between 21.90 km and 29.70 km, its identified water level is located at an elevation of -646 m and the 2D measured surface is 1 564.0 km^2. The shoreline length is 177.58 km, while the expected sediment thickness range is 1 506 - 1 873 m.
Both the shoreline development and the volume development values for the three considered paleolakes, show that they are close to the values characterizing the Crater Lake in Oregon (Hutchinson, 1957), which approaches the circular shape typical of impact meteor craters.
Despite the different dimensions, we made a comparison between them by computing the hypsographic curves of the three paleolakes. Hypsographic curves are plots of stratum surface area versus depth. Representing these curves as the percent of the total lake volume lying above a particular percentage depth, we single out the sediment thickness differences among various paleolakes. We measured the 2D surface area at different paleolake depths, with a step of 10 meters starting from the surface water level: from 0 to -150 m for paleolake I, from 0 to -390 m for paleolake II and from 0 to -530 m for paleolake III. By plotting the percent of the surface area lying above a particular percent depth, we created a meaningful method to compare the degree of sediment filling for each paleolake. From the study of the hypsograhic curves it is immediately noticeable that paleolake I filling trend is totally different than that of paleolakes II and III, which appear to behave more similarly. In fact, paleolake I reaches an area value of 50% when the depth is 50%, while paleolakes II and III show that a percentage area of 50% is only reached at a depth of 76-78%. A trend change between concavity and convexity appears on paleolake II and III only when the percent area is less than 5%.
The meaning of the presented hypsographic curves relates to the sedimentary maturity degree of the paleolake floor. The absolute value of sediment thickness range would indicate that the paleolake which is "more" filled is the second one, but if we consider

what the hypsometric plot shows, we see that the paleolake I floor has undergone a more mature sedimentation with respect to the dimension of the crater hosting the paleolake. The quantity of sediments layered on paleolakes II and III floors show that a percent area of 80% is only reached at a depth of 55%, while for paleolake I is at a depth of 25%. As from Schon *et al.* (2012), the impact crater shape is related to its depth by the Garvin *et al.* (2003) depth-diameter relationship, unless it is a complex crater formed on another existing crater or prominent cliff (Garvin *et al.*, 1998, 2000, 2003). Craters I, II and III are regular craters and hence what we would expect for the craters hosting paleolakes II and III is that if they could have reached the same degree of sediment maturity of paleolake I, the plots' trend would have followed more closely paleolake I trend. Nevertheless the sediments filling would have reached a bigger value reaching a higher elevation towards the crater's rim.

The mineralogical analysis:
We selected two main areas of interest where to perform our mineralogical analysis. The first region is located 170°00'00"W - 164°00'00"W and 7°00'00"S - 11°00'00"S and it is centered on the complex hydrological network where the paleolakes I and II were found, while the second one spans from 169°54'E - 170°60'E and 16°57'S in longitude and 17°18'S in latitude. This second region is located inside the Durius Vallis drainage basin and contains the crater which hosts the paleolake III. The instrument used to perform our mineralogical studies is the hyper spectral camera CRISM. This camera onboard the NASA *Mars Reconnaissance Orbiter* provides multiband hypercubes with a spatial resolution of 15-19 m covering the wavelength range between 0.36 and 3.92 μm. One of the main goal of this instrument is mapping and characterizing the composition, geology and stratigraphy of surface deposits, which has been the aim of this last section of this work. Within the near-UV, the Visible and the IR wavelength range the detection of several mineralogical components was possible. On top of the two above-mentioned areas of interest we identified six different hypercubes covering three paleolake floors, a tributary and outlet, two riverbeds' valleys and one crater's rim.

Besides the different geomorphological and hydrological origins which characterize the selected areas, we found two different mineralogical components on the Martian surfaces. On one side we identified minerals belonging to the igneous silicate family as the orthopyroxene and likely olivine and also pyroxene, which are rocks which typically derives from the cooling and the solidification of magma whether below the surface or on the surface itself. On the other side we found out a widespread coverage of oxidized iron minerals, as magnetite, goethite and hematite, that derive from the weathering of the above-mentioned igneous rocks.
The identification of minerals formed through prolonged warm and wet environment, as one could expect from the morphology we studied in the paleoriverbeds and paleolakes chapters, has not been found. The above spectra show neither clay minerals nor sulfate minerals, both requiring depositional and wet environments.
There are several explanations that can justify these findings. The first one is that the CRISM instrument is a spectrometer that is remotely sensing only the first microns of the surface of the planet and derives the spectral behavior of these layers. As is the case of the three discovered paleolakes, hundreds of meters of sediments are expected on their floors, deposited by the ancient tributaries, but if on top of these thick layers a few-microns thin dust layer is superimposed, there is no way to derive the spectral signature of the sediments underneath unless outcrops and veins emerge.

The analysis performed by the NASA *Spirit Mars Exploration Rover* on Gusev

crater confirms this behavior, indicating that most of the rocks observed throughout the mission contain a fine coating of magnetic dust (Gelbert *et al.*, 2004), typically one millimeter thick (Christensen *et al.*, 2004), which covers all surfaces. Spirit demonstrated that the magnetic dust originates from the great quantities of the mineral magnetite present on the surface of Mars (Bertelsen *et al.*, 2004).

Mars is a dusty and windy planet with periodic dust storms; so there is no surprise if dusty material is then found almost everywhere on the surface.
The typical mineralogical composition of the rocks laying on the plains of the Gusev crater is pyroxene, olivine, plagioclase and magnetite (McSween *et al.*, 2004; Arvidson *et al.*, 2004). These minerals have been only very slightly altered by the presence of water despite their location, which is considered an ancient paleolake where the Ma'adim vallis was flowing in (Cabrol *et al.*, 2003; Irwin *et al.*, 2009). Spirit found the evidence of slight weathering on Gusev plains, but not at the expected levels (Irwin *et al.*, 2004). It is believed that the Gusev crater may have held a lake in the past, but since then igneous materials have covered it. This is an open question that requires further investigations.
Nevertheless, thanks to the spatial and spectral resolutions reachable through remote sensing, specific sites, observed through the CRISM instrument, have shown the presence of hydrothermal clay-carbonate (Brown *et al.*, 2010), of hydrated silicate-bearing outcrops (Loizeau *et al.*, 2012), or hydrated silicate minerals (Ehlmann *et al.*, 2009b). This shows that the identification of hydrated-minerals locations on the surface of Mars is still open and accessible through orbiting satellites and can be extensively confirmed and widen through the *in situ* analysis.
A possible cover of successive volcanic extrusions, volcanic ashes or dust covering the surface can be the first explanation of the spectral behavior we find. It is also possible that the studied regions are too wide (hundreds of meters) to allow the identification of small surface outcrops of hydrated minerals. Moreover, when getting the mean ROIs spectra we could have hidden their spectra. The most plausible interpretation of our results is that a simple spectral matching may be not sufficient to identify possible mixtures of materials but only the main spectral overtones.

Through this work, we have acquired numerous and important evidences that the early Mars was characterized by a dense Earth-like atmosphere capable of sustaining a wet and humid climate with abundant rainfalls and accumulation of liquid water on its surface. The presence of the rainfall for several millions years at least is a requirement to justify the crust incisions still observable today. It appears likely that the amount of liquid water on the surface of Mars was sufficient to sustain the formation of a large number of rivers, lakes and seas possibly covering a large part of the northern hemisphere. Nevertheless, as demonstrated by the *Spirit* rover, despite accepted geomorphological and hydrological proofs of a Martian past climate characterized by large quantities of water, there is a problematic lack of corresponding high quantities of hydrated minerals and carbonates on the Mars surface. A planet-wide volcanism that survived for more than 2/3 of the geologic life of the Mars, transport of large quantities of volcanic ashes, acide rains and periodic dust storms have contributed over more that 2.5 billion of years to hide or transform the surficial mineralogy of the planet.
We strongly think that the answer to this fundamental question can be found by exploring the sub-surface at depth larger than one meter. More hints towards this direction will be therefore given by the future 2018 ESA *Exomars* mission, which is supposed to drill and collect samples beneath the surface at a depth of two meters, while the 2016 orbiting mission can provide further evidence on the past climate of Mars.

Appendix A

Refereed Published Articles

This Appendix A contains the refereed published articles where Maurizio Pajola have worked on and published during the 3 PhD years (2011-2013).

A.1 Phobos as a D-type Captured Asteroid, Spectral Modeling from 0.25 to 4.0 μm

The Astrophysical Journal, Volume 777, Issue 2, article id. 127, 6 pp. (2013).
Authors: **M. Pajola**, M. Lazzarin, C. M. Dalle Ore, D. P. Cruikshank, T. L. Roush, S. Magrin, I. Bertini, F. La Forgia, and C. Barbieri.

This paper describes the spectral modeling of the surface of Phobos in the wavelength range between 0.25 and 4.0 μm. We use complementary data to cover this spectral range: the OSIRIS (Optical, Spectroscopic, and Infrared Remote Imaging System on board the ESA *Rosetta* spacecraft) reflectance spectrum that Pajola *et al.* merged with the VSK-KRFM-ISM (Videospectrometric Camera (VSK)-Combined Radiometer and Photometer for Mars (KRFM)-Imaging Spectrometer for Mars (ISM) on board the USSR *Phobos 2* spacecraft) spectra by Murchie & Erard and the IRTF (NASA Infrared Telescope Facility, Hawaii, USA) spectra published by Rivkin *et al.* The OSIRIS data allow the characterization of an area of Phobos covering from 86.°8 N to 90° S in latitude and from 126° W to 286° W in longitude. This corresponds chiefly to the trailing hemisphere, but with a small sampling of the leading hemisphere as well. We compared the OSIRIS results with the Trojan D-type asteroid 624 Hektor and show that the overall slope and curvature of the two bodies over the common wavelength range are very similar. This favors Phobos being a captured D-type asteroid as previously suggested. We modeled the OSIRIS data using two models, the first one with a composition that includes organic carbonaceous material, serpentine, olivine, and basalt glass, and the second one consisting of Tagish Lake meteorite and magnesium-rich pyroxene glass. The results of these models were extended to longer wavelengths to compare the VSK-KRFM-ISM and IRTF data. The overall shape of the second model spectrum between 0.25 and 4.0 μm shows curvature and an albedo level that match both the OSIRIS and Murchie & Erard data and the Rivkin *et al.* data much better than the first model. The large interval fit is encouraging and adds weight to this model, making it our most promising fit for Phobos. Since Tagish Lake is commonly used as a

spectral analog for D-type asteroids, this provides additional support for compositional similarities between Phobos and D-type asteroids.

A.2 Spectrophotometric investigation of Phobos with the Rosetta OSIRIS-NAC camera and implications for its collisional capture

Monthly Notices of the Royal Astronomical Society, Volume 427, Issue 4, pp. 3230-3243. (2012).
Authors: **M. Pajola**, M. Lazzarin, I. Bertini, F. Marzari, D. Turrini, S. Magrin, F. La Forgia, N. Thomas, M. Kueppers, R. Moissl, F. Ferri, C. Barbieri, H. Rickman, H. Sierks and the OSIRIS Team.

The Martian satellite Phobos has been observed on 2007 February 24 and 25, during the pre- and post-Mars closest approach (CA) of the ESA *Rosetta* spacecraft Mars swing-by. The goal of the observations was the determination of the surface composition of different areas of Phobos, in order to obtain new clues regarding its nature and origin. Near-ultraviolet, visible and near-infrared (263.5-992.0 nm) images of Phobos's surface were acquired using the Narrow Angle Camera of the OSIRIS instrument onboard Rosetta. The six multi-wavelength sets of observations allowed a spectrophotometric characterization of different areas of the satellite, belonging respectively to the leading and trailing hemisphere of the anti-Mars hemisphere, and also of a section of its sub-Mars hemisphere. The pre-CA spectrophotometric data obtained with a phase angle of 19° have a spectral trend consistent within the error bars with those of unresolved/disc-integrated measurements present in the literature. In addition, we detect an absorption band centred at 950 nm, which is consistent with the presence of pyroxene. The post-CA observations cover from NUV to NIR a portion of the surface (0° to 43°E of longitude) never studied before. The reflectance measured on our data does not fit with the previous spectrophotometry above 650 nm. This difference can be due to two reasons. First, the OSIRIS observed area in this observation phase is completely different with respect to the other local specific spectra and hence the spectrum may be different. Secondly, due to the totally different observation geometry (the phase angle ranges from 137° to 140°), the differences of spectral slope can be due to phase reddening. The comparison of our reflectance spectra, both pre- and post-CA, with those of D-type asteroids shows that the spectra of Phobos are all redder than the mean D-type spectrum, but within the spectral dispersion of other D-types. To complement this result, we performed an investigation of the conditions needed to collisionally capture Phobos in a way similar to that proposed for the irregular satellites of the giant planets. Once put in the context of the current understanding of the evolution of the early Solar system, the coupled observational and dynamical results we obtained strongly argue for an early capture of Phobos, likely immediately after the formation of Mars.

A.3 Geological map and stratigraphy of asteroid 21 Lutetia

Planetary and Space Science, Volume 66, Issue 1, p. 125-136. (2012).
Authors: M. Massironi, S. Marchi, **M. Pajola**, C. Snodgrass, N. Thomas, C. Tubiana, J. B. Vincent, G. Cremonese, V. Da Deppo, F. Ferri, S. Magrin, H. Sierks, C. Barbieri, P. Lamy, H. Rickman, R. Rodrigo, D. Koschny, The OSIRIS team.

The OSIRIS (Optical, Spectroscopic, and Infrared Remote Imaging System) images acquired during the recent *Rosetta* fly-by of Lutetia (10th of July 2010), enabled us to unravel the long geological history of the asteroid. This is recorded on its highly varied surface which displays geological units of disparate ages. In particular, using images of the closest approach, five main regions (in turn subdivided into minor units) have been discriminated on the basis of crater density, overlapping and cross-cutting relationships, and presence of linear features (*i.e.*, fractures, faults, grooves, troughs). Other regions, with still unclear stratigraphic position, were also recognized on images of lower resolution on the bases of geomorphological properties such as crater density, relationship with scarp and ridges, and sharp morphological boundaries. In this work the geological evolution of Lutetia surface is reconstructed through the description of its main units and related contacts. The oldest regions imaged during the closest approach (Achaia and Noricum) are pervasively affected by fractures and grooves and display surfaces so heavily cratered to be dated back to a period not far from the Late Heavy Bombardment (yielding Achaia a crater retention age of 3.6-3.7 Ga). A crater of 55 km diameter, named Massilia and corresponding to the Narbonensis region, cuts both Achaia and Noricum regions and probably represents the most prominent event of the Lutetia history. The considerable crater density on its floor and walls, the absence of discernable deposits related to the impact event, and the intense deformation of it floor - all attest to its relatively great age. The North Polar Cluster (Baetica region) is associated with smooth ejecta broadly mantling the surrounding units and displays few craters and no linear features, demonstrating its relatively young age (estimated at less than 300 Ma). The North Polar Crater Cluster is the product of superimposed impacts; the last one of 24 km of diameter excavated the pre-existing ejecta up to the bedrock which locally outcrops at the crater rim. The ejecta of this last impact were involved in several gravitational phenomena testified by the great variety of deposits made up of mega-boulders diamictons, fine materials, gravitational taluses and debris, and landslide accumulations. A part from the big cratering events generating Massilia and the North Polar Crater Cluster, the Lutetia geological history is also punctuated by minor events still recorded by its stratigraphic record well imaged by the closest approach data.

A.4 Search for satellites near (21) Lutetia using OSIRIS Rosetta images

Planetary and Space Science, Volume 66, Issue 1, p. 64-70. (2012).
Authors: I. Bertini, W. Sabolo, P. J. Gutierrez, F. Marzari, C. Snodgrass, C. Tubiana, R. Moissl, **M. Pajola**, S. C. Lowry, C. Barbieri, F. Ferri, B. Davidsson, H. Sierks,The OSIRIS Team.

On 2010 July 10 the ESA *Rosetta* mission flew by the large asteroid (21) Lutetia. One of the scientific goals of the onboard OSIRIS instrument was the search for satellites of the asteroid, with more than 20 images specifically dedicated to this topic. An observational campaign was devised with a selection of filters and exposure times tailored to maximize the possibility of detecting small companions and determining their bound orbits. Data were analyzed with suitable methods to remove cosmic ray hits and known background objects, in order to search for persistent detections of potential interesting flux sources. We found no unambiguous detections of a satellite larger than 160 m inside the entire sphere of gravitational influence. Our search confirmed the absence of bound companions larger than 30 m inside 20 primary radii. These limits are a factor of 30 smaller than the values reported so far from large ground-based telescopes using adaptive optics and from the Hubble Space Telescope.

A.5 (21) Lutetia spectrophotometry from Rosetta OSIRIS images and comparison to ground-based observations

Planetary and Space Science, Volume 66, Issue 1, p. 43-53. (2012).
Authors: S. Magrin, F. La Forgia, **M. Pajola**, M. Lazzarin, M. Massironi, F. Ferri, V. Da Deppo, C. Barbieri, H. Sierks, The OSIRIS Team.

Here we present some preliminary results on surface variegation found on (21) Lutetia from *Rosetta*-OSIRIS images acquired on 2010-07-10. The spectrophotometry obtained by means of the two cameras NAC and WAC (Narrow and Wide Angle Cameras) is consistent with ground based observations, and does not show surface diversity above the data error bars. The blue and UV images (shortward 500 nm) may, however, indicate a variegation of the optical properties of the asteroid surface on the Baetica region (Sierks *et al.*, 2011). We also speculate on the contribution due to different illumination and to different ground properties (composition or, more probably, grain size diversity). In particular a correlation with geologic units independently defined by Massironi *et al.* (2012) is evident, suggesting that the variegation of the ground optical properties is likely to be real.

Bibliography

Aharonson, O., et al. 2002, *Drainage basins and channel incision on Mars*, Proc. National Academy of Science, Vol. 99, pp. 1780-1783.

Ansan, V., et al. 2006, *New observations of Warrego Valles, Mars: Evidence for precipitation and surface runoff*, Planet. Space Sci., Vol. 54, pp. 219-242.

Ansan, V., et al. 2008, *Topography of valley networks on Mars from Mars Express High Resolution Stereo Camera digital elevation models*, JGR, Vol. 113, pp. 7006-7036.

Arvidson, R. E., et al. 2004, *Localization and physical properties experiments conducted by Spirit at Gusev Crater*, Science, Vol. 305, pp. 821-824.

Baker, V. R., et al. 1974, *Erosion by catastrophic floods on Mars and Earth*, Icarus Vol. 23, pp. 27-41.

Baker, V. R., et al. 1985, *Models of fluvial activity on Mars*, Models in Geomorphology, edited by M. Woldenberg et al., pp. 287 - 312, Allen and Unwin, Boston, Mass.

Batson, R. M., et al. 1979, *Atlas of Mars: the 1:5,000,000 map series*, Federal Government Series: NASA SP - 438.

Bertelsen, P., et al. 2004, *Magnetic Properties on the Mars Exploration Rover Spirit at Gusev Crater*, Science, Vol. 305, pp. 827-829.

Bibring, J. P., et al. 2004, *OMEGA: Observatoire pour la Mineralogie, l'Eau, les Glaces et l'Activité*, In: Mars Express: the scientific payload. Ed. by Andrew Wilson, scientific coordination: Agustin Chicarro. ESA SP-1240, Noordwijk, Netherlands: ESA Publications Division, ISBN 92-9092-556-6, 2004, pp. 37 - 49.

Bishop, J. L., et al. 2008, *Phyllosilicate Diversity Observed by CRISM in Mawrth Vallis: Identification of Nontronite, Montmorillonite, Kaolinite, and Hydrated Silica*, In: 39th Lunar and Planetary Science Conference, (Lunar and Planetary Science XXXIX), held March 10-14, 2008 in League City, Texas. LPI Contribution No. 1391., pp. 2124

Brown, A.J., et al. 2010, *Hydrothermal formation of Clay-Carbonate alteration assemblages in the Nili Fossae region of Mars*, EPSL Vol. 297, pp. 174-182.

Cabane, M., 2010, *Mars Science Laboratory (MSL) and the future missions to Mars*, Highlights of Astronomy, Vol. 15, p. 710-711.

Cabrol, N.A., et al. 1999, *Distribution, classification, and ages of Martian impact crater lakes*, Icarus Vol. 142, pp. 160-172.

Cabrol, N.A., et al. 2001, *The evolution of lacustrine environments on Mars: Is Mars only hydrologically dormant?*, Icarus Vol. 149, pp. 291-328.

Cabrol, N.A., et al. 2003, *Exploring Gusev Crater with Spirit: Review of science objectives and testable hypotheses*, JGR, Vol. 108, E12.

Carr, M. H., et al. 1981, *Martian channels and valleys: their characteristics, distribution, and age*, Icarus, Vol. 48, pp. 91-117.

Carr, M. H. (1995), *The Martian drainage system and the origin of valley networks and fretted channels*, JGR, Vol. 100, pp. 7479-7507.

Carr, M. H. (1997), *Martian drainage densities*, JGR, Vol. 102, E4, pp. 9145-9152.

Carr, M. H. (1999), *Retention of an atmosphere on early Mars*, JGR, Vol. 104, pp. 21897-21909.

Carr, M. H. (2006), *The Surface of Mars*, Cambridge University Press, 2006.

Carter, J., et al. 2013, *Hydrous minerals on Mars as seen by the CRISM and OMEGA imaging spectrometers: Updated global view*, JGR, Vol. 118, Issue 4, pp. 831-858.

Christensen, P. R., et al. 2003, *Morphology and composition of the surface of Mars: Mars Odyssey THEMIS results*, Science, Vol. 300, pp. 2056-2061.

Christensen, P. R., et al. 2004, *Initial Results from the Mini-TES Experiment in Gusev Crater from the Spirit Rover*, Science, Vol. 305, pp. 837-842.

Clark , R. N., 1999, *Spectroscopy of Rocks and Minerals, and Principles of Spectroscopy*, derived from Chapter 1 in: Manual of Remote Sensing John Wiley and Sons, Inc A. Rencz, Editor New York 1999 .

Craddock, R. A., et al. 2002, *The case for rainfall on a warm, wet early Mars*, JGR, Vol. 107, Issue E11, pp. 21-1.

Davies, M. E., et al. 1992, *Geodesy and Cartography*, Eds. Mars. University of Arizona Press: Tucson, 1992.

De Hon, R.A., 1992. *Martian lake basins and lacustrine plains*, Earth Moon Planets 56, 95-122.

Di Achille, G., et al. 2010, *Ancient ocean on Mars supported by global distribution of deltas and valleys*, Nature Geoscience, Vol. 3, pp. 459-463.

Ehlmann, B. L., et al. 2009, *Detection of Serpentine on Mars by MRO-CRISM and Possible Relationship with Olivine and Magnesium Carbonate in Nili Fossae*, 40th Lunar and Planetary Science Conference, (Lunar and Planetary Science XL), held March 23-27, 2009 in The Woodlands, Texas, id.1787

Ehlmann, B. L., et al. 2009, *Identification of hydrated silicate minerals on Mars using MRO-CRISM: Geologic context near Nili Fossae and implications for aqueous alteration*, JGR, Vol. 114, E00D08

Fairbridge, R. W., 1968, *Playfair's law*, Geomorphology Encyclopedia of Earth Science 1968, pp. 871-872.

Fasset, C. I., et al. 2008a, *The timing of Martian valley network activity: Constraints from buffered crater counting*, Icarus Vol. 195, pp. 61-89.

Fassett, C. I., et al. 2008b, *Valley network-fed, open-basin lakes on Mars: Distribution and implications for Noachian surface and subsurface hydrology*, Icarus, Vol 198, pp. 37-56.

Fraeman, A. A., et al. 2012, *Analysis of disk-resolved OMEGA and CRISM spectral observations of Phobos and Deimos*, JGR, Vol 117, E00J15.

Garvin, J. B., et al. 1998, *Geometric properties of Martian impact craters: Preliminary results from the Mars Orbiter Laser Altimeter*, Geophysical Research Letters, Vol. 25, Issue 24, pp. 4405-4408

Garvin, J. B., et al. 2000, *North Polar Region Crater-forms on Mars: Geometric Characteristics from the Mars Orbiter Laser Altimeter*, Icarus, Vol. 144, pp. 329- 352.

Garvin, J. B., et al. 2003, *Craters on Mars: global geometric properties from ridde MOLA topography*, Sixth International Conference on Mars (2003), pp. 3277.

Gelbert, R., et al. 2004, *Chemistry of Rocks and Soils in Gusev Crater from the Alpha Particle X-ray Spectrometer*, Science, Vol 305, pp. 829-832.

Goldspiel, J. M., et al. 1991, *Ancient aqueous sedimentation on Mars*, Icarus Vol. 89, pp. 392-410.

Grant, J. A. (2011), *A lake in Uzboi Vallis and implications for Late Noachian-Early Hesperian climate on Mars*, Icarus, Vol. 212, pp. 110-122.

Greeley, R. (1987), *Release of juvenile water on Mars: estimated amounts and timing associated with volcanism*, Science, Vol. 236, pp. 1653-1654.

Grotzinger, J. P. (2012), *Mars Science Laboratory Mission and Science Investigation*, Space Science Reviews, Vol. 170, Issue 1-4, pp. 5-564.

Hartmann, W. K. (2001), *Cratering Chronology and the Evolution of Mars*, Space Science Reviews, Vol 96, pp. 165–194.

Hynek, B. M., et al. 2001, *Evidence of extensive denudation of the Martian highlands*, Geology, Vol. 29, pp 407-410.

Hynek, B. M., et al. 2003, *New data reveal mature, integrated drainage systems on Mars indicative of past precipitation*, LPS XXXIV, 2003.

Hynek, B. M., et al. 2010, *Updated global map of Martian valley networks and implications for climate and hydrologic processes*, JGR, Vol 115, pp. 9008.

Hoke, M. R. T., et al. 2009, *Roaming zones of precipitation on ancient Mars as recorded in valley networks*, JGR, Vol. 114, pp. E08002.

Horton, R. E. (1945), *Erosional development of streams and their drainage basins; hydrophysical approach to quantitative morphology*, Bulletin of Geological Society of America, Vol. 56, pp. 275-370.

Hutchinson, G.E. 1957. *A treatise on limnology* v.1. Geography, Physics and Chemistry. Wiley. 1015pp.

Irwin, R. P., et al. 2004, *Geomorphology and hydraulics of Ma'adim Vallis, Mars, during a noachian/hesperian boundary paleoflood*, LPSC XXXV, Abstract 1852.

Irwin, R. P., et al. 2009, *Geomorphology of Ma'adim Vallis, Mars, and associated paleolake basins*, JGR, Vol. 109, E12009.

Jain, N. (2013), *Study of Carbonates, Hydrous Sulfates and Phyllosilicates from the Capri Chasma Region of Valles Marineris on Mars Based on MRO-CRISM Observations*, 44th Lunar and Planetary Science Conference, held March 18-22, 2013 in The Woodlands, Texas. LPI Contribution No. 1719, pp. 1388.

Jaumann, R. (2005), *Martian valley networks and associated fluvial features as seen by the Mars Express High Resolution Camera (HRSC)*, LPSC XXXVI, Abstract 1815.

Jenson, S. K. (1988), *Extracting Topographic Structure from Digital Elevation Data for Geographic Information System Analysis*, Photogrammetric Engineering and Remote Sensing, Vol. 54, pp. 1593-1600.

Laskar, J., 2005, *Chaotic Evolution of the Rotational and Orbital Elements of Mars*, American Geophysical Union, Fall Meeting 2005, Abstract P31B-020.

Laskar, J., 2008, *Chaotic diffusion in the Solar System*, Icarus, Vol. 196, pp. 1-15.

Loizeau, D., et al. 2012, *Characterisation of hydrated silicate-bearing outcrops in Tyrrhena Terra, Mars: Implications to the alteration history of Mars*, Icarus, Vol. 219, pp. 476-497.

Luo, W., et al. 2006, *Topographically derived maps of valley networks and drainage density in the Mare Tyrrhenum quadrangle on Mars*, GRL, Vol. 33, pp. 18202.

Luo, W., et al. 2009, *Computer-generated global map of valley networks on Mars*, JGR, Vol. 114, pp. 11010.

Malin, M. C., et al. 1998, *Early views of the Martian surface from the Mars Orbiter Camera of Mars Global Surveyor*, Science, Vol. 279, pp. 1681-1685.

Malin, M. C., et al. 1999, *Groundwater formation of Martian valleys*, Nature, Vol. 397, pp. 589-592.

Malin, M. C., et al. 2000, *Evidence for recent groundwater seepage and surface runoff on Mars*, Science, Vol. 288, pp. 2330-2335.

Mangold, N. (2004), *Evidence for Precipitation on Mars from Dendritic Valleys in the Valles Marineris Area*, Science, Vol. 305, pp. 78–81.

Mangold, N. (2006), *Detailed study of an hydrological system of valleys, a delta and lakes in the Southwest Thaumasia region*, Icarus, Vol. 180, pp. 75-87.

Marks, D. J., et al. 1984, *Automated basin delineation from digital elevation data*, Geo-Processing, Vol. 2, pp. 299-311.

Masson, Ph., et al. 2004, *New observations of valley networks using THEMIS (Mars Odyssey) and HRSC data (Mars Express)*, Second Conference on Early Mars 2004, pp. 8019.

Matsubara, Y., et al. 2011, *Hydrology of early Mars: Lake basins*, JGR, Vol. 116, E04001.

McEwen, A., et al. 2011, *HISCI Experiment On Exomars Trace Gas Orbiter*, The Fourth International Workshop on the Mars Atmosphere: Modelling and observation, pp. 496-497.

McSween, H. Y., et al. 2004, *Basaltic Rocks Analyzed by the Spirit Rover in Gusev Crater*, Science, Vol. 305, pp. 842-845.

Mest, S. C., et al. 2010, *Watershed modeling in the Tyrrhena Terra region of Mars*, JGR, Vol. 115, pp. 9001.

Milton, D. J., et al. 1973, *Water and processes of degradation in the Martian landscape*, JGR, Vol. 78, pp. 4037-4047.

Molloy, I., et al. 2007, *Automatic mapping of valley networks on Mars*, Computer & Geosciences, Vol. 33, pp. 728-738.

Morgan, F., et al. 2011, *Improved Algorithm for CRISM Volcano Scan Atmospheric Correction*, 42nd Lunar and Planetary Science Conference, held March 7-11, 2011 at The Woodlands, Texas. LPI Contribution No. 1608, pp. 2453

Murchie, S., et al. 2007, *Compact Reconnaissance Imaging Spectrometer for Mars (CRISM) on Mars Reconnaissance Orbiter (MRO)*, JGR, Vol. 112, Issue E5, CiteID E05S03.

Neukum, G., et al. 2004, *HRSC: The High Resolution Stereo Camera of Mars Express.*. In Mars Express: The Scientific Payload, ESA SP-1240, ESA Publications Division, European Space Agency, Noordwijk, the Netherlands.

Noe Dobrea, E. Z., et al. 2013, *Hydrated Minerals on Endeavour Crater's rim, Interior, and Surrounding Plains: New Insights from CRISM Data*, 44th Lunar and Planetary Science Conference, held March 18-22, 2013 in The Woodlands, Texas. LPI Contribution No. 1719, pp. 3079.

O'Callaghan, J. F., et al. 1984, *The extraction of drainage networks from digital elevation data*, Computer Vision, Graphics and Image Processing, Vol. 28, pp. 323-344.

Orlandini, S., et al. 2012, *Evaluation of flow direction methods against field observations of overland flow dispersion*, Water Resources Research, Vol. 48, pp. 10523-10535.

Ori G. G., et al. 2000, *Martian paleolacustrine environments and their geological constrains on drilling operations for exobiological research*, Planet. Space Sci., Vol. 48, pp. 1027-1034.

Parker, T. J., et al. 1993, *Coastal geomorphology of the Martian northern plains*, JGR, Vol. 98, pp. 11061-11078.

Pelkey, S. M., et al. 2007, *CRISM multispectral summary products: Parameterizing mineral diversity on Mars from reflectance*, JGR, Vol. 112, E08S14.

Penido, J. C., et al. 2013, *Scaling relationships and concavity of small valley networks on Mars*, Planet. Space Sci., Vol. 75, pp. 105-116.

Peucker, T. K., et al. 1975, *Detection of surface specific points by local parallel processing of discrete terrain elevation data*, Computer Graphics and Image Processing, Vol. 4, pp. 375-387.

Pieri, D. C., 1976, *Distribution of small channels on the Martian surface*, Icarus, Vol. 27, pp. 25-50.

Pieri, D. C., 1979, *Global distribution of Martian valley systems*, Reports of Planetary Geology Program, pp. 353-356.

Pieri, D. C., 1980, *Geomorphology of Valleys on Mars: A summary of morphology, distribution, age, and origin*, Science, Vol. 210, pp. 895-897.

Pieri, D. C., 1981, *Morphology and network patterns of Martian valleys*, MSAIS, Vol. 52, pp. 483-486.

Pieri, D. C., 1983, *Martian Landforms*, Science, Vol. 220, pp. 847-848.

Pieri, D. C., 1984, *Junction angles in drainage networks*, JGR, Vol. 89, B8, pp. 6878-6884.

Pollack, J. B., et al. 1987, *The case for a warm wet climate on early Mars*, Icarus, Vol. 71, pp. 203-24.

Rieger, W., 1992, *Automated river line and catchment area extraction for DEM data*, Proceedings of the 17th ISPRS Congress.

Rosgen, D. L., 1994, *A classification of natural rivers*, Catena, Vol. 22, pp. 169-199.

Schon, S. C., et al., 2012, *An overfilled lacustrine system and progradational delta in Jezero crater, Mars: Implications for Noachian climate*, Planet. Space Sci., Vol. 67, pp. 28-45.

Schultz, P. H., et al. 1973, *Martian lineaments from Mariner 6 and 7 images*, JGR, Vol. 78, pp. 8415-8427.

Schumm, S., 1956, *Evolution of drainage systems and slopes in badland at Perth Amboy, New Jersey*, Bulletin of Geological Society of America, Vol. 67, pp. 597-646.

Seelos, F. P., et al. 2011, *CRISM Data Processing and Analysis Products Update - Calibration, Correction, and Visualization*, 42nd Lunar and Planetary Science Conference, held March 7-11, 2011 at The Woodlands, Texas. LPI Contribution No. 1608, pp.1438

Sharp, R. P., et al. 1975, *Channels on Mars*, Geol. Soc. Am. Bull., Vol. 86, Issue 5, pp. 593-609.

Shreve, R.L., 1966, *Statistical law of stream numbers*, Journal Geology, Vol. 74, pp. 17-37.

Smith, D.E., et al. 1999, *The global topography of Mars and implications for surface evolution*, Science Vol. 284, pp. 1495-1503.

Smith, D.E., et al. 2001, *Mars Orbiter Laser Altimeter: Experiment summary after the first year of global mapping of Mars*, JGR, Vol. 106, E10.

Soderblom, L. A., et al. 2004, *Soils of Eagle Crater and Meridiani Planum at the Opportunity Rover Landing Site*, Science, Vol. 305, pp. 1723-1726.

Som, S. M., et al. 2009, *Scaling relations for large Martian valleys*, JGR, Vol. 114, E02005.

Squyres, S. W., et al. 1994, *Early Mars: how warm and how wet?*, Science, Vol. 265, pp. 744-8.

Squyres, S. W., et al. 2004a, *The Spirit Rover's Athena Science Investigation at Gusev Crater, Mars*, Science, Vol. 305, pp. 794-800.

Squyres, S. W., et al. 2004b, *The Opportunity Rover's Athena Science Investigation at Meridiani Planum, Mars*, Science, Vol. 305, pp. 1698-1703.

Steel, R. G. D., et al. 1960, *Principles and Procedures of Statistics with Special Reference to the Biological Sciences.*, McGraw Hill, 1960, pp. 187, 287.

Stepinski, T. F., et al. 2003, *Drainage densities of computationally extracted Martian drainage basins*, 6th International Conference on Mars, Lunar and Planet. Inst., Pasadena, Calif.

Stepinski, T. F., et al. 2004, *Computational analysis of drainage basins on Mars:appraising the drainage density*, LPS XXXV, 2004.

Strahler, A.N., 1952, *Dynamic basis of geomorphology*, Geological Society of America Bulletin, Vol. 63, 923-938.

Szwast, M. A., et al. 2006, *Surface dust redistribution on Mars as observed by the Mars Global Surveyor and Viking orbiters*, JGR, Vol. 111, pp. 11008-11040.

Tanaka, K. L., 1986, *The Stratigraphy of Mars*, JGR, Vol. 91, pp. 139-158.

Tanaka, K. L., 2009, *Progress in Global Geologic Mapping of Mars*, 40th Lunar and Planetary Science Conference , id. 1975

Tarboton, D. G., 2003, *Terrain Analysis Using Digital Elevation Models in Hydrology*, 23rd ESRI International Users Conference, San Diego, California, July 7-11.

Vago, J.L., et al. 2010, *The ExoMars Rover Mission to Search for Signs of Life*. Astrobiology Science Conference 2010: Evolution and Life: Surviving Catastrophes and Extremes on Earth and Beyond, held April 26-20, 2010 in League City, Texas. LPI Contribution No. 1538, p.5318.

Vincenzo, G., et al. 2008, *Exomars mission description and architecture*. 37th COSPAR Scientific Assembly. Held 13-20 July 2008, in Montreal, Canada., p.1019.

Wetzel, R.G., and Likens, G.E.. 1991. *Limnological Analyses*. 2nd. Ed. Springer-Verlag. 391 pp.

Williams, R. M. E., et al. 2001, *Morphometric measurements of Martian valley networks from Mars Orbiter Laser Altimeter (MOLA) data*, JGR, Vol. 106, pp. 23737-23751.

Yamaguchi, Y., et al. 2009, *Mapping Valley Networks in the Noachian Terrain around Naktong Vallis, Mars: Topographic Control on Drainage Density*, 40th Lunar and Planetary Science Conference, (Lunar and Planetary Science XL), held March 23-27, 2009 in The Woodlands, Texas, id.1630.

Zuber, M. T., et al. 1992, *The Mars Observer laser altimeter investigation*, JGR, Vol. 97, pp. 7781-7797.

Zurek, R. W., et al. 2007, *An overview of the Mars Reconnaissance Orbiter (MRO) science mission*, JGR, Vol. 112, Issue E5, CiteID E05S01.

I would personally thank my father Roberto, my mother Antonella and my sister Giuliana, because they are MY example of life I have always followed: they have taught me how to work and how to achieve my dreams through perseverance and self-sacrifice. I thank my beloved grandmother Lucilla, She is always there, I feel constantly Her presence, She is the brightest star in my Firmament.

I warmly thank my California family, first of all Prof. Marcello Coradini who is not my boss, he is my friend. He brought me to California, at the Jet Propulsion Laboratory, he helped me in settling down like a father would have done, he hosted me at his house, he introduced me to LA parties (!!!), he cooked for me, he run with me, we traveled together around California, Arizona & Nevada. Our scientific discussions about Martian paleohydrology lead to this PhD Thesis. He also read and corrected my entire PhD Thesis, improving the quality of it. Thank you Marcello for all the support you have given me and of course... thank you for bringing me to IKEA, and for bringing me out of that store when I started becoming compulsive in front of the different types of pillows, scented candles, and colored frames! I thank Dr Karen McBride for her kindness, friendliness, for our runs in Culver city, for introducing me to Trader Joe's and hosting me together with Marcello the first days I've arrived in LA. I thank them both for the experiences we all shared together, you guys are family!

I would like to thank my girlfriend Claudia for having accepted my scientific insanity. Thank you for having me helped in the darkest moments, truly supporting me: shining again has been made easier thanks to your help.

I thank Dr Dave Pieri for introducing me to JPL and to the Martian paleohydrology. Thank you Dave for our Martian discussions and for helping me when the several JPL bureaucratic storms appeared on the horizon: your help has been constant and fundamental.

I thank Prof. Barbieri for introducing me to the OSIRIS Rosetta team making my future come true and giving me the freedom and the support to go to JPL to follow my Martian dream.

Thanks to Dr Monica Lazzarin for sustaining me throughout the entire PhD period, permitting me to go to to several meetings presenting our work on Phobos: she supported my Phobos papers more then anyone else.

I would like to thank Dr Sara Magrin and Dr Ivano Bertini for teaching me how to carry out my research work with firmness, calmness, perseverance and tranquillity.

I'm deeply grateful to Dr Fedele Colosimo, our talks together all around California & Little Tokio, all the experiences we shared together, the hand made pasta, will be the SoCal brightest memories I will keep in my mind and heart.

Thanks to Dr Emanuele Baratti for his friendship and his scientific rigor and reliability, it is has been a great fortune to start working together on the Mars paleohydrology.

Thanks to Dr Andrea Sottoriva for hosting me a week at his home in Pasadena and thanks to Dr Francesco Marsili for our great parties together. Both Andrea and

Francesco gave me such important working advices, which made me clearer the scientific path I want to follow. Thank you guys because surfing with you has been exciting and unique.

I warmly thank the city of Los Angeles and the entire Southern California, you stay classy, hella classy ma dear!